



UNIVERSITÀ
DEGLI STUDI
FIRENZE

PhD in
Physics and Astronomy

CYCLE XXXVII

COORDINATOR Prof. Giovanni Modugno

**Ultracold ${}^6\text{Li}$ - ${}^{53}\text{Cr}$ Fermi mixtures:
From resonantly interacting fermions
to paramagnetic bosonic dimers**

Academic Discipline (SSD) FIS/03

Doctoral Candidate
Dr. Finelli Stefano

Stefano Finelli

Supervisors

Dr. Zaccanti Matteo
Prof. Modugno Giovanni

Matteo Zaccanti

Giovanni Modugno

Coordinator
Prof. Modugno Giovanni

Giovanni Modugno

The consultation of the thesis is free. Unless a specific authorization is obtained from the author, the thesis can be, however, downloaded and printed only for strictly personal purposes related to study, research and teaching, with the explicit exclusion of any use that has – even indirectly – a commercial nature.



UNIVERSITÀ
DEGLI STUDI
FIRENZE

DIPARTIMENTO DI FISICA E ASTRONOMIA

CORSO DI DOTTORATO
IN FISICA E ASTRONOMIA

Ultracold ${}^6\text{Li}$ - ${}^{53}\text{Cr}$ mixtures: From resonantly interacting fermions to paramagnetic bosonic dimers

Candidate

Stefano Finelli (ID number DT31249)

Thesis Advisor

Dr. Matteo Zaccanti

Co-Advisor

Prof. Giovanni Modugno

Academic Year 2023/2024

Thesis defended on June 16, 2025
in front of a Board of Examiners composed by

Prof. Gabriele Ferrari

Prof. Marco Fattori

Prof. Pierbiagio Pieri

Ultracold ${}^6\text{Li}$ - ${}^{53}\text{Cr}$ mixtures: From resonantly interacting fermions to paramagnetic bosonic dimers

Ph.D. Thesis, University of Florence

2025 Stefano Finelli.

This thesis has been typeset by \LaTeX and the UniFiTh class.

Version: June 30, 2025

Author's email: stefano.finelli@unifi.it

“Fermions are real individualists!”
– Deborah S. Jin

Abstract

In this Thesis, I report on the main scientific results that I obtained during my Ph.D., carried out at the University of Florence in the Li-Cr lab, under the supervision of Dr. Matteo Zaccanti and Prof. Giovanni Modugno. My research activity on Li-Cr began with my Master Thesis and seamlessly progressed into my doctoral studies. During these years, starting from an early-stage experiment, we significantly advanced in the exploration and understanding of such a novel system, so far uniquely available in our lab worldwide, achieving numerous important scientific breakthroughs.

Our first major result is the realization of quantum degenerate Fermi mixtures of ultracold ${}^6\text{Li}$ alkali and ${}^{53}\text{Cr}$ transition-metal atoms. We have devised and optimized a simple and robust cooling strategy, based on an all-optical approach with an overall duty cycle of about 13 s, with which we routinely produce large samples of more than 4.5×10^5 ${}^6\text{Li}$ and 1.5×10^5 ${}^{53}\text{Cr}$ atoms. Both components are quantum degenerate, at final temperatures around 200 nK. More specifically, in our experimental sequence atoms are first collected in a double-species magneto-optical trap (MOT), where different laser cooling stages are applied to reach temperatures of a few hundreds of microkelvins, close to the Doppler limit. Within an overall MOT loading time of 8 s, we produce cold clouds containing up to 10^9 ${}^6\text{Li}$ and 8×10^7 ${}^{53}\text{Cr}$ atoms, at temperatures of about 300 μK . The significant gain in the collected ${}^{53}\text{Cr}$ MOT atom number, relative to previous studies, is achieved by finding an experimental configuration where light-assisted losses are drastically suppressed for such species. Lithium and chromium atoms are then directly loaded from the MOT into a bichromatic optical dipole trap (bODT), realized by overlapping a high-power infrared laser beam (confining more tightly Li than Cr) with a green beam at 532 nm (tightly confining Cr and anti-confining Li). The choice of this trap, primarily motivated by the possibility to tune the (absolute and relative) trap depth of both species during the final evaporation stage, is also found to be rather convenient to circumvent a known technical challenge connected with the direct loading of chromium from the MOT into a purely infrared (IR) optical trap: In fact, this was found problematic, due to a detrimental light shift of the Cr cooling transition caused by the intense IR beam. However, thanks to nearby transitions at 533 nm, connecting the excited 7P_4 level to ${}^7D_{3,4,5}$ states, the green light in our bODT can be efficiently exploited to (over)compensate for the IR-induced redshift, creating a “safe” dark spot for chromium atoms in correspondence of the optical trap. In this way, we are able to load the bODT with more than 4×10^6 ${}^{53}\text{Cr}$ atoms, together with roughly 2×10^7 ${}^6\text{Li}$ atoms, at temperatures of about 250 μK . We subsequently reach the ultracold regime through efficient evaporative cooling of the two lowest Zeeman states of lithium, performed slightly above the broad homonuclear Feshbach resonance at 832 G, and simultaneous sympathetic cooling of the chromium component, polarized in its lowest Zeeman sublevel. After a 5-s-long evaporation stage, only slightly longer than the optimum one for single-species Li samples, we obtain spin-polarized Fermi mixtures comprising up to 3.5×10^5 ${}^6\text{Li}$ and 1×10^5 ${}^{53}\text{Cr}$, at ultralow temperatures of about 200 nK. In this configuration, i.e. within the sole main bODT, lithium is deeply degenerate with $T_{\text{Li}}/T_{\text{F,Li}} \sim 0.2$, while chromium only features a “mild” degeneracy, with $T_{\text{Cr}}/T_{\text{F,Cr}} \sim 0.5$. We overcome this issue by exploiting an additional bichromatic optical dipole trap, which crosses the main one from the vertical direction, and thus allows us to significantly increase the confinement along the main bODT axis. Such a crossed bODT enables the access to a broad parameter space, where we can controllably vary the density and degree of degeneracy of the two components almost independently. This allows us to reach configurations where both species show $T/T_{\text{F}} \simeq 0.25$. Remarkably, our strategy also provides an efficient pathway to produce single-species Fermi gases, or spin mixtures, of ultracold (weakly) dipolar ${}^{53}\text{Cr}$ atoms.

Our progress toward quantum degeneracy was accompanied (and indeed enabled) by a parallel, thorough investigation of the elastic and inelastic collisional properties of our novel fermionic mixture. By performing extensive loss spectroscopy on six different scattering channels, we discovered more than 50 interspecies ${}^6\text{Li}$ - ${}^{53}\text{Cr}$ Feshbach resonances (FRs), well isolated from each other and exhibiting a non-chaotic pattern. Our experimental data provided the fundamental input to build a full coupled-channel model for the Li-Cr system, which was developed by our theory collaborator Prof. A. Simoni, world-renown expert in such calculations. Importantly, his model allowed us to connect all observed features to well-defined LiCr molecular levels with known quantum numbers, and provides us accurate knowledge of two-body Li-Cr interactions. In particular, we identified and characterized a subset of high-field s -wave FRs, with magnetic-field widths of about 0.5 G, featuring a character similar to Li-K ones but immune to two-body losses. Despite their comparatively narrow nature, combined with their high-field location above 1.4 kG, these FRs enable resonant control of Li-Cr interactions. In addition, exciting future prospects are offered by the presence of peculiar p -wave resonances with anomalously large splitting of the three m_ℓ components, that are thus intrinsically chiral in nature.

The existence of suitable s -wave ${}^6\text{Li}$ - ${}^{53}\text{Cr}$ FRs also provides an optimal starting point for the formation of bosonic Feshbach dimers. During the second part of my Ph.D. period, we have successfully produced ultracold gases comprising up to 5×10^4 ${}^6\text{Li}$ - ${}^{53}\text{Cr}$ Feshbach molecules, at temperatures around 200 nK and peak phase-space densities exceeding 0.1. Leveraging on the immunity to two-body decay and on the good collisional stability against three-body recombination of our fermionic mixture, we achieved efficient magneto-association with ramp rates slower than the two-body-adiabatic regime by more than two orders of magnitude. We directly confirmed the paramagnetic nature of LiCr molecules through Stern-Gerlach-type experiments, and demonstrated precise control of their quantum state via a novel optical measurement of the open-channel fraction and binding energy. Moreover, through the characterization of the dominant loss mechanisms affecting our Feshbach dimers, we have identified an experimental configuration where their lifetime exceeds 0.2 s.

Parallel to our experimental progress, our theory collaborator Prof. M. Tomza and his group developed a state-of-the-art quantum chemical model for the LiCr molecule, with which they could accurately predict the properties of its ground and excited electronic states. In particular, their *ab initio* model – which is able to reproduce the experimentally determined value of the Li-Cr octet scattering length – predicts a large electric dipole moment (exceeding 3 D) for the rovibrational $X \Sigma^+$ ground state, which adds to the sizable magnetic one of $5 \mu_B$. Furthermore, the results of M. Tomza and colleagues suggest that our Feshbach dimers, already created in the least bound rotationless level of the $X {}^6\Sigma^+$ electronic ground state, could be efficiently transferred to the absolute rovibrational ground state via stimulated Raman adiabatic passage, with optical transitions at experimentally accessible wavelengths.

Within the very last months of my Ph.D., I have also performed a characterization of the transport properties of lithium impurities, resonantly interacting with a surrounding, non-degenerate gas of chromium atoms, which acts as a thermal bath for the Li component. By exploring different temperature and density regimes of our mixture, and exploiting the magnetic control of the interspecies interactions enabled by the same s -wave resonance employed for the realization of LiCr dimers, we have revealed a rather unexpected and surprising behavior, that has not found a conclusive explanation at the time of the submission of this Thesis. Contrarily to the case of homonuclear Fermi mixtures, that in the strongly-interacting region were found to exhibit a minimum of the diffusion coefficient of only a few “quanta of diffusion” \hbar/m_{Li} when approaching quantum degeneracy ($T/T_F \sim 1$), in

our experiment we disclosed a low-temperature regime in which the lithium impurities feature anomalous dynamics. Specifically, the mean square displacement of a Li cloud, once released within the Cr gas and under resonantly-interacting conditions, was found to grow sub-linearly in time, in contrast with the linear trend characterizing normal diffusive transport. When this regime was accessed in the experiment, the expansion of the lithium cloud became extremely slow, marked variations from a Gaussian density envelope were revealed, and a sizable portion of the atomic distribution was found to be essentially stuck over the whole observation time. These latest results share intriguing similarities with previous experimental observation reported for matter-wave transport in disordered media: Indeed, our findings appear consistent with a picture in which heavy Cr atoms effectively act for the light Li impurities as a quasi-static, random potential landscape of point-like scatterers, promoting their localization due to quantum interference effects. While our findings lack a rigorous theoretical understanding, yet, they provide a first, clear example of how a large mass asymmetry can profoundly impact on the many-body dynamics of ultracold Fermi mixtures, fostering qualitatively new phenomena already in the non-degenerate regime, with respect to their equal-mass, homonuclear counterparts. The realization of this novel ${}^6\text{Li}$ - ${}^{53}\text{Cr}$ Fermi mixture with tunable interactions, and its first exploitation in the context of ultracold molecule formation and of quantum transport experiments – successfully achieved during the three years of my Ph.D., pave the way to a wealth of several future developments: From the investigation of a variety of few- and many-body phenomena of highly-correlated fermionic matter completely unexplored, yet, to the realization of quantum gases of paramagnetic polar molecules, and their subsequent application as novel kinds of quantum simulators.

Contents

Introduction	xi
List of publications	xv
1 Elements of scattering theory	1
1.1 Basics of two-body scattering	1
1.2 Low-energy scattering	3
1.3 Resonant scattering	4
1.4 Magnetic Feshbach resonances	5
1.5 Scattering near a narrow Feshbach resonance	6
1.6 Feshbach molecules	7
1.7 Zero-range approximation in a real physical system	8
2 Production of degenerate ${}^6\text{Li}$-${}^{53}\text{Cr}$ Fermi mixtures	11
2.1 Overview of the experimental apparatus	12
2.2 ${}^6\text{Li}$ MOT	13
2.3 ${}^{53}\text{Cr}$ MOT	14
2.4 Optimized loading of a dual species ${}^6\text{Li}$ - ${}^{53}\text{Cr}$ MOT	18
2.5 Loading into a bichromatic optical dipole trap	18
2.6 Evaporative and sympathetic cooling stages	23
2.7 Enhanced thermalization near a narrow Feshbach resonance	26
2.8 Increasing quantum degeneracy in a crossed bODT	29
2.9 Conclusive remarks	31
3 Feshbach spectrum and collisional properties of ${}^6\text{Li}$-${}^{53}\text{Cr}$ mixtures	33
3.1 Feshbach loss spectroscopy	34
3.2 Coupled-channel model	37
3.2.1 Origin of the low-field p -wave resonance patterns	38
3.2.2 Testing the model on a high-field resonance	40
3.3 Resonantly-interacting Li-Cr Fermi mixtures	41
3.3.1 The coupled oscillator model	44
3.3.2 Transition from the collisionless to the collisionally hydrodynamic regime	45
3.4 Collisional stability of the atomic mixture	46
3.5 Conclusive remarks	49
4 Making, probing and understanding LiCr Feshbach molecules	51
4.1 Parent atomic mixture and typical initial conditions	52
4.2 Detection of LiCr dimers	53
4.3 Magneto-association and two-body adiabaticity	55
4.4 Optimization and molecule PSD	57
4.5 Trap-light-induced losses	59
4.6 Stability of atom-molecule mixtures	61
4.7 Magnetic dipole moment of LiCr Feshbach dimers	62
4.8 New optical measurement of open-channel fraction and binding energy	65
4.9 Realization of pure, long-lived molecular samples	69

4.9.1	Probing the purity of molecular samples: experimental protocols . . .	70
4.10	Quantum chemical model of LiCr: Summary of LiCr properties	73
4.10.1	Ground state properties	73
4.10.2	Excited electronic states	74
4.10.3	Prospects for STIRAP	75
4.11	Conclusive remarks	78
5	Anomalous diffusion of light impurities in a heavy fermion gas	79
5.1	Normal and anomalous diffusion	83
5.2	Sample preparation	88
5.3	Semi-classical Monte Carlo simulator	94
5.3.1	Numerical simulator: basic form	94
5.3.2	Wigner’s retardation time	99
5.4	The “high-temperature” regime	103
5.5	The “low-temperature” regime	111
5.6	Temperature dependence of the subdiffusive dynamics	118
6	Technical upgrades of the experimental setup	125
6.1	Magnetic field stabilization	125
6.2	High-field imaging setups	128
6.3	FORT optical setup	130
6.4	Double-loading scheme for lithium	131
	Conclusions and outlook	135
	Acknowledgments	139

Introduction

Strongly interacting quantum mixtures composed of two unequal kinds of fermionic particles, such as quarks of different colors or electrons belonging to different lattice bands, exhibit a great variety of exotic phenomena [1–6], qualitatively distinct from those characterizing single-component, mass-balanced systems. The interplay between quantum statistics, mass asymmetry, and a different response to external fields indeed provides an increased level of complexity, with a strong impact both at the few- and many-body level. In particular, this holds true for ultracold mixtures of chemically different atomic species: The combination of strong and tunable inter-species interactions, enabled by the presence of Feshbach resonances (FRs) [7], with a heavy-light mass imbalance, $M > m$, is predicted to promote a variety of unconventional regimes that are hard, or even impossible to attain with their homonuclear counterparts.

At the few-body level, notable examples are peculiar few-particle clusters predicted to form for mass ratios in the range $8.2 \leq M/m \leq 13.6$ [8–22]. These elusive *non-Efimovian* states, still lacking direct experimental detection thus far,¹ are expected to exhibit universal character and to be characterized by a distinctive *p*-wave orbital symmetry. Notably, they are extremely relevant also from a many-body viewpoint, in light of their expected collisional stability. In fact, owing to the halo nature of such *non-Efimovian* clusters, largely exceeding in size the van der Waals range of the interatomic interaction potential, their existence is expected not to trigger an increase of inelastic decay processes [14], in stark contrast to the widely explored *Efimovian* case [8, 24–29]. Therefore, the presence of fermionic trimers [9, 13, 17] and bosonic tetramers [15, 20] – predicted to exist in three dimensions for $8.17 \leq M/m \leq 13.6$ [9] and $8.86 \leq M/m \leq 13.6$ [20], respectively – may uniquely allow one to experimentally attain qualitatively new many-body regimes, within which strong few-body correlations add to, or may even possibly overcome, the standard two-body ones [30, 31]. These new appealing scenarios, characteristic of mass-imbalanced fermionic systems, include novel types of impurity physics [32–35] and mediated quasiparticle interactions [36–38], which in turn may promote the emergence of elusive many-body states featuring unconventional superfluid pairing [30, 39–49] or peculiar magnetic phases [50–54].

Moreover, weakly bound (bosonic) dimers created from a mass-imbalanced Fermi mixture – thanks to their increased collisional stability near a *s*-wave FR, inherited from the fermionic statistics [55, 56] – represent an appealing starting point to realize ultracold gases of ground-state polar molecules [57–62]. Notably, ultracold samples of molecules with permanent electric dipole moments offer unprecedented opportunities to investigate novel quantum chemistry and many-body physics [63–65]. In particular, *doubly-polar* molecules, possessing both an electric and a magnetic dipole moment, have recently attracted great attention, as they could offer even richer prospects: while the electric dipole gives rise to the long-range anisotropic interactions, the magnetic one, arising from a nonzero electronic spin, provides an additional degree of tunability in the system, compared to singly-polar compounds. A high phase-space density gas of such doubly-polar molecules may open up new venues in the context of quantum simulation [66–69] and computation [70, 71], as well as quantum controlled chemistry [72]. This is exemplified by the pioneering work on excited-state NaLi dimers [73], which – despite featuring weak electric and magnetic dipole moments – provided new insights into ultracold reactive collisions [72, 74].

¹Indirect few-body effects related to the existence of fermionic trimers have been disclosed in Li-K mixtures, see Ref. [23].

Despite tremendous progress in the field [75], realization of quantum degenerate gases of doubly-polar molecules remains an unsurpassed challenge. To date, the only experimental realizations of degenerate gases of ground-state singly-polar molecules [76–78] exploit ultracold atomic mixtures as their starting point: Atom pairs are first converted into weakly bound molecules by sweeping the magnetic field across a Feshbach resonance, and then transferred to the absolute molecular ground state via stimulated Raman adiabatic passage (STIRAP) [79]. However, this two-step method has only been demonstrated on bi-alkali systems, whose ground state has zero electronic spin, and thus negligible magnetic moment. Combining alkali species with closed-shell atoms, which would endow ground-state molecules with the additional spin and magnetic moment, is currently under investigation, following the experimental discovery of FRs in alkali-alkaline-earth systems [80–82]. Yet, the extremely narrow character of such resonances, despite impressive technical effort [83], has so far hindered the first association step. Another proposed pathway to realize *paramagnetic* ground-state molecules relies on binding highly magnetic lanthanides with either alkali or closed-shell elements [84], and association of ultracold KDy Feshbach dimers has indeed been recently demonstrated [85]. Nonetheless, STIRAP transfer of such molecules to their absolute ground state appears a formidable challenge, owing to the lack of spectroscopic data combined with the complex electronic configuration of these elements, which makes *ab initio* methods poorly reliable, if not unemployable.

During my Ph.D., carried out in the Li-Cr lab in Florence under the supervision of Dr. Matteo Zaccanti, I addressed four different main topics: (i) The experimental realization of a novel degenerate Fermi mixture made of ${}^6\text{Li}$ alkali and ${}^{53}\text{Cr}$ transition-metal atoms; (ii) the extensive characterization of elastic and inelastic scattering properties of the ${}^6\text{Li}$ - ${}^{53}\text{Cr}$ system; (iii) the realization and characterization of large ultracold gases of bosonic paramagnetic LiCr Feshbach molecules, featuring phase-space densities exceeding 0.1 and lifetimes longer than 0.2 s; and (iv) an ongoing study of transport properties of Li impurities embedded within a larger Cr bath, exploring different temperature and interaction regimes.

The choice to experimentally realize and explore such a novel system was originally motivated by two main reasons: First, the special chromium-lithium mass ratio, $M_{\text{Cr}}/m_{\text{Li}} \simeq 8.8$, is extremely close to the aforementioned critical values above which both three- and four-body *non-Efimovian* states are predicted to emerge [9, 13, 15, 17, 20], potentially making such a bi-atomic combination an unparalleled framework to explore a different class of elastic few-body effects and their impact at the many-body level [17, 20]: For instance, this non-trivial and rather unusual few-body physics could lead to the emergence of novel types of quasi-particles in the investigation of the light impurity problem [32, 35], and trigger the emergence of exotic superfluid and normal states, such as trimer Fermi gases [30], or so-called quartet superfluidity of shallow bosonic tetramers [31]. In addition, in the regime of strong repulsive interactions, three-body recombination processes are predicted to be drastically suppressed for the specific $M_{\text{Cr}}/m_{\text{Li}}$ mass ratio [86]. Li-Cr Fermi mixtures thus may represent also a pristine platform to explore Stoner’s ferromagnetism [87] and related phenomena [88–92], immune to the pairing instability.

Secondly, from a molecular perspective, binding lithium alkali with transition-metal chromium atoms appears as an extremely promising route toward ground-state doubly-polar molecules. In fact, the interaction between Li (${}^2S_{1/2}$) and Cr (7S_3) has only weak magnetic anisotropy and leads to two spin multiplicities, similarly to standard bi-alkali systems. While the latter feature a singlet ($X\ {}^1\Sigma^+$) ground and a triplet ($a\ {}^3\Sigma^+$) first excited state [7], the LiCr system exhibits a *sextet* ($X\ {}^6\Sigma^+$) and an *octet* ($a\ {}^8\Sigma^+$) symmetry. In its absolute ground state, the LiCr molecule is thus expected to combine a high electronic spin with a strong $\text{Li}^{\delta+}\text{Cr}^{\delta-}$ dipolar character [93]. Most importantly, the existence of just two spin

multiplicities, combined with the almost isotropic van der Waals interactions, makes the creation of ground-state LiCr molecules experimentally feasible with current technology: On the one hand, it leads to non-chaotic, bi-alkali-like Feshbach spectra, well suited for molecule association. On the other hand, it allows for state-of-the-art molecular structure calculations with predictive power over ground and lowest-lying electronic states, considerably simplifying the task of finding suitable STIRAP paths. In particular, recent *ab initio* calculations carried out by M. Tomza’s group [94] foresee, for the LiCr absolute ground state $X\ ^6\Sigma^+$ (first excited state $a\ ^8\Sigma^+$), a sizable electric dipole moment exceeding 3 D (0.7 D). This, combined with the magnetic one of $5\ \mu_B$ ($7\ \mu_B$), strongly motivates the choice of Li-Cr mixtures to realize ultracold paramagnetic polar molecules.

This Thesis is organized as follows:

- First, in Chapter 1, I summarize a few key concepts of low-energy scattering theory, relevant to describe pairwise collisions between neutral atoms at ultralow temperatures. In particular, I highlight the role of Feshbach resonances, emphasizing the difference between *broad* and *narrow* ones.
- Second, in Chapter 2, I provide an overview of the experimental protocols we devised and optimized to produce quantum degenerate mixtures of fermionic ^6Li and ^{53}Cr atoms. The procedures described in this Chapter represent the foundation for the studies presented in the subsequent ones.
- In Chapter 3, I present the results of our thorough characterization of the elastic and inelastic scattering properties of ^6Li - ^{53}Cr mixtures. Our experimental effort to unveil more than 50 interspecies FRs constituted the necessary input for a full coupled-channel model [7], developed by our collaborator Prof. A. Simoni, that is able to unambiguously assign the features we observed to well-defined LiCr molecular states. In particular, we identified and characterized a set of high-field *s*-wave FRs, with magnetic field widths of about 0.5 G, that provide an optimal starting point to form (bosonic) Feshbach dimers.
- In Chapter 4, I report on our experimental findings concerning the production, characterization, and optimization of high phase-space density gases of ultracold bosonic LiCr Feshbach molecules, of which we directly revealed the paramagnetic nature and demonstrated precise control over their internal quantum state. Parallel to our progress in the lab, our collaborator Prof. M. Tomza and his group developed a state-of-the-art *ab initio* quantum chemical model for the LiCr molecule, with which they predict a sizable electric dipole moment, exceeding 3 D, in the absolute ground state. Additionally, their model provides fundamental guidelines for the future identification and implementation of suitable STIRAP transfer schemes.
- In Chapter 5, I present the main results of a (still partially ongoing) investigation of transport properties in our system. By studying the expansion of a small thermal gas of Li atoms, acting as “light impurities”, embedded within a larger Cr gas, playing the role of a medium of “heavy fermions”, we observed a progressive transition from the ballistic to the diffusive regime, as the collision rate was resonantly enhanced near a *s*-wave FR. Furthermore, for sufficiently low temperatures, the slowest observed dynamics showed strong signatures of *sub-diffusive* behavior, a feature often interpreted as a precursor of localization effects. I personally developed a semi-classical Monte Carlo simulator to analyze and interpret our measurements. Interestingly, the simulator is able to describe the dynamics in the high-temperature regime remarkably well, but it fails to reproduce the observed *sub-diffusive* dynamics at low temperatures.

This suggests that non-trivial, beyond-two-body quantum interference effects, not included in my semi-classical simulation, may play an important role in this regime, promoting anomalous transport dynamics and, possibly, fostering the emergence of an Anderson-like localized state.

- Finally, in Chapter 6, I briefly describe the main technical upgrades to the experimental setup that I contributed to implement during my Ph.D.

List of publications

The research topics presented in this Thesis have been published in the following papers:

- A. Ciamei, S. Finelli, A. Trenkwalder, M. Inguscio, A. Simoni, and M. Zaccanti, *Exploring ultracold collisions in ${}^6\text{Li}$ - ${}^{53}\text{Cr}$ Fermi mixtures: Feshbach resonances and scattering properties of a novel alkali-transition metal system*, Phys. Rev. Lett. **129**, 093402 (2022)
- A. Ciamei, S. Finelli, A. Cosco, M. Inguscio, A. Trenkwalder, and M. Zaccanti, *Double-degenerate Fermi mixtures of ${}^6\text{Li}$ and ${}^{53}\text{Cr}$ atoms*, Phys. Rev. A **106**, 053318 (2022)
- S. Finelli, A. Ciamei, B. Restivo, M. Schemmer, A. Cosco, M. Inguscio, A. Trenkwalder, K. Zaremba-Kopczyk, M. Gronowski, M. Tomza, and M. Zaccanti, *Ultracold LiCr: A new pathway to quantum gases of paramagnetic polar molecules*, PRX Quantum **5**, 020358 (2024)

Chapter 1

Elements of scattering theory

In this Chapter, I briefly recall a few key concepts of scattering theory that will be useful through the rest of this manuscript. Specifically, I will focus on the case of ultracold *s*-wave collisions near a *narrow* Feshbach resonance [7], which is particularly relevant for the Li-Cr system (see Chapter 3). This introduction is by no means an exhaustive review of the subject: rather, it has to be considered as a practical way to introduce the relevant quantities and the adopted notation. A more detailed discussion can be found in several textbooks, see e.g. Refs. [95–101], and partially in my Master Thesis [102].

This Chapter is organized as follows:

- In Sec. 1.1, I briefly introduce the two-body scattering problem in non-relativistic quantum mechanics, showing the connection between the main relevant quantities and the scattering amplitude.
- In Sec. 1.2, I focus the discussion on the low-temperature regime, relevant to describe collisions between pairs of non-magnetic ultracold atoms.
- In Sec. 1.3, I provide a short overview of resonant scattering, remarking the connection between the scattering length a , the effective range parameter R^* , and the intrinsic parameters of the scattering resonance.
- In Sec. 1.4, I introduce (magnetic) Feshbach resonances (FRs), showing how the scattering length can be effectively tuned near the resonance pole.
- In Sec. 1.5, I remark on the distinction between *broad* and *narrow* FRs, highlighting a few key aspects of elastic scattering near a narrow resonance.
- In Sec. 1.6, I summarize the main properties of Feshbach molecules, focusing mainly on their binding energy, magnetic moment, and on the role of the *closed-channel fraction*.
- Finally, in Sec. 1.7, I briefly compare the main results summarized in this Chapter with the case of a real physical system.

1.1 Basics of two-body scattering

Let us consider binary collisions of neutral atoms at ultra-low temperatures, interacting via a *short-ranged*, central potential $V(r)$, where $\vec{r} = \vec{r}_1 - \vec{r}_2$, and $\vec{r}_{1,2}$ are the positions of the two atoms. The problem can be tackled in the center of mass frame, where the Schrödinger equation reads

$$\left[\frac{p_{\text{rel}}^2}{2m_{\text{red}}} + V(r) \right] \psi(\vec{r}) = E \psi(\vec{r}), \quad (1.1)$$

where $m_{\text{red}} = m_1 m_2 / (m_1 + m_2)$ is the reduced mass, $\vec{p}_{\text{rel}} = \hbar \vec{k}_{\text{rel}} = m_{\text{red}} (\vec{v}_1 - \vec{v}_2)$ is the relative momentum,¹ and $E = (\hbar k_{\text{rel}})^2 / (2m_{\text{red}}) > 0$ is the scattering energy. We can model the incoming effective single-particle wavefunction ψ_i with a plane wave propagating

¹Note the difference between \vec{p}_{rel} and $\vec{p}_1 - \vec{p}_2$ in the mass-imbalanced case $m_1 \neq m_2$.

along the z -axis, and (at large distances) the scattered fraction $\psi_s - \psi_i$ with an outgoing spherical wave, the amplitude of which is defined as the *scattering amplitude* $f(k_{\text{rel}}, \vartheta)$:

$$\psi_i(\vec{r}) \simeq e^{i k_{\text{rel}} z} \quad (1.2a)$$

$$\psi_s(\vec{r}) \simeq e^{i k_{\text{rel}} z} + f(k_{\text{rel}}, \vartheta) \frac{e^{i k_{\text{rel}} r}}{r} \quad (\text{for large } r). \quad (1.2b)$$

In Eq. (1.2b) we assumed elastic scattering (i.e. k_{rel} is conserved) and cylindrical symmetry. The scattering amplitude encodes all the information about the collision: For instance, it can be readily shown [97] that its squared modulus directly equals the differential (elastic) scattering cross section $d\sigma/d\Omega$, such that the total one is given by

$$\sigma_{\text{el}}(k_{\text{rel}}) = 2\pi \int_0^\pi d\vartheta \sin(\vartheta) |f(k_{\text{rel}}, \vartheta)|^2. \quad (1.3)$$

One way of treating the scattering problem relies on the partial-wave expansion of the incident and scattered waves. After some algebraic manipulations, one finds [102]:

$$f(k_{\text{rel}}, \vartheta) = \frac{\sqrt{4\pi}}{k_{\text{rel}}} \sum_{\ell=0}^{\infty} \sqrt{2\ell+1} e^{i\delta_\ell(k_{\text{rel}})} \sin(\delta_\ell(k_{\text{rel}})) Y_{\ell,0}(\vartheta), \quad (1.4a)$$

$$\sigma_{\text{el}}(k_{\text{rel}}) = \frac{4\pi}{k_{\text{rel}}^2} \sum_{\ell=0}^{\infty} (2\ell+1) \sin^2(\delta_\ell(k_{\text{rel}})) = \frac{4\pi}{k_{\text{rel}}} \Im \left[f(k_{\text{rel}}, \vartheta=0) \right], \quad (1.4b)$$

where $Y_{\ell,m}(\vartheta, \phi)$ are the spherical harmonics, and $\delta_\ell(k_{\text{rel}})$ the scattering phase shifts, which completely determine $f(k_{\text{rel}}, \vartheta)$. In Eq. (1.4b), one can see that the maximum contribution of each partial wave to the total cross section, the so-called *unitary limit*, is set by $4\pi(2\ell+1)/k_{\text{rel}}^2$, and it is reached when $\delta_\ell(k_{\text{rel}}) = \pi/2 + n\pi$ ($n \in \mathbb{Z}$). Further, the last relation in Eq. (1.4b), known as the *optical theorem*, essentially expresses the conservation of the probability current [97]: In other words, the scattering cross section quantifies the removal of particles from the incident flux.

I note here that, from Eq. (1.4a), one can conveniently define the partial scattering amplitudes $f_\ell(k_{\text{rel}})$ as

$$f_\ell(k_{\text{rel}}) = \frac{1}{k_{\text{rel}}} e^{i\delta_\ell(k_{\text{rel}})} \sin(\delta_\ell(k_{\text{rel}})) = \frac{1}{k_{\text{rel}} \cot(\delta_\ell(k_{\text{rel}})) - ik_{\text{rel}}}. \quad (1.5)$$

Importantly, I also remark that in the case of two indistinguishable particles, Eqs. (1.4) must be modified to take into account the symmetry (antisymmetry) properties of the pair of bosons (fermions) under particle exchange: Given that the spherical harmonics have $(-1)^\ell$ parity, the partial wave expansion for identical bosons (fermions) will contain only even (odd) waves. Moreover, a factor of 2 appears in front of Eq. (1.4b) for identical particles, arising from the (anti-)symmetrization of the wavefunction.

From the scattering cross section, assuming an ensemble of fixed scattering centers with constant density n_{scatt} ,² one retrieves the (elastic) scattering rate Γ_{el} , which quantifies the number of collision events per unit time (for each incident particle):

$$\Gamma_{\text{el}}(k_{\text{rel}}) = n_{\text{scatt}} \sigma_{\text{el}}(k_{\text{rel}}) v_{\text{rel}} = \frac{4\pi \hbar}{m_{\text{red}}} n_{\text{scatt}} \Im \left[f(k_{\text{rel}}, \vartheta=0) \right], \quad (1.6)$$

with $v_{\text{rel}} = \hbar k_{\text{rel}}/m_{\text{red}}$, and having used Eq. (1.4b). Furthermore, the scattering amplitude $f(k_{\text{rel}}, \vartheta)$ also provides information about the energy shift $\hbar \delta\nu_{\text{mf}}$, experienced by one

²In the more general case of a inhomogeneous ensemble of *thermal* scatterers, in Eqs. (1.6) and (1.7) one should average over the density and velocity distributions.

particle due to its interaction with the surrounding medium. Within the framework of the so-called *impact theory of pressure broadening* [103, 104], one finds that

$$\delta\nu_{\text{mf}}(k_{\text{rel}}) = -\frac{\hbar}{m_{\text{red}}} n_{\text{scatt}} \Re \left[f(k_{\text{rel}}, \vartheta = 0) \right]. \quad (1.7)$$

As a general result, a positive (negative) value of the real part of $f(k_{\text{rel}}, \vartheta = 0)$ corresponds to a net attractive (repulsive) interaction energy.

1.2 Low-energy scattering

For central, *short-ranged* potentials, i.e. falling off as $r^{-\alpha}$ with $\alpha > 3$ for $r \rightarrow \infty$, at very low collision energies the leading contribution to the sums in Eqs. (1.4) arises from s -wave ($\ell = 0$) collisions, and one can show that $\delta_0(k_{\text{rel}} \rightarrow 0) \propto k_{\text{rel}}$ [7, 105]. In that case, under non-resonant conditions, one can define a momentum-independent parameter, namely the *s-wave scattering length* a :

$$a = -\lim_{k_{\text{rel}} \rightarrow 0} \frac{\tan(\delta_0(k_{\text{rel}}))}{k_{\text{rel}}}. \quad (1.8)$$

By making use of Eq. (1.8) in Eq. (1.4b), one finds

$$\sigma_{\text{el}}(k_{\text{rel}} \rightarrow 0) = 4\pi a^2. \quad (1.9)$$

The latter is a celebrated result of scattering theory: for a central, short-ranged interaction potential, off-resonant scattering at low energies is to first order isotropic, and the total cross section approaches a constant value, solely determined by the s -wave scattering length (and not by k_{rel}).

The case of low-energy scattering is indeed relevant when we consider collisions between pairs of non-magnetic ultracold atoms, which feature a van der Waals interaction of the kind $V_{\text{vdW}}(r) = -C_6/r^6 = -E_{\text{vdW}} \cdot (R_{\text{vdW}}/r)^6$, characterized by the range $R_{\text{vdW}} = (2m_{\text{red}}C_6/\hbar^2)^{1/4}$ and energy $E_{\text{vdW}} = \hbar^2/(2m_{\text{red}}R_{\text{vdW}}^2)$, respectively [7]. In particular (see e.g. Refs. [102, 106] for details), the net effect of $V(r)$ on the two-body system at large interparticle separation, $r \gg R_{\text{vdW}}$, can be formally taken into account by imposing a boundary condition at the origin for the log-derivative of the radial wavefunction $R_{\ell,m}(r)$ (*zero-range approximation*):

$$\left. \frac{R'_{0,0}(r)}{R_{0,0}(r)} \right|_{r \rightarrow 0} = k_{\text{rel}} \cot(\delta_0(k_{\text{rel}})), \quad (1.10)$$

where the prime denotes differentiation with respect to r . Generally speaking, replacing $V(r)$ with the condition in Eq. (1.10) does not simplify the problem, as knowledge of the phase shift $\delta_0(k_{\text{rel}})$ is still required. However, this approach becomes a useful tool in the low-energy limit, for $k_{\text{rel}} R_{\text{vdW}} \ll 1$: In this regime, one can perform the *effective range expansion*

$$k_{\text{rel}} \cot(\delta_0(k_{\text{rel}})) \simeq -\frac{1}{a} - k_{\text{rel}}^2 R^*, \quad (1.11)$$

where a is the scattering length and R^* the effective range parameter.³ The combination of Eqs. (1.10) and (1.11) is often referred to as *Bethe-Peierls boundary condition* [106, 107]. Note that, for $R^* = 0$, Eq. (1.11) reduces to Eq. (1.8).

³Some authors, see e.g. Ref. [7], parametrize Eq. (1.11) expansion in terms of $r_0 = -2R^*$.

Importantly, by inserting Eq. (1.11) into Eq. (1.5), one obtains for $\ell = 0$:

$$f_0(k_{\text{rel}}) \simeq -\frac{1}{\frac{1}{a} + k_{\text{rel}}^2 R^* + ik_{\text{rel}}}. \quad (1.12)$$

Thus, considering also Eq. (1.4b), the total s -wave scattering cross section is given by

$$\sigma_0(k_{\text{rel}}) \simeq \frac{4\pi a^2}{(1 + k_{\text{rel}}^2 R^* a)^2 + k_{\text{rel}}^2 a^2}. \quad (1.13)$$

The key point here is that the two-body scattering problem in the s -wave regime can be solved by imposing the Bethe-Peierls boundary condition, depending only on two momentum-independent parameters that can potentially be determined experimentally, without requiring knowledge of the exact form of the true interaction potential. In fact, the specific details of the short-range potential are irrelevant: All such potentials are equivalent as long as they yield the same values for a and R^* . As a result, one can arbitrarily choose an idealized zero-range (pseudo-)potential that reproduces Eq. (1.12).

1.3 Resonant scattering

One important feature of Eq. (1.12) is that it exhibits the well-known Breit-Wigner resonance shape [108], relevant to describe low-energy collisions where the scattering state, at energy $E = (\hbar k_{\text{rel}})^2 / (2m_{\text{red}})$, is coupled to a quasi-stationary state of energy E_{res} , with a coupling amplitude $\tilde{\gamma}$. This becomes apparent by recasting Eq. (1.12) in energy units:

$$f_0(E) \simeq -\frac{\frac{\hbar}{\sqrt{2m_{\text{red}}}} \tilde{\gamma}}{E - E_{\text{res}} + i\tilde{\gamma}\sqrt{E}}, \quad (1.14)$$

with $\tilde{\gamma} = \hbar / (\sqrt{2m_{\text{red}}} R^*)$ and $E_{\text{res}} = -\tilde{\gamma}^2 R^* / a$. In particular, in terms of a and R^* :

$$a = -\frac{\hbar \tilde{\gamma}}{\sqrt{2m_{\text{red}}} E_{\text{res}}}, \quad (1.15a)$$

$$R^* = \frac{\hbar}{\sqrt{2m_{\text{red}}} \tilde{\gamma}}. \quad (1.15b)$$

A few important remarks should be made here. First, while a depends on both $\tilde{\gamma}$ and E_{res} , R^* is only determined by the coupling amplitude. In other words, the coupling energy between the scattering and quasi-stationary states equals $\tilde{\gamma}^2 = \hbar^2 / (2m_{\text{red}} R^{*2})$. Strong (weak) couplings thus correspond to small (large) effective range values in the scattering amplitude, and vice versa. In addition, the parameter

$$\tilde{\Gamma}_d = \frac{2\tilde{\gamma}\sqrt{E}}{\hbar} \quad (1.16)$$

represents the decay rate of the quasi-bound state that produces the scattering resonance [106]. Therefore, both $\tilde{\gamma}$ and R^* are positive-defined quantities.

Second, from Eq. (1.15a) one realizes how the sign of the scattering length is determined by the one of E_{res} : Namely, $a > 0$ for $E_{\text{res}} < 0$, i.e. the scattering length is positive only if a real bound state exists. Vice versa, $a < 0$ when the quasi-stationary level is a virtual state at $E_{\text{res}} > 0$.

Third, the magnitude of a can be arbitrarily tuned if the energy of the quasi-stationary state can be varied around the scattering threshold. In particular, when $E_{\text{res}} \rightarrow 0$, $|a| \rightarrow \infty$ and, correspondingly, $\delta_0 \rightarrow (2n + 1)\pi/2$. However, it is important to realize that, while a

may effectively diverge near a scattering resonance, the total cross section actually does not, for any finite k_{rel} value. This was already pointed out as a comment to Eq. (1.4b), and it can also be inferred from Eq. (1.13): The s -wave scattering cross section cannot exceed $\sigma_0^{\text{max}}(k_{\text{rel}}) = 4\pi/k_{\text{rel}}^2$, the so-called *unitary limit*, reached when $k_{\text{rel}}^2 R^* a = -1$ (for $R^* \rightarrow 0$, this condition becomes $1/a \rightarrow 0$).

1.4 Magnetic Feshbach resonances

In most physical cases, the energy E_{res} appearing in Eq. (1.14) is fixed. However, for several ultracold systems this parameter can be tuned via the Zeeman effect, giving rise to the Feshbach resonance phenomenon [7]. This occurs when the wavefunction of two atoms in a certain combination of hyperfine and Zeeman states (the *open channel*) is coupled through a nonzero $\tilde{\gamma}$ to a *nearly-degenerate* molecular state, supported by an interatomic potential asymptotically connected with a different hyperfine domain (the *closed channel*). Here, “nearly-degenerate” means that the energy of such molecular state is very close to the scattering energy. Due to a non-vanishing differential magnetic moment $\delta\mu = \mu_{\text{cc}} - \mu_{\text{oc}}$ between closed and open channels, one thus obtains in this case $E_{\text{res}} = \delta\mu(B - B_0)$, B denoting an external magnetic-field bias, and B_0 the magnetic field value at which the bound state in the closed channel becomes degenerate with the zero-energy scattering threshold. Consequently, near a FR, Eq. (1.15a) shows that the scattering length is resonantly enhanced relative to its background value, with a B -field dependence of the form

$$a_{\text{res}}(B) = - \frac{\hbar\tilde{\gamma}}{\sqrt{2m_{\text{red}}}\delta\mu(B - B_0)}. \quad (1.17)$$

Accounting also for a nonzero off-resonant contribution a_{bg} , Eq. (1.17) can be recast in the familiar form [7]

$$a(B) = a_{\text{bg}} \left(1 - \frac{\Delta_{\text{B}}}{B - B_0} \right), \quad (1.18)$$

with the magnetic-field width Δ_{B} given by

$$\Delta_{\text{B}} = \frac{\hbar\tilde{\gamma}}{\sqrt{2m_{\text{red}}}\delta\mu a_{\text{bg}}}. \quad (1.19)$$

By combining Eqs. (1.19) and (1.15b), we obtain a useful expression for the effective range parameter [106]:

$$R^* = \frac{\hbar^2}{2m_{\text{red}}\delta\mu a_{\text{bg}}\Delta_{\text{B}}}. \quad (1.20)$$

Recalling that large (small) values of $\tilde{\gamma}$ physically correspond to strong (weak) coupling between the scattering channel and the quasi-bound level, a Feshbach resonance can be classified as *broad* or *narrow* depending on whether the effective range parameter in Eq. (1.20) is small or large relative to the true range of the potential: $R^* \ll R_{\text{vdW}}$ indicates a broad resonance, while $R^* \gg R_{\text{vdW}}$ implies a narrow one. A similar classification is presented in Ref. [7], using the *dimensionless resonance strength parameter*, which can be expressed as $s_{\text{res}} \sim R_{\text{vdW}}/R^*$: broad (narrow) Feshbach resonances are characterized by large (small) s_{res} values.

Finally, I also report here the magnetic field dependence of the R^* parameter [109, 110]:

$$\tilde{R}^*(B) = R^* \cdot \left(1 - \frac{a_{\text{bg}}}{a(B)} \right)^2. \quad (1.21)$$

1.5 Scattering near a narrow Feshbach resonance

In practical terms, the difference between broad and narrow FRs is better clarified by inspecting how the scattering cross-section $\sigma_0(k_{\text{rel}})$, obtained from Eq. (1.13), is affected by the parameter R^*/a , in turn characterizing the “narrowness” of the resonance. To this end, following Ref. [111], let us consider the dimensionless form

$$\frac{\sigma_0(k_{\text{rel}})}{4\pi a^2} = \frac{1}{(1 + k_{\text{rel}}^2 R^* a)^2 + k_{\text{rel}}^2 a^2}. \quad (1.22)$$

Figure 1.1 shows the trend of Eq. (1.22) as a function of $k_{\text{rel}} |a|$, for different negative (solid lines) and positive (dashed lines) a values. Several key features can be observed: First, as $k_{\text{rel}} \rightarrow 0$, all curves converge to unity, corresponding to $\sigma_0(0) = 4\pi a^2$, yielding a cross section which solely depends on the scattering length (reflecting the *broad resonance limit*). Second, for small but finite k_{rel} , when $R^*/|a| \gg 1$ a noticeable asymmetry appears between the $a > 0$ and $a < 0$ cases, which vanishes instead when $R^*/|a| \ll 1$ (see magenta lines). Specifically, for $a < 0$ and $R^*/|a| \gg 1$, $\sigma_0(k_{\text{rel}})$ exhibits a pronounced peak centered at

$$\tilde{k}_{\text{rel}} = \frac{1}{R^*} \sqrt{\frac{R^*}{|a|} - \frac{1}{2}}, \quad (1.23)$$

where the cross-section reaches its unitary value⁴

$$\sigma_0(\tilde{k}_{\text{rel}}) \simeq 4\pi/\tilde{k}_{\text{rel}}^2 \simeq 4\pi a^2 (R^*/|a|). \quad (1.24)$$

The peak value of the scattering cross section can significantly exceed $\sigma_0(0)$, and the feature persists as long as $R^*/|a| > 1/2$, while being entirely absent for any positive a . Third, at low momenta, the curves for $R^*/|a| \gg 1$ consistently lie above (for $a < 0$) or below (for $a > 0$) those with $R^*/|a| \ll 1$.

In conclusion, it is important to realize that, from a two-body perspective, any “broad” resonance effectively “narrows” when the relative momentum or the magnetic-field detuning becomes sufficiently large. Conversely, “narrow” resonances can behave like “broad” ones when k_{rel} and δB are sufficiently small, ensuring that $R^* k_{\text{rel}}^2 \ll 1/|a|$ in Eq. (1.12). However, the distinction between “broad” and “narrow” FRs actually becomes highly relevant in practical scenarios given that: (i) one has to deal with a finite magnetic field stability, which limits the experimental precision required to probe the $|a| \gg R^*$ regime; and (ii) one should consider finite momentum distributions, arising either from thermal effects at $T > 0$ or, for fermionic systems, from the existence of a finite Fermi momentum k_{F} , even at zero temperature. Focusing on the fermionic case, for broad resonances, where $R^* \ll 1/k_{\text{F}}$, all (relative) momenta k_{rel} will simultaneously reach the unitary condition $\delta_0(k_{\text{rel}}) = (2n + 1)\pi/2$ when $1/a \rightarrow 0$. This situation has been experimentally realized in ultracold homonuclear ⁶Li and ⁴⁰K mixtures, see e.g. Refs. [112–115]. By contrast, in the case of narrow resonances, for realistic particle densities $n = k_{\text{F}}^3/(6\pi^2)$, one always has $R^* k_{\text{F}} \gg 1$, causing different momenta to reach the unitary limit at different detunings, as shown in Fig. 1.1. As a consequence, the many-body low-temperature regimes accessible near broad and narrow resonances differ qualitatively, as discussed in Refs. [116–119].

⁴To be more precise, the unitary limit is nominally reached at $k_{\text{rel}}^* = 1/\sqrt{R^*|a|}$ (with $a < 0$), see Eq. (1.13). For $R^*/|a| \gg 1$ one has $k_{\text{rel}} \simeq k_{\text{rel}}^*$, but in general $\tilde{k}_{\text{rel}} < k_{\text{rel}}^*$. In other words, for any given combination of $R^* > 0$ and $a < 0$ with $R^*/|a| > 1/2$, the maximum possible value of the cross section at finite momentum is set by $\sigma_0(\tilde{k}_{\text{rel}}) = 4\pi R^{*2}/(R^*/|a| - 1/4)$, which is smaller than $4\pi/\tilde{k}_{\text{rel}}^2 = 4\pi R^{*2}/(R^*/|a| - 1/2)$ (and thus nominally *not* unitary limited), but somewhat larger than $4\pi/k_{\text{rel}}^{*2} = 4\pi R^{*2}/(R^*/|a|)$. The difference between \tilde{k}_{rel} and k_{rel}^* becomes more striking for $R^*/|a| \sim 1$, where anyway the peak of $\sigma_0(k_{\text{rel}})$ is less pronounced.

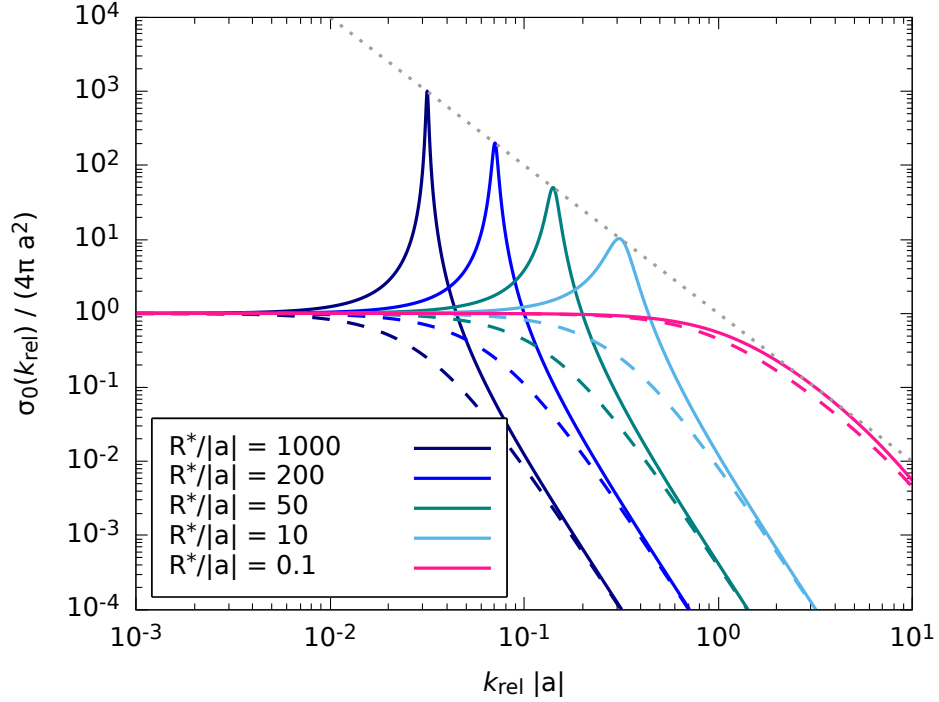


Figure 1.1 – Normalized scattering cross section $\sigma_0(k_{\text{rel}})/(4\pi a^2)$ as a function of $k_{\text{rel}}|a|$, for different values of $R^*/|a|$, see legend. Solid (dashed) lines refer to negative (positive) values of a . For $a > 0$ (dashed lines) and $R^*/a \gg 1$, $\sigma_0(k_{\text{rel}})$ is maximum at $k_{\text{rel}} = 0$, and lies systematically below the result corresponding to the broad resonance limit $R^*/a \ll 1$ (see magenta curves). For $a < 0$, instead, as long as $R^*/|a| \geq 1/2$, the cross section exhibits a sharp, low-momentum peak centered at \tilde{k}_{rel} , where it reaches its unitary-limited value $\sigma_0^{\text{max}}(\tilde{k}_{\text{rel}}) = 4\pi/\tilde{k}_{\text{rel}}^2$, indicated by the gray dotted line.

1.6 Feshbach molecules

Let us now consider how the finite coupling with the open channel modifies the properties of the bound state near the FR, otherwise represented by a closed-channel molecule for $\tilde{\gamma} = 0$. To this end, following Refs. [106, 111], we look for a pole of $f_0(k_{\text{rel}})$ at negative energy. Namely, in Eq. (1.12) we replace $k_{\text{rel}} \rightarrow i\kappa$ (with $\kappa > 0$),⁵ and we impose

$$\frac{1}{a} - R^*\kappa^2 - \kappa = 0. \quad (1.25)$$

It is straightforward to verify that the solution we are seeking, only possible for $a > 0$, is

$$\kappa_* = \frac{1}{2R^*} \left(\sqrt{1 + \frac{4R^*}{a}} - 1 \right), \quad (1.26)$$

with associated dimer binding energy

$$E_b = -\frac{\hbar^2 \kappa_*^2}{2m_{\text{red}}}. \quad (1.27)$$

The above result interpolates between two familiar forms obtained in the limits of small and large R^*/a values, respectively: For $R^*/a \ll 1$ – i.e. close to the resonance pole, or in

⁵With this choice, one obtains a dimer binding energy $E_b = -(\hbar\kappa)^2/(2m_{\text{red}})$, with the associated wavefunction decaying as $\psi_b(r) \sim e^{-\kappa r}/r$ at large $r \gg R_{\text{vdW}}$.

the broad resonance case – one has $\kappa_* \sim 1/a$, so that Eq. (1.27) becomes simply

$$E_b \Big|_{R^*/a \ll 1} \simeq -\frac{\hbar^2}{2m_{\text{red}} a^2}. \quad (1.28)$$

In this case, the bound state energy features a typical parabolic trend $E_b \propto -1/a^2 \propto -(B - B_0)^2$: the dimer is a halo state whose energy and wavefunction solely depend on the scattering length a (“universal regime”).

In the opposite limit of $R^*/a \gg 1$, instead, $\kappa_* \sim 1/\sqrt{aR^*}$ and, exploiting Eqs. (1.17) and (1.20), one finds for the dimer binding energy

$$E_b \Big|_{R^*/a \gg 1} \simeq -\frac{\hbar^2}{2m_{\text{red}} a R^*} = \delta\mu (B - B_0). \quad (1.29)$$

In this case, the bound state energy depends linearly on the magnetic field detuning $\delta B = B - B_0$, and it coincides with that of the bare closed-channel molecule.

It is important to emphasize that the dimensionless parameter R^*/a also quantifies the closed (open) channel fraction Z ($1 - Z$) characterizing the dressed Feshbach molecule in the zero-range approximation. Referring the interested reader to Ref. [106] for the formal derivation of the result, one finds

$$Z(\delta B) = 1 - \frac{1}{\sqrt{1 + \frac{4R^*}{a_{\text{res}}(\delta B)}}}, \quad (1.30)$$

with R^* and $a_{\text{res}}(\delta B)$ given by Eqs. (1.20) and (1.17), respectively. In terms of the closed channel fraction, it can be readily shown that, for $Z \rightarrow 0$, the dimer binding energy follows the universal behavior of Eq. (1.28), whereas, in the opposite limit $Z \rightarrow 1$, the Feshbach state essentially coincides with the bare closed-channel molecule, with E_b given by Eq. (1.29). In general, at all detunings, the magnetic moment associated with the Feshbach dimer is given by

$$\mu_d(\delta B) = \frac{\partial E_b}{\partial B} = Z(\delta B) \mu_{\text{cc}} + (1 - Z(\delta B)) \mu_{\text{oc}}. \quad (1.31)$$

Consequently, experimental measurement of the dimer magnetic moment around a FR provides direct information about the magnetic-field dependence of the closed-channel fraction, and thereby of R^*/a , see Secs. 4.7 and 4.8. In general, the transition from one regime to the other will occur at magnetic field detunings that depend on the character of the resonance considered: For broad resonances, the universal regime Eq. (1.28), with $Z \sim 0$, will extend over a B -field region of order Δ_B from the resonance center B_0 , whereas for narrow FRs this will only occur for detunings $|B - B_0| \ll \Delta_B$.

1.7 Zero-range approximation in a real physical system

To conclude this Chapter, I emphasize how the seemingly simple results of the zero-range approximation summarized above can actually provide a quantitatively accurate description of real physical systems. As an example, in Fig. 1.2 I show the magnetic-field dependence of the scattering length $a(B)$ [panel (a), green circles] and the effective range parameter $\tilde{R}^*(B)$ [panel (b), cyan circles] near one s -wave FR occurring in the ${}^6\text{Li}$ - ${}^{53}\text{Cr}$ system around 1461 G, obtained by our theory collaborator Prof. A. Simoni from coupled-channel (CC) calculations, which were optimized by fitting more than 50 FRs that we experimentally determined (see Chapter 3). The CC data are fitted to the corresponding simple analytic

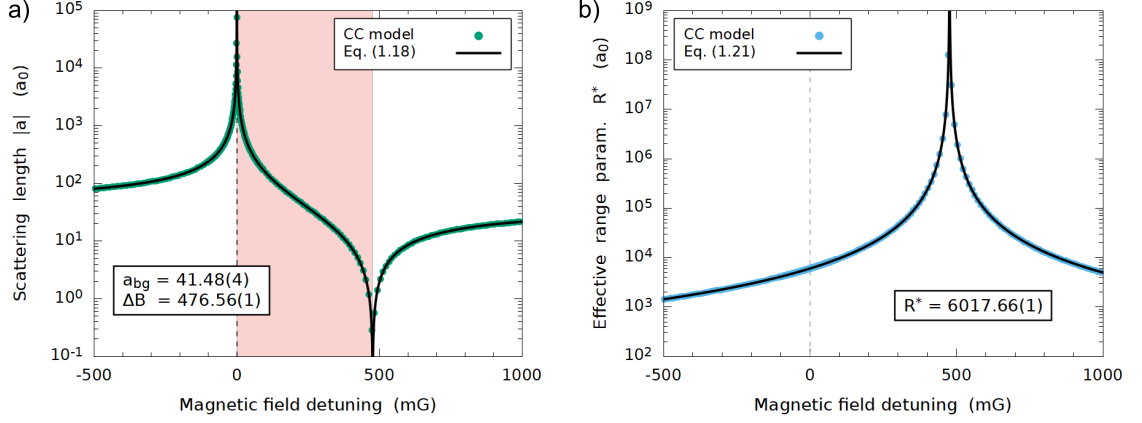


Figure 1.2 – Modulus of the scattering length $|a|$ [panel (a), green circles] and effective range parameter R^* [panel (b), cyan circles] as a function of the magnetic field detuning $\delta B = B - B_0$, for one Li-Cr FR located around 1461 G, as obtained by A. Simoni from coupled-channel calculations (see Chapter 3). The numerical results of the coupled-channel calculations are fitted to the corresponding simple analytical formulas provided by the zero-range approximation [Eqs. (1.18) and (1.21), respectively], see black solid lines and best fitted values. The simple zero-range model is able to reproduce the results of the (much more involved) CC calculations with remarkable accuracy. The red shaded area in panel (a) marks the region where $a < 0$.

formulas given by the zero-range approximation [Eqs. (1.18) and (1.21), respectively], which describe the numerical results with remarkable accuracy; see black solid lines. From the best-fitted values $a_{\text{bg}} = 41.48(4) a_0$, $\Delta_B = 476.6(1) \text{ mG}$, and $R_0^* = 6017.7(1) a_0$, using Eq. (1.20) we obtain a differential magnetic moment of $\delta\mu \simeq 2 \mu_B$. Additionally, for the same FR, in Fig. 1.3 I show the dimer binding energy E_b (blue circles), together with the decay rate of the virtual state (red circles), also obtained by A. Simoni with his coupled-channel model. The CC data are compared with the corresponding trends (black solid lines) given by the zero-range approximation – see Eqs. (1.26)-(1.27) and Eqs. (1.15)-(1.16), respectively – inserting the above values for the best-fitted parameters.

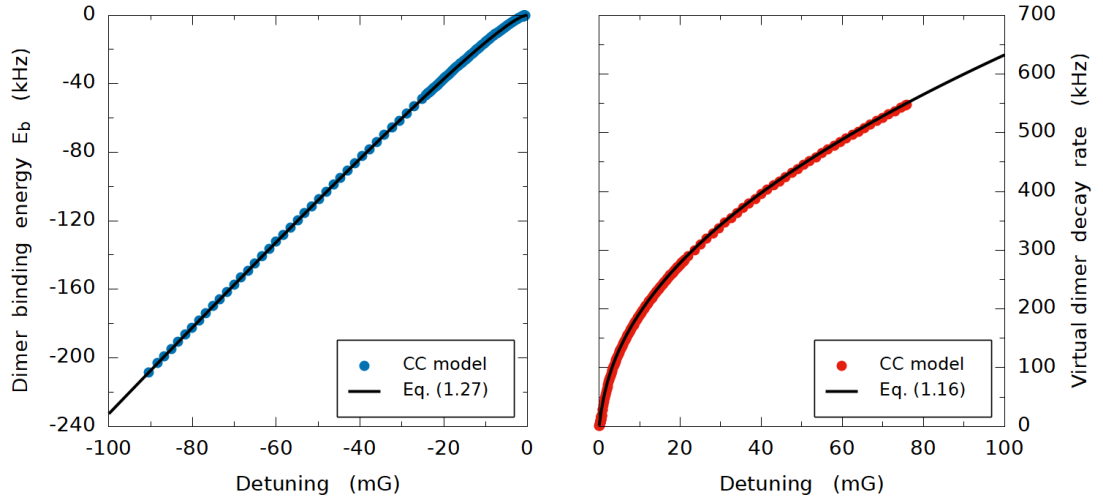


Figure 1.3 – Dimer binding energy E_b (left, blue circles) and decay rate of the quasi-stationary state $\tilde{\Gamma}_d$ (right, red circles), obtained by A. Simoni from coupled-channel calculations for one Li-Cr FR located around 1461 G (see Chapter 3). Both are compared with the corresponding trends (black solid lines) provided by the zero-range approximation discussed in this Chapter, see in particular Eqs. (1.27) and (1.16). The simple zero-range model is able to reproduce the results of the (much more involved) CC calculations with remarkable accuracy.

Overall, one can notice how the simple analytic formulas summarized in this Chapter provide a remarkable description of the low-energy physics obtained from (the much more complex!) CC calculations of the real Li-Cr interaction potential. Similar agreement can be found near isolated FRs of any other two-body system, which makes the zero-range approximation a valuable simple tool, able to quantitatively reproduce the physics of resonantly interacting atomic gases at ultralow temperatures [111].

Finally, I also mention here that, while analyzing the CC data of A. Simoni, I semi-empirically found a simple analytical formula that accurately describes the energy of the *virtual* (i.e. for $a < 0$) Feshbach dimer, relative to the atomic scattering threshold (at zero collision energy):

$$E_\star = \frac{\hbar^2 \kappa_\star^2}{2 m_{\text{red}}}, \quad (1.32a)$$

where

$$\kappa_\star = \frac{1}{2R^\star} \sqrt{\sqrt{1 + \left(\frac{4R^\star}{a}\right)^2} - 1}. \quad (1.32b)$$

As shown in Fig. 1.4, near the resonance pole E_\star deviates from the simple linear trend characterizing the purely closed-channel molecule [$E_\star \propto \delta\mu \delta B \propto 1/(a R^\star)$], featuring instead a quadratic scaling $E_\star \propto 1/a^2$, similarly to the case of negative detunings [see again Eqs. (1.28) and Eq. (1.29)].

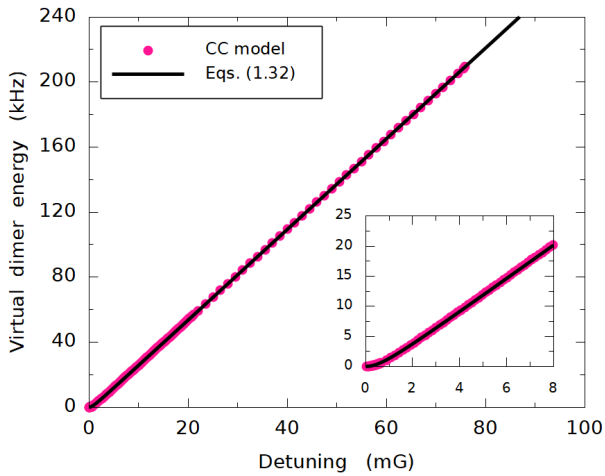


Figure 1.4 – Resonance position at positive detunings, i.e. for $a < 0$, as calculated by A. Simoni (magenta circles), compared to the trend given by Eqs. (1.32) (black curve).

Chapter 2

Production of degenerate ${}^6\text{Li}$ - ${}^{53}\text{Cr}$ Fermi mixtures

In this Chapter, following the lines of our Ref. [120], I describe the experimental procedures we devised and optimized to produce quantum degenerate mixtures of fermionic ${}^6\text{Li}$ and ${}^{53}\text{Cr}$ atoms. The experimental apparatus that we employed – apart from targeted changes in the optical setup (summarized below), and a few key upgrades described in Chapter 6 – was already developed before the start of my Ph.D., and has been described in depth in previous papers and theses from our group [121–123], including my Master Thesis [102], to which I refer the interested reader for more details.

Our strategy to produce degenerate lithium-chromium Fermi mixtures relies on an all-optical approach, similar to the one employed in the lithium-potassium experiment in Innsbruck [124]. The process consists of the following main steps:

- (i) realization of a cold mixture in a dual-species magneto-optical trap (MOT) [121];
- (ii) direct loading of the two components into an optical dipole trap (ODT);
- (iii) evaporative cooling of a two-state lithium mixture and simultaneous sympathetic cooling of chromium.

Despite its conceptual simplicity, applying this approach to Li-Cr mixtures required overcoming several challenges, mostly connected with fermionic chromium and its somewhat limited experimental investigation [121, 125, 126]. Specifically, we encountered a few major issues that made the production of ultracold ${}^{53}\text{Cr}$ gases nontrivial. First, chromium suffers from rather strong light-assisted inelastic collisions [125] which – before our investigation – had limited the ${}^{53}\text{Cr}$ number collected in the MOT to roughly 10^6 [121]. Second, direct loading of chromium atoms from the MOT into an infrared optical dipole trap has proved challenging, owing to detrimental light shifts affecting the Cr cooling transition [127, 128]. Finally, efficient sympathetic cooling of chromium with lithium should not be taken for granted. Although the Li-Cr background scattering length, of about $42 a_0$ (see Chapter 3), is close to the Li-K one, of about $65 a_0$ [129, 130], and thus in principle sufficient to guarantee a good thermalization rate, efficient Li-Cr sympathetic cooling in a standard 1070 nm optical trap is hard to achieve, given that the chromium polarizability at such wavelength is about $1/3$ of the lithium one, in contrast with a potassium-to-lithium polarizability ratio of about 2 in the same spectral range [124].

In the following, I describe how we could overcome these challenges in the experiment, obtaining degenerate samples comprising more than 2×10^5 Li and 10^5 Cr atoms, polarized in their lowest Zeeman states, at temperatures of about 200 nK, corresponding to $T/T_{\text{F,Li}} \sim T/T_{\text{F,Cr}} \sim 0.25$. This Chapter is organized as follows:

- In Sec. 2.1, I provide a synthetic overview of the experimental setup, with the purpose of contextualizing the reader to the following Sections.
- In Secs. 2.2, 2.3, and 2.4, I describe our new protocol to produce a dual-species Li-Cr MOT. In particular, in Sec. 2.3, I discuss how the ${}^{53}\text{Cr}$ MOT atom number can be

substantially increased with respect to previous studies [121, 125], reaching up to 8×10^7 within a 2-s loading time and in the presence of a large Li MOT of about 10^9 atoms.

- In Sec. 2.5, I present our efficient scheme to simultaneously load Li and Cr atoms in a bichromatic optical dipole trap (bODT) directly from the MOT, based on the implementation of a *dark spot* obtained through a weak green beam at 532 nm, superimposed onto the main trapping beam at 1070 nm.
- In Sec. 2.6, I show the evaporation trajectories followed by the two components and, together with the more detailed analysis of Sec. 2.7, I discuss how the sympathetic cooling efficiency at ultralow temperatures can be substantially increased by exploiting a narrow interspecies Feshbach resonance.
- Finally, in Sec. 2.8, I describe how a crossed bichromatic beam, added to our main bODT, allows us to greatly improve the chromium degree of degeneracy, and to simultaneously reach deeply degenerate conditions for both atomic components.

2.1 Overview of the experimental apparatus

In this first Section I provide a concise description of the experimental apparatus available in our lab, which is meant to be a contextualizing introduction to the following Sections. The interested reader can find more details in previous papers and theses from our group [121–123], including my Master Thesis [102].

The Li-Cr experimental setup comprises two separate optical tables. On the first one, we prepare all laser lights to cool and trap lithium and chromium atoms. A detailed description of this part of the optical setup, including all the relevant laser schemes, is presented in my Master Thesis [102]. The second table hosts the vacuum and magnetic coils setup, as sketched in Fig. 2.1. As one can see, two different Zeeman slower (ZS) tubes connect the Li and Cr ovens to the main experimental chamber. This choice is motivated

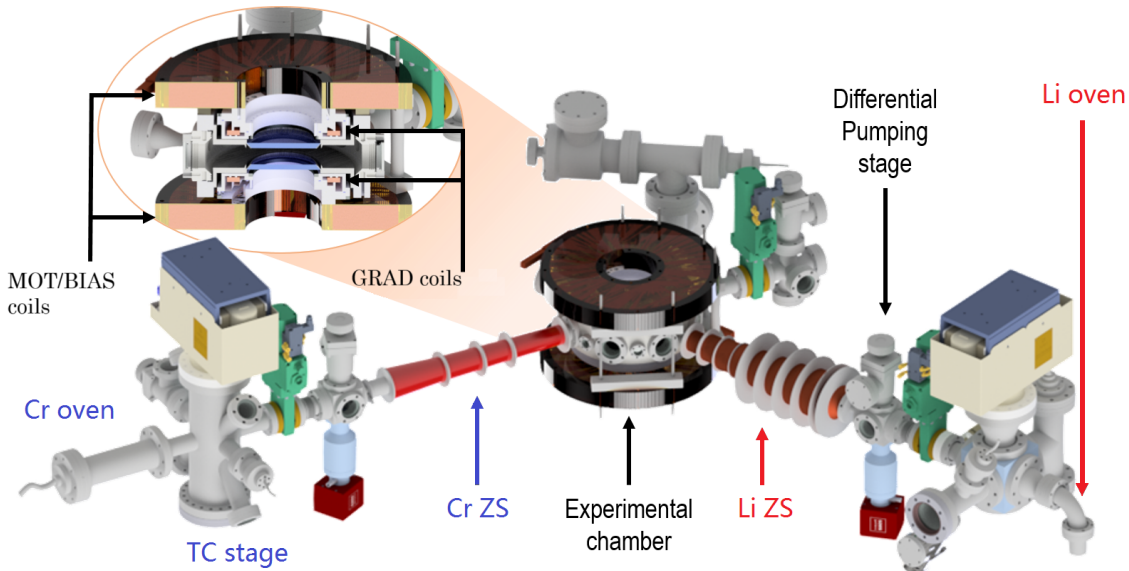


Figure 2.1 – Sketch of the vacuum and magnetic coils setup in our lab. Two different Zeeman slower tubes connect the Li and Cr ovens to the main chamber. The latter is surrounded by two main pairs of coils, placed along the vertical direction, which are referred to as the “MOT/BIAS” coils and the “GRAD” coils, respectively, see inset. Two smaller additional sets of coils, named “COMP” and “AC-COMP” coils, respectively, not shown in the figure, are used on top of the main ones to finely tune and stabilize the magnetic field, see Sec. 6.1. Figure adapted from Ref. [121].

by the rather different sublimation temperatures employed for the two species: about 400 °C for lithium, and 1500 °C for chromium, respectively. The experimental chamber is surrounded by two main sets of coils, namely the “MOT/BIAS” coils and the “GRAD” coils, respectively. The former ones are used in anti-Helmholtz configuration during the loading of the MOT, and subsequently in Helmholtz configuration to produce bias fields up to 1.5 kG, needed to access the high-field s -wave Feshbach resonances featured by Li-Cr (see Chapter 3). The “GRAD” coils are always used in anti-Helmholtz configuration, producing the B -field gradient for the final part of the MOT stage (see Sec. 2.4), as well as to compensate for the (relative) gravitational sag of the two species within our bODT, see Sec. 2.6. Additionally, two smaller sets of coils, not shown in Fig. 2.1, referred to as the “COMP” and “AC-COMP” coils, respectively, are employed for the fine-tuning and stabilization of the magnetic field (see Sec. 6.1). I also mention here that both ZS fields are matched with the MOT coils field, effectively making both Zeeman slower end at the MOT quadrupole center.

2.2 ${}^6\text{Li}$ MOT

To produce the lithium MOT, we essentially follow the scheme developed in the Lithium lab at LENS, which is detailed in Ref. [131]. Laser cooling and trapping of fermionic Li is well established and it requires only two laser lights addressing the D2 (${}^2S_{1/2} \rightarrow {}^2P_{3/2}$) atomic line at 671 nm: the cooling light, addressing the $F = 3/2 \rightarrow F' = 5/2$ transition, and the repumper light, blue detuned by 228 MHz from the cooling one, nearly resonant with the $F = 1/2 \rightarrow F' = 3/2$ transition, see Fig. 2.2. With respect to the Li MOT performance previously reported by our group [121], a further optimized shaping of both MOT and Zeeman slower (ZS) beams has allowed us to increase the lithium atom number collected in the MOT from 4×10^8 to 10^9 , after a typical loading time of 6 s. A comprehensive list of the optimum parameters employed for the Li MOT is reported in my Master Thesis [102].

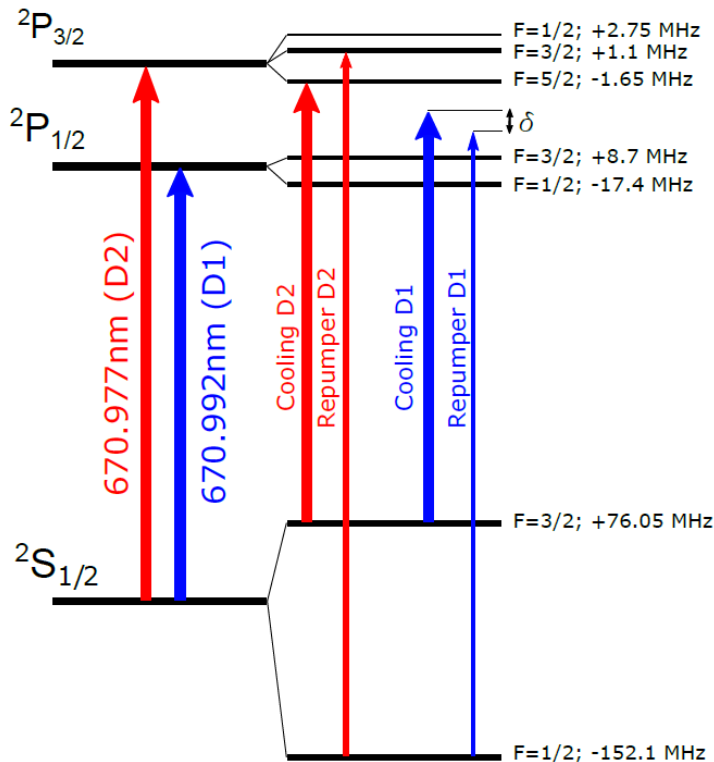


Figure 2.2 – Cooling scheme for ${}^6\text{Li}$. Two independent master lasers (Toptica TA Pro) provide the lights addressing the D1 and D2 transitions, respectively. The former is employed to realize the Li MOT and CMOT stages, while the latter is exploited for a grey molasses stage that follows the loading into the optical dipole trap (see Sec. 2.5). Figure taken from Ref. [121].

2.3 ${}^{53}\text{Cr}$ MOT

For the ${}^{53}\text{Cr}$ component, a much more substantial increase in the MOT atom number is reported here, resulting in an improvement by almost two orders of magnitude relative to previous studies, both by the Paris group [125, 126] and by our team before the start of my Ph.D. [121].

As described in Refs. [121, 125], laser cooling of fermionic chromium relies on the ${}^7S_3 \rightarrow {}^7P_4$ ($F_S = 9/2 \rightarrow F'_P = 11/2$) atomic line. Figure 2.3 shows a sketch of the energy-level diagram and the relevant optical transitions. Besides the cooling light, three blue repumpers, denoted by BR1, BR2, and BR3, respectively, are required to operate the MOT. Furthermore, even with all blue repumpers switched on, the Cr cooling transition remains slightly leaky, since optically excited atoms can decay from the 7P_4 state onto underlying 5D_3 and 5D_4 metastable states. Therefore, three additional red repumpers, denoted by RR1, RR2, and RR3 in order of repumping efficiency, are needed to fully close the cooling cycle. In particular, implementation of RR3, not yet accomplished in Ref. [121] (see details in Ref. [102]), resulted in a further 10% increase in the steady-state MOT atom number.

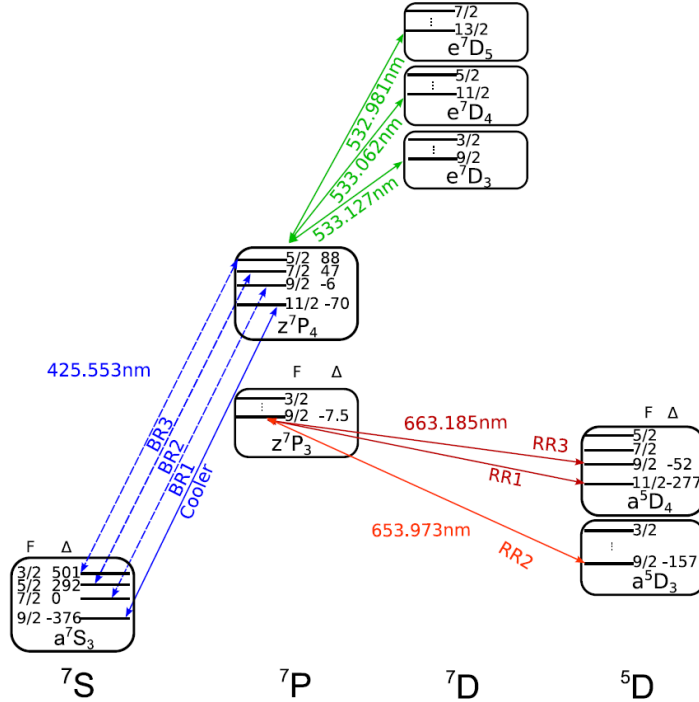


Figure 2.3 – Sketch of energy levels and optical transitions addressed for the laser cooling of ${}^{53}\text{Cr}$ atoms (not to scale). For each relevant hyperfine level originating from the nonzero nuclear spin $I = 3/2$, the F quantum number and the detuning Δ in MHz, referenced to an assumed $I = 0$ state, are shown. A single frequency-doubled laser at 425.5 nm delivers the light exciting atoms from 7S_3 to 7P_4 , addressing the main cooling transition labeled “Cooler” (solid blue), and the repumping transitions denoted by BR1, BR2, and BR3 (dashed blue) in order of decreasing gain on the steady-state MOT number. Metastable 5D states onto which 7P_4 atoms decay by spontaneous emission are repumped back into the cooling cycle by three additional red repumper beams labeled as RR1, RR2, and RR3, with the same indexing used for the blue ones. These lights are delivered by two independent master oscillators at 663 and 654 nm (see Ref. [121] for more details). Here RR1 and RR3, detuned from each other by only 225 MHz, are obtained by two separate sets of acousto-optic modulators. The three green transitions around 533 nm, coupling the 7P_4 to the ${}^7D_{3,4,5}$ states, are relevant for the operation of the dark spot discussed in Sec. 2.5.

To improve our Cr MOT performance, we carefully optimized the size of all laser beams shone onto the cloud, with the possibility of changing the power repartition between different beams, but under the constraint of a maximum available blue power of about 500 mW. In particular, we enlarged the MOT and repumper beam waists by about a factor of 2 relative to the setup originally developed in the lab [121], now featuring $1/e^2$ radii of about 6.5 mm, effectively increasing the capture volume by almost one order of magnitude. Notably, these improvements on the chromium setup enabled us to identify a peculiar region in the detuning-intensity plane of the MOT cooling light (not investigated in Ref. [121]), within which light-assisted losses are drastically suppressed, as shown in the following.

In order to understand our strategy and the experimental data presented below, it is useful to first recall some textbook results about the loading dynamics in a MOT. Quite generally, the atom number in a MOT follows a time evolution defined by the rate equation

$$\frac{dN}{dt} = R_{\text{load}} - \alpha_{1b} N(t) - \frac{\beta_{\text{lac}}}{\langle V \rangle} N^2(t), \quad (2.1)$$

where R_{load} is the loading rate, α_{1b} is the one-body decay rate, β_{lac} is the rate coefficient per unit volume for light-assisted collisions, and $\langle V \rangle$ denotes the density-weighted volume of the cloud. Since in our experiment we exploit all (blue and red) repumping lights, we can neglect the one-body loss term and safely set $\alpha_{1b} = 0$. Equation (2.1) then yields the asymptotic value for the collected atom number

$$N_{\infty} = \sqrt{\frac{\langle V \rangle R_{\text{load}}}{\beta_{\text{lac}}}}. \quad (2.2)$$

From Eq. (2.2) one can immediately see that, in order to increase N_{∞} , one needs to maximize R_{load} , enlarge $\langle V \rangle$, and minimize β_{lac} . Let us consider how these three quantities depend upon the normalized detuning δ/γ and saturation parameter $s_0 = I/I_{\text{sat}}$ of the MOT (I is the intensity of a single laser beam). Note that, for the $^7S_3 \rightarrow ^7P_4$ chromium line, the natural linewidth is $\gamma = 2\pi \times 5.02$ MHz, with saturation intensity $I_{\text{sat}} = 8.52$ mW/cm 2 . First, from textbook calculations of the MOT temperature (T_{MOT}) and trap frequency (ω_{MOT}) [132–134], we have

$$k_B T_{\text{MOT}} = \frac{\hbar\gamma}{2} \frac{1 + 6s_0 + (2\delta/\gamma)^2}{4|\delta|/\gamma}, \quad (2.3a)$$

$$M_{\text{Cr}} \omega_{\text{MOT}}^2 = 4(\mu' b k_L) s_0 \frac{2|\delta|/\gamma}{[1 + 6s_0 + (2\delta/\gamma)^2]^2}, \quad (2.3b)$$

$$\sigma_{\text{MOT}} = \sqrt{\frac{k_B T_{\text{MOT}}}{M_{\text{Cr}} \omega_{\text{MOT}}^2}}, \quad (2.3c)$$

$$\langle V \rangle = 4\pi^{3/2} \sigma_{\text{MOT}}^3, \quad (2.3d)$$

where k_B denotes the Boltzmann constant, M_{Cr} the chromium mass, k_L the laser wave vector, b the magnetic field gradient, μ' the effective differential magnetic moment for the cooling transition, and σ_{MOT} the $1/\sqrt{e}$ size of a Gaussian-shaped cloud.

Second, the dominant light-assisted loss processes that affect a chromium MOT are known to involve pairs of one ground S - and one excited P -state atom [121, 125]. Thus, denoting by Π_P the P -state population, on quite general grounds one expects the rate coefficient to scale as $\beta_{\text{lac}} \propto \Pi_P (1 - \Pi_P)$, where the standard result for Π_P for a two-level atom [132, 133], considering all six MOT beams, reads

$$\Pi_P = \frac{1}{2} \frac{6s_0}{1 + 6s_0 + (2\delta/\gamma)^2}. \quad (2.4)$$

Third, the loading rate R_{load} depends mainly on the transverse cooling and Zeeman slowing parameters, as long as the capture velocity v_{cap} of the MOT is larger than the typical exit velocity v_{ZS} of the ZS. However, at very low s_0 or large $|\delta|/\gamma$ values, this condition may not hold. Given the expression for v_{cap} [135] and our typical $v_{\text{ZS}} \sim 15$ m/s [121], we have

$$v_{\text{cap}} = \left(\frac{32 w_{\text{MOT}} \hbar k_L^2}{M_{\text{Cr}}} \right) \frac{6 s_0 |\delta|/\gamma}{[1 + 6s_0 + (2\delta/\gamma)^2]^2}, \quad (2.5a)$$

$$R_{\text{load}} \propto \int_0^{v_{\text{cap}}} n_{\text{ZS}}(v) dv \propto \frac{1}{2} \left[\text{erf} \left(\frac{v_{\text{cap}} - v_{\text{ZS}}}{\sqrt{2} \sigma_{\text{ZS}}} \right) + \text{erf} \left(\frac{v_{\text{ZS}}}{\sqrt{2} \sigma_{\text{ZS}}} \right) \right]. \quad (2.5b)$$

Here $w_{\text{MOT}} = 6.5$ mm is the waist of the MOT beams, and we have assumed a Gaussian exit-velocity distribution $n_{\text{ZS}}(v)$ from the ZS, centered around v_{ZS} with variance σ_{ZS}^2 .

Before proceeding further, it is instructive to study the result for N_∞ in the limit $s_0 \ll 1$ and $|\delta| \gg \gamma$:

$$N_\infty \propto \frac{\sqrt{R_{\text{load}}} (\delta/\gamma)^4}{b^{3/4} s_0^{5/4}}. \quad (2.6)$$

From the overall trend of Eq. (2.6), one can see how, for a given loading rate R_{load} , light-assisted losses can be mitigated (thereby increasing N_∞) by working at low s_0 values, large detunings, and weak field gradients of the MOT, although a compromise must be found in order to guarantee a sufficiently strong force and a high capture velocity. A well-known system, where very strong light-assisted losses are successfully circumvented by following these concepts, is metastable ${}^4\text{He}^*$ [133, 136]: In that case, operating the MOT at large detunings on the order of $|\delta| \sim 40 \gamma$, while keeping large $s_0 > 10$ values to maintain a sufficiently high capture velocity, it is possible to collect more than 10^9 atoms within a few-second loading time.

However, for the ${}^{53}\text{Cr}$ system, this strategy is challenging to follow. On the one hand, the saturation intensity (linewidth) of chromium is more than 50 times (3 times) larger than the one of He^* and the limited amount of blue power available does not allow us to reach $s_0 \gg 1$ without diminishing the performance of transverse cooling and hyperfine pumping stages at the chromium oven [121], thus decreasing R_{load} . Moreover, contrarily to metastable He, ${}^{53}\text{Cr}$ features a rich and rather dense hyperfine spectrum which, in combination with large s_0 and $|\delta|/\gamma$ values, may allow the cooling light to address undesired transitions. Indeed, the small optimum Zeeman slower detuning and low exit velocity shown in Ref. [121] have already been interpreted as highly sensitive to residual Doppler shifts during the MOT capture. Hence, we opted to follow a strategy opposite to the one of ${}^4\text{He}^*$, based on minimizing s_0 while keeping relatively small light detunings of a few γ .

In practice, to test the feasibility of the strategy discussed above, we measured the atom number collected in the MOT after a loading time of 2 s, exploring different s_0 values. For each of these values, we scanned the light detuning until the maximum number was observed, whereas the B -field gradient was kept constant at $b = 25$ G/cm (along the vertical direction). In order to better count the collected atoms, after the 2-s loading time we performed a compressed MOT (CMOT) stage (lasting about 6 ms), with the effect of significantly reducing the cloud size, while leaving the atom number unaffected. Finally, we turned off both MOT gradient and lights, and we acquired an absorption image after a 2-ms time of flight, out of which we extracted the atom number through a two-dimensional Gaussian fit.

Our results are summarized in Fig. 2.4. The atom number (black circles, left axis) is plotted as a function of the normalized single-beam peak intensity I/I_{sat} , together with the corresponding optimum detuning that we experimentally identified (blue squares, right axis). First, the behavior of the optimum $|\delta|/\gamma$ versus s_0 can be nicely fit to a power law,

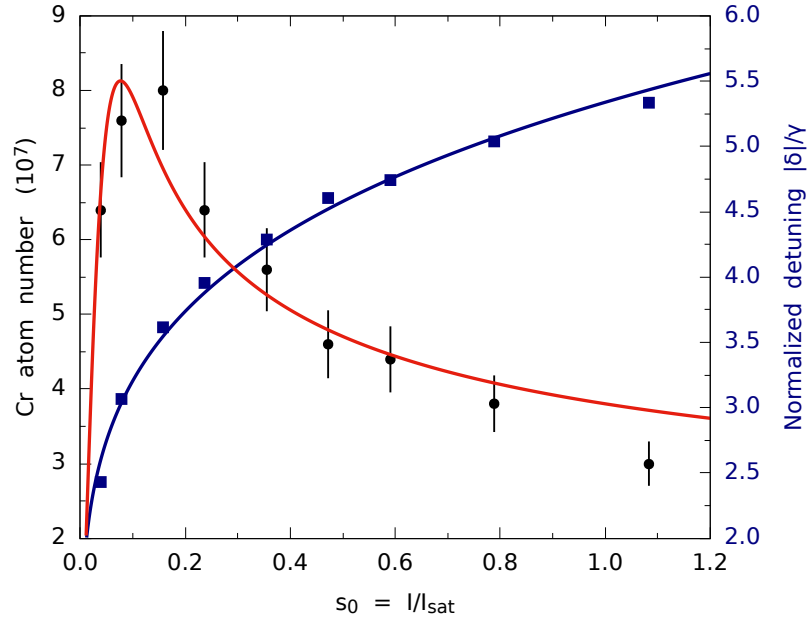


Figure 2.4 – Characterization of the maximum chromium atom number collected in the MOT after 2 s of loading, as a function of $s_0 = I/I_{\text{sat}}$ (black circles, left axis). Here $I = 2P/(\pi w_{\text{MOT}}^2)$ is the peak intensity of one single MOT beam, characterized by a $1/e^2$ radius $w_{\text{MOT}} = 6.5$ mm. Each data point is the average of at least five independent measurements, exhibiting a constant 10% uncertainty. For each value of I/I_{sat} , the corresponding optimum detuning $|\delta|/\gamma$, experimentally determined, is shown as blue squares, right axis. The blue line shows the best fit to a power law $|\delta|/\gamma \propto (I/I_{\text{sat}})^q$, yielding $q = 0.22(1)$. The red line shows instead the best fit of N_∞ given by Eq. (2.2) (see discussion in text), assuming the best-fitted power-law dependence of $|\delta|/\gamma$, and allowing σ_{ZS} together with an overall multiplicative constant A_∞ as free parameters. The fit returns $\sigma_{\text{ZS}} = 2.8(8)$ m/s and $A_\infty = 2.33(8) \times 10^4$.

with exponent $q = 0.22(1)$ (see the blue curve). Second, one can notice how, throughout the scanned parameter space, a considerable increase in the collected Cr atoms is observed, relative to what reported in Ref. [121], and samples ranging from 3×10^7 to 8×10^7 particles can be obtained. The general trend of N_∞ is nicely reproduced by a fit of Eq. (2.2) (red curve), allowing σ_{ZS} and an overall multiplicative constant as free parameters.

The identification of a region of MOT parameters able to substantially mitigate light-assisted losses allowed us to greatly speed up and simplify the experimental routine to produce a (large) ^6Li - ^{53}Cr mixture in the cold regime. Since a loading time of 2 s is sufficient to reach the steady-state N_∞ for chromium, and the Cr MOT performances summarized in Fig. 2.4 are not affected by the presence of an overlapping lithium cloud, there is no longer a need for us to pursue accumulation of Cr atoms in magnetically trapped D states [125] – a procedure previously tested in the lab, that required significantly longer loading times and whose efficiency was found to be limited by the presence of a large Li MOT [121].

As a final remark, I emphasize that, while the optimum loading conditions summarized in Fig. 2.4 greatly reduce the Cr MOT density, they do not limit the capture efficiency of the CMOT stage, operated at constant cooling light parameters. As a consequence, the large increase in the MOT atom number directly turns into a significant density increase after the CMOT, hence providing a substantial gain for the successive step of optical trap loading within our experimental routine (see Sec. 2.5).

2.4 Optimized loading of a dual species ${}^6\text{Li}$ - ${}^{53}\text{Cr}$ MOT

The possibility to rapidly collect a large number of ${}^{53}\text{Cr}$ atoms directly into the MOT considerably simplified the process of devising and optimizing a sequential loading scheme for the Li-Cr mixture in our dual-species magneto-optical trap. In this Section, I summarize the most convenient strategy that we experimentally identified. A more detailed list of the optimum parameters employed, including time diagrams, is reported in my Master Thesis [102].

- (i) We first load lithium atoms for about 6 s, at an optimum gradient of about $b = 45$ G/cm along the vertical direction. During this time, the chromium lights and ZS field are already on, although only a little Cr atom number is collected at this stage.
- (ii) We switch off the Li Zeeman slower and decrease the MOT gradient down to $b = 25$ G/cm, which is the optimum value found for chromium. The light detuning for lithium is correspondingly slightly diminished to ensure a good storage of this species during the chromium MOT loading.
- (iii) We operate the Cr MOT for about 2 s with the optimum light parameters reported in Fig. 2.4.
- (iv) We then turn off the Cr Zeeman slower (light and field) and adiabatically transfer the cold Li-Cr mixture from the quadrupole field of the “MOT” coils¹ into that of a smaller set of “GRAD” coils, yielding the same gradient but allowing for a faster switch off.
- (v) Finally, a 6-ms-long CMOT phase is applied on both species simultaneously, in order to compress and cool the mixture. This is done without changing the field gradient, by diminishing the intensity of the MOT lights and moving the cooling frequency closer to resonance. Specifically, for chromium the CMOT detuning is set to about -1.4γ and the laser intensity is reduced to about 20%, relative to that employed during the loading. For lithium, the detuning is moved from about -7 to -1.7 natural linewidths ($\gamma_{\text{Li}}/2\pi = 5.87$ MHz) and the light intensity is substantially reduced, passing from more than $17 I/I_{\text{sat}}^{\text{Li}}$ at the loading stage down to about $0.5 I/I_{\text{sat}}^{\text{Li}}$ ($I_{\text{sat}}^{\text{Li}} = 2.54$ mW/cm²).

At the end of this procedure, lasting 8 s overall, we obtain cold Li-Cr mixtures comprising 10^9 Li and 8×10^7 Cr atoms, at a temperature of about 300 μK .

2.5 Loading into a bichromatic optical dipole trap

As anticipated at the beginning of this Chapter, our experimental strategy is based on an all-optical approach conceptually analogous to the one employed for Li-K mixtures in the Innsbruck experiment [124]. As a crucial step, this requires an efficient loading of the cold Li-Cr mixture, delivered by our dual-species MOT discussed in the previous sections, into a high-power optical dipole trap. However, also in this case a few factors make the Li-Cr system more challenging than the Li-K one. In this Section, I discuss these issues and the methods we follow to overcome them.

First, the chromium polarizability for standard infrared (IR) laser trapping lights at 1064 or 1070 nm is only about 30% of the lithium one [see red profiles in Fig. 2.5(a)], making the resulting IR trap not suited to guarantee an efficient sympathetic cooling of Cr. Indeed, a 1070 nm beam, characterized by power P_{1070} (expressed in watts) and $1/e^2$ waist

¹The “MOT” coils are the “BIAS” coils used in anti-Helmoltz configuration during the first part of the MOT stage, see Sec. 6.1.

w_{1070} (in microns), yields a maximum trap depth for lithium and chromium that, expressed in millikelvin, are given by $U_{1070}^{\text{Li}} \simeq -38.3 P_{1070}/w_{1070}^2$ and $U_{1070}^{\text{Cr}} \simeq -12.7 P_{1070}/w_{1070}^2$, respectively. We mitigate this issue by superimposing a green beam at 532 nm onto the IR trap. This second light is tightly confining for chromium, whereas it anticonfines lithium [see green profiles in Fig. 2.5(a)]. Denoting the power and waist of the green beam by P_{532} and w_{532} , respectively, one finds in this case $U_{532}^{\text{Li}} \simeq +39.2 P_{532}/w_{532}^2$ and $U_{532}^{\text{Cr}} \simeq +23.5 P_{532}/w_{532}^2$. Therefore, by tuning the relative power of the two lights in this bichromatic optical dipole trap, one can control the overall trap depth ratio for the two species [see black profiles in Fig. 2.5(a)].

Experimentally, the bODT is realized by overlapping our IR trap, already discussed in Ref. [122] and based on a multimode fiber laser module from IPG Photonics (YLR-300) delivering up to 300 W, with a high-power laser at 532 nm. For the latter we currently employ a Sprout-G source by Lighthouse Photonics, nominally delivering up to 15 W, now limited to about 10 W due to aging.² The two bODT beams, propagating in the horizontal (x, y) plane, are recombined on a dichroic mirror and then focused onto the center of the Li-Cr MOT clouds, with waists along the vertical (horizontal) directions of $w_{z,1070} = 44 \mu\text{m}$ ($w_{y,1070} = 58 \mu\text{m}$) and $w_{z,532} = 48 \mu\text{m}$ ($w_{y,532} = 45 \mu\text{m}$) for the IR and green light, respectively. Not surprisingly, we find that the relative alignment of these two beams is a critical parameter for the overall performance of the experiment. For this reason, in order to finely adjust it in a reproducible fashion (and to correct for day-to-day fluctuations), we employ a single motorized mirror (Newport, Picomotor 8301NF) on the

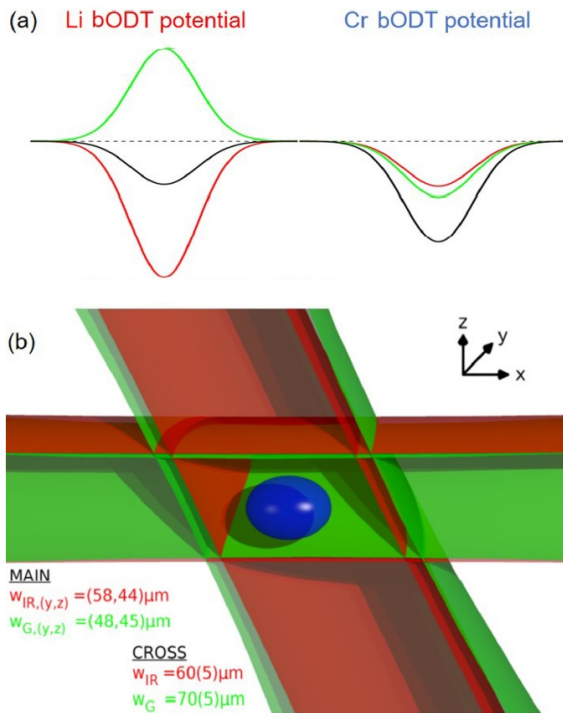


Figure 2.5 – (a) Sketch of the optical potentials experienced by Li (left) and Cr (right) atoms confined in the bODT. The IR light (red curves) yields a trapping potential about 3.3 times deeper for Li than for Cr atoms, whereas the green beam (green curves) anticonfines lithium and tightly confines chromium (see the text for details). By adjusting the parameters of these two beams, in these panels assumed to feature equal waists and an IR-to-green power ratio of 2, one can obtain an overall bODT potential (black curves) deeper for the Cr than for the Li component. (b) Schematic view of our bODT setup. Two overlapped IR and green beams, propagating in the horizontal plane along the x direction and featuring waists indicated in the figure, provide the primary trapping potential for the atomic mixture, sketched in blue. A secondary bichromatic trap, realized by two additional overlapped IR and green circular beams with waists of about 60 and 70 μm , respectively, crosses the main bODT at an angle of about 17° from the vertical direction. The crossed bODT beam, turned on at the end of the evaporation stage, allows us to tune the densities of the two mixture components independently while not modifying the trap depth (see Sec. 2.8 for details).

²We also tested two additional green laser sources: The first (IPG Photonics GLR-50), delivering up to 50 W, was found problematic in terms of power stability, and it even broke two times. The second (Coherent Verdi V-5), with output power limited to 5 W, was not sufficient to achieve the desired trap depth ratio for Li and Cr atoms, without significantly reducing its beam waist compared to the IR one.

green laser path, placed immediately before the dichroic mirror that combines the two bODT lights.

A second complication of Li-Cr, relative to the Li-K system, is that the direct loading of Cr atoms from the MOT into the optical trap, contrarily to the lithium case (see, e.g., Ref. [131]), has been found to be challenging [127, 128, 137]. Besides increasing light-assisted losses owing to an increased density of the trapped cloud, the IR light shifts both the 7S_3 and the 7P_4 atomic levels (connected by the main cooling transition, see Fig. 2.3) to lower energy, with a shift for the excited state larger than the one of the ground state. Therefore, the detuning $|\delta|$ of the MOT light, experienced by Cr atoms within the IR trap, is effectively reduced (and it may even possibly change sign). Light-shift measurements, performed by monitoring the resonance frequency of absorption imaging of a cold Cr cloud in the presence of our IR beam [102], yielded a trap-averaged shift of $-0.021(2)$ MHz/W. This implies that the (C)MOT detuning, experienced by atoms at the center of the IR trap with $P_{1070} \sim 200$ W, is moved towards resonance by about $+1\gamma$. It thus becomes almost impossible to simultaneously guarantee a good efficiency of the CMOT stage for Cr atoms both inside and outside the IR trap, especially given the inhomogeneous intensity distribution of the trapping beam.

One way to circumvent this problem is to flash the IR trap only once the (C)MOT lights are turned off. This procedure, given our large Cr MOT atom number and the high IR power at our disposal, allows us to capture about 10^6 ${}^{53}\text{Cr}$ atoms within the IR beam at a typical power of 130 W. However, such a non-adiabatic loading method considerably heats up the sample and it is far from being optimum also for the lithium component. More involved loading schemes, alternative to the instantaneous flash of the IR trap, have been devised for chromium [127, 128, 137], and rely on the accumulation of metastable D -state atoms in a combined magnetic and optical potential.

In our case, we found a convenient way, directly offered by our bODT setup, to successfully overcome this major technical issue. The key point is that the 532-nm light dramatically perturbs the cooling transition, owing to the presence of three atomic lines that connect the 7P_4 level to the 7D states (see Fig. 2.3), all centered around 533 nm and featuring linewidths ranging from 0.9 to about 10 MHz. A relatively weak laser field near 532 nm, blue detuned from these lines by less than 1 nm, thus suffices to greatly shift the ${}^7S_3 \rightarrow {}^7P_4$ transition towards higher frequencies. Contrarily to the IR case discussed above, this implies that the effective detuning of the MOT light experienced by atoms within a 532-nm beam is strongly redshifted out of resonance. The green light of our bODT can thus be efficiently exploited to (over)compensate for the detrimental effect of the IR main beam on the Cr CMOT, realizing an effective *dark spot* in correspondence of the dipole trap.

We tested the feasibility of this loading strategy by increasing the IR beam up to 130 W, and simultaneously the green beam to a variable power level, through 3-ms-long linear ramps starting 1 ms before the chromium CMOT stage. For this experiment, the laser cooling light parameters were kept fixed at the optimum values that we experimentally found in the absence of the optical trapping potential. We let the system evolve for 5 ms after the end of the bODT ramps, then we switched off both MOT lights and gradient. At this stage, turning off the cooling light 20 μs before the repumping ones ensures the Cr component is in the $F_S = 9/2$ hyperfine ground state. After an additional hold time of 100 ms, we turned off the bODT and recorded the number of Cr atoms collected in the trap, through absorption imaging following a time-of-flight expansion.

The results of this characterization are summarized in Fig. 2.6, which shows the chromium number loaded into the optical trap, normalized to its maximum value, as a function of the power of the green light (blue circles). One can notice how, without

the green beam being applied, almost no atoms are collected in the IR potential. By increasing the power of the 532-nm light instead, we observed a sharp enhancement of the atom number which, for our specific bODT beam parameters, reaches its maximum at $P_{532} = 0.53(2)$ W. A further increase of the green beam power beyond this optimum value progressively diminishes the Cr atom number. For $P_{532} \geq 1.25$ W, this approaches the value obtained by instantaneously flashing the IR trap right at the end of the CMOT stage, marked by the horizontal gray line in Fig. 2.6. This behavior can be understood by considering that, once the green light reaches this power level, atoms falling within the bODT volume are effectively transparent to the CMOT light and thus completely unaffected by it. Owing to the strong inhomogeneity of the light shift experienced by the Cr CMOT atoms throughout the bODT region at the loading, it is hard to quantify the actual light shifts based on the method employed to characterize the IR beam at high temperature. From a measurement performed in the ultracold regime, where the radial $1/\sqrt{e}$ -size of the Cr sample (of about $8 \div 10$ μm) is much smaller than the beam waist of the green laser [see Fig. 2.5(b)], we obtained a peak shift of $+38(5)$ MHz/W, characterized by a (positive) slope almost 2000 times larger than the IR (negative) one. Correspondingly, at the optimum value shown in Fig. 2.6, atoms residing at the center of the green beam experience an effective redshift of the cooling light of about -3.6γ .

A quantitative analysis of the observed loading dynamics is quite involved, and has not been carried out in our lab. Anyway, a few general points should be emphasized: First, throughout the power range explored in Fig. 2.6, the green beam has a negligible impact on the total trap depth, which is solely set by the high-power IR beam. Second, depending on the specific laser source employed for realizing the green bODT beam, the optimum power may quantitatively move to higher or lower values, but the qualitative trend remains unaffected, as long as the wavelength of the green light remains close to, but shorter than, 532.9 nm. Namely, similar characterizations performed with two different green laser sources previously employed in the lab (IPG Photonics GLR-50 and Coherent Verdi V-5) yielded features completely analogous to that reported in Fig. 2.6, modulus a rescaling of the horizontal axis. Third and most importantly, such a scheme leads to a substantial enhancement of the optical trapping efficiency, compared to the instantaneous

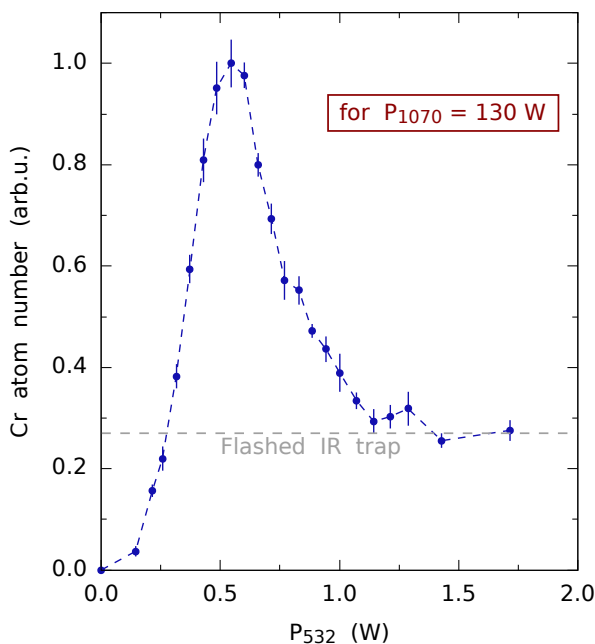


Figure 2.6 – Characterization of the chromium atom number collected in the bODT directly from the CMOT, as a function of the green beam power acting as a dark spot. The Cr population (blue circles), recorded in the bODT after a hold time of 100 ms through absorption imaging following a time-of-flight expansion of 200 μs , is normalized to the maximum value found throughout the scan, centered at $0.53(2)$ W. The horizontal dashed line marks the value obtained by instantaneously flashing the IR trap at the end of the CMOT stage. For this dataset, the IR beam has a fixed power of 130 W and the parameters of the CMOT stage are kept constant at their optimum values, obtained in the absence of the bODT. The Sprout-G module used to realize the dark spot has a wavelength of 532.2 nm.

flash of the IR beam, as it yields more than a fourfold improvement in the bODT atom number, and it does not cause any detectable excitation or heating of the atomic sample. Under optimum conditions, this strategy allows us to store up to 4×10^6 ${}^{53}\text{Cr}$ atoms in the optical trap, at temperatures of about 250 μK , slightly lower than the typical CMOT one. Finally, I also remark that the absolute number of atoms that can be transferred into the bODT from the MOT with this strategy is found to scale linearly with the MOT atom number itself, as shown in Fig. 2.7: Up to the largest MOT clouds we can produce, no saturation effect on the optically trapped samples is observed, with a constant 5.5% MOT-to-bODT transfer efficiency. This observation demonstrates how our strategy indeed allows us to maintain light-assisted losses negligible up to the highest achievable densities, thereby making the ODT loading dynamics of chromium as simple as the one of lithium and other alkali metals.

Besides enabling the collection of a significant number of ${}^{53}\text{Cr}$ atoms, which may be appealing also for single-species setups dealing with cold (fermionic or bosonic) chromium, this direct loading method is especially advantageous in our mixture experiment. Indeed, the presence of the weak green laser field is essentially irrelevant for the loading of the lithium component: Up to 2×10^7 ${}^6\text{Li}$ atoms, with temperatures of about 300 μK , are stored in the bODT when the IR trap power is set to 130 W, with transfer efficiencies similar to those reported in Ref. [131] for the single-species case. Since the two species feature similar temperatures, the simultaneous loading of the Li-Cr mixture in the bODT does not perturb too strongly the chromium performance, although the initial trap depth ratio, uniquely set by the IR beam, yields (at 130 W) $U_{1070}^{\text{Li}} \sim 1.9$ mK and $U_{1070}^{\text{Cr}} \sim 0.65$ mK, thus causing a rather large asymmetry in the temperature-to-trap-depth ratio between the two components. Indeed, while $\eta_{\text{Li}} = U_{1070}^{\text{Li}}/(k_{\text{B}} T_{\text{Li}}) \sim 7$, for chromium we obtain $\eta_{\text{Cr}} = U_{1070}^{\text{Cr}}/(k_{\text{B}} T_{\text{Cr}}) \sim 3$. For this reason, the chromium bODT population, after a hold time of 100 ms, in the presence of the overlapping Li sample, is found to drop by almost a factor of 3.

This effect is partly reduced by applying a 350- μs -long D1 molasses phase on lithium within the bODT [131], about 3 ms after the end of the CMOT stage, once the magnetic-field quadrupole gradient has been zeroed. This allows us to reduce the lithium temperature, although not substantially, from 300 down to approximately 220 μK , a value slightly lower than the chromium one. At the end of the D1 cooling, a 20- μs -long hyperfine pumping pulse is applied [131], which transfers all lithium atoms into the $F = 1/2$ ground-state manifold, see Fig. 2.2. Finally, within 20 ms the green power is linearly ramped up to its maximum value, corresponding to a net power of 7 W on the atoms, leading to about a

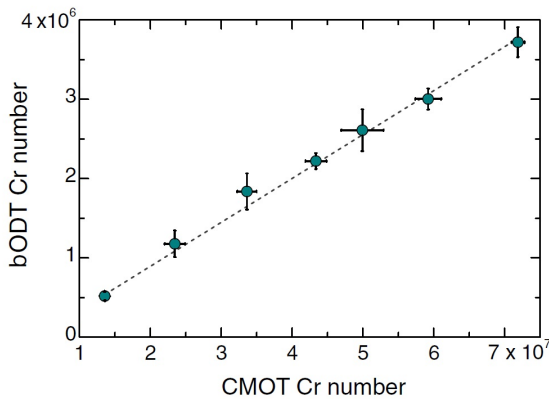


Figure 2.7 – Dependence of the number of chromium atoms collected in the bODT upon the CMOT atom number. The latter was adjusted by reducing the MOT loading time while not varying the MOT parameters. The IR beam was set to a power of 130 W and the green light was adjusted to the optimum value shown in Fig. 2.6. Data were recorded, after a hold time of 100 ms in the bODT, through absorption imaging that followed a time-of-flight expansion of 200 μs . Each point corresponds to the average value of at least four independent measurements, with error bars representing the standard deviation of the mean. A linear fit to the data (dashed line) yields an overall MOT-to-bODT transfer efficiency of 5.5(2)%.

11% increase (6% decrease) of the chromium (lithium) trap depth.

The application of the bODT loading method for ^{53}Cr discussed above, and its integration within our two-species experimental cycle, allow us to store in our optical trap cold Li-Cr mixtures at about 250 μK , composed of 2×10^7 ^6Li atoms populating the two lowest Zeeman states $m_F = \pm 1/2$ of the $F = 1/2$ manifold, coexisting with about 2×10^6 ^{53}Cr atoms, asymmetrically distributed among the four lowest-lying Zeeman states of the $F = 9/2$ hyperfine level. Specifically, without performing any Zeeman-selective optical pumping stage, about 55% of the Cr sample is found in the lowest Zeeman state $m_F = -9/2$. The remaining Cr atoms are distributed among the three higher-lying levels $m_F = -7/2, -5/2,$ and $-3/2$, with relative populations of 25%, 13%, and 7%, respectively. This represents our starting point for the successive stages of evaporative and sympathetic cooling, which are discussed in the next Section. For convenience, in the following I denote the different Zeeman levels of both species by $|\text{Li}|i\rangle$ and $|\text{Cr}|j\rangle$, respectively, with $i, j = 1, 2, \dots$ labeling the atomic state starting from the lowest-energy one.

2.6 Evaporative and sympathetic cooling stages

In our experimental routine, once the two species are loaded into the bODT, while the green beam is ramped up to its maximum power, within 55 ms we also linearly increase the magnetic-field bias up to 880 G, i.e., about 50 G above the broad Feshbach resonance occurring between the two lowest Zeeman states of lithium $|\text{Li}|1\rangle$ - $|\text{Li}|2\rangle$. At this field [7], intraspecies lithium collisions are unitary-limited at all temperatures above $T \simeq 300$ nK [138], whereas interspecies Li-Cr collisions are at their background level, characterized by a scattering length $a_{\text{bg}} \simeq 42 a_0$ (see Chapter 3). The magnetic-field curvature of our coils provides an additional in-plane harmonic confinement, characterized by a lithium (chromium) frequency of about 8.5 Hz (7.0 Hz), which adds to the bODT potential. The initial trap depth ratio between the two components $U^{\text{Li}}/U^{\text{Cr}} \sim 3$ and the comparably low initial value of $\eta_{\text{Cr}} \sim 3$ are not optimal for an efficient storage of chromium atoms in the presence of the lithium sample. For this reason, we find it experimentally convenient to start the evaporation immediately after the green beam has been raised.

The evaporative cooling ramps, overall lasting for about 5 s, are performed by decreasing the power of the bODT beams, hence the trap depth, through a series of exponential ramps, shown in Fig. 2.8(a) for the IR and green lights, respectively. In the same Figure, panels (b) and (c) show the corresponding evolution of the normalized atom number and temperature, for the $|\text{Li}|1\rangle$ (red circles) and $|\text{Cr}|1\rangle$ (blue circles) component, respectively, extracted from Gaussian fits to the density distributions, monitored via spin-selective absorption imaging following time-of-flight expansion. The $|\text{Li}|2\rangle$ sample, not shown, throughout the evaporation stage is found at a temperature equal to the one of $|\text{Li}|1\rangle$ and the corresponding atom number, relative to that of $|\text{Li}|1\rangle$, is roughly constant at a value $N_{|\text{Li}|2\rangle}/N_{|\text{Li}|1\rangle} = 0.71(5)$. Additionally, Fig. 2.8(d) displays the ratio between the chromium and lithium temperatures throughout the evaporation stage.

During the first 400 ms, evaporative cooling of lithium is established by decreasing only the IR beam power, from 130 W down to 28 W. This first step, sufficiently slow to allow for intraspecies thermalization of lithium, is somewhat too fast for the chromium component, the temperature of which is found to be about 50% higher than the lithium one. Despite the rather poor efficiency of sympathetic cooling observed within this initial stage, such a ramp allows us to rapidly diminish the $U^{\text{Li}}/U^{\text{Cr}}$ ratio, from the initial value of 3 down to about 1. In order to maintain the chromium cloud well overlapped with the lithium one at all times, we also minimize the differential gravitational sag of the two components by applying a magnetic-field gradient b along the vertical direction, to counterbalance the

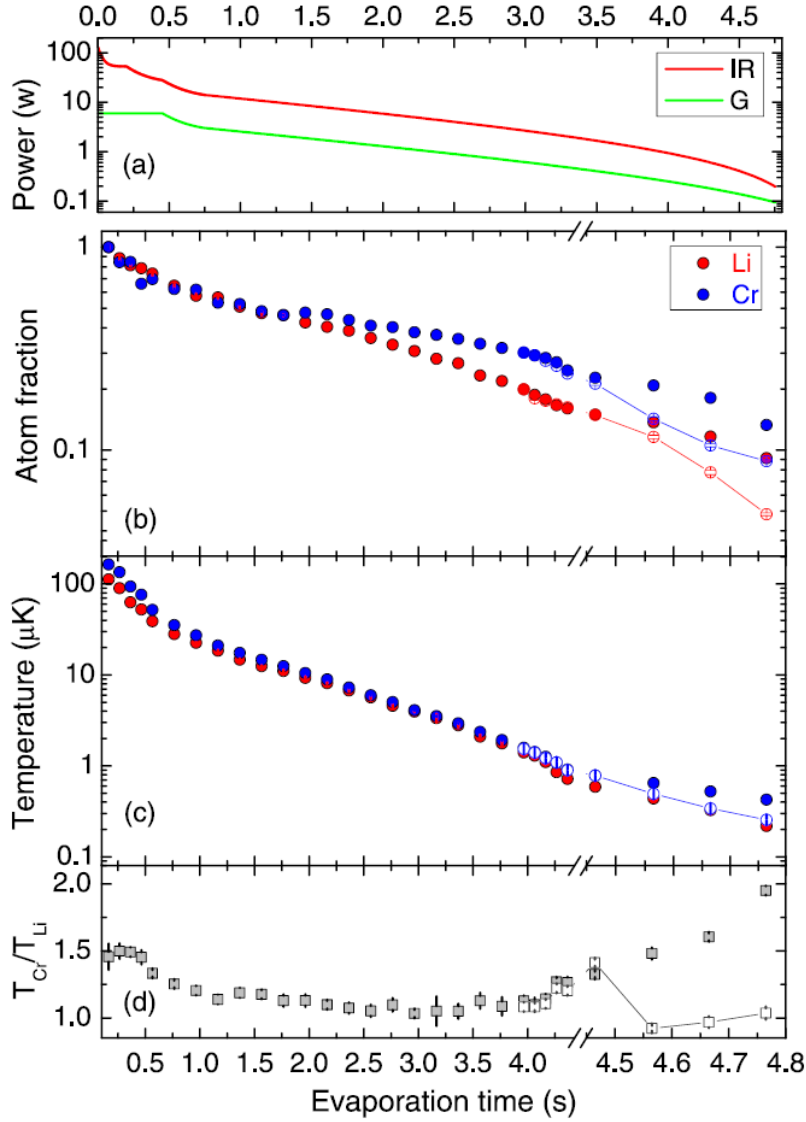


Figure 2.8 – (a) Evolution of the IR and green bODT powers during the evaporation ramp. The IR power is reduced through four consecutive exponential ramps, lasting 0.2, 0.25, 0.3, and 4 s, respectively, and characterized by $1/e$ decay times $\tau_1 = 30$ ms, $\tau_2 = 125$ ms, $\tau_3 = 150$ ms, and $\tau_4 = 1.6$ s. The green power is decreased through two consecutive ramps, simultaneous to the last two IR ones and featuring the same durations and decay times. (b) Evolution of the $|\text{Li}\rangle$ (red circles) and $|\text{Cr}\rangle$ (blue circles) atom number during the evaporation ramps. Both data sets are normalized to the atom numbers recorded after the first 165 ms of evaporation, where $N_{|\text{Li}\rangle} = 5.1(1) \times 10^6$ and $N_{|\text{Cr}\rangle} = 1.05(3) \times 10^6$. Open symbols refer to the number evolution when the *Feshbach cooling* stage is applied (see Sec. 2.7). (c) Same as in (b) but for Li and Cr temperatures. For both (b) and (c), numbers and temperatures are obtained from Gaussian fits to the atomic distributions, imaged after variable time-of-flight expansion. Note that, for the coldest samples, the temperature extracted from the Gaussian fit overestimates the real one, owing to Fermi degeneracy, up to about 40%. Each data point is the average of at least three independent measurements and error bars account for the standard deviation of the mean. Open symbols refer to the temperature evolution when the *Feshbach cooling* stage is applied. (d) Ratio between chromium and lithium temperatures, without (closed squares) and with (open squares) application of the *Feshbach cooling* stage.

gravitational force. Experimentally, we found an optimum value of about 1.5 G/cm, which corresponds to an almost perfect levitation of the chromium component and to an effective weak “antigravity” for lithium of about $-g/2$.

For evaporation times longer than 0.5 s, where $U^{\text{Li}}/U^{\text{Cr}} \sim 1$, the observed trajectories signal a good interspecies thermalization and a satisfactory sympathetic cooling. The observed decrease in atom number is indeed significantly smaller for the Cr than for the Li component [see Fig. 2.8(b)], while the chromium temperature closely follows the lithium one with less than 15% mismatch [see panels (c) and (d)], up to about 4 s. Here we obtain about 3×10^5 Cr|1) atoms at $T_{\text{Cr}} \sim 1.5$ μK , coexisting with about 1.1×10^6 Li|1) and 7.5×10^5 Li|2) atoms at $T_{\text{Li}} \sim 1.35$ μK , close to the onset of quantum degeneracy for both lithium components.

By further decreasing the bODT trap depth following the trajectories shown in Fig. 2.8(a), we observe a progressive increase of $T_{\text{Cr}}/T_{\text{Li}}$ [see Fig. 2.8(d)]. A convenient way to circumvent such a limited interspecies thermalization is offered by the presence of various s -wave Li-Cr Feshbach resonances, located at fields above 1400 G (see Chapter 3). In particular, the Li|1)-Cr|1) mixture possesses an approximately 0.5-G-wide Feshbach resonance at 1414 G and the Li|2)-Cr|1) combination exhibits a resonance of similar character around 1461 G. Both features are immune to two-body losses and, despite their relatively narrow character, allow us to tune the Li-Cr scattering length a and thus to increase the Li-Cr elastic scattering cross section well above its background value.

In order to exploit such a possibility, about 1.5 s after the start of the evaporation stage, we linearly ramp the magnetic field from 880 G up to 2 G above the center of one of either resonances. There, the Li-Cr scattering length is not significantly different from its background value $a \sim a_{\text{bg}}$ and also the intraspecies Li|1)-Li|2) scattering length, of about $-2500 a_0$, approaches its large, negative background value [138]. About 4 s after the start of the evaporation, we then reduce the magnetic field detuning to less than approximately 100 mG from the resonance center, correspondingly tuning the Li-Cr scattering length to $a \lesssim -200 a_0$, yet not causing a significant enhancement of interspecies three-body losses. While a more detailed characterization of such a *Feshbach cooling* mechanism near a narrow resonance is presented in the following Sec. 2.7, the open symbols in Figs. 2.8(b)-2.8(d) highlight its impact on the final part of the evaporation ramps. One can see how, for fixed bODT power ramps, an increased Li-Cr scattering rate negligibly affects the Li temperature, whereas it causes a large decrease of the Cr one, allowing us to perfectly cancel the relative temperature mismatch [see the open squares in Fig. 2.8(d)]. The much quicker interspecies thermalization is accompanied by a more sizable atom loss of both species, see the blue (red) open circles in Fig. 2.8(b) for the Cr (Li) component. However, this only moderately decreases the degree of degeneracy of lithium, while for chromium the atom loss is outweighed by the large temperature reduction, resulting in a substantial increase in the Cr phase-space density.

This protocol, overall lasting less than 5 s, allows us to produce degenerate Li-Cr Fermi mixtures, comprising up to 3.5×10^5 Li|1) and 2.5×10^5 Li|2) atoms at $T/T_{\text{F,Li}} \sim 0.25$, coexisting with about 10^5 Cr|1) atoms at $T/T_{\text{F,Cr}} \sim 0.5$. The corresponding degree of degeneracy $T/T_{\text{F,X}}$ ($X = \text{Li,Cr}$) is obtained by fitting time-of-flight images to finite-temperature Fermi-Dirac distributions. For both species, this is compatible with the value estimated on the basis of the measured atom number and trap frequencies,³ and given the temperature $T = 130(20)$ nK, obtained by fitting the low-density wings of the density distributions.

³At the end of evaporation, the trap frequencies $\nu_{x,y,z}$ provided by the combination of the bODT and the B -field curvature are, within a 20% uncertainty: 17, 115, and 156 Hz (14, 124, and 118 Hz) for Li (Cr) atoms, respectively.

During the evaporation, the additional chromium minority components $\text{Cr}|j > 1\rangle$, initially loaded within the bODT, are selectively removed using resonant light pulses, without affecting the $\text{Cr}|1\rangle$ population.⁴

Additionally, we have tested that the evaporation trajectories summarized in Fig. 2.8(a) can be also adapted to produce single-species samples of either species. For lithium, this is straightforward: Without loading the chromium component, the same bODT power ramps discussed above yield crossover superfluids of more than 4.5×10^5 pairs when the bias field is tuned towards the pole of the broad intraspecies Feshbach resonance at 832 G [138]. This number can be further increased up to about 6×10^5 when the same time evolution of the trap depth is realized by means of the sole IR light of the bODT, resulting in performances similar to, and even slightly better than, those reported in Ref. [131] by the Li lab at LENS.

To realize polarized Fermi gases of ${}^{53}\text{Cr}$, the protocols discussed above can be modified only partially, owing to the fact that quantum degeneracy of this species relies in our setup on its sympathetic cooling with lithium. However, a slight increase of the green-to-IR power ratio during the evaporation allows us to obtain about 70% larger Cr samples at 220(20) nK, at the expense of a significant reduction of both Li components, which can be eventually completely removed at the end of the evaporation stage by further increasing the power of the green bODT arm. Sympathetic cooling of ${}^{53}\text{Cr}$ with ${}^6\text{Li}$ thus appears as a promising route to realize large Fermi gases of this (yet poorly explored) atomic species that, before the work summarized in this Chapter, had been produced only in combination with its most abundant bosonic isotope ${}^{52}\text{Cr}$ [126]. In fact, the possibility to exploit the different Li and Cr polarizabilities to the IR and green lights of our bODT, absent when isotopic Cr mixtures are considered, combined with our improvements of the Cr MOT performance, have provided us an almost 200-fold increase in the ${}^{53}\text{Cr}$ atom number brought to $T_{\text{Cr}}/T_{\text{F,Cr}} \leq 1$, relative to previous studies [126].

2.7 Enhanced thermalization near a narrow Feshbach resonance

In this Section, I discuss with more detail the ‘‘Feshbach cooling’’ stage mentioned in Sec. 2.6, providing additional experimental characterizations of such a thermalization dynamics near a narrow FR. A more systematic experimental study and theoretical analysis, which will considerably benefit from the numerical simulator I developed for the transport measurements of Chapter 5, will be the subject of future work.

As discussed in Sec. 2.6, the background Li-Cr scattering length, of about $42 a_0$, suffices to ensure inter-species thermalization during a large part of the evaporation stage, from the initial temperature of about 250 μK down to a few μK . However, from that point on, i.e. once lithium approaches the quantum-degenerate regime, such a background value turns out to be somewhat too small, and the chromium-to-lithium temperature ratio, $T_{\text{Cr}}/T_{\text{Li}}$, is found to progressively grow as the bODT trap depth is further decreased, see again Fig. 2.8(d). Rather than circumventing this issue by significantly extending the evaporation ramps in this final stage, we opted to exploit the presence of various narrow s -wave Li-Cr Feshbach resonances (see Chapter 3), located at fields above 1400 G, where the $\text{Li}|1\rangle$ - $\text{Li}|2\rangle$ scattering length is still large and negative [138].

To investigate the impact of an increased inter-species scattering rate during the final part of the evaporative cooling stage, about 800 ms before evaporation ends – i.e. when temperatures are on the order of 1.5 μK [see Fig. 2.8(c)] – in 550 ms we linearly decreased the magnetic field detuning from $\delta B = B - B_0 \simeq +2$ G to a target value δB_{hold} (relatively)

⁴These spin-selective optical removals are performed employing light resonant with the $\text{Cr}|1\rangle$ state at 1414 G (see Sec. 6.2), but lowering the B field such that it becomes resonant with the desired $\text{Cr}|j \geq 2\rangle$ spin state.

close to the resonance pole, without crossing it. There, while evaporation ramps were ongoing, we held the sample for 230 ms (i.e. essentially for the remaining evaporation time), before eventually ramping the B -field to an off-resonant value $\delta B \sim \Delta_B \sim 0.5$ G, i.e. close to the zero-crossing. We then took absorption images of the two atomic clouds, following time-of-flight expansion, from which we extracted atom numbers and temperatures via 2D Gaussian fits.

In Fig. 2.9 I present the results of this study, as a function of the target detuning δB_{hold} . Besides atom numbers [panel (a)] and temperatures [panel (b)], I also show normalized phase-space densities [panel (c)], estimated via the classical relation $\text{PSD} \propto N/T^3$. As one can see, for $\delta B_{\text{hold}} \gtrsim +150$ mG, where the Li-Cr scattering length $-90 a_0 < a < 0$, no significant difference with respect to the background is observed. However, for $\delta B_{\text{hold}} \lesssim +100$ mG, the chromium temperature exhibits a clear decrease – without dramatic losses of Cr atoms – at the expense of a reduction in the Li population. In particular, the Cr PSD, normalized to its background value, features a pronounced maximum around $\delta B_{\text{hold}} \simeq +35$ mG (corresponding to $a \simeq -500 a_0$), where up to a sixfold relative increase is recorded. Parallel to this, the Cr temperature essentially approaches the Li one, with a moderate drop of N_{Cr} of about 30%. Further lowering δB_{hold} with respect to the optimum point, over the selected timescales, results in strong losses for both atomic components, ultimately causing a severe drop of the Cr PSD.

As a second step, we characterized the temperature dependence of the optimum magnetic field detuning that maximizes the Cr PSD. For this experiment, we truncated the evaporation ramps at $t_{\text{evap}} = 4$ s, deliberately introducing a controlled temperature mismatch (with Li always being colder than Cr) by adjusting the final values of IR and green light in our bODT. Specifically, we moved in this parameter space by keeping an approximately constant temperature ratio $T_{\text{Cr}}/T_{\text{Li}} \sim 3$. Similarly to the procedure described above, we

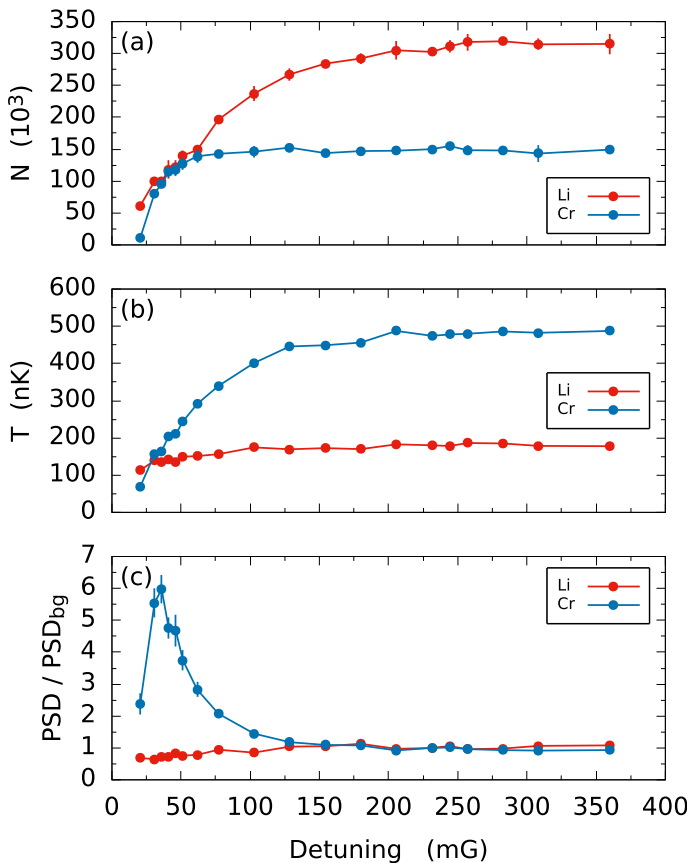


Figure 2.9 – Effect of a 230-ms-long thermalization time at the target detuning δB_{hold} , during the final part of evaporation. (a) Atom numbers, (b) temperatures, and (c) normalized PSDs are derived from absorption imaging following time-of-flight expansion under non-interacting conditions. The PSD is obtained from the classical relation $\text{PSD} \propto N/T^3$, and it is normalized to its off-resonant value. In every panel, red (blue) points correspond to Li (Cr), and the line segments connecting them are simply guides to the eye.

linearly decreased the magnetic field detuning to a target, variable value $\delta B_{\text{hold}} \lesssim +100$ mG, where we allowed interspecies thermalization to occur for $t_{\text{hold}} = 150 \div 200$ ms. After that, we quickly moved to $\delta B \sim \Delta_B$, where we recorded absorption images of the two freely-expanding clouds at long time of flight.

The results of this second characterization are summarized in Fig. 2.10, which shows the Cr PSD versus δB_{hold} , for a series of different temperatures (see legend in μK), normalized for each dataset to its background, non-resonant value. First, one can notice how, for each initial temperature, there is an optimum detuning $\delta B_{\text{opt}} > 0$ (where the Cr PSD reaches a maximum value) which is experimentally found to linearly decrease with the initial system temperature, see inset of Fig. 2.10. Second, the lower is the sample temperature, the more sizable is the gain in PSD that can be achieved. Third, by tracing the time evolution of the chromium temperature at such δB_{opt} (not shown), the extracted thermalization rate is found inversely proportional to $\langle v_{\text{rel}} \rangle$, i.e. to the estimated Li-Cr mean relative velocity, obtained by averaging over the momentum distributions of the two components. Finally, although not shown here, thermalization data taken at negative detunings, i.e. at $a > 0$ values, do not exhibit any appreciable resonant enhancement as the one presented in Fig. 2.10. Such a peculiar trend qualitatively matches the expectation from the two-body scattering theory discussed in Sec. 1.5 for narrow FRs. Indeed, as shown already in Fig. 1.1, for $R^*/|a| \gg 1$ the cross-section becomes unitary-limited at finite $a < 0$ values – i.e. finite $\delta B > 0$ in our case – when $k_{\text{rel}}^2 R^* a = -1$. By equivalently expressing this relation in terms of collision energy $E_{\text{coll}} = \hbar^2 k_{\text{rel}}^2 / (2m_{\text{red}})$, and exploiting Eqs. (1.18) and (1.20) for $a(\delta B)$ and R^* , respectively, it is straightforward to obtain that collisions at energy E_{coll} are resonantly enhanced at the magnetic-field detuning δB for which $E_{\text{coll}} = \delta B \delta\mu$: Namely, when the collision energy equals the one of the (virtual) closed-channel molecule. Although this result does not account for thermal averaging over all Li-Cr collision energies, it qualitatively matches our observation of a linear dependence of δB_{opt} upon the initial lithium temperature, see the inset of Fig. 2.10. Additionally, when the detuning is set at δB_{opt} for a given (relative) momentum class $\hbar k_{\text{rel}} = m_{\text{red}} v_{\text{rel}}$, the corresponding scattering rate Eq. (1.6) is expected to scale as $\Gamma_{\text{el}} \propto 1/v_{\text{rel}}$, again in agreement with our experimental observation.

While a more quantitative theoretical analysis of this so-called ‘‘Feshbach cooling’’ has not been carried out yet, I remark that the identification of this resonant thermalization mechanism has been crucially relevant in our experimental routine to attain large, degenerate samples of lithium and chromium atoms, see Sec. 2.6. Besides being a key tool for the

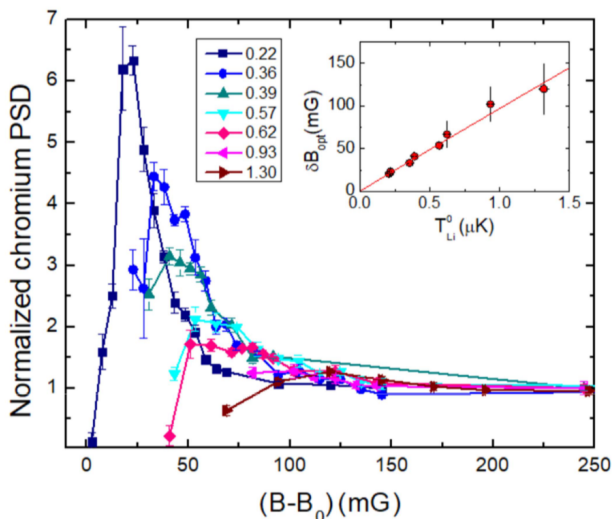


Figure 2.10 – Main panel: Chromium PSD, normalized to its off-resonant value, is plotted as a function of the magnetic field detuning δB_{hold} , where Cr is let to thermalize with Li for $150 \div 200$ ms. Different datasets refer to different initial lithium temperatures, specified in the legend in μK units. For each measurement, the initial temperature mismatch was kept at $T_{\text{Cr}}^0/T_{\text{Li}}^0 \sim 3$. Inset: the optimum detuning δB_{opt} where the Cr PSD gain is found to be maximum, is plotted as a function of T_{Li}^0 . The solid line is the best-fit to the data with a power-law function, yielding an exponent $\alpha = 0.99(3)$.

Li-Cr system, such a phenomenon, primarily determined by elastic scattering, may find application also on other ultracold mixtures – Bose-Fermi, Bose-Bose, atom-ion, etc. – and also single-species experiments, whenever narrow FRs (eventually not s -wave) are available. For instance, we are aware that qualitatively similar observations have been obtained on Li-K (both Fermi-Bose and Fermi-Fermi) mixtures, as well as on homonuclear Dy Bose gases (Private communications by R. Grimm and G. Modugno’s teams, respectively).

2.8 Increasing quantum degeneracy in a crossed bODT

As discussed in Sec. 2.6, the degree of degeneracy obtained at the end of the evaporation stage is quite different for the two components, with lithium being highly degenerate while chromium features a “mild” degeneracy, with $T_{\text{Cr}}/T_{\text{F,Cr}} \sim 0.5 \div 1$. Further decreasing the bODT trap depth does not lead to any substantial gain in phase-space density, a reduced temperature being counterbalanced by a drop in the atomic densities for both species.

To overcome this problem, we implemented a second bichromatic trapping beam, which crosses the main bODT at an angle of about 17° from the vertical direction, see Fig. 2.5(b). Such a secondary beam, that we only switch on once the evaporation stage has ended, is obtained by exploiting the same laser sources, recycling part of the IR and green powers of the main bODT, damped at the end of the evaporation procedure. Both IR and green crossed beams are almost circular and at the atom position they feature waists of about 60 and 70 μm , respectively. Being oriented almost vertically, this second bichromatic beam does not significantly modify the overall trap depth experienced by the two atomic components,⁵ and hence their temperature, whereas it allows us to control the confinement, and thus the density and Fermi energy, of each cloud almost independently.

In order to test this possibility, after the evaporation stage we raised up the crossed bODT at various IR and green power levels through a 50-ms linear ramp. After about 50 ms, we then recorded time-of-flight images of both Li $|1\rangle$ and Cr $|1\rangle$ and obtained the corresponding atom number and degree of degeneracy by fitting the atomic clouds to a finite-temperature Fermi-Dirac distribution. The employed timings, although not exceeding the typical axial ones in the sole main bODT trap, did not cause any detectable excitation or trigger subsequent dynamics of the Li and Cr clouds. Exploitation of much longer ramps or hold times resulted instead in a poorer collection efficiency of the lithium component within the crossing region.

The results of this characterization are summarized in the color maps in Fig. 2.11: Panels (a) and (c) show the chromium and lithium normalized temperatures $T/T_{\text{F,Cr}}$ and $T/T_{\text{F,Li}}$, respectively, as a function of green and IR powers of the crossed beam. Panel (b) presents the corresponding trend for the Li $|1\rangle$ atom number, normalized to 3.5×10^5 , which is the value obtained without application of the crossed beam. The chromium component, characterized by an axial size in the main bODT roughly two times smaller than the lithium one, could be efficiently transferred into the crossed trap at all green and IR powers that we explored, resulting in a Cr number (not shown) which varies less than 15% throughout the investigated parameter space. From Fig. 2.11, one can notice the qualitatively different response of the two mixture components to the crossed bODT. On the one hand, for chromium, application of either crossed beam leads to a substantial increase in the degree of degeneracy: As shown in Fig. 2.11(a), several IR and green combinations yield a twofold decrease of $T/T_{\text{F,Cr}}$, passing from about 0.5 down to 0.25, solely caused by the large Cr density increase within the crossed trap. On the other hand, for lithium, application of one single (IR or green) crossed beam causes a decrease of the atom number [see Fig. 2.11(b)] together with a reduction of the degree of degeneracy [see Fig. 2.11(c)].

⁵Given the beam waists of the main bODT of our setup, the trap depth is set by the vertical direction.

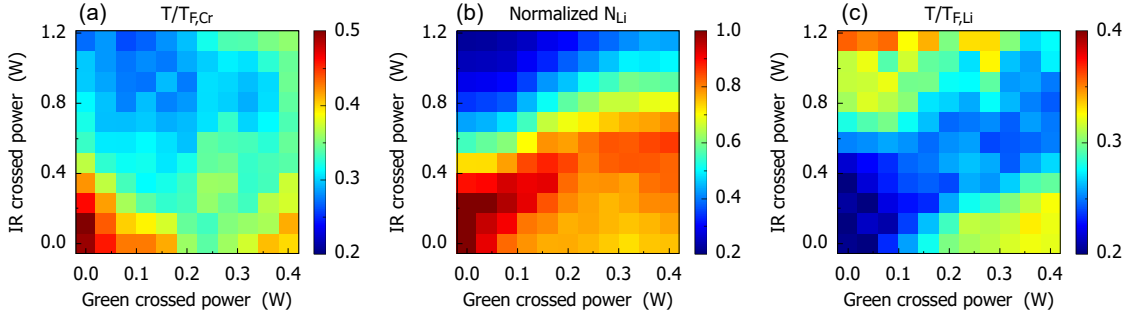


Figure 2.11 – (a) Normalized chromium temperature $T_{\text{Cr}}/T_{\text{F,Cr}}$ monitored as a function of green and IR powers of the crossed bODT. The degree of degeneracy is obtained as the average value extracted from fitting at least four independent Cr images, acquired after 4.6 ms of time-of-flight. (b) Lithium atom number, normalized to its value measured in the sole main bODT at the end of the evaporation ramp, as a function of green and IR powers of the crossed bODT. (c) Same as in (a) but for the reduced lithium temperature $T_{\text{Li}}/T_{\text{F,Li}}$. For lithium, a 3-ms time-of-flight expansion was employed. In all panels, the value of each pixel is averaged over the vertical and horizontal nearest-neighbors.

The response to the IR trap can be explained by the initially larger cloud size and mean energy-to-trap depth ratio, compared to the Cr ones, which implies a limited collection efficiency and a progressively increased anharmonicity of the experienced potential, leading to a reduction of local density and degree of degeneracy. The response to the green crossed trap can instead be explained by the anti-confining (rather than confining) effect on the Li species: Even for low green powers, the atom-number reduction is accompanied by a drop of local density within the crossing region, and hence of Fermi degeneracy. However, when both IR and green lights are applied, over a quite wide range of parameters we observe an efficient storage of lithium atoms in the crossed bODT, at an almost constant $T/T_{\text{F,Li}}$ [see Fig. 2.11(c)]. As expected, this occurs roughly around the diagonal of panels (b) and (c), where the anti-confinement of the green beam is (more than) counterbalanced by the IR light and where anharmonicities of the experienced potential, estimated through trap frequency measurements, appear to be negligible.

These observations highlight how the crossed bODT significantly enhances the parameter space which can be explored with the Li-Cr mixture in our setup: By simply tuning the (absolute and relative) powers of the two crossed lights, one can pass from the regime where lithium is highly degenerate and chromium is an almost thermal gas, to the opposite one. Most importantly, over a sizable range of parameters we can simultaneously achieve a high degree of degeneracy for both ${}^6\text{Li}$ and ${}^{53}\text{Cr}$ components. As an example, in Fig. 2.12 I show axially integrated density profiles (black circles) of lithium and chromium Fermi gases, obtained from absorption images (see the insets), acquired after time-of-flight expansion from the sole main bODT trap [panels (a) and (b)] and from a crossed bODT [panels (c) and (d)]. Data are compared with best fits to a Gaussian and to a Fermi-Dirac distribution function, shown in red and blue, respectively. In both configurations, the lithium sample features a roughly constant and low $T/T_{\text{F,Li}}$ value [see panels (a) and (c)] and a corresponding constant peak density of about $1 \times 10^{12} \text{ cm}^{-3}$. For the chromium component, application of the crossed beam negligibly affects the gas temperature and the atom number, constantly about 1.0×10^5 , while it greatly modifies the peak density, which increases from slightly less than $2 \times 10^{12} \text{ cm}^{-3}$ in the sole main bODT to about $4 \times 10^{12} \text{ cm}^{-3}$ within the crossed trap. Correspondingly, the chromium degree of degeneracy is substantially improved, with the initial $T/T_{\text{F,Cr}} = 0.45(7)$ being lowered to $0.26(2)$ [see panels (b) and (d)].

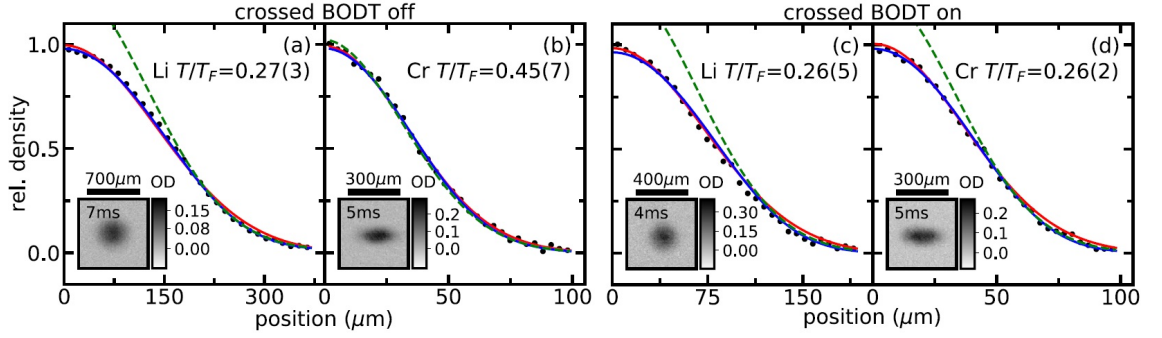


Figure 2.12 – Axially integrated density profiles (black circles) of (a) a lithium and (b) a chromium Fermi gas, simultaneously prepared in the main bODT trap only. Profiles are obtained from the average of about 20 independent absorption images, acquired after time-of-flight expansion and shown as insets. Experimental data are compared with best fits to a Fermi-Dirac (blue line) and a Gaussian (red line) distribution. A Gaussian fit to the low-density tails of the density distributions (green line) accurately captures the atom temperatures, whereas it overestimates the central density of highly degenerate samples. For each component, the reduced temperature T/T_F obtained from the former fit, together with the fit uncertainty, is specified in the panel. (c) and (d) Same as (a) and (b) but for a Li-Cr mixture released from a crossed bODT with IR and green powers set to (c) 0.81 and (d) 0.20 W. Application of such a crossed bODT does not alter the lithium degree of degeneracy, whereas it allows us to greatly reduce $T_{Cr}/T_{F,Cr}$ and to obtain Li-Cr mixtures with both components at one-fourth of their Fermi temperature.

2.9 Conclusive remarks

In this Chapter, I have detailed the experimental procedures, which we devised during the first year of my Ph.D., that allowed us to produce the first quantum degenerate mixtures of fermionic ${}^6\text{Li}$ and ${}^{53}\text{Cr}$ atoms.

In particular, we successfully addressed different issues and challenges related to the cooling and trapping of (fermionic) chromium. Key achievements of our work include the mitigation of light-assisted losses during the Cr MOT stage, and the implementation of an efficient, direct loading scheme for this species into a (bichromatic) optical dipole trap. These important advances have effectively made chromium resemble an “alkali with many repumpers”, significantly simplifying its manipulation and control within ultracold atom experiments. Overall, these protocols allow us to produce deeply degenerate samples with more than 2×10^5 lithium atoms and approximately 10^5 chromium atoms at temperatures around 200 nK.

The procedures described in this Chapter form the foundation for the studies presented in the subsequent ones, laying the groundwork for further exploration of the Li-Cr system.

Chapter 3

Feshbach spectrum and collisional properties of ${}^6\text{Li}$ - ${}^{53}\text{Cr}$ mixtures

In this Chapter, I present the results of our thorough characterization of the elastic (and inelastic) scattering properties of the ${}^6\text{Li}$ - ${}^{53}\text{Cr}$ Fermi mixture, following the lines of our Ref. [139]. Chronologically, these investigations started during the period of my Master Thesis [102], and were finalized in the first months of my Ph.D.: In practice, at that time the experiment was still at a somewhat earlier stage with respect to what described in Chapter 2. Indeed, without knowledge of the interspecies Li-Cr Feshbach resonances (and without many improvements and optimizations developed afterwards), the evaporation stage was only able to reach temperatures on the order of a few μK . Under these conditions we performed extensive loss spectroscopy [7], scanning magnetic fields from 0 up to 1500 G with an average resolution of ~ 60 mG, and exploring up to six different scattering channels. As a result, we were able to identify more than 50 interspecies *s*- and *p*-wave Feshbach resonances (FRs) [7], well suited for the controlled tuning of elastic Li-Cr interactions, and arranged in nonchaotic patterns – despite the dipolar nature and complex level structure of fermionic ${}^{53}\text{Cr}$ (see Fig. 2.3), reminiscent of Dy and Er [140–142]. Our experimental data constituted the fundamental input for a full coupled-channel model [7] developed by our theory collaborator Prof. Andrea Simoni (University of Rennes), a world-renowned expert of multichannel calculations who has pioneered the theoretical study of collisional properties of both ${}^6\text{Li}$ [143] and ${}^{52}\text{Cr}$ [144] atomic gases. Importantly, Andrea’s theoretical work allowed us to obtain a quantum collisional model able to unambiguously connect the (loss) features we observed to well-defined LiCr molecular states. Besides loss spectroscopy, we later experimentally characterized two among such resonances, finding excellent agreement with the model predictions. As a direct consequence, we now have accurate knowledge of the scattering properties of our mixture, crucial for the studies reported in Chapter 5, as well as of the nature of the relevant molecular states, which will be exploited for the studies presented in Chapter 4.

This Chapter – essentially based on our Ref. [139], with a few targeted inclusions from our more recent Ref. [94] – is organized as it follows:

- In Sec. 3.1, I first describe our loss spectroscopy measurements, together with the relevant loss mechanisms. I then present our experimental data, commenting on the fundamental insights they provide.
- In Sec. 3.2, I outline the main concepts and ideas behind the coupled-channel model developed by our theory collaborator, Prof. A. Simoni, and highlight its most important results. In particular, I describe the origin of the peculiar FR patterns observed at magnetic fields below 150 G. Finally, I present a first direct experimental validation of Andrea’s model, obtained through the study of collisionally-damped, in-trap dipole oscillations, performed over a broad magnetic-field range around a selected *s*-wave FR.
- In Sec. 3.3, I present more recent measurements, not contained in Ref. [139], essentially analogous to those reported in Sec. 3.2.2, but performed at significantly lower temperatures and focusing on a narrower magnetic-field region around the resonance

pole. I summarize our methods to analyze experimental data based on a coupled oscillator model, and discuss the transition from the collisionless to the hydrodynamic regime.

- Lastly, in Sec. 3.4, I present a detailed study (also not contained in Ref. [139]) of inelastic three-body losses around a selected s -wave FR, allowing us to quantify the collisional stability of our mixture under resonantly-interacting conditions.

3.1 Feshbach loss spectroscopy

As anticipated in the introduction, our loss spectroscopy scans were performed under less-optimal conditions compared to those reported in Chapter 2. Nonetheless, the procedures we followed to produce ultracold samples of ${}^6\text{Li}$ and ${}^{53}\text{Cr}$ atoms in our bODT were essentially similar. For these measurements, we employed ultracold mixtures at $10(1)$ μK , trapped in the sole IR beam of the main bODT with negligible differential gravitational sag. The samples typically comprised about 10^5 Cr and 1.8×10^6 Li atoms, characterized by Cr (Li) peak densities of 10^{11} cm^{-3} (2×10^{12} cm^{-3}). Spin-state manipulation via radiofrequency (RF) transitions allowed us to explore different binary Li-Cr mixtures. Lithium was prepared in either of the two lowest Zeeman levels of the electronic and hyperfine ground-state manifold ${}^2S_{1/2}$ $|F = 1/2, m_F = \pm 1/2\rangle$, hereafter labeled Li|1) and Li|2), respectively. Chromium, initially produced in the lowest hyperfine and Zeeman level $|F = 9/2, m_F = -9/2\rangle$ of its electronic ground state 7S_3 (hereafter denoted Cr|1)), could also be transferred to the two higher-lying Zeeman states of the $F = 9/2$ manifold, labeled Cr|2) and Cr|3), respectively. We explored all six Li $|i\rangle$ -Cr $|j\rangle$ mixtures with $i = 1, 2$ and $j = 1, 2, 3$, each being characterized by the total spin projection quantum number, $M_F = m_{F,\text{Li}} + m_{F,\text{Cr}} = -i + j - 4$, thus spanning $-5 \leq M_F \leq -2$.

We performed loss spectroscopy through magnetic field scans with typical step size of 60 mG. We kept the sample at a variable field for a fixed time t_{hold} (usually of 4 s), and then monitored the remaining atoms via spin-selective absorption imaging. FRs were

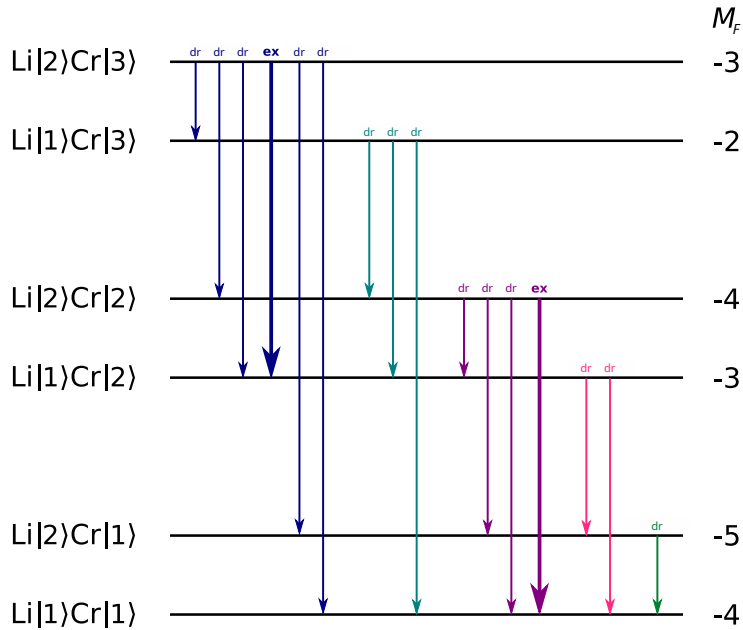


Figure 3.1 – Sketch of allowed two-body decay channels for the six lowest ${}^6\text{Li}$ - ${}^{53}\text{Cr}$ spin combinations. Larger (thinner) arrows labeled as ‘ex’ (‘dr’) denote spin-exchange (dipolar relaxation) processes, see text. Three-body recombination processes affect any mixture.

identified by enhanced atom losses, induced by different processes depending on the spin combination investigated [7]. Any $\text{Li}|i\rangle\text{-Cr}|j\rangle$ mixture but the lowest-energy one, $i = j = 1$, may undergo two-body losses, see Fig. 3.1. Inelastic spin exchange occurs whenever the initial atom pair is coupled to an energetically lower channel with equal M_F and orbital partial wave ℓ . Such a process does not affect excited spin combinations with either Li or Cr in the ground state (i or $j = 1$). Weaker dipolar relaxation processes are enabled by spin-dipole coupling [7] for any excited mixture, that can decay to lower-lying states with different M_F or ℓ , provided that $\Delta\ell = 0, \pm 2$ and $M_{\text{tot}} = M_F + m_\ell$ is conserved, m_ℓ being the projection of ℓ along the magnetic field quantization axis [130]. Three-body recombination processes affect any mixture. While these can in principle involve either two light and one heavy atom or vice versa, only the former case is relevant here, given the Li-Cr density imbalance in these experiments.

Figure 3.2 provides an overview of FR scans for four of the six Li-Cr combinations that we explored, from which important insights can be gained. First, none of the mixtures exhibit

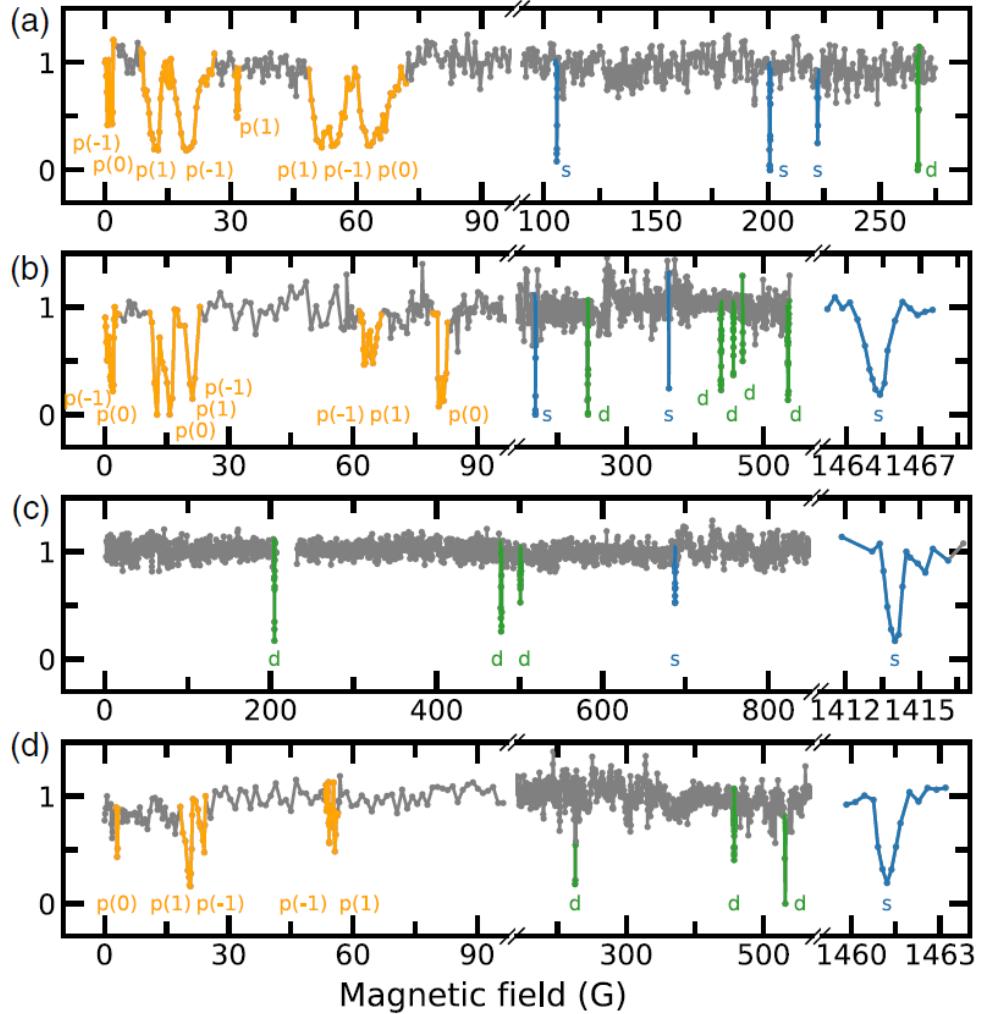


Figure 3.2 – Overview of ${}^6\text{Li}\text{-}{}^{53}\text{Cr}$ loss spectra. The remaining Cr number, recorded after an interaction time t_{hold} with lithium and normalized to its background value, is plotted as a function of the magnetic field for four different combinations: (a) $\text{Li}|2\rangle\text{-Cr}|3\rangle$, $M_F = -3$; (b) $\text{Li}|2\rangle\text{-Cr}|2\rangle$, $M_F = -4$; (c) $\text{Li}|1\rangle\text{-Cr}|1\rangle$, $M_F = -4$; and (d) $\text{Li}|2\rangle\text{-Cr}|1\rangle$, $M_F = -5$. Each point is the average of at least four independent measurements. $t_{\text{hold}} = 4$ s for all but the (c) panel, where $t_{\text{hold}} = 5$ s. Features that A. Simoni’s model (see Sec. 3.2) links to s -, p -, and d -wave molecular levels are colored blue, orange, and green, respectively. Numbers in brackets indicate the assigned m_ℓ .

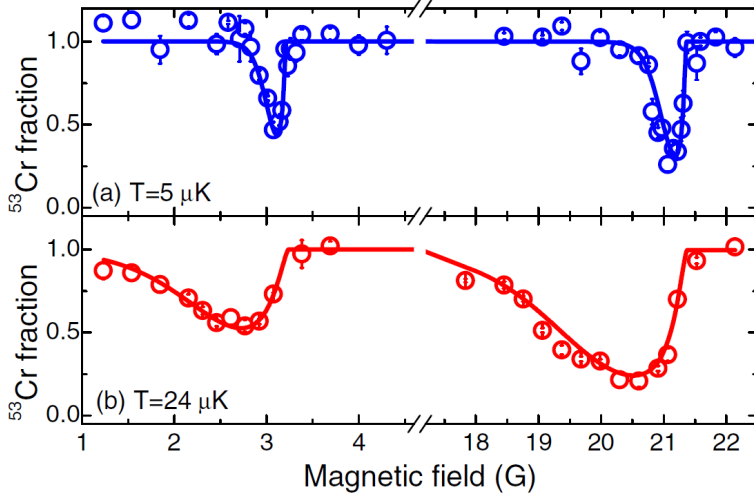


Figure 3.3 – Temperature dependence of atom loss at two low-field FRs of Li|2>-Cr|1>. (a) The remaining Cr fraction, recorded after $t_{\text{hold}} = 4$ s with a Li sample at $5 \mu\text{K}$, is plotted as a function of the magnetic field. (b) Same as (a) but for $24 \mu\text{K}$. Each data point is the average of three independent measurements. Lines are best fits to the model of Eq. (3.1) for p -wave collisions.

a dense FR spectrum, unlike combinations of alkalis with Er or Dy lanthanides [145, 146]. Second, similarly to bi-alkali systems, see e.g., Ref. [129], none of the loss peaks is due to, or overlapped with, Cr-Cr or Li-Li resonances. Additionally, nearly coincident FR locations appear in different spectra, both for mixtures with equal M_F values [see Figs. 3.2(b) and 3.2(c)] and for those with unequal ones. This already suggested, well before the quantitative analysis performed by A. Simoni, that relatively few molecular states, split into different hyperfine levels, are sufficient to explain our observations. Finally, although the high-field spectral regions above 150 G show sparse and narrow features, all scans – except for the Li|1>-Cr|1> mixture – exhibit more complex patterns below 150 G. These patterns include strong loss peaks arranged in doublet or triplet structures; see, e.g., Fig. 3.2(b). This suggests that, in this field region, two-body losses dominate over three-body ones. The observed FRs likely occur in $\ell > 0$ partial waves, split by magnetic dipole-dipole interactions [147, 148] and possibly other couplings [149].

We could confirm this hypothesis by acquiring additional loss measurements under different temperatures near such low-field resonances. Figures 3.3(a) and 3.3(b) show examples of this characterization, displaying loss features measured across two Li|2>-Cr|1> FRs in low-density samples prepared at $5 \mu\text{K}$ and $24 \mu\text{K}$, respectively. Both features are highly asymmetric, and they sensitively widen for increasing temperature, a behavior typical of $\ell > 0$ -wave FRs [147, 148, 150]. Without aiming at a quantitative line shape analysis, these data are well reproduced (see solid lines in Fig. 3.3) by a simple model [151] that assumes $\ell = 1$ collisions and solely accounts for two-body inelastic processes. Specifically, each dataset is fitted assuming exponential decay of the Cr fraction $N_{\text{Cr}}(B, t_{\text{hold}})/N_{\text{Cr},0} = \exp(-\Gamma_{K_2}(B) \cdot t_{\text{hold}})$, with loss rate given by [151]:

$$\Gamma_{K_2}(B) = \langle n_{\text{Li}} \rangle_{\text{Cr}} K_2(B) \sim A (B_0 - B)^{\ell+1/2} \exp\left(-\frac{\delta\mu(B_0 - B)}{k_B T}\right). \quad (3.1)$$

Here $\langle n_{\text{Li}} \rangle_{\text{Cr}}$ is the Li density averaged over the Cr cloud and $K_2(B)$ is the (field-dependent) two-body loss coefficient. The amplitude A (in arb. units), the FR pole B_0 , and the differential magnetic moment $\delta\mu$ in Eq. (3.1) are fitting parameters, whereas the temperature T is kept fixed at the experimentally measured value, and $\ell = 1$.

Another peculiarity of Fig. 3.3 spectra, common to other features in the low-field region of Fig. 3.2, is their thermal tail [147, 148, 150] oriented toward lower fields. This implies that such FRs originate from “anomalous” molecular levels that lay slightly above the atomic threshold at zero field and cross it with negative differential magnetic moments, $\delta\mu < 0$.

3.2 Coupled-channel model

The experimental data reported in the previous Sec. 3.1 constituted the necessary experimental input to build a full coupled-channel model [7], developed by our theory collaborator Prof. A. Simoni, University of Rennes. Following the lines of our Ref. [139], in this section I discuss the general ideas behind Andrea’s model, and its most relevant results regarding our experimental studies.

First, the model accounts for the atomic hyperfine and Zeeman energies [152, 153], which define the asymptotic collision thresholds. Second, the (isotropic) electrostatic interaction is represented by adiabatic Born-Oppenheimer potentials: These potentials are constructed by smoothly matching the *ab initio* (sextet) $X\ ^6\Sigma^+$ and (octet) $a\ ^8\Sigma^+$ molecular potentials given in Ref. [154] to the typical long-range analytical form [7]

$$V_{\text{r}}(R) = -\frac{C_6}{R^6} - \frac{C_8}{R^8} \mp A R^\nu e^{-\beta R}, \quad (3.2)$$

which comprises dispersion and the exchange interactions. Similarly to the singlet and triplet potentials of bi-alkalis, the minus (plus) sign in Eq. (3.2), with $A > 0$, refers to the deeper sextet (shallower octet) Li-Cr potential, characterized by a total electron spin of LiCr dimers equal to $S = 5/2$ ($S = 7/2$). Such potentials are parametrized in terms of sextet a_6 and octet a_8 s -wave scattering lengths, respectively. In Eq. (3.2), the amplitude A , and the constants ν and β , solely depend on the properties of separated atoms. The fit only weakly constrains the exchange-potential parameters, that are thus kept fixed to the nominal values given in Ref. [154].

Besides this strong isotropic interaction, both ℓ and M_F conserving, the model also accounts for weaker anisotropic couplings originating from both the (long-range) magnetic spin and the (short-range) second-order spin-orbit interactions. These two contributions have significantly different radial dependences, but for Σ states they share the same spin structure:

$$V_{\text{s}} \propto \vec{s}_{\text{Li}} \cdot \vec{s}_{\text{Cr}} - 3(\vec{s}_{\text{Li}} \cdot \hat{R})(\vec{s}_{\text{Cr}} \cdot \hat{R}). \quad (3.3)$$

From Eq. (3.3), one notices that these terms can couple different partial waves and hyperfine states, with the selection rules discussed in Sec. 3.1 for dipolar relaxation processes.

Starting from the *ab initio* data and long-range potential parameters of Ref. [154], A. Simoni optimized the (initially unknown) values of a_6 and a_8 , as well as the dispersion coefficients C_6 and C_8 , through least-square iterations by comparison with the experimental data. By tentatively identifying the isolated loss peaks above 1 kG as spin-exchange s -wave FRs associated with $S = 5/2$ rotationless ($\ell_r = 0$) molecular states,¹ the sextet scattering length is strongly constrained to $a_6 = 15.5 a_0$. With such an assumption, the model also reproduces several other features at lower fields, assigned to $\ell_r = 2$ states of the $S = 5/2$ potential, thus confirming the hypothesis. A strong constraint on a_8 is instead provided by the peculiar low-field patterns, characterized by irregularly spaced triplets and several “anomalous” FRs (see Fig. 3.3 and features marked in yellow in Fig. 3.2). A global least-square fit to the observed FRs yields the best-fit parameters $a_6 = 15.46(15) a_0$, $a_8 = 41.48(2) a_0$, $C_6 = 922(6)$ a. u., and $C_8 = 9.8(5) \times 10^4$ a. u., where errors represent one standard deviation obtained from the fit covariance matrix.

The quantum collisional model of A. Simoni accurately reproduces our experimental findings, as shown in Tab. 3.1 for a subset of 20 FRs. Besides the magnetic field location, the relevant quantum numbers for both the entrance channel and molecular state are also

¹I refer to the orbital quantum number of close-channel molecules as ℓ_r , not to be confused with ℓ , the orbital quantum number of the scattering atom pair.

Table 3.1 – Selection of ${}^6\text{Li}$ - ${}^{53}\text{Cr}$ Feshbach resonances immune to inelastic spin-exchange decay. Experimental B_{exp} and theoretical B_0 locations are compared for Li-Cr (i, j) channels. B_{exp} are obtained from the zeroes of the numerically-computed first derivative of loss data. A conservative 200 mG uncertainty combines our field stability with day-by-day field drifts and systematic errors. For incoming s -wave (p -wave) FRs, background scattering lengths $a_{\text{bg}}^{(0)}$ (volumes $a_{\text{bg}}^{(1)}$) and magnetic widths Δ_{el} are computed in the zero-energy limit (at collision energy $E/k_{\text{B}} = 10$ μK). Coupled s - and d -waves (p -wave only) are included for s -wave (p -wave) resonances. The differential magnetic moment $\delta\mu$, the electron spin S_r , and the rotational angular momentum ℓ_r of the molecular state are also listed. Additional data are reported in [155].

i, j, ℓ, m_ℓ	B_{exp} (G)	B_0 (G)	S_r, ℓ_r	$a_{\text{bg}}^{(\ell)}$ ($a_0^{2\ell+1}$)	Δ_{el} (G)	$\delta\mu$ (μ_{B})
1, 1, 0, 0	204.6	204.7	5/2, 2	41.3	7.0×10^{-3}	3.7
1, 1, 0, 0	477.6	478.1	5/2, 2	41.5	1.8×10^{-3}	2.0
1, 1, 0, 0	501.0	501.9	5/2, 2	41.5	3.8×10^{-4}	2.0
1, 1, 0, 0	687.4	687.1	5/2, 2	41.5	2.3×10^{-4}	4.0
1, 1, 0, 0	1414.0	1414.1	5/2, 0	41.5	0.47	2.0
2, 1, 1, 0	3.05	2.3	7/2, 1	-1.6×10^5	-3.70	-0.56
2, 1, 1, 1	21.1	20.9	7/2, 1	8.2×10^3	119	-0.28
2, 1, 1, -1	24.2	24.2	7/2, 1	2.5×10^4	37.8	-0.24
2, 1, 1, -1	54.3	54.8	7/2, 1	1.4×10^5	-4.56	0.27
2, 1, 1, 1	55.6	56.1	7/2, 1	-1.1×10^5	5.08	0.31
2, 1, 0, 0	225.7	225.8	5/2, 2	41.3	7.4×10^{-3}	3.8
2, 1, 0, 0	457.0	456.7	5/2, 2	41.5	3.6×10^{-4}	2.0
2, 1, 0, 0	531.4	531.8	5/2, 2	41.5	2.3×10^{-4}	2.0
2, 1, 0, 0	1461.2	1461.2	5/2, 0	41.5	0.48	2.0
1, 2, 0, 0	65.0	65.9	7/2, 0	39.5	6.6×10^{-3}	3.1
1, 2, 0, 0	135.7	135.7	5/2, 2	40.8	3.7×10^{-5}	5.0
1, 2, 0, 0	139.5	140.4	7/2, 0	40.8	1.9×10^{-3}	3.0
1, 2, 0, 0	483.5	484.2	5/2, 2	41.5	1.7×10^{-2}	2.0
1, 2, 0, 0	1418.1	1417.9	5/2, 0	41.5	0.47	2.0

given, together with the associated resonance parameters: background scattering length $a_{\text{bg}}^{(0)}$ (or volume $a_{\text{bg}}^{(1)}$), magnetic width Δ_{B} , and differential magnetic moment $\delta\mu$ of the molecular state relative to the atomic threshold. I remark that the a_{bg} value obtained by A. Simoni agrees well with the (more recent) *ab initio* estimate by M. Tomza’s group, see Sec. 4.10.

The low-field spectral region is entirely dominated by p -wave FRs, featuring m_ℓ splittings much larger than those found in alkali systems [147–149], owing to the increased role of spin-spin dipole coupling in Li-Cr mixtures and to the coincidentally small relative magnetic moment of the molecular states involved, see Sec. 3.2.1 below.

We could also identify various s -wave FRs in different spin combinations, including the absolute Li-Cr ground state. Owing to the relatively small values of a_6 and a_8 [7], similarly to the Li-K case [129, 130], these features are generally narrow. In particular, the coupled-channel model connects all FRs above 1400 G to $\ell_r = 0$ molecular levels of $X {}^6\Sigma^+$ potentials, predicting negligible two-body loss rates, magnetic-field widths $\Delta_{\text{B}} \sim 0.5$ G, and associated effective-range parameters [7, 156] of about 6000 a_0 . Experimental characterizations of such high-field resonances are presented in Secs. 3.2.2, 3.3 and 3.4.

3.2.1 Origin of the low-field p -wave resonance patterns

The Feshbach spectra at low magnetic fields (below 100 G), observed in the Li|2)-Cr|1), Li|2)-Cr|2), and Li|2)-Cr|3) hyperfine combinations (see Fig. 3.2), present a peculiar pattern

comprising a first low-field p -wave triplet of “anomalous” resonances (bound state crossing the atomic threshold from above with increasing B) below 30 G, accompanied by a second “standard” (bound state crossing the atomic threshold from below with increasing B) resonance triplet, located at higher fields. On top of these six features, the low-field pattern may include additional peaks, depending on the specific collision channel.

The origin of the main six-resonance pattern based on A. Simoni’s model is illustrated in Fig. 3.4 for the $\text{Li}|2\rangle\text{-Cr}|1\rangle$ combination. For p -wave collisions, $\ell = 1$, $m_\ell = 0, \pm 1$, and the three projections $-4, -5, -6$ of the exactly conserved quantum number M_{tot} must be accounted for. Let us first turn artificially to zero all relativistic interactions, such that the potential is fully isotropic (see Ref. [155] for details on the interaction potential): With reference to the lower panel (red dashed line), one can observe a unique molecular level crossing the atomic threshold first with negative, then with positive relative magnetic moment, with relatively small values $|\delta\mu| \lesssim 0.5 \mu_B$. The red dashed line in the upper panel of Fig. 3.4 correspondingly shows the real part of the energy-dependent scattering volume, that near the location where the bound state crosses threshold is tuned to large (positive and negative) values.

In the presence of anisotropic interactions, instead, the threefold m_ℓ degeneracy is lifted, and the single molecular level splits into the three components, shown as solid lines in Fig. 3.4. This splitting creates a resonance pattern composed of two sets of triplet peaks, which appear symmetrically around the center of the pattern. Note that, at low fields, the splitting is generally non-perturbative, and the two resonances for $m_\ell = \pm 1$ collisions are not expected to occur at the same location. This phenomenon has been already observed in alkalis [157], albeit in a less pronounced manner. Given its high sensitivity to small perturbations, this fragile pattern represents an ideal testing ground for *ab initio* quantum chemistry calculations, and it has been crucial for the fine adjustment of the parameters in Andrea’s model.

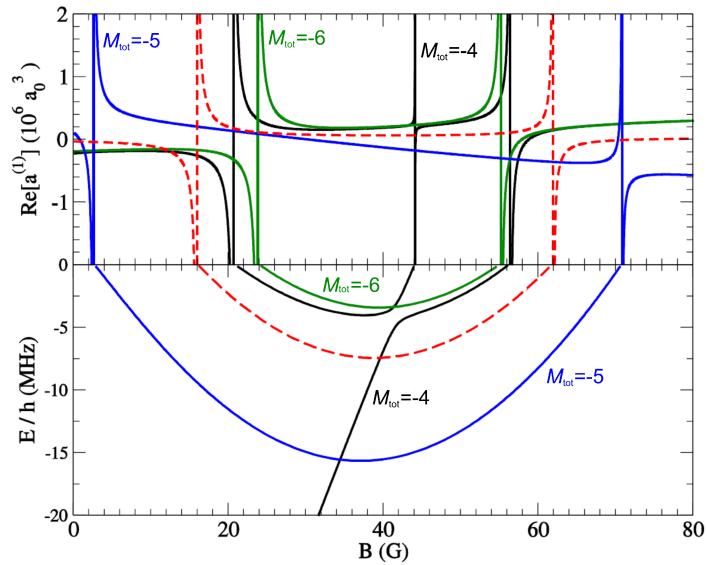


Figure 3.4 – Upper panel: the real part of the energy-dependent p -wave scattering volume for $\text{Li}|2\rangle\text{-Cr}|1\rangle$ collisions for the triplet components $M_{\text{tot}} = -6, -5, -4$. Calculation is performed at a finite collision energy $E/k_B = 5 \mu\text{K}$. Two mirror-image triplet patterns are visible with an extra resonance near 45 G arising from an additional perturbing state. Lower panel: energies of the corresponding resonant molecular states with quantum number M_{tot} below the $\text{Li}|2\rangle\text{-Cr}|1\rangle$ atomic threshold, fixed as zero energy. Pairs of resonances are induced for each M_{tot} by the same molecular level crossing twice the atomic threshold first with negative, then with positive relative magnetic moment. In the absence of anisotropic spin dipolar and second-order spin-orbit interactions the three components would be degenerate and reduce to the dashed lines in both panels.

Finally, it is important to emphasize that the $m_\ell = -1$ resonance near 24 G, shown in Fig. 3.4 (green solid line), with $M_{\text{tot}} = -6$, is predicted to exhibit negligible two-body loss rates. Such a feature could thus allow us, in the future, to investigate Li-Cr mixtures with resonant p -wave interactions, intrinsically chiral in nature.

3.2.2 Testing the model on a high-field resonance

Once the theoretical results of A. Simoni's model became available, we experimentally tested them by characterizing the s -wave FR located at 1461 G in the $\text{Li}|2\rangle\text{-Cr}|1\rangle$ channel. As anticipated previously, at the time this study was performed, we were working essentially with thermal samples, especially for what concerns the Cr component. Additionally, the magnetic field stability was not yet optimized (see Sec. 6.1), leaving us with a B -field uncertainty of about ~ 50 mG near the resonance locations. Under these conditions, we conducted a somewhat preliminary investigation of inelastic and elastic scattering properties: Our primary goal here was to measure the magnetic field width Δ_B of the selected FR, taken as the distance between the resonance pole (experimentally identified as the loss peak) and the minimum of the scattering rate (i.e. the zero-crossing of the scattering length). More precise and thorough characterizations of elastic and inelastic (resonant) scattering were performed later, with colder samples and a stable magnetic field, see Secs. 3.3 and 3.4.

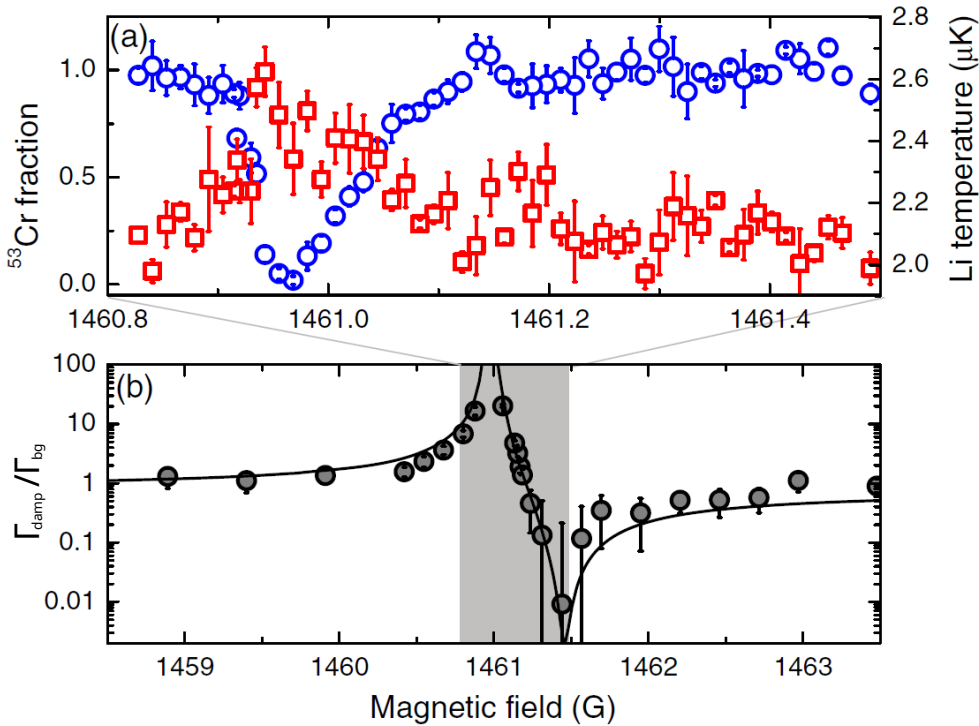


Figure 3.5 – Inelastic and elastic scattering at a $\text{Li}|2\rangle\text{-Cr}|1\rangle$ s -wave FR. (a) Magnetic-field dependence of the remaining Cr fraction (blue circles, left axis) and final Li temperature (red squares, right axis), recorded on a mixture at 2 μK after 150 ms interaction time. Each data point is the average of at least three independent measurements. The loss peak corresponds to a $1/e$ lifetime of 40(3) ms. (b) Field dependence of the collision-induced damping rate Γ_{damp} of a Li cloud at 2 μK , sloshing along the weak axis of the bODT in the presence of a Cr cloud at rest. The experimentally determined normalized $\Gamma_{\text{damp}}/\Gamma_{\text{bg}}$ is compared with the thermally averaged elastic scattering rate given by A. Simoni's model (solid line). Error bars account for the statistical error of the fit of the oscillation data to a damped sinusoidal function. The shaded area marks panel (a) boundaries.

First, to pinpoint the resonance pole, we employed a mixture initially produced at 2 μK , comprising about 5×10^5 Li and 10^5 Cr atoms, respectively, and characterized by a Li (Cr) peak density of about $4 \times 10^{12} \text{ cm}^{-3}$ (10^{12} cm^{-3}). Through a 30 ms-long linear ramp, we lowered the magnetic field from 1464 G to the final value, where we held the sample for 150 ms. The observed loss feature, shown in Fig. 3.5(a) for the Cr component (blue circles), is strongly asymmetric, as expected for narrow FRs [158]. Contrary to the low-field FRs of Fig. 3.3, here the lithium-to-chromium loss ratio is consistent with 2 within experimental uncertainty. This points to Li-Li-Cr three-body processes that overcome two-body ones, in agreement with A. Simoni's model expectation of a small dipolar relaxation rate $K_2 < 10^{-14} \text{ cm}^3/\text{s}$ at 2 μK . At the same time, we observed a sizable temperature increase of the Li cloud [see red squares in Fig. 3.5(a)], pointing to anti-evaporation dynamics driven by recombination processes [7].

In the second part of this experiment, we investigated the magnetic-field dependence of the Li-Cr elastic scattering across this FR. We selectively excited a sloshing motion of the lithium cloud along the weak axis of our bODT, and monitored the damping of the Li oscillations caused by interspecies collisions. For each field, we traced the Li center-of-mass motion and we fitted it to a damped sinusoidal function to extract the damping rate Γ_{damp} . Indeed, as detailed further in Sec. 3.3, for weak interactions, with only few scattering events per oscillation period, Γ_{damp} is directly proportional to the elastic scattering rate, thus ultimately to a^2 . Figure 3.5(b) shows the experimentally determined Γ_{damp} , normalized to the background value Γ_{bg} measured far from the resonant region (circles), together with the thermally averaged elastic scattering rate obtained from the collisional model (solid line). The close agreement between experimental and theoretical data validates the model, confirming the expected magnetic-field width $\Delta_B \sim 0.5 \text{ G}$.

3.3 Resonantly-interacting Li-Cr Fermi mixtures

Before proceeding to the next Chapters, I present here and in the next Sec. 3.4 further and more recent characterizations of the elastic and inelastic scattering properties of ${}^6\text{Li}$ - ${}^{53}\text{Cr}$ mixtures. These additional studies, performed on high-field s -wave FRs at lower temperatures and with improved B -field stability (see Sec. 6.1) compared to our Ref. [139], are also presented in our (latest) Ref. [94]. In particular, in this Section, I report a study of the bi-atomic mixture in the resonantly-interacting, quantum degenerate regime, exploiting protocols similar to those employed in Sec. 3.2.2, but at significantly lower temperatures and focusing on the vicinity of the resonance pole. The selected FR is in this case the one occurring around 1414 G in the $|\text{Li}|1\rangle$ - $|\text{Cr}|1\rangle$ spin combination: In light of its high-field location and of its narrow nature, this refined study represented for us a crucial, preliminary step towards any subsequent experiment with s -wave resonant Li-Cr mixtures: from the realization and characterization of ultracold LiCr dimers (see Chapter 4), to the study of the transport properties of Li impurities in a Cr bath (see Chapter 5).

In this experiment, exploiting our improved control over magnetic fields in the setup (details in Sec. 6.1), we accurately located the FR pole, across which we extracted both the elastic and inelastic collision rates per minority Cr atom, denoted Γ_{el} and Γ_{loss} , respectively. We simultaneously measured these two observables as a function of the magnetic field detuning $\delta B = B - B_0$, where B_0 is the FR pole, through the study of in-trap collective-mode dynamics, see the sketch in Fig. 3.6(a). Our probing method here was based on the simultaneous monitoring, as a function of time, of the atom numbers N_{Cr} and N_{Li} , as well as of the axial sloshing of both species in terms of their center-of-mass (c.o.m.) coordinates. We fitted exponential decays to the minority Cr atom number to obtain Γ_{loss} , associated with the dominant three-body Li-Li-Cr recombination process, see also Sec. 3.4.

The elastic collision rate Γ_{el} was instead extracted from the analysis of the c.o.m. evolution of the two mixture components via a two-coupled harmonic oscillator model [159–162]; see Fig. 3.6(b) and Sec. 3.3.1 for details about the model. By fitting the c.o.m. position of the atomic clouds x_{com} as a function of time, and taking into account the observed loss in atom number, Γ_{el} could be reliably extracted.

The measurement started by preparing a non-interacting Li-Cr mixture, within the sole IR trapping beam of our main bODT, near the zero crossing of the selected FR, i.e. at an initial detuning $\delta B \sim +0.48$ G. By means of an optical kick, imparted with a quick pulse of green light, on purpose slightly misaligned with respect to the IR beam axis, we selectively displaced the Li cloud out of the axial potential minimum at $x = 0$, while leaving Cr almost unaffected; see sketch in Fig. 3.6(a). Parallel to that, we quickly set δB to variable values around the FR pole. We then monitored the subsequent number and c.o.m. evolution as a function of time.

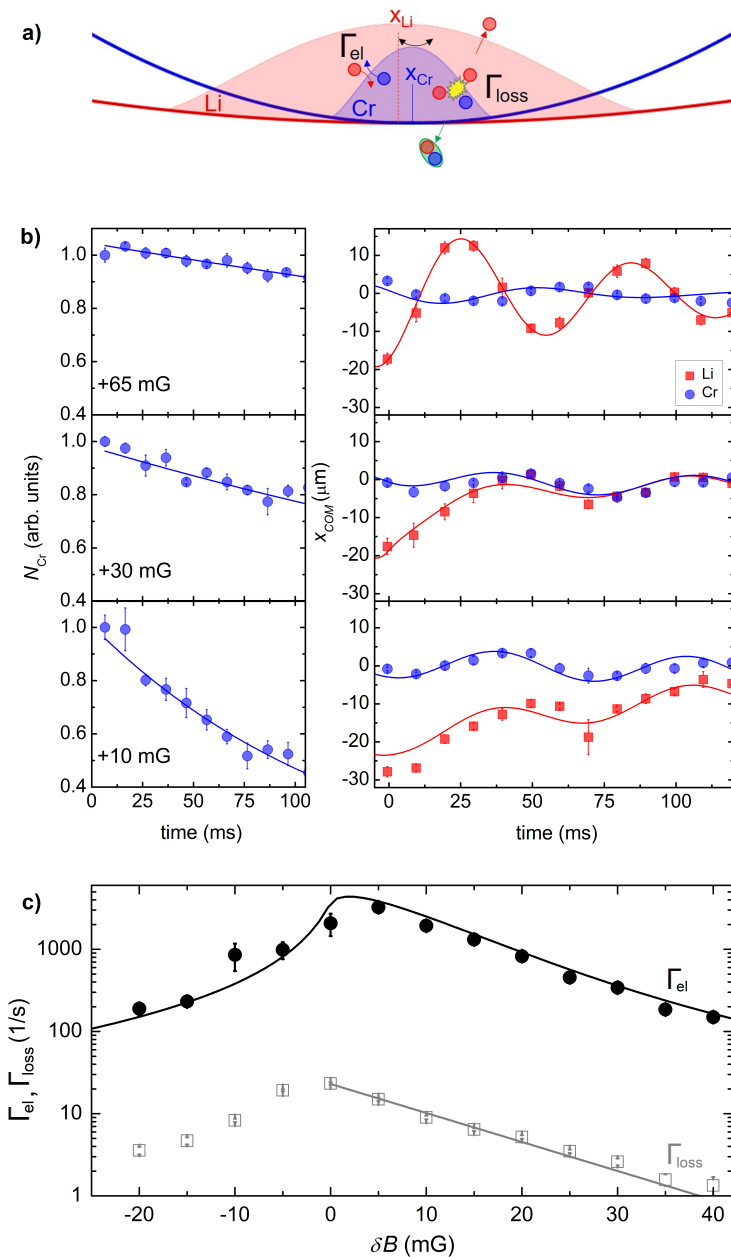


Figure 3.6 – Elastic and inelastic scattering properties of resonantly interacting Li-Cr Fermi mixtures. (a) Sketch of the experimental configuration employed to simultaneously extract Γ_{loss} from the minority Cr number evolution, and Γ_{el} from the Li and Cr c.o.m. dynamics through the analysis developed in Refs. [159–162]; see the text for details. (b) Examples of the observed dynamics, recorded at different magnetic-field detunings specified in the legend, of the chromium atom number (left panels), and of the centers of mass of both Cr (blue circles) and Li (red squares) components (right panels). Lines are best fits to the data of the models described in the text, through which we extract Γ_{loss} and Γ_{el} , respectively. (c) Experimentally determined rates for elastic (filled circles) and inelastic (open squares) collision events per Cr atom, as a function of the magnetic field detuning δB . Black and gray curves are best fits of Γ_{el} and Γ_{loss} , respectively, to the theoretically expected trends; see the text for details.

At the initial detuning, i.e., under non-interacting conditions, atom losses were found negligible, and lithium underwent small, undamped oscillations characterized by a single oscillation frequency of about 17 Hz. Simultaneously, chromium, featuring a bare axial trap frequency of 14 Hz, was found at rest at all evolution times. As the resonance was approached, the effects of both inelastic and elastic processes became more pronounced. Examples of the observed dynamics at various $\delta B > 0$ are presented in Fig. 3.6(b) in order of increasing interaction strength from top to bottom. The minority chromium number N_{Cr} (left panels) and the c.o.m. coordinates for both species (right panels) are shown as a function of time. The Cr number evolution, always well fitted by a single exponential decay [see the solid lines in the left panels of Fig. 3.6(b)], reveals a progressively reduced lifetime (i.e. increased loss rate), as the resonance pole is approached from above, $\delta B \rightarrow 0^+$. In parallel, the barycenters of the two mixture components exhibit more interesting dynamics, which qualitatively change close enough to the FR pole. In particular, for $|\delta B| \gtrsim 30$ mG (small interaction strength), we observed a damping of the Li c.o.m. oscillations – accompanied by weak damped oscillations of the Cr cloud at its bare axial frequency. This damping becomes progressively more pronounced as $|\delta B|$ is reduced, consistently with the expected behavior in the collisionless regime [159–162]. For $|\delta B| \lesssim 30$ mG, instead, the barycenters of the two clouds exhibit weakly-damped, in-phase oscillations, characterized by one single frequency, intermediate between the unperturbed Li and Cr ones. This observation is consistent with a collisionally hydrodynamic behavior of our Fermi mixture near the FR center, which is expected to arise in the strongly interacting region, once Γ_{el} greatly exceeds the axial trap frequencies [159–162]; see Sec. 3.3.2 below for more details. Despite the c.o.m. evolution drastically changes between the collisionless and the hydrodynamic regimes, it is well reproduced at all detunings by the coupled oscillator model Eqs. (3.4), with Γ_{el} as the only free parameter; see the best-fit curves in the right panels of Fig. 3.6(b).

The main results of this characterization are summarized in Fig. 3.6(c), which shows the experimentally determined Γ_{el} (filled circles) and Γ_{loss} (open squares) as a function of the magnetic field detuning across the resonance region. The inelastic loss rate, for $\delta B \geq 0$, exhibits an exponential growth [gray line in Fig. 3.6(c)] as the resonance pole is approached, in qualitative agreement with the trend expected for the three-body recombination rate coefficient near a narrow FR [158]; see Sec. 3.4 for a more detailed discussion. After reaching a maximum value at $\delta B \sim 0$, the extracted Γ_{loss} is found to progressively drop as the field is further decreased, consistent with previous observations on other atomic systems [158]. However, since in this $\delta B < 0$ region Feshbach dimers can be formed and contribute to the detected atom signal (see Chapter 4), Γ_{loss} can no longer be interpreted solely in terms of three-atom recombination processes.²

Contrarily to the inelastic case, Γ_{el} could be analyzed as an elastic Li-Cr scattering rate across the entire region of explored detunings. We obtained the theory estimate as $\Gamma_{\text{el}} = \langle n_{\text{Li}} \rangle_{\text{Cr}} \cdot \langle \sigma_{\text{el}}(\delta B) v_{\text{rel}} \rangle_T$ [see Eq. (1.6)], with $\sigma_{\text{el}}(\delta B)$ denoting the magnetic-field-dependent cross section for Li-Cr collisions, v_{rel} the relative velocity, $\langle n_{\text{Li}} \rangle_{\text{Cr}}$ the Li density averaged over the Cr cloud, and $\langle \rangle_T$ thermal averaging; see details in Sec. 3.3.1. Since the overlap density and temperature of the sample are directly accessible via absorption imaging, and since $\sigma_{\text{el}}(\delta B)$ is completely determined by the parameters of our FR, the pole location B_0 represented the only free parameter. The theory fits the experimental Γ_{el} remarkably well across the entire FR region; see the solid black line in Fig. 3.6(c). This characterization allowed us to pinpoint the resonance pole with ± 3 -mG accuracy.

²A theoretical analysis of atom losses in homonuclear ($M = m$) mixtures on the repulsive, molecular side of a broad ($R^* = 0$) Feshbach resonance was developed in Ref. [163]. Its extension to $M/m \neq 1$ and $0 < R^* < +\infty$ is generally not trivial, and – to the best of my knowledge – has not been developed so far.

Finally and most importantly, the Fig. 3.6(c) data reveal the collisional stability of the Li-Cr mixture under resonant interactions. This is signaled by the elastic rate greatly exceeding the inelastic one over a comparably wide range of magnetic field detunings across the Feshbach resonance, with a *good-to-bad* collision ratio $\Gamma_{\text{el}}/\Gamma_{\text{loss}}$ found to reach values up to 200. We ascribe the observed stability to the fact that, in spite of the narrow nature of the FR used, three-body processes involving identical fermions are suppressed by antibunching due to Fermi statistics of our mixture components [55, 164], relative to the bosonic case. As it will be shown later in Sec. 4.3, this is extremely advantageous for the efficient magnetoassociation of LiCr dimers and, more generally, it is very promising in light of future many-body studies of strongly interacting Li-Cr Fermi mixtures.

3.3.1 The coupled oscillator model

The c.o.m. dynamics of the lithium and chromium cloud, explored throughout different interaction regimes, as described in Sec. 3.3, were analyzed in terms of a well-established model of two coupled oscillators, already tested on both homo- and hetero-nuclear atomic mixtures [159–162]. In this framework, the c.o.m. evolution of the two clouds along the axial (x) direction is described by two coupled differential equations that we express as

$$M_{\text{Cr}}\ddot{x}_{\text{Cr}} = -M_{\text{Cr}}\omega_{\text{Cr}}^2 x_{\text{Cr}} - \frac{4}{3}m_{\text{red}}\Gamma_{\text{el}}(\dot{x}_{\text{Cr}} - \dot{x}_{\text{Li}}), \quad (3.4a)$$

$$m_{\text{Li}}\ddot{x}_{\text{Li}} = -m_{\text{Li}}\omega_{\text{Li}}^2 x_{\text{Li}} - \frac{4N_{\text{Cr}}}{3N_{\text{Li}}}m_{\text{red}}\Gamma_{\text{el}}(\dot{x}_{\text{Li}} - \dot{x}_{\text{Cr}}). \quad (3.4b)$$

Here $\omega_{\text{Cr(Li)}}$ and $N_{\text{Cr(Li)}}$ denote the Cr (Li) axial trap frequency and atom number, respectively, and $m_{\text{red}} = m_{\text{Li}}M_{\text{Cr}}/(m_{\text{Li}} + M_{\text{Cr}})$ is the Li-Cr reduced mass. The sloshing dynamics of the two clouds are coupled through the rightmost damping terms in Eqs. (3.4). The damping rates scale with the mean number of elastic Li-Cr collisions per unit of time experienced by each component, and are here expressed in terms of the scattering rate per minority Cr atom Γ_{el} . By fixing the axial frequencies and initial conditions [$x_i(0)$, $\dot{x}_i(0)$ for $i = \text{Li, Cr}$] to their experimentally determined values, and accounting for the measured atom number evolution, we fitted Eqs. (3.4) to the recorded oscillation dynamics – see the examples in the right panels of Fig. 3.6(b) – and thus extracted Γ_{el} as the sole free fitting parameter. In Fig. 3.6(c), the experimentally determined Cr collision rate is compared with the theory expectation, which we evaluated from Eq. (1.6) as:

$$\Gamma_{\text{el}} = \langle n_{\text{Li}} \rangle_{\text{Cr}} \langle \sigma_{\text{el}}(a, R^*, k_{\text{rel}}) \cdot v_{\text{rel}} \rangle_T, \quad (3.5)$$

where $\langle n_{\text{Li}} \rangle_{\text{Cr}} = \int n_{\text{Li}}(\vec{r}) n_{\text{Cr}}(\vec{r}) d\vec{r} / N_{\text{Cr}}$ denotes the lithium density averaged over the chromium one, k_{rel} is the relative momentum for Li-Cr collisions, and $v_{\text{rel}} = \hbar k_{\text{rel}} / m_{\text{red}}$ the corresponding relative velocity. Here $\sigma_{\text{el}}(a, R^*, k_{\text{rel}})$ represents the (field- and momentum-dependent) elastic cross section and $\langle \rangle_T$ indicates thermal averaging over all relative momenta. To a good approximation, $\langle n_{\text{Li}} \rangle_{\text{Cr}}$ remains constant to the experimentally determined value of $1.2 \times 10^{11} \text{ cm}^{-3}$ at all detunings and evolution times, given the moderate atom loss of the Li majority component. The elastic cross section is given by Eq. (1.13), reported here for sake of clarity:

$$\sigma_{\text{el}}(a, R^*, k_{\text{rel}}) = \frac{4\pi a^2}{(1 + k_{\text{rel}}^2 R^* a)^2 + k_{\text{rel}}^2 a^2}, \quad (3.6)$$

where $R^* \simeq 6000 a_0$ and $a(\delta B) = a_{\text{bg}}(1 - \Delta_{\text{B}}/\delta B)$, with $a_{\text{bg}} = 41.48 a_0$ and $\Delta_{\text{B}} = 0.48 \text{ G}$ for our FR. For simplicity of the calculation, the thermal averaging was performed by neglecting the Cr thermal distribution within the momentum integral. This was justified by

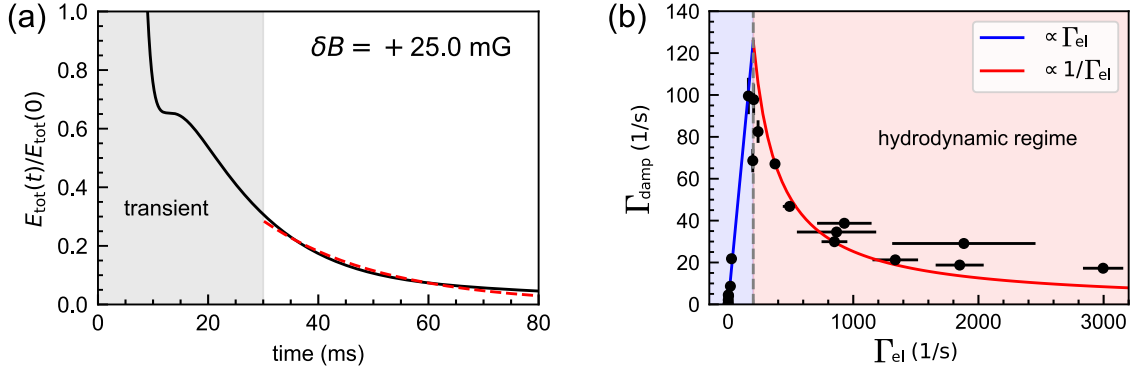


Figure 3.7 – (a) Time evolution of the total energy, extracted from the fits of Eqs. (3.4) to the data, characterized by an initial transient behavior, and a subsequent almost pure exponential decay. Here, E_{tot} is shown for $\delta B = 25$ mG (black solid line), corresponding to $\Gamma_{\text{el}} = 490$ Hz. The red dashed line is the fitted exponential decay after the transient behavior. (b) Identification of the transition from the collisionless to the collisionally hydrodynamic regime via the analysis of the damping rate Γ_{damp} as a function of Γ_{el} : a scaling of $\Gamma_{\text{damp}} \propto \Gamma_{\text{el}}$ is visible in the collisionless regime (blue line and shaded region), while a scaling $\propto 1/\Gamma_{\text{el}}$ characterizes the hydrodynamic regime (red line and shaded region). Both lines are guides to the eye.

the fact that, owing to the large mass imbalance of our mixture, $M_{\text{Cr}}/m_{\text{Li}} \simeq 8.8$, the Li-Cr relative velocity is mainly set by the sole lithium one. Under this approximation, averaging over a Fermi-Dirac distribution at $T_{\text{Li}}/T_{\text{F,Li}} \sim 0.3$, or over a Boltzmann-gas weight at an effective temperature of 700 nK, yields nearly identical results throughout the interaction regime we explored.

We employed Eq. (3.5) to fit the experimental data of Fig. 3.6(c) [black filled circles], with the resonance pole position B_0 as the single free parameter implicitly entering Eq. (3.6), while fixing all other quantities to the corresponding values experimentally determined or given by the quantum collisional model of Sec. 3.2. It should be reminded how our sizable R^* parameter implies that the maximum of the cross section Eq. (3.6) – where $\sigma_{\text{el}} = 4\pi/k_{\text{rel}}^2$ – is reached at a large but finite (negative) scattering length $a < 0$, for which $1/a + R^* k_{\text{rel}}^2 = 0$, see again Sec. 1.5. This feature, which also persists after thermal averaging [see Eq. (3.5)], causes the maximum of Γ_{el} to occur at a small $\delta B > 0$ value, as visible in Fig. 3.6(c).

3.3.2 Transition from the collisionless to the collisionally hydrodynamic regime

Previous studies [159–162] identified the transition from the collisionless to the hydrodynamic regimes by analyzing the scaling of the damping rate Γ_{damp} of the coupled oscillations with respect to the collision rate Γ_{el} . Specifically, in the collisionless regime, Γ_{damp} linearly grows with Γ_{el} , whereas in the hydrodynamic regime it exhibits a progressive reduction proportional to $1/\Gamma_{\text{el}}$. However, in our case, extracting Γ_{damp} from a fit to the c.o.m. dynamics was found rather challenging, owing to the concurrent oscillatory motion, especially when considering the initial short-time evolution near the resonantly interacting region; see the example of Fig. 3.6(b) at $\delta B = 30$ mG.

A convenient way to extract the damping rates at all detunings, given our limited observation time over a few oscillation periods, was to employ the fitted $x_{\text{Li}}(t)$ and $x_{\text{Cr}}(t)$ to obtain the total energy $E_{\text{tot}}(t) = E_{\text{kin}}(t) + E_{\text{pot}}(t)$, with $E_{\text{kin}} = \frac{1}{2}(m_{\text{Li}}\dot{x}_{\text{Li}}^2 + M_{\text{Cr}}\dot{x}_{\text{Cr}}^2)$ and $E_{\text{pot}} = \frac{1}{2}(m_{\text{Li}}\omega_{\text{Li}}^2 x_{\text{Li}}^2 + M_{\text{Cr}}\omega_{\text{Cr}}^2 x_{\text{Cr}}^2)$. As shown in the example in Fig. 3.7(a), the evolution of $E_{\text{tot}}(t)$ (black line) is in fact less affected by the oscillatory dynamics, such that a damping rate can be more easily extracted. Indeed, after an initial, short transient

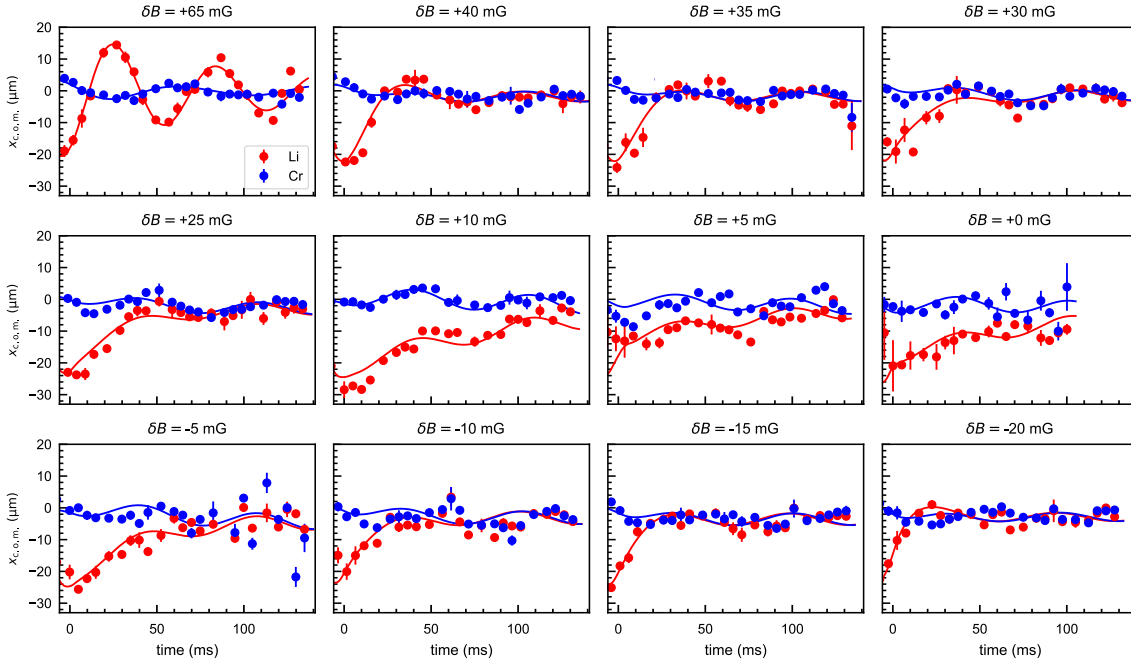


Figure 3.8 – Examples of in-trap oscillations of Li (red circles) and Cr (blue circles) centers of mass, recorded for different magnetic field detunings δB across the FR region. The solid lines, with corresponding color code, represent the fit results of the coupled oscillator model Eqs. (3.4).

time of about 30 ms, excluded from the fit, $E_{\text{tot}}(t)$ exhibits a clean decay that is fitted by an exponential function (red dashed line), from which we obtained Γ_{damp} at all detunings. The extracted damping rate Γ_{damp} is shown in Fig. 3.7(b), plotted as a function of the experimentally determined Γ_{el} . The observed non-monotonic trend is indeed found to follow the expected transition from collisionless to collisional hydrodynamics scaling [159–162], approximately once Γ_{el} starts exceeding the axial trapping frequencies of the two atomic components. For our experimental conditions, this happens for magnetic field detunings $\delta B \leq 30$ mG, below which, as shown by the data presented in Fig. 3.8, a rapid phase locking of the two c.o.m. dynamics was observed and, correspondingly, Γ_{damp} was strongly reduced. I emphasize that this observation indicates our experimental capability to access the hydrodynamic regime not only along the weak, axial direction of our trap, but – once $\Gamma_{\text{el}} > \omega_{y,z}$ – also along the transverse ones.

3.4 Collisional stability of the atomic mixture

To further characterize the stability of the atomic mixture in the strongly interacting region, as well as to pinpoint the (absolute) magnetic field location B_0 of the FR pole, we performed additional studies of inelastic three-body recombination processes, in addition to those described in Sec. 3.3. While such a survey has been conducted for each of the two high-field FRs occurring in Li $|i\rangle$ -Cr $|1\rangle$ combinations (with $i = 1, 2$), in the following I summarize our experimental procedures and findings by focusing on the absolute ground-state mixture Li $|1\rangle$ -Cr $|1\rangle$, and on the associated FR at 1414 G. Conceptually, this additional characterization was based on protocols and analysis closely following those already discussed in Sec. 3.3 to extract Γ_{loss} : After preparing a weakly-interacting mixture at a large and positive detuning from the FR pole, we quickly ramped the magnetic field towards the resonance region at small, variable δB values, at which we monitored the subsequent atom number decay $N_{\text{Cr}}(t)$ of the Cr minority component, as a function of time.

In absence of two-body losses, $N_{\text{Cr}}(t)$ evolves according to the rate equation

$$\dot{N}_{\text{Cr}}(t) = -K_3 \langle n_{\text{Li}}^2 \rangle_{\text{Cr}} N_{\text{Cr}} = -\Gamma_{\text{loss}} N_{\text{Cr}}, \quad (3.7)$$

where K_3 is the three-body loss coefficient.

Experimentally, we carefully calibrated each investigated magnetic field bias against the $\text{Li}|1\rangle \leftrightarrow \text{Li}|2\rangle$ RF transition, both before and after each decay measurement. Contrarily to Sec. 3.3, however, here we opted to investigate steady mixtures – i.e., not exhibiting in-trap sloshing dynamics – that were prepared within our bODT trap, rather than in the sole IR beam. On the one hand, this allowed, at each magnetic field value, for a more accurate determination of the mean squared Li density $\langle n_{\text{Li}}^2 \rangle_{\text{Cr}}$, found to be constant over time. This, combined with the Γ_{loss} values extracted from exponential fits to the Cr atom number evolution, as for the measurements in Sec. 3.3, allowed us to obtain, at each bias field, the three-body rate coefficient for the dominant Li-Li-Cr recombination processes as $K_3 = \Gamma_{\text{loss}} / \langle n_{\text{Li}}^2 \rangle_{\text{Cr}}$. On the other hand, exploitation of the green beam of our bODT, on top of the IR one, allowed for an alternative, precise detection of the FR pole location B_0 : Indeed, as I will show in Sec. 4.5, we found that even a relatively low power level of green light induces strong photo-excitation losses once LiCr Feshbach dimers are formed. As such, once the magnetic field is lowered below B_0 on the molecular side of the FR, this light-induced, strong decay channel is opened, and it greatly overcomes the three-body collisional one. When this happens, the sample lifetime is markedly reduced, hence yielding an enhanced Γ_{loss} . This experimental protocol thus allowed us to accurately determine both the three-body recombination rate coefficient K_3 for $B \geq B_0$, as well as to obtain an additional measure of B_0 itself – besides that obtained from the fit of Γ_{el} presented in the previous Sec. 3.3 – solely based on the study of inelastic losses.

The results of this characterization are summarized in Fig. 3.9, which shows the experimentally determined K_3 coefficient as a function of the magnetic field across the resonance region. We interpret the sudden jump between the red and blue data points as the crossing of the resonance pole, below which Feshbach dimers form and are quickly lost due to the fast trap-induced photo-excitation process (see Sec. 4.5). The jump is centered at $B_0 = 1413.886(5)$ G, and the error budget accounts for residual AC field noise, calibration of the COMP coils, magnetic field inhomogeneity, and residual long-term drifts, in order of importance. The experimental data marked in blue ($\delta B < 0$) can no longer be interpreted as a K_3 coefficient for three-atom collisions and their interpretation goes beyond the scope of our work. On the other hand, for positive detunings ($B > B_0$), similarly to the Γ_{loss} trend presented in Sec. 3.3, the extracted K_3 exhibits an exponential growth as the resonance pole is approached from above ($\delta B \rightarrow 0^+$), in qualitative agreement with previous observation on homonuclear Fermi mixtures near narrow Feshbach resonances [158].

Following the theoretical analysis of Ref. [158], valid for an infinitely narrow FR ($R^* \rightarrow +\infty$), the K_3 coefficient for a thermal mixture is expected to vary, for $\delta B \geq 0$, as

$$K_3(\delta B, T) = K_3^0(T) \exp\left(-\frac{\delta\mu \delta B}{k_B T}\right). \quad (3.8)$$

Here $K_3^0(T)$ is the (temperature-dependent) maximum value of K_3 , reached at the resonance pole, $\delta\mu$ is the differential magnetic moment between the open and closed channels associated with the FR, T is the gas temperature, and k_B is the Boltzmann constant. In the case of degenerate samples, Eq. (3.8) can still be used by defining an effective temperature T_{eff} that is connected to the mean kinetic energy of the system. In our case, this is essentially determined by the majority Li Fermi gas, and we evaluated T_{eff} by setting $3/2 k_B T_{\text{eff}} = \langle E_{\text{kin,Li}}(T/T_{\text{F,Li}}) \rangle$. Taking the experimentally determined value of

$T/T_{\text{F,Li}} = 0.27(2)$, with $T_{\text{F,Li}} = 1.25(5)$ μK , and considering that, for an ideal Fermi gas, $\langle E_{\text{kin,Li}}(0.27) \rangle \sim 0.55 k_{\text{B}} T_{\text{F}}$, we obtained $T_{\text{eff}} \sim 460$ nK.

However, by fixing T_{eff} to this value and setting the magnetic moment to $\delta\mu = 2 \mu_{\text{B}}$, i.e., to the value characterizing each of the high-field FRs of Li-Cr (see Tab. 3.1), Eq. (3.8) yielded a trend significantly steeper than that experimentally determined. Interestingly, this mismatch arises from the fact that our resonance is indeed not *infinitely narrow*, featuring instead a sizable but finite R^* value. Extension of the theory of Ref. [158] to finite effective-range values [D. Petrov, unpublished] yields a trend for K_3 qualitatively analogous to that of Eq. (3.8), but with an effective magnetic moment $\delta\mu^*$ that is progressively decreased for decreasing R^* values. In particular, such an extended theory model predicts, for the Li-Cr FRs here investigated (featuring $R^* \sim 6000 a_0$), an effective $\delta\mu^* = 0.77 \delta\mu$. A functional fit of Eq. (3.8) to the red dataset in Fig. 3.9, where we set $\delta\mu^* = 0.77 \times 2 \mu_{\text{B}}$ while leaving both T and K_3^0 as free parameters, is shown in the figure as a solid red line. The fit, which nicely reproduces our data, returns $K_3^0 = 0.35(5) \times 10^{-22} \text{ cm}^3/\text{s}$ and $T = 490(40)$ nK, the latter matching within uncertainty the estimated T_{eff} value. A fit based on the same extended theory model was employed to analyze the Γ_{loss} data shown in Fig. 3.6(c).

I conclude this Section by mentioning that similar protocols – based on the identification of B_0 as the loss peak, with B -field calibrated against Li RF spectroscopy – were employed to precisely pinpoint the pole of all four s -wave FRs occurring between the two lowest spin states of Li and Cr at high fields. The results of this characterization are summarized in Tab. 3.2.

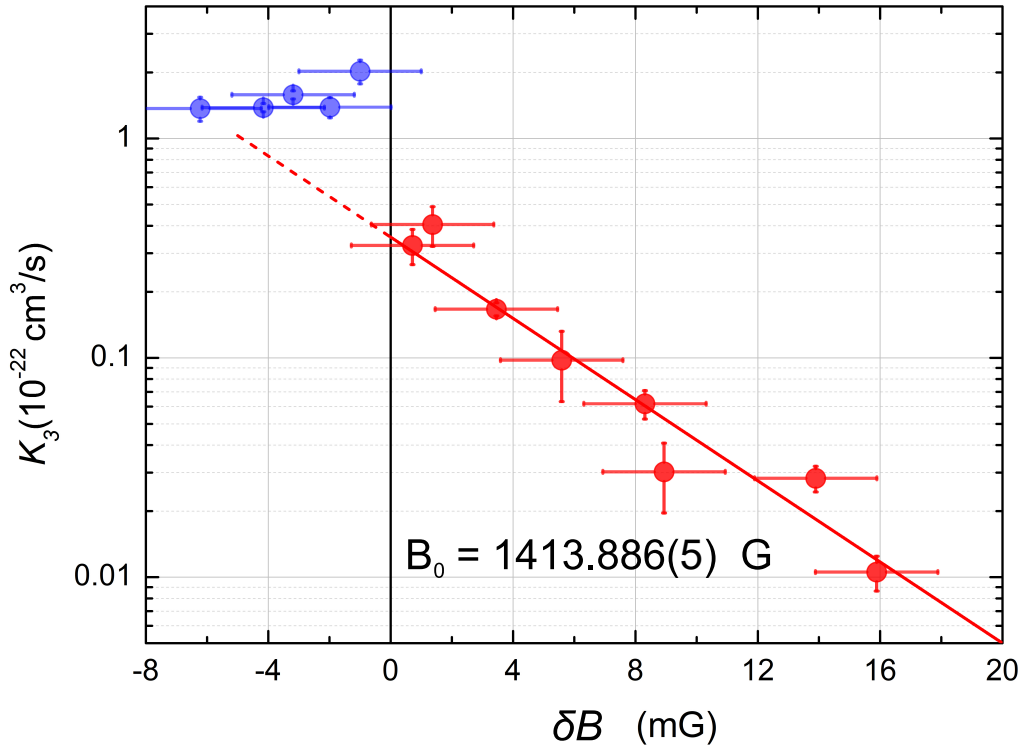


Figure 3.9 – Three-body recombination rate coefficient for Li-Li-Cr collisions as a function of magnetic field across the FR region, obtained for mixtures prepared in the bODT trap by following the analysis described in the text. Strong photoexcitation losses, induced by the green light of our trap for $\delta B \leq 0$, results in a sharp increase in the derived K_3 , marked by the different color of the experimental data. This enables us to pinpoint the absolute resonance pole position B_0 with a 5-mG accuracy; see the text and Tab. 3.2. Red line is the best fit of the data above the FR pole to Eq. (3.8), fixing $\delta\mu^* = 0.77 \times 2 \mu_{\text{B}}$ while leaving both T and K_3^0 as free parameters.

Table 3.2 – Precise determination, through loss-spectroscopy measurements in the bODT, of the magnetic-field location of the high-field s -wave Feshbach resonances for all $\text{Li}|i\rangle\text{-Cr}|j\rangle$ combinations with $i, j = 1, 2$, already reported in Tab. 3.1 with lower accuracy. Error budget, in brackets, accounts for residual AC field noise, calibration of the COMP coils, magnetic-field inhomogeneity and residual long term drifts, in order of importance.

	Cr 1⟩	Cr 2⟩
Li 1⟩	1413.886(5)	1417.937(30)
Li 2⟩	1460.933(5)	1464.159(30)

3.5 Conclusive remarks

In conclusion, in this Chapter I have discussed the first and thorough investigation of elastic and inelastic collisional properties of ultracold ${}^6\text{Li}\text{-}{}^{53}\text{Cr}$ Fermi mixtures under resonantly-interacting conditions.

From loss spectroscopy measurements, started during my Master Thesis and finalized during the first year of my Ph.D., we found that the Li-Cr system is characterized by isolated and nonchaotic FRs. Thanks to the theoretical analysis of our collaborator A. Simoni, we could unambiguously connect the observed resonances to molecular states with well-defined quantum numbers: LiCr thus combines the simplicity of bi-alkali systems with richer molecular structures as those of alkali-lanthanide or alkali-alkaline-earth mixtures [80, 81, 145, 146]. In particular, we identified several strong and isolated s -wave FRs, with widths exceeding a few 100 mG, that provide an optimal starting point to form (bosonic) Feshbach dimers, laying the groundwork for the studies presented in Chapter 4 and, in general, for the realization of ultracold gases of ground-state paramagnetic polar molecules.

Furthermore, it is important to remark that the s -wave FRs of ${}^6\text{Li}\text{-}{}^{53}\text{Cr}$ that we identified in this joint experimental and theoretical study exhibit a character similar to the Li-K ones [129, 130], but immune to two-body losses. This, combined with the peculiar mass ratio $M_{\text{Cr}}/m_{\text{Li}} \simeq 8.8$, makes Li-Cr mixtures an unparalleled framework for the experimental investigation of *non-Efimovian* few-body physics [9, 10, 17, 19, 20].

Finally, the measured lifetimes of Li-Cr mixtures, exceeding tens of ms in the vicinity of both s - and p -wave FRs, although significantly shorter than those observed in homonuclear ${}^6\text{Li}$ mixtures near broad resonances, appear quite similar to those reported for ${}^{40}\text{K}$ Fermi gases [165, 166]. This appears promising also for future many-body studies with mass-imbalanced Li-Cr Fermi mixtures with resonant (s - or p -wave) interactions.

Chapter 4

Making, probing and understanding LiCr Feshbach molecules

As anticipated in the Introduction, quantum gases of doubly-polar molecules represent appealing frameworks for a variety of cross-disciplinary applications, encompassing quantum simulation and computation, controlled quantum chemistry, and precision measurements. In this Chapter, I present our experimental results concerning the production, characterization, and optimization of large and ultracold samples of (bosonic) paramagnetic LiCr Feshbach molecules. These topics constituted the main focus of my research activity for essentially half of my Ph.D.: from the second half of the first year (i.e. after we finalized the experimental procedures described in Chapter 2), to the first months of my third (and last) year.

As for most of newly-created chemical species, knowledge of the LiCr system was rather scarce when we started our investigation [93]. In practice, from an experimentalist point of view, this meant that several pieces of information had to be put together before the general picture started to be clear. One direct example is given by the different loss mechanisms affecting LiCr Feshbach dimers, involving both inelastic collisions with unpaired atoms and photo-excitation losses accidentally caused by our bODT lights: Initially, we considerably struggled to understand what was the main limiting factor to the dimers lifetime – which for long times never exceeded a few ms – as the two dominant processes (i.e. inelastic collisions with Li atoms and photo-excitation from the 532-nm beam) were happening on very similar timescales. On top of that, even when limiting the discussion to photo-excitation losses alone, it was not straightforward to expect that the single-mode 532-nm light was nearly a hundred times worse than the multi-mode, few-nm-wide IR one at 1070 nm. Parallel to all this, an additional, hidden source of instability was originating from the magnetic-field noise affecting our main set of coils. In this case, the subtlety – intrinsically connected with the narrow character and high-field location of the Li-Cr *s*-wave FRs (see Chapter 3) – arises from the technical challenge of measuring small (\sim mG-level) variations on top of a $\gtrsim 1.4$ kG bias field, and to identify efficient strategies to reduce the magnetic field noise.

The implementation of a few key technical upgrades to the experimental setup (see Chapter 6), together with the devise and refinement of experimental protocols (according to the progressively acquired knowledge), allowed us to decouple and overcome these major issues. As a result, we could finally produce large and ultracold samples of LiCr Feshbach molecules, purified from leftover unpaired atoms, featuring lifetimes longer than 0.2 s and PSDs exceeding 0.1. By also developing new probing methods, we thoroughly characterized our molecular samples, demonstrating the paramagnetic nature of LiCr dimers and the precise control of their internal quantum state. Following this storyline, the title of this Chapter is a lighthearted personal homage to Refs. [167] and [168], which have undoubtedly guided and inspired me in my journey as an atomic physicist.

Parallel to our experimental efforts in the lab, the group of M. Tomza (University of Warsaw) developed a new, *ab initio* quantum chemical model for the LiCr molecule. Their findings, completely independent from our experimental work, point to a sizable electric dipole moment (exceeding 3 D) for LiCr in its absolute ground state, i.e. the lowest rotationless level of the sextet $X^6\Sigma^+$ potential [see Fig. 4.1(a)]. Additionally, they provide

fundamental guidelines for the future identification and implementation of STIRAP schemes, with which Feshbach dimers will be coherently transferred to deeply-bound levels. Such a synergetic joint experimental and theoretical study depicts Li-Cr as a very promising candidate to realize ultracold gases of doubly-polar molecules, with significant electric (3.3 D) and magnetic ($5 \mu_B$) dipole moments.

This Chapter is organized as it follows:

- First, in Secs. 4.1 and 4.2, I summarize the typical starting conditions of all our experiments with LiCr Feshbach molecules (recalling also the nature of the FRs involved), and I describe our molecule detection protocols, based on either positive or negative signals.
- Second, in Secs. 4.3 and 4.4, I present our characterization of the magneto-association process (based on a standard Landau-Zener model), and I summarize the initial optimization of molecule number and phase-space density.
- Third, in Sec. 4.5, I report on our study of trap-light-induced losses, which initially represented one of the main limiting factors to the molecule lifetime. Additionally, in Sec. 4.6, I discuss inelastic atom-dimer losses, addressing the collisional stability of atom-molecule mixtures.
- In Sec. 4.7, I present our measurement of the magnetic dipole moment of LiCr Feshbach molecules, which importantly testified their paramagnetic nature and further confirmed the assignment of the molecular state yielding the FR.
- In Sec. 4.8, I describe our new optical method to fast and reliably measure the open-channel fraction and the molecule binding energy. Then, to conclude the experimental part of the Chapter, in Sec. 4.9 I summarize our procedure to realize pure and long-lived samples of LiCr Feshbach molecules.
- Finally, in Sec. 4.10 I present the quantum chemical model for LiCr developed by M. Tomza and colleagues – leaving all technicalities to Refs. [94] and [169] – focusing on the most important implications for our (future) experimental activity, e.g., the identification of a suitable STIRAP scheme.

4.1 Parent atomic mixture and typical initial conditions

The starting point of all experiments described in the following Sections is a weakly interacting, spin-polarized mixture of ${}^6\text{Li}$ and ${}^{53}\text{Cr}$ atoms produced through the all-optical protocol detailed in Chapter 2. As described there, the atomic sample is produced within our main bichromatic optical dipole trap, combining IR (1070 nm) and green (532 nm) lights. The gravitational sag between the two clouds is compensated upon application of a weak, vertically-oriented magnetic field gradient b of about 1.5 G/cm. For all studies reported in this Chapter, the axial confinement is solely provided by the magnetic field curvature generated by our main set of coils (BIAS coils). Owing to the fact that the Cr magnetic moment is six times larger than the Li one, the resulting axial trapping is six times tighter for Cr than for Li,¹ see sketch in Fig. 3.6(a).

Although the atom number, temperature, and degree of degeneracy of the two species can be widely tuned by adjusting the (absolute and relative) power of the two bODT beams (see Chapter 2), our experiments typically start with a Fermi gas of about 1.5×10^5 Li atoms at $T_{\text{Li}}/T_{\text{F,Li}} = 0.25$ with $T_{\text{Li}} = 130(20)$ nK, coexisting with a moderately degenerate sample of 0.8×10^5 Cr atoms at $T_{\text{Cr}}/T_{\text{F,Cr}} \gtrsim 0.5$ and $T_{\text{Cr}} = 220$ nK, with peak densities of about

¹The magnetic field curvature of the BIAS coils is $\partial^2 B/\partial x^2 \simeq 12$ G/cm² at 1414 G, resulting in axial harmonic frequencies of $\omega_x/(2\pi) \simeq 17$ Hz (14 Hz) for $\text{Li}|i\rangle$ ($\text{Cr}|i\rangle$) atoms, with $i = 1, 2$.

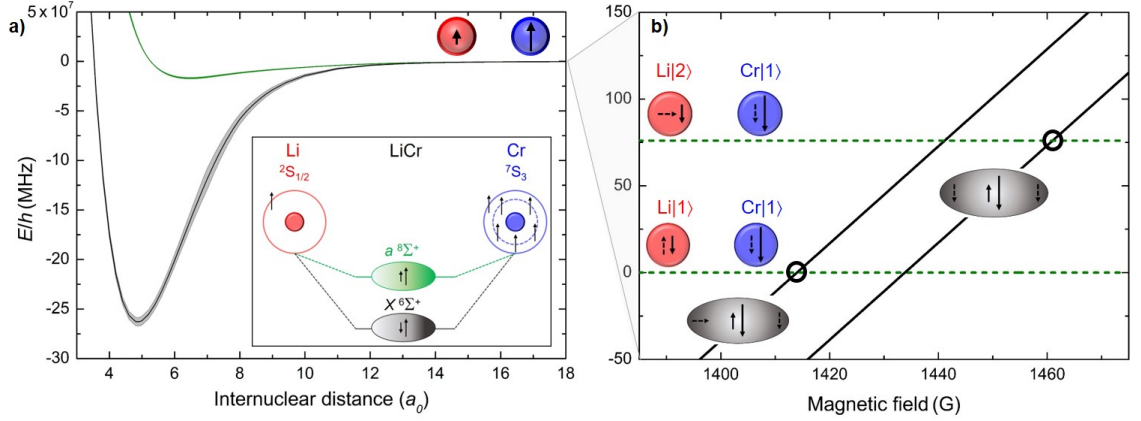


Figure 4.1 – Doubly polar LiCr dimers. (a) *Ab initio* potential energy curves, as calculated by the group of M. Tomza, for the $X^6\Sigma^+$ ground state and the $a^8\Sigma^+$ first excited state in Hund’s case (a) representation. The inset shows a pictorial representation of the valence electrons for Li and Cr, and the resulting sextet and octet molecules with nonzero electronic spin and polarized charge density. (b) Energy of the atom pairs in the $\text{Li}|1\rangle\text{-Cr}|1\rangle$ and $\text{Li}|2\rangle\text{-Cr}|1\rangle$ channels, of pure octet character (dashed green lines), and of the molecular sextet levels (solid black lines) inducing the FRs relevant for this Chapter (circled). Atomic Zeeman levels are labeled in order of increasing energy. Solid and dashed arrows indicate electronic and nuclear spins, respectively.

10^{12} cm^{-3} for both components (here T_F denotes the Fermi temperature of a harmonically trapped Fermi gas). Resonant tuning of Li-Cr interactions, as well as magneto-association of atom pairs into LiCr dimers via magnetic field sweeps, are enabled by exploitation of interspecies *s*-wave FRs, already characterized in Chapter 3. In particular, we focus on the specific *s*-wave resonances that occur in the $\text{Li}|1\rangle\text{-Cr}|1\rangle$ and $\text{Li}|2\rangle\text{-Cr}|1\rangle$ scattering channels, located at high fields around 1414 and 1461 G, respectively; see Fig. 4.1(b). Our choice is motivated by the fact that these two features exhibit the largest magnetic field width $\Delta_B \simeq 0.48 \text{ G}$ available in our mixture, combined with zero or negligible two-body loss rates. Most importantly for the studies of this Chapter, these FRs are induced by hyperfine coupling with the least bound, rotationless vibrational level of the $X^6\Sigma^+$ ground-state Born-Oppenheimer potential; see Fig. 4.1(a) and Tab. 3.1.

4.2 Detection of LiCr dimers

Before discussing the formation and characterization of LiCr dimers in the following Sections, I summarize here the methods that we employed for detecting them in the experiment. Indeed, as discussed later, molecule formation through magneto-association results in general in a mixture comprising both dimers and leftover unpaired atoms. As such, one must employ detection protocols able to unequivocally distinguish the former from the latter ones.

In our lab, in order to experimentally show LiCr dimer formation, count their number, and characterize their density or momentum distribution, we use either “negative” or “positive” signals, depending on the task at hand. By “negative” signals I denote atomic loss signals that unambiguously determine the molecule number. This is relatively straightforward in our system: On the one hand, two-body losses are absent² and three-body recombination is much slower than typical molecule association times (see Sec. 3.4 and the next Sec. 4.3). On the other hand, as I will show in Sec. 4.5, the green light at 532 nm of our bODT induces strong photo-excitation losses for LiCr Feshbach dimers, limiting

²Two-body losses are totally absent in the ground-state mixture $\text{Li}|1\rangle\text{-Cr}|1\rangle$, and are negligible at the 1461 G resonance in the $\text{Li}|2\rangle\text{-Cr}|1\rangle$ spin combination, see Chapter 3 and Ref. [155].

their lifetime to a few milliseconds for the typical powers employed. The net result is that, for short timescales and in the presence of green light, after magneto-association all and only atoms bound into molecules are lost. This represents a valuable tool to monitor molecule formation through “negative” signals at short hold times t_{hold} , unaffected by inelastic scattering (three-atom, atom-dimer, dimer-dimer) processes. The reliability of this method is demonstrated by the data presented in Fig. 4.2(a): There, I show the Cr loss signals measured at $t_{\text{hold}} = 3$ ms as a function of the final detuning, which is reached through magnetic field ramps starting either far above ($B_{\text{in}} > 0$, blue squares) or far below ($B_{\text{in}} < 0$, red circles) the FR pole. In the former configuration – that allows for magneto-association of LiCr dimers – we reveal a strong drop of the Cr signal as the FR pole is crossed. By contrast, in the latter case – for which molecule formation can only occur via three-body recombination processes, and only collisional losses may reduce the signal – the Cr population remains constant within experimental noise across the entire resonance region. It is thus legitimate to attribute the observed drop of the blue data in Fig. 4.2(a) solely to molecule formation via magneto-association, since spurious effects due to three-body processes are negligible at short t_{hold} values. Indeed, collisional losses, which add to those induced by photo-excitation of LiCr dimers, become sizable only at significantly longer hold times, see again Sec. 3.4. This is further testified by Fig. 4.2(b), where the magneto-association line shape obtained with $t_{\text{hold}} = 3$ ms (blue squares), and already shown in Fig. 4.2(a), is compared with that measured after a hold time of 25 ms (green circles). As one can see, only for such long t_{hold} values inelastic collisions start yielding, near the resonance pole, a signal contribution comparable with that due to molecule formation.

By “positive” signals I denote instead those that originate from previously associated atoms, which give then rise to a measurable optical density on the atomic Li and Cr imaging transitions; see the detailed discussion in Sec. 4.8 below. In our experiments, we employ two different schemes to obtain such “positive” signals. The first one relies on Stern-Gerlach separation, where the molecule cloud is spatially resolved from the atomic ones thanks to a different acceleration and a sufficiently long time of flight (TOF). Indeed, under the combined effect of gravity and a magnetic field gradient b along the vertical direction, the

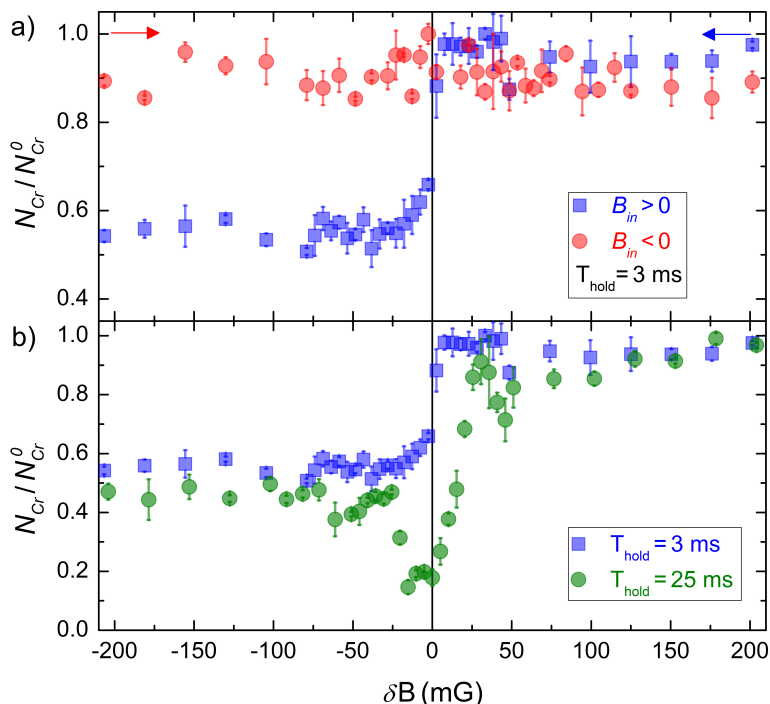


Figure 4.2 – (a) Fractional Cr loss measured in the bODT as a function of the magnetic field detuning that is reached through a ramp starting at a bias field B_{in} either far above (blue squares) or far below (red circles) the FR pole. The signal is detected after a hold time at the final field of $t_{\text{hold}} = 3$ ms. (b) Comparison of the Cr loss line shapes, obtained with magnetic field ramps starting from $B_{\text{in}} > 0$, and measured after a hold time $t_{\text{hold}} = 3$ ms (blue squares) and $t_{\text{hold}} = 25$ ms (green circles).

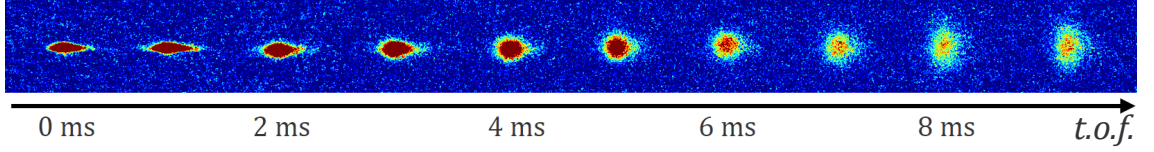


Figure 4.3 – Absorption images of a LiCr molecular cloud in time-of-flight, acquired with imaging light resonant with the atomic Li transition. Each frame is manually displaced along the horizontal and vertical directions for display purposes. See Sec. 4.8 for a detailed discussion concerning absorption imaging of Feshbach dimers on atomic transitions.

total center-of-mass acceleration is given by $g + \mu_X b/m_X$, where g is the gravitational acceleration, μ_X is the magnetic dipole moment of species X ($X = \text{Li}, \text{Cr}, \text{LiCr}$), and m_X is the corresponding mass (see also the measurement of μ_{LiCr} in Sec. 4.7). Therefore, the displacement between the cloud barycenters of different species grows quadratically in time, and linearly with both the magnetic field gradient and the difference between the magnetic-moment-to-mass ratios, i.e.:

$$|\Delta z_{12}(t)| = \frac{1}{2} \left| \frac{\mu_1}{m_1} - \frac{\mu_2}{m_2} \right| b t^2. \quad (4.1)$$

At the same time, after release from the optical trap, the clouds expand in time-of-flight along the vertical direction. For non-degenerate gases in the “far-field”, the characteristic size grows linearly in time as $\sigma_z(t) \sim \sqrt{k_B T_X/m_X} \cdot t$, where T_X is the temperature of species X . It is clear that one must allow for a sufficiently long time of flight in order to spatially resolve the two clouds. In our case, it is more convenient to resolve the molecule cloud from the atomic Li one, as $|\mu_{\text{Li}}/m_{\text{Li}} - \mu_{\text{LiCr}}/M_{\text{LiCr}}| > |\mu_{\text{Cr}}/M_{\text{Cr}} - \mu_{\text{LiCr}}/M_{\text{LiCr}}|$. For our typical temperatures $T_X \sim 200$ nK, and for $b = 1.5$ G/cm, one has $|\Delta z(t)| \gtrsim \sigma_z^{\text{Li}}(t) + \sigma_z^{\text{LiCr}}(t)$ for $t \gtrsim 8$ ms.

The second “positive detection” method exploits fast (few hundred microsecond-long) RF transfers of unpaired Li and Cr atoms to dark states that do not interact with the high-field imaging light, thereby leaving a zero-background molecular signal. Importantly, since the dimer binding energy grows as 2.8 kHz/mG (i.e. $\delta\mu = 2 \mu_B$), a detuning of a few milligauss on the repulsive side of the FR is enough to ensure a negligible RF transfer of paired atoms. This allows us to probe the LiCr sample also at shorter times, and thus to trace the entire time-of-flight trajectory of the molecular cloud, as shown in Fig. 4.3.

Finally, I remark that only positive signals allow access to further information about the molecule sample, such as thermodynamic quantities. However, negative signals often turn out to be quite convenient to detect molecule formation and count their number; see, e.g., the following Sec. 4.3.

4.3 Magneto-association and two-body adiabaticity

In this Section, I describe the study of the conversion process of Li and Cr atoms into LiCr Feshbach molecules via magneto-association. Magneto-association is an adiabatic conversion of scattering atom pairs into weakly bound molecules, induced by a magnetic field sweep across the Feshbach resonance pole, from the attractive ($B_i > B_0$) to the repulsive side ($B_f < B_0$) [see Fig. 4.4(a)]. We characterized the molecule conversion efficiency as a function of the magnetic-field sweep rate \dot{B} across the FR. As already reported for bi-alkali homo- and hetero-nuclear systems [170–175], also in our case the magneto-association efficiency depends on the Feshbach resonance parameters, the conditions of the parent atomic gases, and on \dot{B} [176].

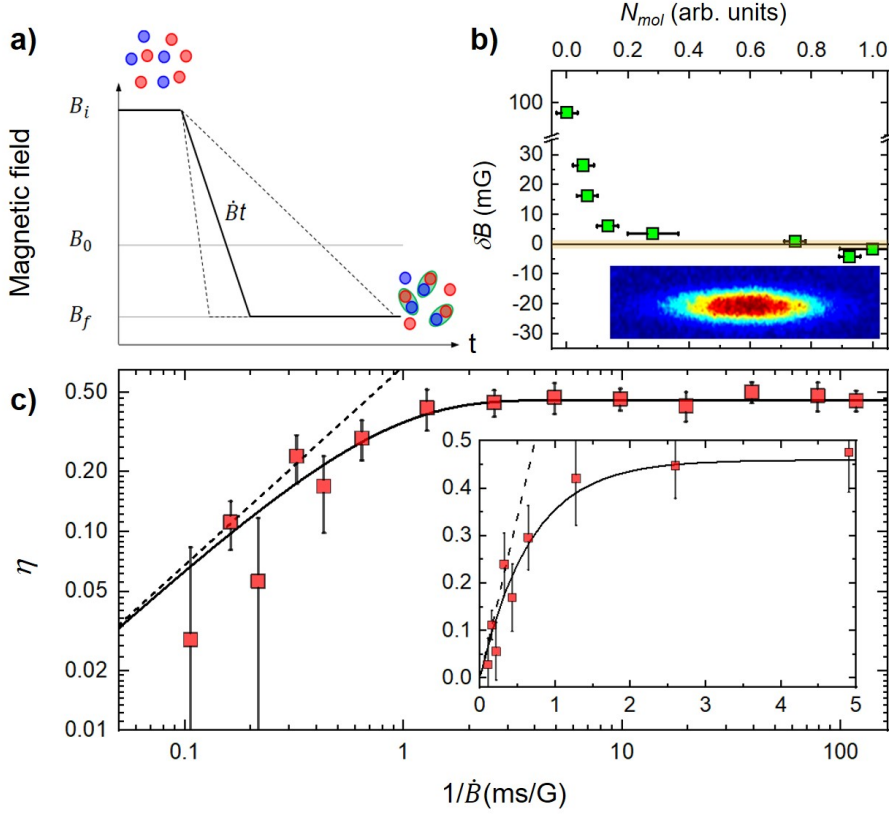


Figure 4.4 – Magneto-association efficiency and two-body adiabaticity. (a) Sketch of the experimental sequence: the magnetic field is swept from B_i across the FR pole B_0 down to $B_f < B_0$ with variable rate \dot{B} , after which the number of created molecules is measured through either positive or negative signals; see the text for details. (b) Normalized number of molecules formed via magneto-association as a function of B_f across the FR for fixed $1/\dot{B} = 90$ ms/G. The inset is an example of a positive signal of LiCr via direct absorption imaging with Li light after a 2-ms TOF. (c) Association efficiency η , referenced to the Cr minority component, as a function of the inverse ramp speed $1/\dot{B}$. The solid black line shows the best functional fit of Eq. (4.2) to the data, while the dashed line represents its approximation in the fast-sweep limit.

First, we exploited “positive” molecule signals obtained from direct absorption imaging to reveal the sensitivity of the associated molecules to the final magnetic field detuning. As shown in Fig. 4.4(b), the number of detected molecules features a sharp rise from zero background to saturation in a B -field region of a few tens of milligauss. Complementarily – leveraging on the stability of our Fermi mixtures (see Sec. 3.4), and exploiting the strong photo-excitation rate induced by the 532-nm light in our bODT (see Sec. 4.5) – a “negative” signal was used to quantify the number of associated molecules. Indeed, as discussed in Sec. 4.2, after a short hold time following the B -field sweep, only atoms that were converted into dimers are (entirely) lost, and the conversion efficiency is nothing but the fractional loss between the initial and final atom numbers.

We measured the association efficiency as the fractional loss of the Cr minority component as a function of the inverse magnetic sweep rate $1/\dot{B}$; see Fig. 4.4(c). For this specific dataset, we started the experiment by preparing the $\text{Li}|1\rangle\text{-Cr}|1\rangle$ mixture about +100 mG above the resonance. The $\text{Li}|1\rangle$ gas was degenerate, with $T_{\text{Li}}/T_{\text{F,Li}} = 0.20(5)$ at $T_{\text{Li}} = 170$ nK and a peak density of $1.3(2) \times 10^{12}$ cm^{-3} , while $\text{Cr}|1\rangle$ was essentially thermal, with $T_{\text{Cr}}/T_{\text{F,Cr}} \sim 1$ at $T_{\text{Cr}} = 240$ nK and a peak density of $0.74(3) \times 10^{12}$ cm^{-3} . The magnetic field was swept to $\delta B < 0$ with ramps of variable speed, after which we measured the number of associated molecules.

As for other experiments, our results are well captured by a Landau-Zener model [170–175]. Thus, according to Ref. [175], we fitted the following functional form to the data:

$$\eta = \eta_0 \left[1 - \exp \left(- \frac{\Gamma_{\text{LZ}} \langle n_{\text{Li}} \rangle_{\text{Cr}}}{\eta_0} \dot{B}^{-1} \right) \right]. \quad (4.2)$$

Here η_0 represents the saturated efficiency, $\langle n_{\text{Li}} \rangle_{\text{Cr}}$ is the density of the majority component (Li) averaged over the density of the minority one (Cr), and Γ_{LZ} is only a function of the collision parameters, i.e.

$$\Gamma_{\text{LZ}} = (2\pi)^2 \frac{\hbar}{m_{\text{red}}} |a_{\text{bg}} \Delta_{\text{B}}|, \quad (4.3)$$

where $a_{\text{bg}} = 41.48(3) a_0$ is the background s -wave scattering length, $\Delta_{\text{B}} = 0.48 \text{ G}$ is the magnetic field width, and m_{red} is the reduced mass. While the adiabatic regime ($\eta \simeq \eta_0$) depends on the overall PSD overlap of the atomic mixture and lacks an analytical description to date, the fast-sweep regime, where $\eta \simeq \Gamma_{\text{LZ}} \langle n_{\text{Li}} \rangle_{\text{Cr}} / \dot{B}$, can be straightforwardly tested against the experimental results.

From a functional fit of Eq. (4.2), with an observed Li|1> density averaged over the Cr|1> cloud of $\langle n_{\text{Li}} \rangle_{\text{Cr}} = 0.62(5) \times 10^{12} \text{ cm}^{-3}$, we derived $\Gamma_{\text{LZ,meas}} = 1.1(1) \times 10^{-12} \text{ cm}^3 \text{ G/ms}$; see the solid line in Fig. 4.4(c). The dashed line marks the linear, fast-sweep regime. The fitted $\Gamma_{\text{LZ,meas}}$ is in satisfactory agreement with the theoretically expected value $\Gamma_{\text{LZ,th}} = 0.479 \times 10^{-12} \text{ cm}^3 \text{ G/ms}$, using the FR parameters of the coupled-channel model of Chapter 3. The mismatch of about a factor of 2 might be due to an underestimation of the overlap density during molecule association, where the mixture experiences strong attractive interactions.

Importantly, I emphasize that, as expected from the extremely favorable mixture stability shown in Secs. 3.3 and 3.4, we can perform magneto-association with field rates slower than the two-body adiabatic criterion by more than two orders of magnitude, without affecting the conversion efficiency nor the molecule number.

4.4 Optimization and molecule PSD

In this Section, I discuss how the number of associated LiCr dimers was found to depend on the initial conditions (e.g. temperature, density) of the parent atomic gases. This study was conducted primarily with the aim of maximizing the final PSD of the molecular sample. In order to identify the best working conditions, we characterized the molecule association efficiency as a function of the Li-Cr density overlap, deep in the two-body adiabatic regime ($1/\dot{B} = 90 \text{ ms/G}$). This was accomplished by only varying the number of atoms initially loaded into the bODT, with fixed evaporation and final trap parameters. In this experiment, we spatially resolved atomic and molecular clouds thanks to Stern-Gerlach separation, and simultaneously counted the number of Li, Cr, and LiCr.

In Fig. 4.5(a), I show the measured molecule number as a function of the pair density $\langle n_{\text{Li}} n_{\text{Cr}} \rangle = \int n_{\text{Li}} n_{\text{Cr}} d\vec{r}$. On general grounds, neglecting atom-molecule thermalization, the molecule number depends on the PSD overlap between the parent atomic clouds during association [175, 177]. However, for Maxwell-Boltzmann gases at constant temperature, this is proportional to $\langle n_{\text{Li}} n_{\text{Cr}} \rangle$. Since, for this experiment, the temperatures $T_{\text{Cr,Li}}$ were kept fixed, with $T_{\text{Cr}}/T_{\text{F,Cr}} \geq 0.5$ and almost constant $T_{\text{Li}}/T_{\text{F,Li}} = 0.30(5)$, we expect this relation to hold to first approximation. Indeed, the experimental data are well captured by a linear fit, as shown by the solid black line in Fig. 4.5(a).

From the same experimental data we also extracted the conversion efficiency η as a function of $\langle n_{\text{Li}} \rangle_{\text{Cr}}$, see Fig. 4.5(b). It is important to stress that, although Cr atoms were always lower in number compared to Li atoms [except for the leftmost point of

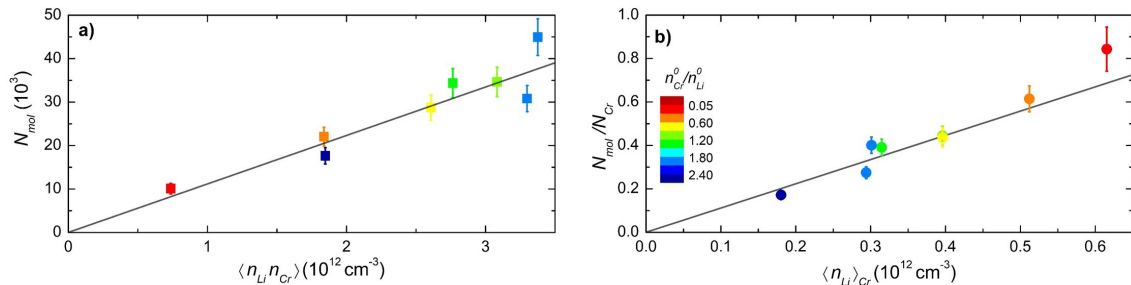


Figure 4.5 – (a) Number of associated molecules N_{mol} as a function of the Li-Cr pair density $\langle n_{\text{Li}} n_{\text{Cr}} \rangle$. The black line shows a linear fit to the data with zero intercept. (b) Magneto-association efficiency with respect to Cr as a function of the Li density averaged over the Cr cloud $\langle n_{\text{Li}} \rangle_{\text{Cr}}$. The black line shows a linear fit to the data with zero intercept. In both panels the same color code indicates the corresponding imbalance between the peak densities of Cr and Li atomic clouds.

Fig. 4.5(b) with the lowest Li density], their peak density could overcome the Li one. Hence, through this characterization, we explored different regimes in which the majority component is locally either Cr or Li; see the color scale. Also in this case, η exhibits a linear increase with $\langle n_{\text{Li}} \rangle_{\text{Cr}}$, showing no saturation effects up to the highest densities we explored. Comparing Figs. 4.5(a) and 4.5(b), one can see that intermediate mixture imbalance enables the production of the largest molecule samples, of nearly 5×10^4 molecules, and a comparatively good conversion efficiency of $40 \div 50\%$. These results are in line with the values previously reported on ${}^6\text{Li}{}^{40}\text{K}$ Feshbach molecules [124, 174], and even slightly better than the 30% efficiency shown on ${}^{40}\text{K}{}^{161}\text{Dy}$ [85].³ However, our data also show a maximum conversion efficiency of about 80%, at the expense of a lower but still considerable molecule number of $2 \div 3 \times 10^4$. This regime is comparable with results on deeply degenerate homonuclear spin mixtures of ${}^{40}\text{K}$ [172], where both components shared the same degree of degeneracy. The ability to create large molecule samples with tunable density imbalance of the parent atomic mixture may help in the future to sympathetically cool molecules down to degeneracy with leftover Cr atoms, which do not appear to limit the molecule lifetime at our typical densities; see Sec. 4.6 below.

As shown in Fig. 4.5, the molecule population sensitively depends upon the Li-Cr pair density of the initial atomic mixture. After careful optimization, we studied the ballistic expansion of Feshbach dimers after variable time of flight via the Stern-Gerlach separation method, comparing it with the expansion of the atomic clouds. Once the bODT is switched off, atoms and molecules expand into the magnetic saddle potential generated by our coils. We obtained our record PSD starting magneto-association with atom numbers $N_{\text{Li}} = 3 \times 10^5$ and $N_{\text{Cr}} = 1 \times 10^5$ and temperatures $T_{\text{Li}} = 0.15 T_{\text{F,Li}} = 70$ nK and $T_{\text{Cr}} = 0.5 T_{\text{F,Cr}} = 180$ nK. From this starting condition we obtained $36(4) \times 10^3$ molecules at 180 nK, with peak spatial density of $0.75(10) \times 10^{12} \text{ cm}^{-3}$, and peak PSD of $n_{\text{LiCr}} \lambda_{\text{dB}}^3 = 0.12(2)$, where $\lambda_{\text{dB}} = \sqrt{2\pi\hbar^2/(mk_{\text{B}}T)}$ is the corresponding de Broglie wavelength. Our result compares well with the highest reported PSDs in other mass-imbalanced Fermi mixture experiments [56, 85], and even higher LiCr PSDs may be obtained by adding a crossed dipole trap (see, e.g., Sec. 2.8), not employed for the studies described in this Chapter. Although the employed magneto-association ramp was deep in the two-body-adiabatic regime, the molecular samples we created had not reached full thermal equilibrium. This last point, together with the possibility to further evaporate Cr, thereby sympathetically cooling LiCr, will be the subject of a future study.

³I am aware of unpublished data on ${}^{40}\text{K}{}^{161}\text{Dy}$ molecules, where a 45% association efficiency is achieved in a 1550-nm crossed dipole trap (priv. comm. from A. Canali).

4.5 Trap-light-induced losses

One key question about our novel LiCr Feshbach molecules concerns their stability against inelastic loss processes. In fact, in our setup magneto-association results typically in a mixture of LiCr dimers with unpaired Li and Cr atoms, confined by an optical dipole trap. Therefore, various inelastic mechanisms may contribute to limit the molecule lifetime: Quite generally, these can arise both from off-resonant scattering of LiCr towards electronically excited levels – accidentally induced by the trapping lights employed in the experiment – as well as from inelastic scattering in dimer-dimer and atom-dimer collisions. In this Section, I address the first of these two contributions, while the latter will be discussed in the next Sec. 4.6.

The bODT configuration that we exploited in Sec. 4.4 to reach optimal magneto-association efficiency and high PSD of LiCr molecules was experimentally found to strongly limit the molecule lifetime to the few-millisecond timescale, resulting not suitable to trap LiCr Feshbach molecules. In order to properly characterize the detrimental effect of the bODT lights on the LiCr sample, and to decouple it from possible atom-dimer collisional losses (see Sec. 4.6), we purified the molecule sample right after the end of the magneto-association ramp by removing the leftover atoms. In particular, $\text{Li}|1\rangle$ was removed via the combination of a 0.5-ms-long RF π -pulse resonant with the $\text{Li}|1\rangle \longleftrightarrow \text{Li}|2\rangle$ transition, followed by an optical blast of the $\text{Li}|2\rangle$ component. The procedure was repeated two times consecutively to ensure a negligible remaining population of unpaired $\text{Li}|1\rangle$ atoms. $\text{Cr}|1\rangle$ was instead directly spilled from the trap (on a typical timescale of $10 \div 20$ ms), which, for this species, in the presence of infrared light only (see below) is significantly shallower than for both Li and LiCr components.⁴ The purification protocol is better detailed in Sec. 4.9.

We first isolated the effect of the multimode 1070-nm ODT beam by extinguishing the green light right before molecule association. Once the unpaired atoms were completely removed, we ramped the IR power to a variable value, where we recorded the subsequent molecule number drop. We extracted the loss rates from exponential fits to the decay data, similarly to what was done in Ref. [85] for DyK molecules. The results are reported in Fig. 4.6(a) (red squares) as a function of the laser intensity, together with a linear fit to the data (red line). Using the fitted slope and taking into account a finite open-channel fraction $1 - Z > 0$ (see Sec. 1.6) at the probe detuning $\delta B = -100$ mG, we derived $\Gamma_{\text{cc}} = 5.9(2)$ Hz/(kW cm⁻²).

Secondly, since the 532-nm green beam is anti-trapping for our molecules, we studied its effect by ramping it up to a (small) variable power while keeping the IR ODT power fixed. The corresponding experimental loss rates, shown in Fig. 4.6(a) as green triangles, yield a significantly higher slope of $\Gamma_{\text{cc}} = 397(14)$ Hz/(kW cm⁻²). This value, about two orders of magnitude larger than the IR one, confirms the detrimental effect of 532-nm light on LiCr Feshbach molecules, and sets a strong constraint on the possible timescales for manipulation of the LiCr sample in the combined bODT.⁵

Such a significantly higher Γ_{cc} value measured for the (single-mode) 532-nm beam, compared to the (multi-mode) 1070-nm one, points to a stronger off-resonant photon scattering for increasing photon energy. Following also similar observation on KDy molecules (A. Canali and R. Grimm, priv. comm.), we decided to test the effect of a far-off-resonant trap (FORT) at 1560 nm. We therefore implemented a new trapping beam at such wavelength, which we overlapped to the main bODT in a counter-propagating configuration (see sketch in Fig. 6.4 and details on the setup in Sec. 6.3). For the purposes of this characterization, before creating molecules, we transferred the atomic mixture from the bODT to the FORT, through 100-ms-long (linear) power ramps that completely extinguished the bODT lights. The FORT power was initially increased to an optimum value, experimentally determined, that yielded the

⁴Dynamic polarizabilities of Feshbach molecules are expected to be the sum of the atomic ones. In our case: $\alpha_{\text{LiCr}}(532 \text{ nm}) = -109$ a. u., $\alpha_{\text{LiCr}}(1070 \text{ nm}) = 359$ a. u., $\alpha_{\text{LiCr}}(1560 \text{ nm}) = 284$ a. u., of which the last two are consistent with our measurements.

⁵On the other hand, fast photo-excitation losses caused by the green light can be exploited to detect molecules as negative signals (see Sec. 4.2), or to check the purity of the molecular sample (see Sec. 4.9).

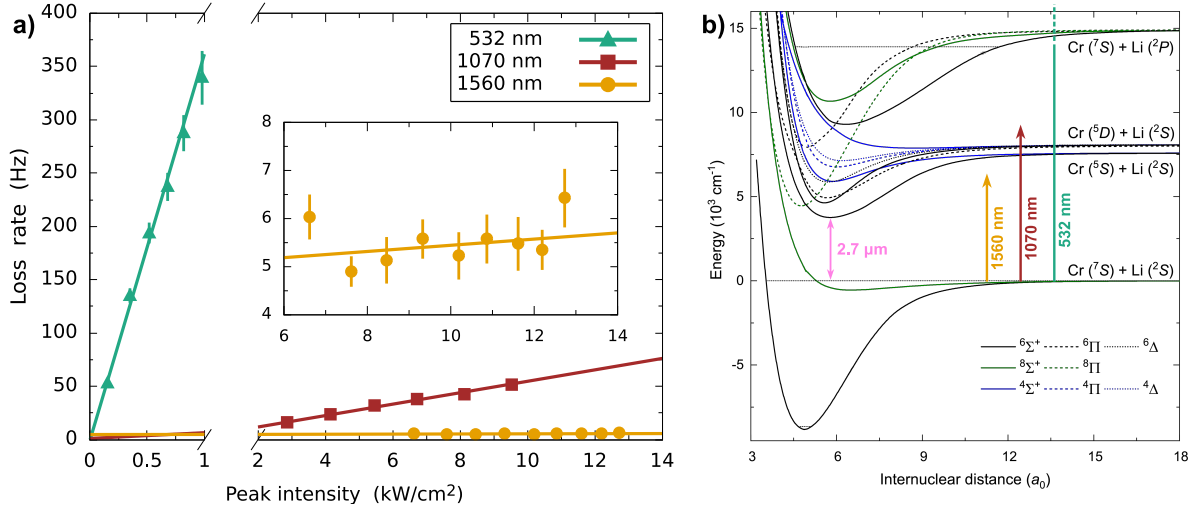


Figure 4.6 – (a) Loss rates as a function of light intensity for the trap wavelengths explored in this work. Green triangles, red squares, and yellow circles show the experimental exponential loss rates for 532, 1070, and 1560 nm, respectively. Best linear fits to the data are plotted as solid lines with matching color code. (b) Potential energy curves of the LiCr molecule in the ground and excited electronic states, as calculated by the group of M. Tomza, see Sec. 4.10. The three vertical arrows with the same color code as panel (a) show the energy of photons at 532, 1070, and 1560 nm, respectively. The pink arrow shows a hypothetical transition at 2.7 μm, coupling the Feshbach dimer to the lowest excited electronic state.

best magneto-association conditions. After molecule creation, the FORT power was quickly lowered to start the spilling of Cr atoms. Once a pure molecular sample was obtained, the 1560-nm power was ramped to the target value for the lifetime measurement. In this case, the analysis discussed above yields a photo-excitation rate consistent with zero within experimental uncertainty; see the yellow circles in Fig. 4.6(a) and corresponding inset. I point out here that, for each dataset and trapping light, the systematic error of Γ_{cc} arising from intraspecies LiCr-LiCr inelastic collisions was negligible, since the dimer density was kept fixed at all power levels explored, within our experimental accuracy.

In conclusion to this Section, I remark that our experimental observation qualitatively agrees with the *ab initio* calculations of M. Tomza’s group, that I will present later in Sec. 4.10 (see also Refs. [94] and [169]). Their theoretical model predicts, for increasing photon energy, progressively larger transition dipole moments and higher spontaneous decay rates of molecular states coupled to the Feshbach dimer. For the moment, at least at a qualitative level, one could compare our experimental findings with the theoretical results presented in Fig. 4.6(b), which shows the potential energy curves of the LiCr molecule for the ground and first few excited electronic states. The 532-nm light, with photon energy $\simeq 18\,800\text{ cm}^{-1}$, can in principle couple the Feshbach state to a multitude of excited molecular states, lying above the $\text{Cr}(^7S) + \text{Li}(^2P)$ asymptote, and below the $\text{Cr}(^7P) + \text{Li}(^2S)$ one (see green vertical arrow, falling outside the plot range). By contrast, 1070-nm (photon energy $\simeq 9\,350\text{ cm}^{-1}$) and 1560-nm (photon energy $\simeq 6\,400\text{ cm}^{-1}$) transitions that start from the Feshbach state both fall below the $\text{Cr}(^7S) + \text{Li}(^2P)$ dissociation threshold, potentially addressing fewer levels, see red and yellow vertical arrows, respectively. In light of these considerations, one can see that, ideally, the safest choice to optically trap LiCr Feshbach molecules would be to employ wavelengths longer than 2.7 μm (photon energy $< 3\,700\text{ cm}^{-1}$), that do not couple the Feshbach dimer to any excited molecular level.⁶

⁶In practice, this option cannot be easily tested on our experimental setup, since the coating of our viewports, chosen at the early build-up stage of the experiment to be optimal for the bODT lights [123], are not suitable for such long wavelengths.

4.6 Stability of atom-molecule mixtures

In this Section I discuss the stability of atom-molecule mixtures against inelastic collision processes. These studies were performed before the implementation of the FORT beam at 1560 nm, and were carried out in the sole IR trap at 1070 nm. In fact, following the discussions in Secs. 4.4 and 4.5, we generally found advantageous to keep a small amount of green light in the bODT up to a few milliseconds before molecule formation, to then suddenly switching it off once LiCr dimers were created. This procedure allowed us both to maximize the molecule number and, at our typical IR intensities, to increase the one-body lifetime up to a few tens of milliseconds, allowing us to characterize the stability of the molecular sample against dimer-dimer (D-D) and atom-dimer (A-D) inelastic collisions. This investigation is relevant both in light of future implementation of optical spectroscopy protocols, and of possible subsequent evaporative and sympathetic cooling stages of Feshbach dimers.

As for three-atom recombination discussed in Secs. 3.3 and 3.4, leading to a good-to-bad collision rate of about 200, Fermi-Fermi mixtures are also expected [55, 56, 111] to benefit from Pauli suppression for D-D and A-D inelastic collisions near the FR pole – owing to the fact that these scattering events necessarily involve at least two identical fermions (either unpaired or paired into a shallow dimer). Specifically, the loss rate coefficients β of such processes can be substantially decreased, with respect to their off-resonant background value β_{bg} , as soon as dimers acquire a sizable open-channel fraction, i.e., near the resonance pole. While this qualitative feature is generic to any Fermi-Fermi mixture, the suppression factor $\beta(R^*/a)/\beta_{\text{bg}}$ sensitively depends upon the specific mass ratio between the two constituents. For atom-dimer processes in heteronuclear systems, light-light-heavy inelastic processes are predicted to dominate over the heavy-heavy-light ones in the resonant regime [56, 111]. For our specific mixture, for instance, Jag *et al.* [56] foresaw, already for $R^*/a \lesssim 10$, a suppression for Cr-LiCr collisions more than one order of magnitude larger than that for Li-LiCr ones. Moreover, one also expects in the off-resonant regime that lithium-dimer collisions are dominant, given that the background value of the A-D loss rate coefficient is theoretically given by [56]

$$\beta_{\text{bg}}^{\text{A-D}} \sim \frac{2h R_{\text{vdW}}}{m_{\text{A-D}}}, \quad (4.4)$$

with R_{vdW} the van der Waals length and $m_{\text{A-D}}$ the atom-dimer reduced mass, and that $m_{\text{Cr-D}}/m_{\text{Li-D}} \sim 5$. Also in light of the fact that the Li density exceeds the Cr one in our typical conditions, we observed that collisional losses of LiCr dimers were indeed dominated by Li-D scattering. This was confirmed by a measured Li-to-Cr relative loss of $\Delta N_{\text{Li}}/\Delta N_{\text{Cr}} = 1.93(17)$, and by the fact that, when unpaired Li atoms were removed from the sample, we did not observe any detectable signature of Cr-D or D-D inelastic processes.

We characterized the magnetic field dependence of $\beta_{\text{Li-D}}$ by varying the endpoint of the association ramp at the Li|1⟩-Cr|1⟩ resonance, and tracing the subsequent molecule decay as a function of time. At each detuning, the fitted exponential decay rate, corrected for the residual trap-light-induced loss contribution, yields the Li-D inelastic scattering rate. Dividing the latter by the dimer-weighted Li density $\langle n_{\text{Li}} \rangle_{\text{D}}$, determined experimentally, we thus extracted the inelastic rate coefficient $\beta_{\text{Li-D}}$. The results are shown in Fig. 4.7 as a function of δB (filled red squares). One can notice how $\beta_{\text{Li-D}}$ monotonically decreases down from its off-resonant value as the resonance pole is approached, exhibiting a drop that becomes progressively more pronounced as $\delta B \rightarrow 0^-$. To corroborate the interpretation of our findings in terms of Pauli suppression of collisional losses [56], we repeated the same measurement, but transferring the remaining unbound lithium atoms to the non-resonant

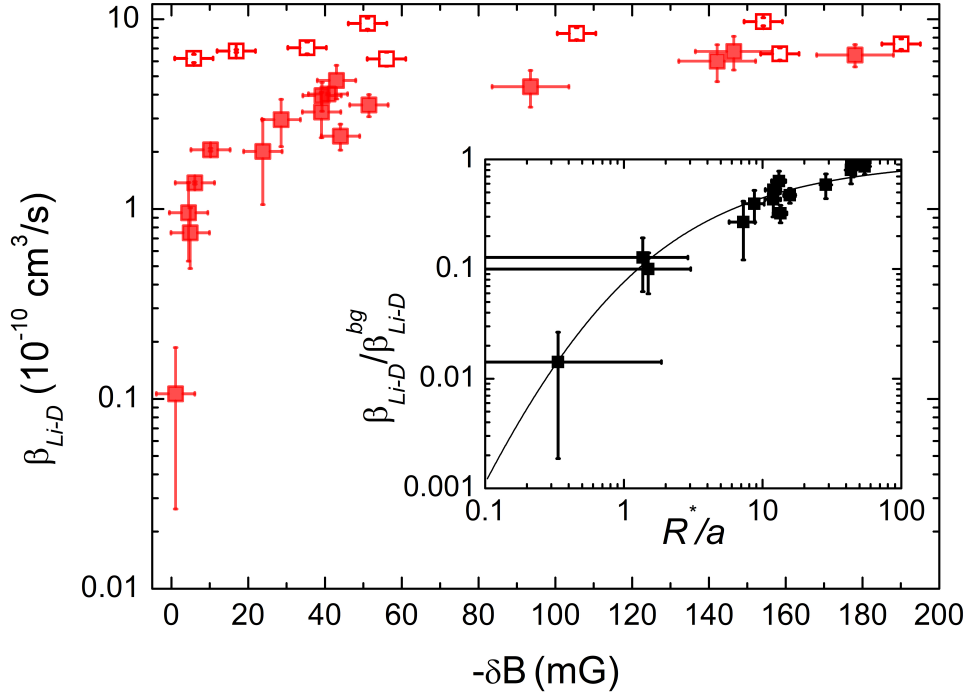


Figure 4.7 – Loss rate coefficient $\beta_{\text{Li-D}}$ for inelastic Li-LiCr collisions as a function of magnetic field detuning. The trend of $\beta_{\text{Li-D}}$, measured for collisions between interacting Li|1> atoms and Li|1>Cr|1> molecules (filled squares), is compared with the constant, non-resonant one, obtained by studying Li|2>-dimer collisions (empty squares). The inset shows the experimentally determined $\beta_{\text{Li-D}}$, normalized to its background value $\beta_{\text{Li-D}}^{\text{bg}} = 7 \times 10^{-10} \text{ cm}^3/\text{s}$, as a function of R^*/a (black symbols), together with the theoretically predicted trend of Ref. [56]. Vertical error bars of $\beta_{\text{Li-D}}$ combine the fit, statistical and systematic uncertainties to the decay data, and the estimated mean density $\langle n_{\text{Li}} \rangle_{\text{D}}$. Horizontal error bars account for the uncertainty in the magnetic field detuning from the FR pole.

spin state Li|2> right after the magneto-association ramp. In this case, where three, rather than two, distinguishable kinds of fermionic atoms were involved in the collisions, we observed a constant rate coefficient at all detunings; see the empty squares in Fig. 4.7. The obtained value, $\beta_{\text{Li|2>-D}} \sim 7 \times 10^{-10} \text{ cm}^3/\text{s}$, nicely matches the background one measured for Li|1>-D collisions, and both agree within a factor of 2 with the theoretical estimate Eq. (4.4). Notably, as shown in the inset of Fig. 4.7, the normalized experimental data $\beta_{\text{Li-D}}/\beta_{\text{Li-D}}^{\text{bg}}$ (black squares) are found to be remarkably reproduced by the predicted suppression function for Li-LiCr inelastic collisions given in Ref. [56] (solid line) as a function of R^*/a . I emphasize here that, in spite of the narrow nature of our FR, at the smallest detunings that we explored we observed a suppression of collisional losses of up to a factor of 70_{-35}^{+160} – a very promising value in light of future studies of resonantly interacting atom-dimer mixtures, and of the possible implementation of a final sympathetic cooling stage for LiCr Feshbach molecules.

4.7 Magnetic dipole moment of LiCr Feshbach dimers

In this Section, I present our direct measurement of μ_d , the magnetic dipole moment of the newly created LiCr Feshbach dimers, discussing also its dependence upon the magnetic field detuning δB . This measurement, based on a Stern-Gerlach (SG) scheme similar to that followed for DyK molecules [85], constituted the first clear experimental evidence of LiCr paramagnetic nature, and it further confirmed A. Simoni’s assignment of the molecular state inducing the FR (see again Sec. 3.2).

Our first goal was to observe a deviation of μ_d both from the atomic values of Li and Cr, which at bias fields ~ 1.4 kG are respectively $\mu_{\text{Li}} = 1 \mu_{\text{B}}$ and $\mu_{\text{Cr}} = 6 \mu_{\text{B}}$ (within a few per mille), as well as from the expected value for purely closed-channel molecules, $\mu_{\text{cc}} = 5 \mu_{\text{B}}$. To this end, we performed a SG-type experiment at a fixed, relatively small $\delta B = -4$ mG, where $R^*/a \sim 1$ and one expects $\mu_d \neq \mu_{\text{cc}}$. In particular, we prepared our molecular sample without any removal or transfer of the unpaired atoms, having care to switch off the bODT immediately after molecule formation. Without the optical trap, we let the particles expand under the combination of gravity and a magnetic field gradient b along the vertical direction, and we recorded the temporal evolution of the center-of-mass positions z_{com} of Li, Cr, and LiCr. For each component, the c.o.m. acceleration is given by $g + \mu_X b/m_X$, where g is the gravitational acceleration, μ_X is the magnetic dipole moment of species X , and m_X is the corresponding mass. The atomic trajectories provided us a straightforward way to precisely calibrate the B -field gradient.⁷ With b being known, μ_d was then obtained from a single-parameter fit to the LiCr trajectory; see the results in Fig. 4.8(a). The extracted value $\mu_d = 5.85(5) \mu_{\text{B}}$, well resolved from both the atomic counterparts, markedly differs also from the magnetic moment μ_{cc} of purely closed-channel molecules, pointing to a sizable admixture with the open-channel wave function, featuring $\mu_{\text{oc}} = 7 \mu_{\text{B}}$.

Our observation is better understood by expressing the Feshbach dimer wavefunction as a superposition of open- and closed-channel components [7, 111, 176]:

$$|\psi_d(R)\rangle = \sqrt{1-Z} \phi_{\text{oc}}(R) |\text{OC}\rangle + \sqrt{Z} \phi_{\text{cc}}(R) |\text{CC}\rangle, \quad (4.5)$$

with the unit-normalized radial wave functions $\{\phi_{\text{oc}}(R), \phi_{\text{cc}}(R)\}$ referring to the open- and closed-channel components with spin states $\{|\text{OC}\rangle, |\text{CC}\rangle\}$, respectively. As discussed in Sec. 1.6, the closed-channel fraction Z , bound to be $0 \leq Z \leq 1$, determines the character of the Feshbach molecule: from open-channel like for $Z \rightarrow 0$, to closed-channel like for $Z \rightarrow 1$. The Feshbach dimer has energy E_d and magnetic moment $\mu_d = \partial_B E_d$. These, if referenced to the scattering continuum, define the binding energy $E_b = E_{\text{oc}} - E_d$ and the differential magnetic moment $\delta\mu = \mu_{\text{oc}} - \mu_d$, which are linked to Z via the Hellmann-Feynman theorem [7, 178], see Eq. (1.31):

$$\mu_d(\delta B) = Z(\delta B) \mu_{\text{cc}} + (1 - Z(\delta B)) \mu_{\text{oc}}. \quad (4.6)$$

As discussed in Sec. 1.6, an analytic solution for $Z(\delta B)$ is available in the effective range expansion [106], see Eq. (1.30):

$$Z(\delta B) = 1 - \frac{1}{\sqrt{1 + \frac{4R^*}{a(\delta B) - a_{\text{bg}}}}}, \quad (4.7)$$

with $a(\delta B)$ the scattering length, a_{bg} its background value, and $R^* = \hbar^2/(2 m_{\text{red}} a_{\text{bg}} \Delta_B \delta\mu)$ [see Eq. (1.20)] the effective range parameter. Equations (4.6) and (4.7) thus provide the expected magnetic field dependence of μ_d , ranging for LiCr (near the investigated FR) from $\mu_{\text{cc}} = 5 \mu_{\text{B}}$ for $Z \rightarrow 1$ (i.e. $|\delta B| \rightarrow \infty$), to $\mu_{\text{oc}} = 7 \mu_{\text{B}}$ for $Z \rightarrow 0$ ($|\delta B| \rightarrow 0$).

By means of experimental protocols similar to those described above, we could experimentally reveal and characterize the B -field dependence of μ_d . In this case, after switching off the bODT, we let the particles expand for a *fixed* time of flight t_{tof} , and we recorded the position $z_{\text{com}}(t_{\text{tof}})$ of the LiCr cloud as a function of δB . In order to minimize temporal and spatial variations of the magnetic field experienced by the molecules, we employed a

⁷The complete analysis also took into account the vertically-oriented magnetic field anti-curvature generated by the BIAS coils, omitted from the discussion here for the sake of simplicity.

short $t_{\text{tof}} = 3.5$ ms, with a 200- μs -long RF cleaning pulse on Cr right before the imaging pulse. Knowledge of the initial *in situ* position of the atoms and the B -field landscape allowed us to directly extract $\mu_d(\delta B)$, which is shown in Fig. 4.8(b). A fit of Eq. (4.6) to the data, with $Z(\delta B)$ given by Eq. (4.7) and the location of the FR pole B_0 as the single free parameter, yields the solid black line in Fig. 4.8(b). We find good agreement with the experimental results, and ascribe the residual discrepancy to the B -field inhomogeneity experienced by the molecules during the time of flight expansion. These results highlight our high degree of control over the applied magnetic field and, most importantly, the paramagnetic nature of the LiCr closed-channel molecule. Moreover, the observed trend of μ_d , asymptotically approaching $\mu_{\text{cc}} = 5 \mu_B$, further confirms the FR assignment of the quantum collisional model for Li-Cr (see Sec. 3.2), and shows our ability to controllably populate the least bound vibrational level of the $X \ ^6\Sigma^+$ ground-state potential. In particular, this is extremely convenient for future STIRAP transfer [79] to the LiCr absolute ground state: A STIRAP scheme for LiCr only requires a change in the vibrational degrees of freedom, circumventing the need for an optically excited state having sizable overlap with both electronic ground-state (sextet and octet) multiplicities, in complete analogy with the case of $^6\text{Li}^{40}\text{K}$ dimers of Ref. [179]; see Sec. 4.10.3 for more details.

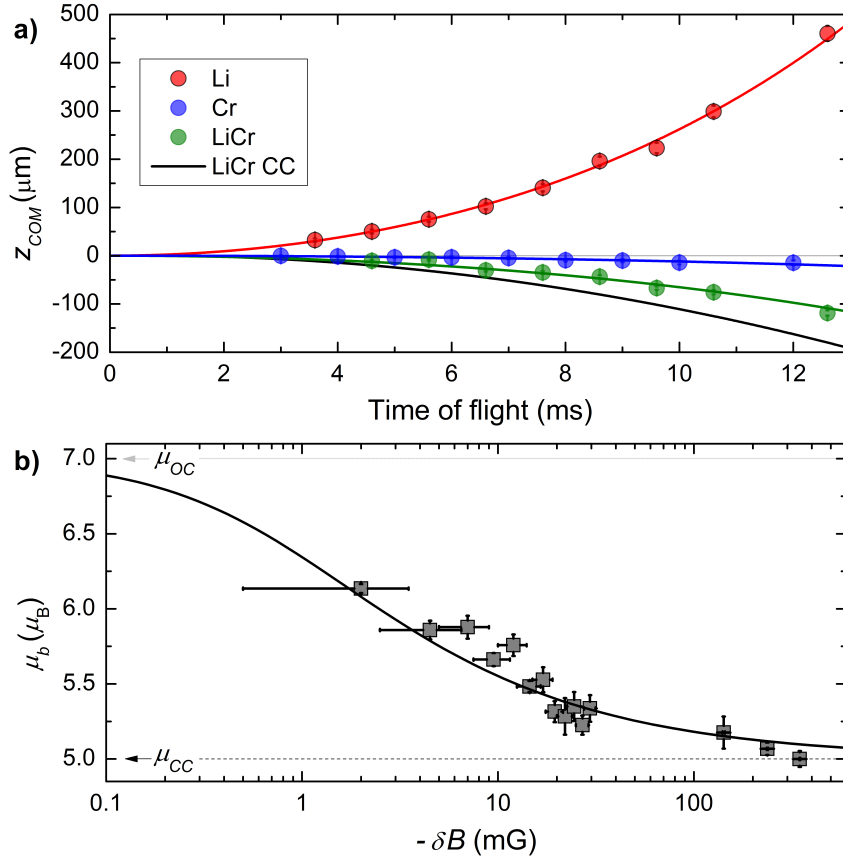


Figure 4.8 – Measurements of magnetic dipole moment. (a) Vertical center-of-mass trajectories for atoms and molecules in time of flight. The red, blue, and green circles show the evolution of the c.o.m. in the vertical direction as a function of the TOF for Li, Cr, and LiCr, respectively. The corresponding lines with matching color code show the fitted theory curves. The black line represents the expected trajectory for a purely closed-channel molecule ($Z = 1$). (b) Magnetic dipole moment μ_d of LiCr Feshbach molecules as a function of the absolute B field detuning from the FR pole. The black curve represents the theory prediction based on Eqs. (4.6) and (4.7) with only the resonance position B_0 as the fitting parameter. The dotted and dashed lines respectively mark the magnetic moments of the scattering atom pair μ_{oc} ($Z = 0$) and of the closed-channel molecule μ_{cc} ($Z = 1$).

4.8 New optical measurement of open-channel fraction and binding energy

As discussed in Sec. 1.6, the closed-channel fraction Z represents an essential feature of the Feshbach dimer. Besides determining the behavior of μ_d , experimentally characterized in the previous Sec. 4.7, Z also affects the collisional stability of Feshbach molecules, as well as the outcome of future STIRAP transfer schemes to deeply bound states: While the former is longest for $Z \rightarrow 0$, the latter is optimal for $Z \rightarrow 1$. An accurate measurement of $Z(\delta B)$ close to a narrow FR at high B field is technically challenging. Indeed, wiggle spectroscopy [180] has limited temporal resolution, RF spectroscopy [143, 171] requires high RF power, potentially perturbing the B -field stabilization, photo-association techniques [181] require an optically excited molecule level and laser light to address it, and, finally, magnetic moment spectroscopy (see Sec. 4.7 and Ref. [85]) suffers from field inhomogeneity and temporal constraints.

In our case, we managed to overcome these issues by developing a convenient and rather general optical method, which exploits absorption imaging of Feshbach dimers with laser light addressing transitions of the parent atomic species. Our method is based on the analysis of the systematic reduction of the molecule signal, recorded as a function of δB , a rather generic trend already reported for various systems; see, e.g., Ref. [175]. Such a seeming drop of the dimer population is illustrated for LiCr in Fig. 4.9(a), where I show the measured number N_{meas} normalized to the real one N_{real} as a function of δB , both for Li (red circles) and Cr (blue circles) imaging lights. For Li, we further compared a long (filled circles) with a short (open circles) pulse duration. One can notice how, despite quantitative differences, in all cases $N_{\text{meas}}/N_{\text{real}}$ monotonically decreases with increasing $|\delta B|$.

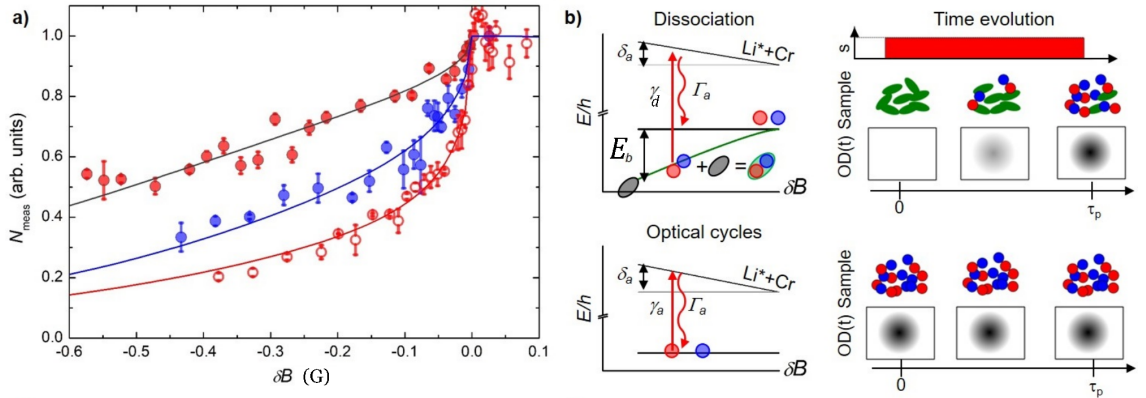


Figure 4.9 – (a) Counted molecule number N_{meas} , normalized to the real one N_{real} , derived from *in situ* absorption pictures taken on the Li (red circles) and Cr (blue circles) imaging transitions on pure molecular samples. I show a comparison between a longer (filled circles) and shorter (open circles) pulse time with the same laser intensity within 10%. The red filled circles are taken with $\tau_p = 40 \mu\text{s}$ and $I_0 = 0.24 \text{ mW/cm}^2$, the red open circles with $\tau_p = 11 \mu\text{s}$ and $I_0 = 0.2 \text{ mW/cm}^2$, and the blue circles with $\tau_p = 21 \mu\text{s}$ and $I_0 = 0.76 \text{ mW/cm}^2$. The solid lines show Alessio’s model prediction Eq. (4.12) with only a common field offset as the fitting parameter and Z given by Eq. (4.7). (b) Sketch illustrating Alessio’s model, explained in the main text. The top-left panel shows the dissociation mechanism at rate γ_d induced by the imaging laser resonant at $\delta B = 0$ with the lithium atomic transition of natural width Γ_a : a detuning of $\delta_d = \delta_a + E_b/h$ is acquired for finite $\delta B < 0$. The bottom-left panel shows the optical cycles Li atoms undergo after molecule dissociation at rate γ_a . The right panels show (from top to bottom) the pulse shape of duration τ_p , the time-dependent OD of the initial molecule sample, and, as a comparison, the constant OD of an atomic sample.

While this effect was previously interpreted in terms of an effective imaging cross section, in the present case the particle number sensitivity on the imaging parameters confutes such an interpretation, and I present here a different one, based on a simple theoretical model developed by my colleague Alessio Ciamei. The main idea, graphically sketched in Fig. 4.9(b), is that the absorption signal of dimers results from the optical density of the atoms, into which molecules are dissociated during the imaging pulse at a rate γ_d , given by the bare atomic scattering rate γ_a weighted by the dimer open-channel fraction $(1 - Z)$. Building on such an intuition, Alessio developed his model, described in more detail below, allowing us to establish a univocal link between $N_{\text{meas}}/N_{\text{real}}$ on one side, and $(1 - Z)$ and the binding energy (E_b) on the other. Hence, this simple theory can be employed to either predict $N_{\text{meas}}/N_{\text{real}}$ once Z and E_b are known [see the lines in Fig. 4.9(a) based on Eq. (4.7)], or vice versa to obtain those quantities from the experimentally recorded dimer signal [see Figs. 4.10(a) and 4.10(b)] without relying on any *a priori* knowledge. In the following, I describe Alessio's theoretical model and our experimental results in more detail.

The model holds under three main assumptions [see also the sketch in Fig. 4.9(b)]:

- (i) closed-channel molecules do not directly interact with the atomic imaging light;
- (ii) Feshbach dimers are dissociated by the imaging light at a rate given by Fermi's golden rule $\gamma_d = \gamma_a |\langle \psi_d | \text{OC} \rangle|^2 = \gamma_a (1 - Z)$, with γ_a denoting the atomic scattering rate;
- (iii) low-intensity atomic imaging is performed on a cycling transition with atomic scattering rate $\gamma_a(s_a, \Gamma_a, \delta_a)$ dependent on the saturation parameter $s_a \ll 1$, the natural width of the transition Γ_a , and detuning δ_a .

Assumptions (i) and (ii) imply that during the imaging pulse the dimer (column) density decreases as

$$n_d^{2\text{D}}(t) = n_{d,0}^{2\text{D}} e^{-\gamma_d t}, \quad (4.8a)$$

while the free-atom one grows as

$$n_a^{2\text{D}}(t) = n_{a,0}^{2\text{D}} \cdot (1 - e^{-\gamma_d t}). \quad (4.8b)$$

Since (iii) implies that the dissociation products decay back to the same open channel of the FR, and that the addressed atomic species undergoes cycling transitions until the end of the imaging pulse, from Eq. (4.8b) we derive the instantaneous optical density (OD)

$$\text{OD}(t) = \sigma_a \cdot n_{d,0}^{2\text{D}} \cdot (1 - e^{-\gamma_d t}), \quad (4.9)$$

where σ_a is the detuning-dependent, atomic absorption cross section. This is in contrast with the standard case of an atomic sample at the same (column) density, that would feature a constant optical density $\text{OD}_a = \sigma_a \cdot n_{a,0}^{2\text{D}}$ [see the sketch in Fig. 4.9(b)]. For $\delta B = 0$, the molecules are dissociated, the imaging light is resonant with cross section $\sigma_a = \sigma_{a,0}$, and the optical density is constant and equal to $\text{OD}_a = \text{OD}_{a,0}$.

Let us derive the observed optical density after an absorption imaging pulse of duration τ_p from the instantaneous time-dependent optical density $\text{OD}(t)$ above. The temporal variation of photon counts N_p on the camera during the probe pulse shining onto the Feshbach molecule sample follows the relation

$$\partial_t N_{p,d} = \eta_q \cdot I_0 \cdot e^{-\text{OD}(t)}, \quad (4.10)$$

where η_q is the overall quantum efficiency of the imaging system and I_0 is the laser intensity. At the end of the pulse, then, one has

$$N_{p,d}(\tau_p) = \eta_q I_0 e^{-\text{OD}_a} \cdot \int_0^{\tau_p} \exp(\text{OD}_a e^{-\gamma_d t}) dt, \quad (4.11a)$$

in contrast with the case of a pure atomic sample, for which

$$N_{p,a}(\tau_p) = \eta_q I_0 \tau_p e^{-\text{OD}_a}. \quad (4.11b)$$

In both cases, the reference image, with neither dimers nor atoms, yields $N_{p,0}(\tau_p) = \eta_q I_0 \tau_p$ counts. Using the definition of optical density $\text{OD} = -\ln(N_p/N_{p,0})$, taking as reference the atomic optical density at resonance $\text{OD}_{a,0}$, we derive the suppression factor

$$\frac{\overline{\text{OD}}(\tau_p)}{\text{OD}_{a,0}} = \frac{\gamma_a}{\gamma_{a,0}} \left[1 - \frac{1}{\text{OD}_a} \ln \left(\frac{1}{\tau_p} \int_0^{\tau_p} \exp(\text{OD}_a e^{-\gamma_d t}) dt \right) \right], \quad (4.12)$$

with

$$\gamma_{a,0} = \gamma(s_a, \Gamma_a, 0), \quad (4.13a)$$

$$\gamma_d = \gamma_a(s_a, \Gamma_a, \delta_a + E_b/h)(1 - Z), \quad (4.13b)$$

where the B -field dependence of Z , δ_a , and E_b is implicit. In our case we have $\delta_a(\delta B) = \mu_B \delta B$ for the Zeeman shifts of the imaging transitions of both Li and Cr. In the limit of low optical density, $\text{OD}_{a,0} \ll 1$, Eq. (4.12) simplifies to

$$\frac{\overline{\text{OD}}(\tau_p)}{\text{OD}_{a,0}} \simeq \frac{1}{1 + (2\delta_a/\Gamma_a)^2} \left[1 - \frac{1 - e^{-\gamma_d \tau_p}}{\gamma_d \tau_p} \right]. \quad (4.14)$$

As the right-hand side of Eq. (4.12) [or the simplified Eq. (4.14)] is independent of $\text{OD}_{a,0}$, it coincides with the relative suppression of the detected number of Feshbach molecules, $N_{\text{meas}}/N_{\text{real}} = \overline{\text{OD}}/\text{OD}_{a,0}$.

As anticipated, Alessio's model Eq. (4.12) allows us to retrieve both the open-channel fraction $1 - Z(\delta B)$ and the binding energy $E_b(\delta B)$ of the Feshbach dimers (at all detunings δB) from the ratio $N_{\text{meas}}/N_{\text{real}}$ measured through absorption images, without any *a priori* knowledge of their functional forms. As long as the binding energy of the Feshbach molecule is negligible with respect to the linewidth, $E_b/h \ll \Gamma_a$, Eq. (4.12) only has $Z(\delta B)$ as the unknown quantity and can easily be inverted, $N_i(\delta B_i) \rightarrow Z_i(\delta B_i)$ (i is an index labeling each data point). If this condition does not hold, we are left, at each experimentally probed δB_i value, with two unknown quantities Z_i and $E_{b,i}$ that cannot be uniquely inferred from N_i . To circumvent this limitation, and without loss of generality, we make use of the properties of the Feshbach state summarized by the Hellman-Feynman theorem [see Eq. (4.6)] and the limiting behavior for $\delta B \rightarrow 0$ of the magnetic moment and binding energy, $\delta\mu \rightarrow 0$ and $E_b \rightarrow 0$, respectively. Thus, instead of extracting from each measurement point $N_i(\delta B_i) \rightarrow Z_i(\delta B_i)$, we iteratively run over consecutive measurement points starting from the largest positive detuning $\max(\delta B_i)$ and moving down to $\min(\delta B_i)$. The algorithm estimates the binding energy at δB_i as $E_{b,i} = E_{b,i-1} + Z_{i-1} \delta\mu(\delta B_{i-1} - \delta B_i)$ and extracts a new open-channel fraction $\{N_i, E_{b,i}\} \rightarrow Z_i$. The algorithm is initialized with ($Z_{i_0} = 0$, $E_{b,i_0} = 0$) and forces ($Z_i = 0$, $E_{b,i} = 0$) for all $\delta B_i > 0$.

In Figs. 4.10(a) and 4.10(b) I show the results of our analysis, plotting the experimentally determined open-channel fraction and binding energy as a function of R^*/a . Notably, extraction of $1 - Z$ and E_b from the three datasets of Fig. 4.9(a) yields consistent results over

a wide range of detunings, from the resonant regime to the background limit, despite the different pulse parameters and atomic species employed for the imaging. Both observables are found to vary over a few orders of magnitude, in excellent agreement with the theory predictions based on Eqs. (4.7) and (4.15), respectively (solid black lines). In particular, one can notice how the nonzero open-channel fraction is reflected in the dimer binding energy that deviates, near the resonance pole for $R^*/a \rightarrow 0$, from that of the bare closed-channel molecule $2\mu_d \delta B$; see the dashed line in Fig. 4.10(b). It is important to emphasize that this probing method works remarkably well even at very small detunings from the FR pole. Finally, similarly to Fig. 4.8(b), Figs. 4.10(a) and 4.10(b) data demonstrate our experimental capability to access the resonant regime with high accuracy, despite the narrow FR at our disposal, a key point for future many-body investigation of Li-Cr mixtures; see, e.g., Chapter 5.

Given the univocal link given by Eq. (4.12) between the measured molecule signal and $(1 - Z)$ and E_b , Alessio's model can equally be exploited to predict N_{meas} assuming $Z(\delta B)$ and $E_b(\delta B)$ to be known. In particular, the solid lines in Fig. 4.9(a) were obtained by assuming Z to be given by Eq. (4.7), and the corresponding binding energy $E_b(\delta B) = \hbar^2 \kappa_*^2 / (2m_{\text{red}})$, with κ_* given by [see Eq. (1.26)]:

$$\kappa_*(\delta B) = \frac{\sqrt{1 + 4R^*/[a(\delta B) - a_{\text{bg}}]} - 1}{2R^*}, \quad (4.15)$$

where now the B -field dependence is made explicit. Note that Eq. (4.15) can also be obtained by integrating Eq. (4.6). In this case, all parameters appearing in the model were known, and we only allowed for a precision fit of the resonance location B_0 common to all datasets in Fig. 4.9(a). The best-fit results of the model (see solid lines) reproduce our experimental observation remarkably well, regardless of the imaged species and employed pulse parameters. From this viewpoint, Alessio's model can be exploited for molecule number calibration with no need for dissociation prior to the imaging pulse, which may introduce systematic heating and excitation of the clouds [182, 183]. In particular, the saturation parameter can be conveniently derived from the reference imaging pulse after calibration of the camera.

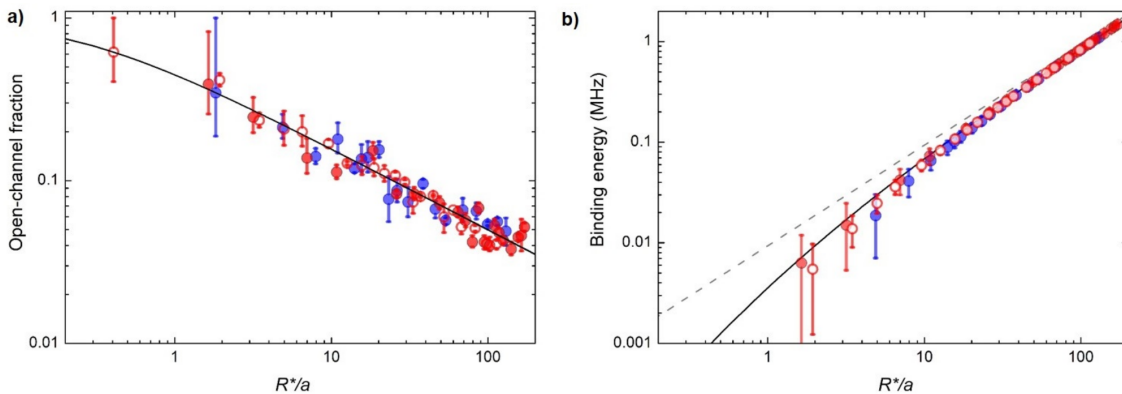


Figure 4.10 – Optically determined open-channel fraction as a function of detuning from the resonance. (a) Open-channel fraction and (b) binding energy as a function of R^*/a , extracted with Alessio's model Eq. (4.12) from the three datasets in Fig. 4.9(a) (with the same symbol choice), together with the theory predictions given by Eqs. (4.7) and (4.15), respectively (solid black lines).

4.9 Realization of pure, long-lived molecular samples

From the studies presented in Secs. 4.5 and 4.6, we learnt that 1560 nm is the most suited wavelength at our disposal to trap LiCr Feshbach molecules, and that the presence of leftover unpaired atoms generally limits the molecule lifetime, except in the close proximity of the FR pole. Thus, to obtain longer dimer lifetimes under robust working conditions, and to perform more precise measurements and characterization of LiCr molecules,⁸ we carefully optimized a procedure to purify the molecule sample right after magneto-association.

In particular, the (usually large) remaining $\text{Li}|1\rangle$ component is quickly removed by driving a 0.5-ms-long π -pulse on the $\text{Li}|1\rangle \longleftrightarrow \text{Li}|2\rangle$ RF transition, which is followed by a spin-selective optical blast of the $\text{Li}|2\rangle$ state. The procedure is repeated two times consecutively to ensure a negligible remaining population of unpaired $\text{Li}|1\rangle$ atoms. The duration of the RF pulse is optimized to be as short as possible without introducing any detectable perturbation to the magnetic field stability discussed in Sec. 6.1. Conversely, owing to a technical limitation of our Cr high-field imaging setup (namely, the absence of $\text{Cr}|2\rangle$ resonant light, see Sec. 6.2), we cannot exploit an analogous scheme to remove unpaired Cr atoms from the mixture. Instead, we find it convenient to rapidly lower the power in the IR optical trap right after molecule formation, such that the resulting trap depth is still sufficient to confine dimers, but too shallow to hold Cr atoms. In fact, at 1070 nm (1560 nm) the Cr polarizability is about a factor 4.0 (3.4) lower than for LiCr. As a result, $\text{Cr}|1\rangle$ is gradually spilled out from the trapping region, on a typical timescale of $10 \div 20$ ms.

To obtain the longest molecule lifetime, substantially increased at all detunings compared to what reported so far in this Chapter, we directly created molecules in the far-off resonant trap (FORT) at 1560 nm, whose wavelength is found to cause negligible light-induced losses (see Sec. 4.5). We first transferred the atomic mixture from the bODT into the FORT following a 100-ms-long linear ramp, throughout which a constant trap depth for the Cr atoms was maintained. We then performed the magneto-association ramp, at the end of which we purified the molecule sample from the atomic components with the methods described above. This overall procedure reduced the initial molecule number by about a factor of 2, but it allowed for a dramatic gain in lifetime even in the off-resonant regime. This is shown in Fig. 4.11, where the molecule number is plotted as a function of the hold time at a final, large detuning $\delta B = -100$ mG. After an initial loss – ascribable to excitation of collective modes in the LiCr cloud during the magneto-association and atom purification stages (see the inset) – we observed a clean exponential decay of the molecule number, characterized by a time constant of 0.24(1) s. This lifetime, much longer than those measured in our system without purification nor FORT trap (limited to a few tens of milliseconds), exceeds by more than one order of magnitude that reported for LiK molecules [174] at similar peak densities, of a few 10^{11} cm^{-3} . The slow exponential decay of LiCr shown in Fig. 4.11 is consistent with residual evaporation dynamics within the relatively low-density molecule cloud, and it appears incompatible with intraspecies LiCr collisional losses, which will be the subject of future studies. The present measurement and analogous ones carried out without the removal of Cr atoms yield in all cases upper-bound estimates for the background values of the recombination rate coefficients, $\beta_{\text{bg}}^{\text{D-D}}$ and $\beta_{\text{bg}}^{\text{Cr-D}}$, of about 1×10^{-10} cm^3/s . This, together with the Pauli suppression of these inelastic processes [56] – expected to be even stronger than that unveiled in Li-D collisions, shown in Fig. 4.7 – is very promising for future implementation of collisional cooling of LiCr Feshbach dimers.

⁸Purity of the molecular sample is a fundamental requirement for the measurements described in Secs. 4.5 and 4.8.

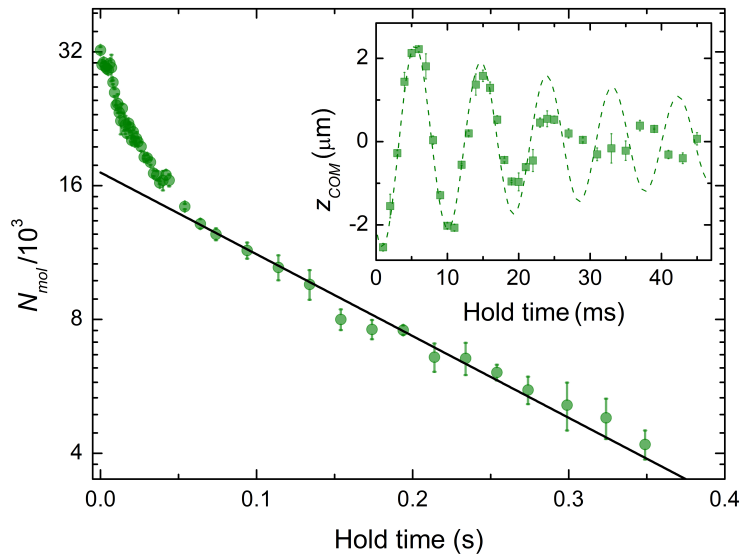


Figure 4.11 – Long-lived pure LiCr samples in the 1560 nm trap at $\delta B = -100$ mG. The main panel shows the molecule number (on a log scale) as a function of the hold time, together with an exponential fit of the long-time decay yielding a time constant of 0.24(1) s. For hold times shorter than 50 ms, we observe a faster loss dynamics, which we ascribe to the initial excitation of collective modes of the LiCr sample (see the inset) induced by the magneto-association and purification stages.

4.9.1 Probing the purity of molecular samples: experimental protocols

To conclude the experimental part of this Chapter, I emphasize here how the knowledge acquired from the studies in Secs. 4.5 and 4.8 can be employed to devise clear experimental protocols to check the purity of the molecular sample. A first, robust method exploits once more the strong photo-excitation rate induced by the 532-nm light, that causes fast molecule losses happening on a few-ms timescale, even for relatively low powers. After purifying the sample, we intentionally switch on the green light in our bODT at a small but nonzero power level, such that the overall trap depth is only slightly perturbed, but a significant one-body loss rate Γ_{532} is introduced (solely) for LiCr dimers; see sketch in Fig. 4.12(a). Following a hold time $t_{\text{hold}} \gtrsim 5/\Gamma_{532}$, i.e. long enough to ensure photo-excitation losses of nearly all molecules, we quickly ramp the magnetic field above the FR pole, and then take an absorption image on each of the two atomic lines. Any detected signal represents a leftover atomic population of the corresponding species, while the simultaneous absence of signal on both images testifies the purity of the molecular sample.

The second method leverages instead on a direct consequence of the (ii) assumption in the model of Sec. 4.8 – i.e., that the first absorbed optical photon effectively dissociates the Feshbach dimer – and on the corresponding momentum and energy transfer to the outgoing atom pair. By generically referring to the interchangeable role of Li and Cr as species A and B, suppose that we wish to check for the presence of possible residual B atoms after the purification procedure. In this case, as sketched in Figs. 4.12(b) and 4.12(c), we deliberately apply a strong, resonant light pulse on the A atomic transition: This breaks the (fragile) dimers apart, and completely expels any A particle from the optical trap, as they scatter a large number of photons. Our interest here is in what happens to the B component. We apply this procedure at intermediate (negative) detunings on the molecular side of the FR: On the one hand, this ensures a still sizeable absorption of atomic light from Feshbach dimers, see Sec. 4.8. On the other hand, it minimizes the possible cross-talk effects of the optical removal of one species onto the other, via elastic or inelastic collisions. In other words, the idea is that any leftover unpaired B atom should be essentially unaffected by the optical blast applied on the A transition, whereas Feshbach dimers should experience a sizable effect. Indeed, without aiming at a completely rigorous treatment, if a diatomic molecule is dissociated due to absorption of a photon with

wavenumber k_L , followed by subsequent spontaneous emission, the average momentum acquired by each outgoing atom is on the order of $\sim \hbar k_L$. Accordingly, if species A is chromium, Li atoms resulting from molecule photo-dissociation acquire a kinetic energy on the order of $(\hbar k_{425\text{ nm}})^2 / (2m_{\text{Li}}) \sim 9 \mu\text{K}$, far exceeding our typical trap depths. When the roles are reversed, i.e. if $A = \text{Li}$, the average kinetic energy transferred to Cr atoms is instead about $(\hbar k_{671\text{ nm}})^2 / (2M_{\text{Cr}}) \sim 400 \text{ nK}$: this value does not exceed the trap depth, but it is nearly twice our typical dimer temperature. Similarly to the previous case, after the optical removal of species A, we hold the sample for $t_{\text{hold}} \sim 10 \text{ ms}$, then we quickly ramp the magnetic field above the FR pole, and take an absorption image on each of the two atomic transitions, following time-of-flight expansion. In this case, if the optical

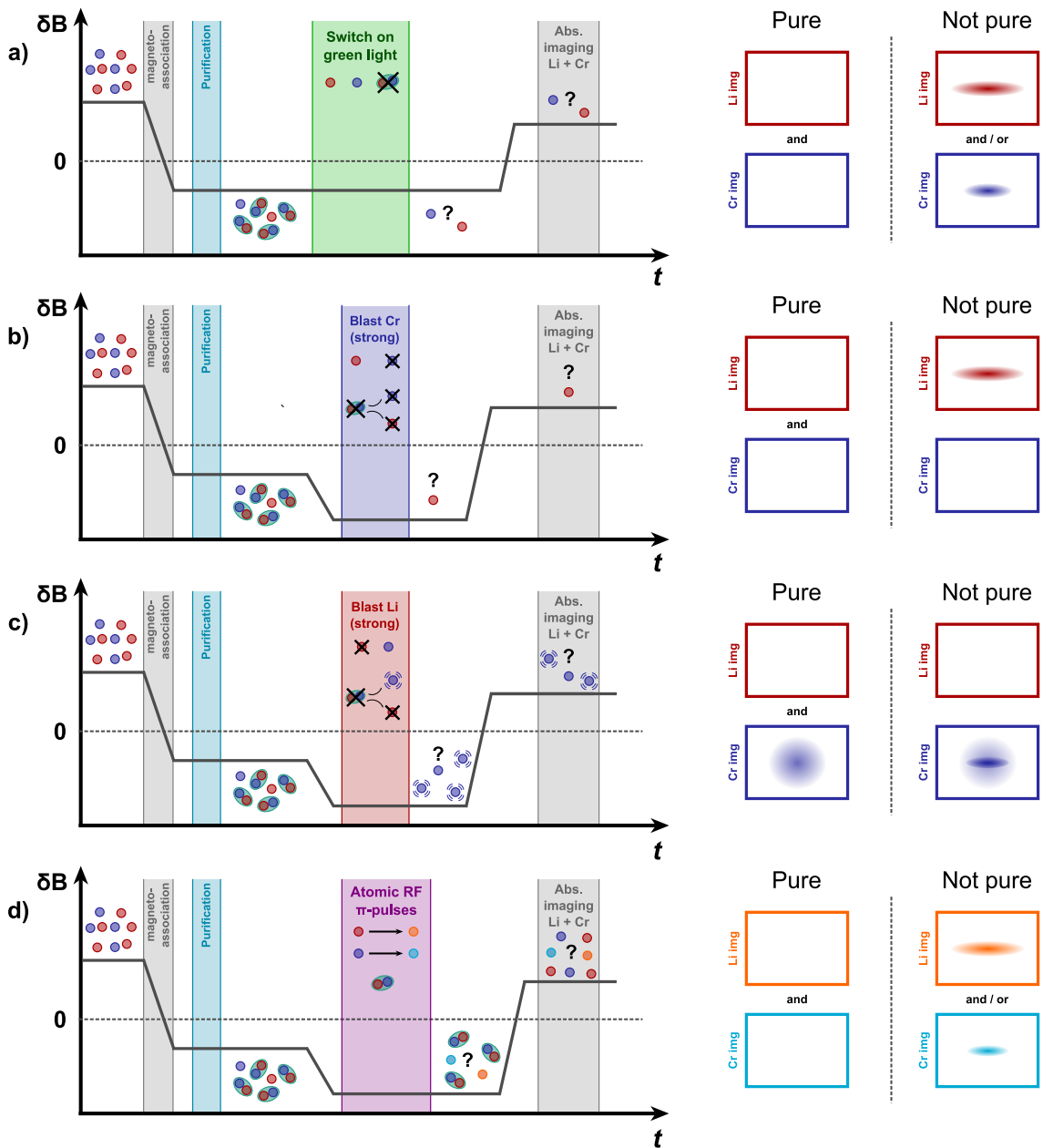


Figure 4.12 – Sketch of the experimental protocols that I developed to probe the purity of our molecular samples, see text for details. For each protocol, the right panels show qualitative examples of the typical expected signals.

removal is working properly, one always expects an empty image for species A. At the same time, when $B = \text{Li}$, owing to the large momentum transfer, all atoms that were previously associated into molecules are lost from the trap. Therefore, in this case, purity of the molecular sample against unpaired Li atoms is testified by an empty Li image; see right panels in Fig. 4.12(b). On the other hand, when $B = \text{Cr}$, the interpretation of this check is more subtle, as the momentum transfer only results in heating of the previously-associated Cr atoms. We thus compare long time-of-flight images acquired with and without the application of the optical removal on Li. Although in this case less striking, the presence of a “cold” fraction of Cr atoms (i.e. not affected by the Li blast) points to the presence of leftover unpaired Cr within the molecular sample, see Fig. 4.12(c).

Lastly, our third method relies on driving RF transitions that only address unpaired atoms, looking then at the transferred fraction. Indeed, since the dimer binding energy grows as $\sim 2.8 \text{ kHz/mG}$, and since we can drive RF transitions with π -pulse times $\tau_p \sim 0.2 \div 1 \text{ ms}$ (corresponding to Fourier-limited spectral width on the order of a few kHz) for both Li and Cr atoms, a detuning of a few tens of mG suffices to shift the molecular spectrum completely out of resonance with respect to the bare atomic transitions. Therefore, application of a RF π -pulse, resonant with the bare atomic frequency, at intermediate (negative) detunings, where also interaction effects are negligible, should transfer all and only atoms that are not associated into Feshbach molecules. After that, one ramps the magnetic field above B_0 and takes a spin-selective absorption image of the arrival atomic state(s). Once again, the absence of signal indicates the purity of the molecular sample, see Fig. 4.12(d).

4.10 Quantum chemical model of LiCr: Summary of LiCr properties from *ab initio* calculations

The ultracold samples of ${}^6\text{Li}{}^{53}\text{Cr}$ Feshbach dimers, thoroughly characterized in the previous sections, represent an excellent starting point for the production of a high phase-space density gas of deeply bound, paramagnetic polar molecules. Yet, LiCr is an almost unexplored species, for which spectroscopic data are completely lacking thus far, except for pioneering electron spin resonance data on thermal samples [93]. Its theoretical study, through advanced quantum chemical calculations, is thus crucial for two reasons: first, to gain information about the ground and electronically excited state properties of the LiCr molecule; second, to identify suitable pathways to coherently transfer LiCr Feshbach dimers to the absolute ground state [176]. In the following, I report on the main results of a quantum chemical model for LiCr, developed by our theory collaborator Prof. M. Tomza (University of Warsaw) and his group, as they are presented in our Ref. [94]. In short, leaving all technical details to Sec. VI-A of our Ref. [94], they employed state-of-the-art *ab initio* quantum chemical methods to build a complete theoretical model for LiCr. By extending (for the first time) the computational strategies already applied to alkali-metal or alkaline-earth-metal dimers to ultracold molecules containing transition-metal atoms, they obtained quantitatively accurate information on both ground and excited electronic states, transition moments, and resulting rovibrational structure and spectra, as summarized below.

4.10.1 Ground state properties

Through their model, M. Tomza and colleagues predicted the well depths D_e of the ground $X\ ^6\Sigma^+$ and first-excited $a\ ^8\Sigma^+$ states to be 8769(140) and 553(11) cm^{-1} , at equilibrium distances R_e of 4.87(1) a_0 and 6.50(2) a_0 , respectively; see the *ab initio* potential curves shown in Fig. 4.1(a). As shown in Fig. 4.13, a large permanent electric dipole moment of 3.3(2) D is expected for ${}^6\text{Li}{}^{53}\text{Cr}$ in the rovibrational ground state ($v = 0$), with even slightly larger values for excited vibrational levels of $X\ ^6\Sigma^+$, up to 3.4(2) D for $v = 14$. Additionally, it should be remarked how sizable electric dipole moment values, exceeding 1 D, are already expected for comparably high vibrational states ($v \lesssim 37$) of the $X\ ^6\Sigma^+$ potential; see Fig. 4.13. At the same time, the high-spin $a\ ^8\Sigma^+$ state also exhibits a significant permanent electric dipole moment of 0.67(3) D in its $v = 0$ level (see Fig. 4.13), a value exceeding the largest one found for spin-triplet alkali molecules [184].

For ${}^6\text{Li}{}^{53}\text{Cr}$, the ground electronic state supports 46(1) vibrational levels and the dissociation energy of the $v = 0$, $j = 0$ level is $D_0 = 8599(140) \text{ cm}^{-1}$. The high-spin state

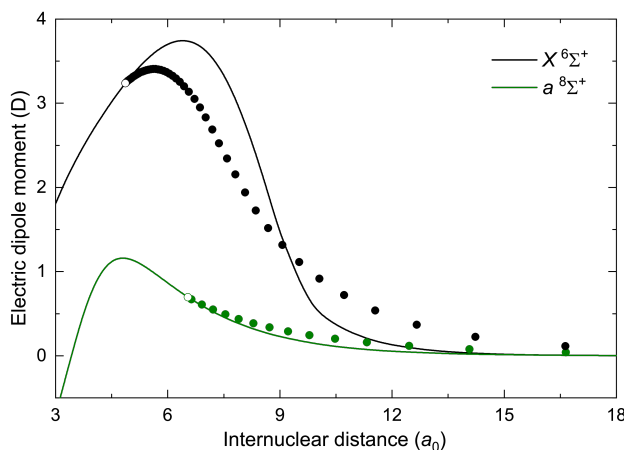


Figure 4.13 – Permanent electric dipole moments of the LiCr molecule in the $X\ ^6\Sigma^+$ and $a\ ^8\Sigma^+$ electronic states, as calculated by the group of M. Tomza. The solid lines present them as a function of the internuclear distance. The open circles mark their values at equilibrium distances, and the filled circles present vibrationally averaged moments d_v calculated for all vibrational levels v supported by the considered electronic states placed at the corresponding vibrationally averaged internuclear distances R_v (last two points for both states are beyond the plot range).

supports exactly 16 vibrational levels with $D_0 = 512(11) \text{ cm}^{-1}$. The rotational constants B_0 for $v = 0$ levels of the $X \ ^6\Sigma^+$ and $a \ ^8\Sigma^+$ states are 14.02(4) and 7.67(3) GHz. The bound vibrational levels exist up to $j_{\text{max}} = 146(2)$ for $X \ ^6\Sigma^+$ and $j_{\text{max}} = 46(1)$ for $a \ ^8\Sigma^+$. Precise knowledge of the number of vibrational states allows, via mass scaling, to infer the scattering properties of all Li-Cr isotopic combinations from the accurate experimental data obtained for $^6\text{Li}^{53}\text{Cr}$ (see Chapter 3 and Refs. [139, 169]).

4.10.2 Excited electronic states

As anticipated, coherent two-photon optical transfer of LiCr Feshbach dimers to the rovibrational ground state requires detailed knowledge of the intermediate, electronically excited levels of the associated transition dipole moments, and of the resulting molecular spectra – completely lacking experimental investigation so far. In the following, I summarize the predictions of the model of M. Tomza and colleagues concerning the properties of excited electronic states of LiCr, which are fundamental to identify suitable transitions for the efficient conversion of Feshbach dimers into tightly bound states, and more generally for the optical manipulation of LiCr.

Figure 4.14 shows the spectrum in Hund’s case (a) representation of all molecular excited electronic states of LiCr up to the $\text{Cr}(^7S) + \text{Li}(^2P)$ asymptote. States of Σ , Π , and Δ spatial symmetries with total electronic spin $S = 3/2, 5/2, 7/2$ exist. The higher-lying energy asymptote, $\text{Cr}(^7P) + \text{Li}(^2S)$, is above $20\,000 \text{ cm}^{-1}$, and it will not be discussed here. Two families of excited electronic states can be seen in Fig. 4.14: a first set dissociating into metastable, excited-state Cr (5S or 5D) and ground-state Li (2S), and another set that dissociates into ground-state Cr (7S) and excited-state Li (2P). The former ones are relatively shallow, especially those associated with Cr in the 5D state with the closed $4s^2$ shell screening interactions with the open $3d^4$ shell. The states belonging to the second family, and connected to the $\text{Cr}(^7S) + \text{Li}(^2P)$ asymptote, are deeper. Despite the large number of states, an avoided crossing is visible only between those with $^6\Pi$ symmetry.

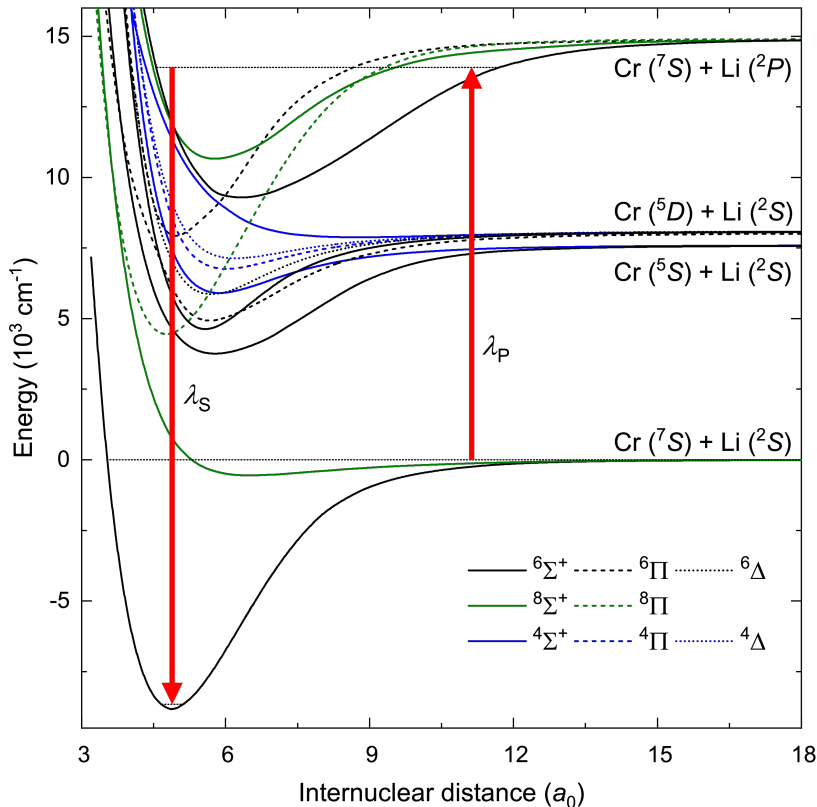


Figure 4.14 – Potential energy curves of the LiCr molecule in the ground and excited electronic states [in Hund’s case (a) representation], as calculated by the group of M. Tomza. The arrows show the proposed pump and Stokes STIRAP transitions at $\lambda_P \approx 720 \text{ nm}$ and $\lambda_S \approx 445 \text{ nm}$, respectively.

The spin-orbit interaction can couple excited electronic states of different spin and spatial symmetries. Its largest strength is expected for states dissociating into $\text{Cr}(^5D) + \text{Li}(^2S)$, which is asymptotically split by hundreds of cm^{-1} . Coupling of crossing states leads to avoided crossings and to enhanced mixing of different spin components. The spin-orbit coupling between electronic states dissociating into $\text{Cr}(^7S) + \text{Li}(^2P)$ should be smaller because of its negligible asymptotic value, although it might be enhanced at small internuclear distances by the presence of Cr. Although this will be discussed in more detail in Sec. 4.10.3, I remark here how the energy landscape of LiCr, shown in Fig. 4.14, is significantly richer than the more familiar one of bialkali systems, and it originates from the involvement of d -shell electrons of Cr. While this results in a more complex scenario, the existence of metastable excited states such as $^4\Delta$ – with large angular momenta and a potentially long lifetime – opens the way for applications of LiCr, primarily in the context of precision measurements [185–187], unattainable with alkali-metal dimers.

4.10.3 Prospects for STIRAP

Having provided an overview of both ground and electronically excited states of LiCr in the previous sections, I now move to discuss possible pathways for the efficient optical transfer of our Feshbach dimers towards deeply bound levels via stimulated Raman adiabatic passage (STIRAP) [79]. This method was successfully employed for a large number of alkali-metal diatomic molecules, and it involves two laser pulses that transfer coherently a molecular population between the initial and final states through an intermediate electronically excited state in a Λ configuration, while never populating it. Accurate knowledge of the energies and dipole moments of the most favorable transitions is needed to execute STIRAP successfully. While such properties can be obtained experimentally through tedious and time-consuming spectroscopic measurements, identification of suitable STIRAP pathways can be highly accelerated when guided by state-of-the-art molecular calculations.

Efficient STIRAP transfer of Feshbach dimers to the absolute ground state necessarily requires pinpointing an intermediate, electronically excited vibrational state that exhibits a significant overlap with both the initial (weakly bound, long-ranged) and the final (deeply bound, short-ranged) levels. In their theoretical search, M. Tomza and colleagues focused on STIRAP paths involving sextet electronic states only. Restricting the survey to this subclass is motivated by the fact that our Feshbach dimers have pure sextet character (see Sec. 4.7), as that of the LiCr rovibrational ground state. This greatly simplified the task, and the corresponding STIRAP scheme is conceptually equivalent to the singlet-to-singlet

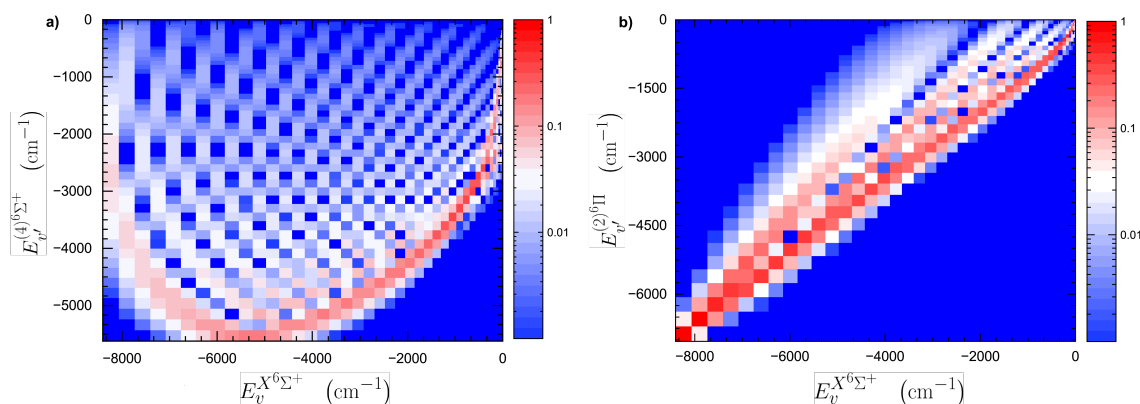


Figure 4.15 – Franck-Condon factors $|\langle v|v'\rangle|^2$ between vibrational levels of the LiCr molecule in the $X\ ^6\Sigma^+$ ground electronic state v and $(4)\ ^6\Sigma^+$ and $(2)\ ^6\Pi$ excited electronic states v' as a function of their energies $E_{v,v'}$: (a) $X\ ^6\Sigma^+ \rightarrow (4)\ ^6\Sigma^+$ and (b) $X\ ^6\Sigma^+ \rightarrow (2)\ ^6\Pi$.

optical transfer of alkali dimers, recently successfully employed to produce ground-state ${}^6\text{Li}{}^{40}\text{K}$ molecules [179].

The $(4) {}^6\Sigma^+$ and $(2) {}^6\Pi$ electronic states dissociating into $\text{Cr}({}^7S) + \text{Li}({}^2P)$ are the most promising ones for providing suitable intermediate levels because they are relatively well separated from other states and should be accessible at convenient optical wavelengths by strong transition dipole moments borrowed from the strong atomic transition ${}^2S \rightarrow {}^2P$ in Li [169]. According to the calculations of M. Tomza’s group [94], they support 54(5) and 48(4) vibrational levels, respectively, while their dissociation energies are around 5700 and 6800 cm^{-1} . Franck-Condon factors (FCFs), $|\langle v|v'\rangle|^2$, between vibrational levels supported by the ground (v) and excited (v') electronic states give the initial insight into possible optical transitions. They are presented in Fig. 4.15 for the relevant sextet states. The overview of the FCFs suggests the $X {}^6\Sigma^+ \rightarrow (4) {}^6\Sigma^+$ transitions [see Fig. 4.15(a)] as the most promising ones for the STIRAP implementation. Similar to alkali-metal dimers, the characteristic bent shape of the largest FCFs indeed reveals the existence of intermediate levels of the excited $(4) {}^6\Sigma^+$ state having noticeable overlap with both weakly and deeply bound levels of the ground $X {}^6\Sigma^+$ state. In contrast, the FCFs for the $X {}^6\Sigma^+ \rightarrow (2) {}^6\Pi$ transitions [see Fig. 4.15(b)] are visibly diagonal, which is not a preferable pattern for an efficient STIRAP transfer.

Figure 4.16 presents the FCFs for transitions from the least bound (denoted here as $v = -1$) and ground ($v = 0$) levels of the $X {}^6\Sigma^+$ electronic ground state to intermediate levels v' supported by the $(4) {}^6\Sigma^+$ excited electronic state. The largest FCFs for the “pump” transition $v = -1 \rightarrow v'$ (red symbols) are expected to connect to the most weakly bound excited-state levels just below the $\text{Cr}({}^7S) + \text{Li}({}^2P)$ atomic threshold, but values above 10^{-4} are predicted up to binding energies $E_{v'}$ of almost 3000 cm^{-1} . These FCFs also give the shape of a photoassociation spectrum. The largest FCFs for the “Stokes” transition $v' \rightarrow v = 0$ (blue symbols) are found to connect to levels in the middle of the interaction potential well, with values above 10^{-2} for binding energies between 1400 and 4400 cm^{-1} . Strong Stokes transitions result from the alignment of the equilibrium distance of the $X {}^6\Sigma^+$ electronic ground state and the inner classical turning point of the $(4) {}^6\Sigma^+$ excited electronic state (see Fig. 4.14). The combination of the pump and Stokes FCFs governs the STIRAP. The largest two-photon FCF, $|\langle -1|v'\rangle \langle v'|0\rangle|$, of 6×10^{-3} , is found for the $v' = 20$ intermediate level with a binding energy around 2400 cm^{-1} . Yet, FCFs exceeding 10^{-3} are expected for most vibrational levels with binding energies up to 3100 cm^{-1} . Thus, to avoid a large power imbalance of the pump and Stokes laser fields, intermediate v' levels with

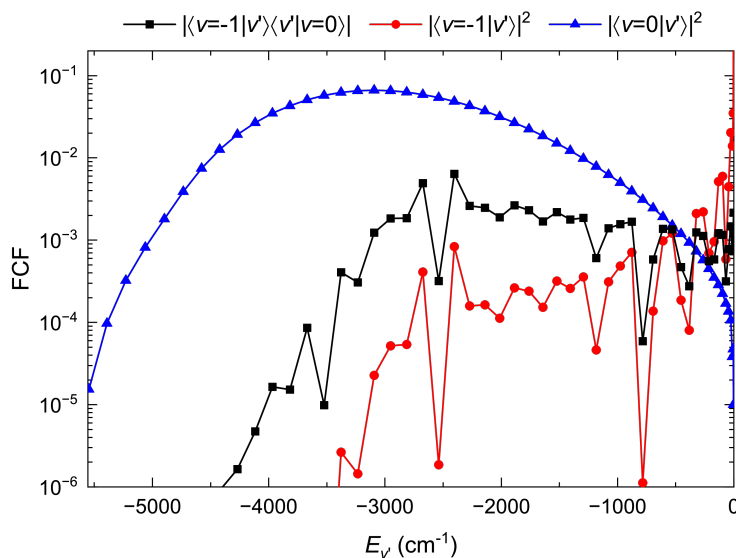


Figure 4.16 – Franck-Condon factors $|\langle v|v'\rangle|^2$ between the initial weakly bound $v = -1$ and final ground $v = 0$ vibrational levels of the $X {}^6\Sigma^+$ ground electronic state and the intermediate vibrational levels v' with energies $E_{v'}$ of the $(4) {}^6\Sigma^+$ excited electronic state and their combination $\sqrt{|\langle -1|v'\rangle|^2 |\langle 0|v'\rangle|^2} = |\langle -1|v'\rangle \langle v'|0\rangle|$ for two-photon transition between the $v = -1$ and $v = 0$ levels.

smaller binding energies around 1000 cm^{-1} can be addressed with convenient wavelengths of $\lambda_P \approx 720\text{ nm}$ and $\lambda_S \approx 445\text{ nm}$, respectively; see Fig. 4.14.

The predicted FCFs for the $X\ ^6\Sigma^+ \rightarrow (4)\ ^6\Sigma^+$ transitions are similar to, or even more favorable than, those found for alkali-metal diatomic molecules, where a STIRAP transfer efficiency as large as 90% was achieved. The theory predictions are robust against the uncertainty of calculated excited electronic states [169], and favorable conditions are persistent, assuming $10 \div 20\%$ errors for the well depth and $0.2 \div 0.5\ a_0$ errors for the equilibrium distance. Including the R dependence of the transition dipole moments also does not affect the presented findings [169]. Also, spin-orbit coupling – neglected in Tomza’s group calculations and that could perturb some levels accidentally close to other ones of different symmetry – is expected, overall, to negligibly affect the theoretical results.

The detailed analysis of the $X\ ^6\Sigma^+ \rightarrow (2)\ ^6\Pi$ transitions, see Fig. 4.15(b), confirms that they are less suited for STIRAP, as they exhibit two-photon FCFs smaller by several orders of magnitude than those for $X\ ^6\Sigma^+ \rightarrow (4)\ ^6\Sigma^+$ transitions [169]. The pump FCFs are smaller because the $(2)\ ^6\Pi$ potential is shallower than the $(4)\ ^6\Sigma^+$ one at intermediate and large distances (see Fig. 4.14). The FCFs noticeably exhibit a diagonal structure that results from the accidental alignment of the equilibrium distances of the $X\ ^6\Sigma^+$ and $(2)\ ^6\Pi$ states. This peculiar feature, inconvenient for STIRAP, may instead allow for direct imaging, and possibly even laser cooling, of ground-state LiCr molecules. While the exact values of diagonal FCFs are very sensitive to the accuracy of underlying electronic states, our collaborators’ model yields FCFs robustly above 0.5 [169], sufficiently large to enable direct optical imaging of ground-state LiCr, e.g., in optical tweezers. Additionally, for their current PECs, the FCFs for $v' = 0 \rightarrow v = 0, 1, 2$ transitions are predicted to be 0.94, 0.056, and 0.0007, respectively. Such a set of values is comparable to those of CaF and similar molecules, and, if experimentally confirmed, could even allow for direct laser cooling of LiCr.

4.11 Conclusive remarks

In summary, in this Chapter I have described the first, extensive exploration of LiCr dimers, that I performed during the central part of my Ph.D. The first result of our study is represented by the experimental ability to produce ultracold gases of up to 50×10^3 bosonic ${}^6\text{Li}{}^{53}\text{Cr}$ Feshbach molecules from atomic Fermi mixtures, reaching phase-space densities exceeding 0.1 at about 200 nK. Thanks to the immunity to two-body decay and the comparably good stability against three-body recombination of our mixture, we could perform magneto-association with B -field rates slower than the two-body adiabatic regime by orders of magnitude. We have directly revealed the paramagnetic nature of the LiCr electronic ground state, and demonstrated precise control of the Feshbach state via a novel optical measurement of the open-channel fraction and binding energy. Further, through the characterization of the relevant loss mechanisms affecting Feshbach dimers, we have identified an experimental configuration where their lifetime exceeds 0.2 s.

In parallel, our theory collaborators developed a quantum chemical model for LiCr employing state-of-the-art *ab initio* methods, with which they determined the fundamental properties of this new molecular species. In particular, for the rovibrational $X\ {}^6\Sigma^+$ ground state, a large electric dipole moment of 3.3(2) D is predicted, on top of a sizable magnetic one ($5\ \mu_B$). Additionally, our Feshbach dimers, already created in the least bound $X\ {}^6\Sigma^+$ vibrational level, are expected to be efficiently transferrable, at convenient wavelengths, via STIRAP through a (4) ${}^6\Sigma^+$ level, to the absolute ground state. There, direct imaging and cooling schemes may be enabled by $X\ {}^6\Sigma^+ \rightarrow (2)\ {}^6\Pi$ optical transitions.

My experimental investigation, together with the theoretical studies by M. Tomza's group, let LiCr emerge as an appealing and promising system for a wealth of fundamental studies and future applications. For instance, our findings suggest that the realization of quantum gases of doubly polar ${}^6\text{Li}{}^{53}\text{Cr}$ bosonic molecules, with large electric and magnetic dipole moments, is within reach. Clearly, identification of the optimal STIRAP transfer will require extensive laser spectroscopy, but this will be greatly facilitated by the *ab initio* model predictions and by the long lifetime of Feshbach dimers, already achieved. Interestingly, electric dipole moments as high as 1 D can already be obtained in relatively shallow vibrational levels of LiCr with $v \simeq 37$ and a binding energy as low as $190\ \text{cm}^{-1}$; see Fig. 4.13. Given the relatively simple spectroscopic survey needed to find these states, this possibility represents an appealing intermediate, short-term step. In particular, such vibrationally excited molecules offer high sensitivity to the electron-to-proton mass ratio m_e/m_p [169], overcoming that of alkali and alkaline-earth dimers, and they could be employed to detect possible variations of m_e/m_p in precision measurements, providing new insight into fundamental physics.

Chapter 5

Anomalous diffusion of light impurities in a heavy fermion gas

In this Chapter, concluding the main scientific achievements of my Ph.D., I present the results – and our current understanding – of a very recent investigation of the transport properties of our fermionic mixture, which started in the last months of my doctorate and is currently being finalized during the writing of this Thesis. This study originated from preliminary, exploratory measurements aimed at observing diffusion phenomena in our system, motivated and inspired by the attendance of my supervisor Matteo Zaccanti at the EMMI workshop “*Deciphering many-body dynamics in mesoscopic quantum gases*” in Heidelberg in spring 2024. Our initial interest was to examine diffusive processes of strongly-interacting Fermi gases in the high temperature limit, and to investigate whether and how a comparably large mass imbalance $M_{\text{Cr}}/m_{\text{Li}}$, combined with the narrow character of Li-Cr Feshbach resonances, could indeed affect the transport properties of our system, compared to the widely explored case of homonuclear ${}^6\text{Li}$ mixtures [90, 188–190]. In particular, the main objective was to inspect if, as in the homonuclear (and broad resonance) case [190], a *minimum value* for the diffusion coefficient D could be identified, in the strongly-interacting regime, as the temperature was lowered. In what follows, I describe how we “successfully failed” in determining such a minimum D value in our system, and how a seemingly simple experiment surprisingly turned into something more exciting.

Following the procedures described in Sec. 5.2, we prepared a small lithium cloud embedded in a larger, cigar-shaped chromium thermal bath, in turn prepared in a non-interacting spin state; see sketch in Fig. 5.1(a). For both species, the radial (\hat{y} , \hat{z}) confinement was provided by a single-beam IR ODT (i.e., our main bODT with no green light), propagating along the \hat{x} axis, and a weak axial confinement resulted from the magnetic-field curvature of our BIAS coils ($\sim 12 \text{ G/cm}^2$). Moreover, as for Chapter 4 experiments on LiCr dimers, the relative gravitational sag was minimized by applying a vertical magnetic field gradient of about 1.5 G/cm. On top of that, the lithium sample was initially squeezed by the presence of an additional (vertical) 1560-nm ODT beam, which considerably compressed the Li cloud along the \hat{x} axis while negligibly affecting Cr, owing to the large difference in the atomic polarizabilities. Our measurements started by abruptly switching off the vertical beam, thereby allowing Li to expand along the axial direction, while simultaneously activating (tunable) Li-Cr interactions, as discussed below in details. We subsequently traced the dynamics of the expanding Li gas [see illustrative example in Fig. 5.1(b)], for different temperatures and interaction strengths, with the mean squared displacement $s_x^2 = \langle x^2 \rangle$ (i.e., the second moment of the spatial density distribution) as our main observable, directly accessible via absorption imaging.

Before discussing our observations, it is important to remark that – in the absence of interactions – after the vertical beam is switched off, Li atoms expand “ballistically” within the Cr bath, which in this case opposes no friction at all. To be more precise, here “ballistic” is used with a slightly unconventional meaning: In fact, due to the presence of the residual weak (magnetic) axial confinement, the sudden removal of the crossed trap actually triggers a *breathing mode* of the Li cloud, which “releases” its excess kinetic energy

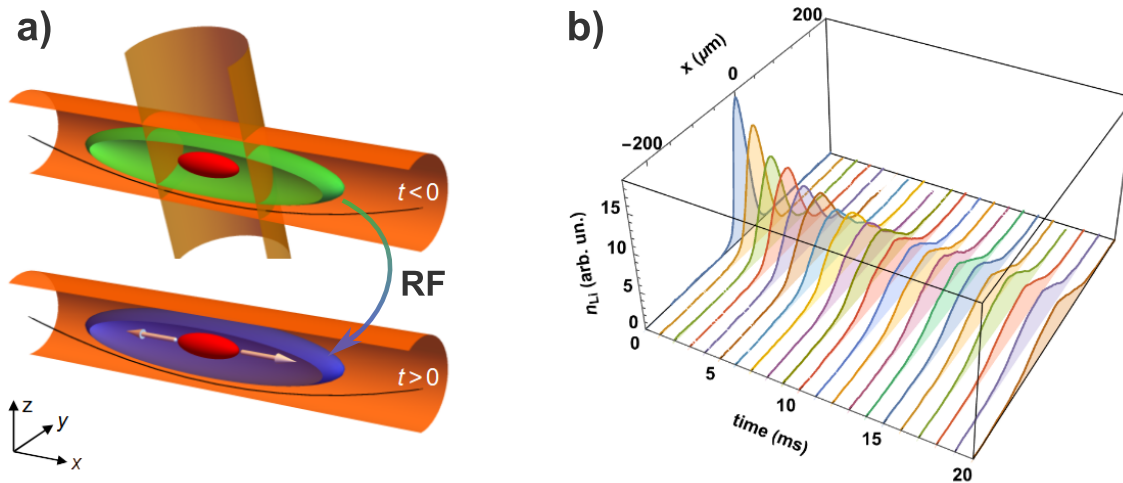


Figure 5.1 – (a) Sketch of our experimental configuration for the transport measurements. A small Li cloud (red ellipsoid) is prepared within a larger cigar-shaped Cr gas (green ellipsoid), initially in a non-interacting state. Both species are radially confined by the 1070-nm beam of our main (b)ODT (horizontal tube), and a weak axial confinement is provided by the B -field curvature of the BIAS coils (black parabolic curve). Additionally, Li atoms are axially compressed by a vertical 1560-nm beam (vertical tube), which only marginally perturbs Cr due to its lower polarizability at that wavelength, compared to the Li one. The experiment starts at $t = 0$, when the vertical beam is abruptly switched off, and Cr is simultaneously RF-transferred to an interacting spin state (sketched in blue). (b) Integrated axial profiles of an expanding Li cloud interacting with the surrounding Cr bath (not shown). To avoid finite-size effects, we typically select a time window corresponding to the first 20 ms, see the discussion at the end of Sec. 5.2.

by oscillating in size in the “new” weaker axial trap, while maintaining a fixed barycenter. This is indeed the expected behavior of a non-interacting ultracold cloud released from a tighter to a weaker harmonic trap, nicely reproducing the trend given in Ref. [168] [and reported here in Eq. (5.7)], see Fig. 5.2. For sufficiently weak final trap frequencies, the initial expansion is well approximated by the free-space result $\langle x^2(t) \rangle = s_0^2 + v_{th}^2 t^2$ (with initial size $s_0 = \sqrt{\langle x^2(0) \rangle}$ and thermal velocity $v_{th} = \sqrt{k_B T/m}$), from which the term “ballistic” is borrowed.

On the other hand, when Li-Cr interactions were turned on, we generally observed a considerable slowdown of the expansion of the lithium gas. In particular, focusing on the initial time dynamics, at high temperatures ($T \sim 0.5 \div 1 \mu\text{K}$) we observed a progressive transition from a ballistic ($\langle x^2 \rangle \propto t^2$) to a diffusive ($\langle x^2 \rangle \propto t$) expansion, as the interaction strength was resonantly increased close to a s -wave FR. This was perfectly consistent with what we expected to happen, and we could indeed extract a diffusion coefficient from the slowest-expanding datasets, not too far from the minimum value of D reported in Ref. [190] for a unitary ${}^6\text{Li}$ Fermi gas, of only a few (< 10) “diffusion quanta” \hbar/m . This already promising scenario surprisingly turned into something even more intriguing when we lowered the temperature of both Li and Cr atoms, yet without crossing $T/T_F = 1$. In fact, besides “strange features” at intermediate interaction strengths, for sufficiently low temperatures and strong interactions we observed distinct signatures of *subdiffusive* behavior, i.e. a somewhat slower-than-diffusion kind of dynamics, not expected within the framework of the standard Fermi liquid theory in ultracold gases [191], and indeed not reported in any homonuclear fermionic mixture so far.

In order to try to understand this phenomenology, in parallel to data acquisition and analysis, I developed a simple semi-classical Monte Carlo simulator that numerically “mim-

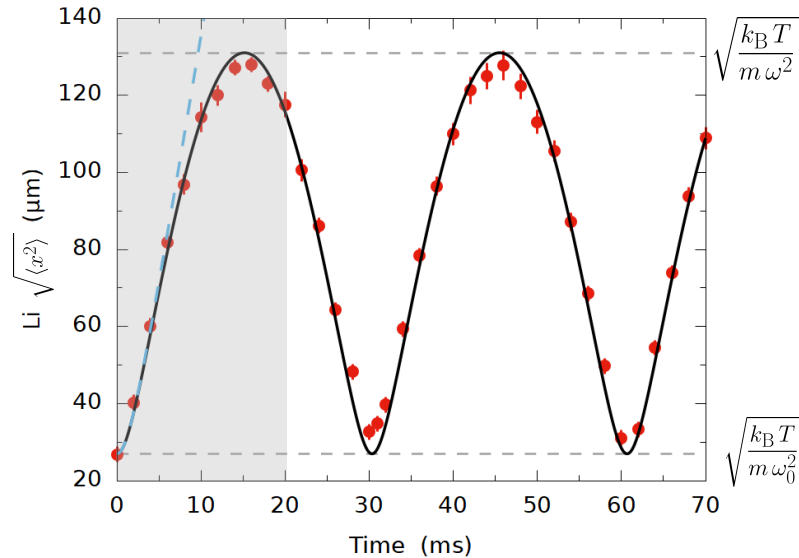


Figure 5.2 – Example of free breathing oscillations of a Li cloud released from a tighter (ω_0) to a weaker ($\omega < \omega_0$) axial trap. The red circles represent the experimentally measured root-mean-squared displacement $s_x(t) = \sqrt{\langle x^2(t) \rangle}$, obtained from two-dimensional Gaussian fits on the recorded absorption images [see Eq. (5.14)]. The black curve is the theory expectation Eq. (5.7), according to Ref. [168]. The cloud size oscillates between the equilibrium values in the tighter and in the weaker trap, marked by horizontal gray dashed lines. The cyan dashed line represents the purely ballistic case, i.e. the limit $\omega \rightarrow 0$. Finally, the shaded area highlights our typical observation-time window when Li-Cr interactions are switched on.

ics” our experimental measurements. In particular, leveraging on the precise knowledge of two-body elastic ${}^6\text{Li}$ - ${}^{53}\text{Cr}$ interactions (see Sec. 1.7), the main purpose of the simulator was to gain insights into the possible role of a relatively large mass imbalance $M_{\text{Cr}}/m_{\text{Li}}$, a large but finite effective range parameter R^* , the inhomogeneous density distribution of the Cr bath, and, last but not least, the external magnetic trap. Interestingly, my numerical simulator – which accounts for the aforementioned effects and incorporates the nature of elastic s -wave collisions (see Sec. 5.3) – has turned out perfectly capable to capture most of our experimental observations, quantitatively reproducing our data, except for the low temperature ones exhibiting strong *subdiffusion*. In this respect, tentative inclusion of “first-order quantum corrections”, such as retardation effects and mean-field interactions, has not changed qualitatively the simulator predictions. This suggests that more complex phenomena, such as quantum interference effects or non-trivial few-body correlations, could possibly play a significant role in our system at such low temperatures, where the thermal de Broglie wavelength of Li atoms starts to exceed the mean Cr interparticle spacing.

This rest of this Chapter is organized as follows:

- In Sec. 5.1, I briefly introduce a few different models that are typically used to describe *normal* or *anomalous* diffusion processes, considering also the case of an external harmonic trapping potential. In the final part, I discuss and motivate our choice among those.
- In Sec. 5.2, I detail the experimental procedures we follow to prepare the initial sample, and I present two complementary ways of acquiring data.
- In Sec. 5.3, I describe in detail the semi-classical Monte Carlo simulator that I

developed to support the interpretation and understanding of our observations.

- In Sec. 5.4, I present the results of our measurements in the high temperature regime, comparing them with the outcome of the simulation. In particular, this represented the first meaningful benchmark of my model, which reproduced our experimental data with remarkable accuracy throughout all interaction regimes experimentally explored.
- In Sec. 5.5, I present a set of measurement in the low temperature regime, which notably showed clear signatures of subdiffusive behavior for sufficiently strong interactions. Moreover, a seemingly faster-than-“ballistic” expansion was observed at intermediate magnetic-field detunings from the FR pole. In this case, the semi-classical Monte Carlo simulation is able to satisfactorily capture both the background and the intermediate-interactions dynamics, yet evidently failing in reproducing the observed subdiffusive expansion in the strongly-interacting region.
- Finally, in Sec. 5.6, I present our characterization of the slowest expansion dynamics across different temperature regimes, which is currently still ongoing during the writing of this Thesis.

5.1 Normal and anomalous diffusion

In this introductory Section to our transport measurements, I provide a short overview of a few simple analytical models available in literature that can be used to describe either normal or anomalous diffusion, including the case of particles confined in a harmonic trap. In particular, the main focus will be on the predicted time evolution of the mean square displacement (MSD) $\langle x^2(t) \rangle$, a key quantity that offers valuable insights into the underlying diffusion dynamics. For the sake of simplicity, I will not provide any mathematical derivation of the results reported below, most of which can be found in standard statistical mechanics textbooks or reviews (see, e.g., Refs. [192–194]). Rather, the main purpose of this introduction is to summarize the most relevant expressions (and physical interpretations) to understand our measurements and analyze our data.

The first model I consider is based on Einstein’s statistical theory of normal diffusion [195], which laid the groundwork for understanding Brownian motion by linking the random motion of Brownian particles to (measurable) macroscopic observables, such as temperature and viscosity, ultimately leading to the confirmation of Dalton’s atomic theory. Importantly, Einstein showed that the mean square displacement $\langle x^2(t) \rangle$ of a diffusing particle grows *linearly* with time (see plot in Fig. 5.3, red line):

$$\langle x^2(t) \rangle = s_0^2 + 2d D_1 t, \quad (5.1)$$

a trend nowadays regarded as a hallmark of *normal diffusion*. In Eq. (5.1), $s_0^2 = \langle x^2(0) \rangle$ is the initial spatial variance of the ensemble of diffusing particles, d is the dimensionality of the system, and D_1 , measured in m^2/s , is the normal diffusion coefficient (the meaning of the subscript will become clear in the following). For simplicity, and in light of our experimental protocol, hereinafter the discussion will be restricted to the one-dimensional case $d = 1$.

Einstein himself was aware that his stochastic description of the interactions with the surrounding medium resulting in Eq. (5.1) would have failed at very short timescales, where the effect of the particle’s inertia becomes significant [196, 197]. In other words, loosely speaking, a certain “minimum number” of collisions of the Brownian particle with the (typically much lighter) surrounding fluid molecules is needed in order to appreciably change the particle’s velocity. Therefore, for very short times, the motion is essentially ballistic. A few years after Einstein’s paper, Langevin introduced a stochastic differential equation that described the dynamics of a particle under the influence of damping and random forces [192, 198]. His result for the time evolution of the MSD reads [192, 193, 198] (see Fig. 5.3, blue line):

$$\langle x^2(t) \rangle = s_0^2 + \frac{2k_B T}{m\Gamma^2} \left(\Gamma t - 1 + e^{-\Gamma t} \right), \quad (5.2)$$

where k_B is the Boltzmann constant, m the mass of the diffusing particle(s), and Γ , with units s^{-1} , is a parameter connected to the viscosity of the medium [192]. In this form, Eq. (5.2) naturally introduces the dimensionless parameter $\tau_B = \Gamma t$, typically referred to as *Brownian time*, which represents the proper “temporal” scale of the process. In fact, notably, Langevin’s model captures the expected progressive transition from ballistic to diffusive motion. This can be easily shown by taking the short time limit $\tau_B \ll 1$ of Eq. (5.2), which returns a quadratic growth of the MSD with time:

$$\langle x^2(t \ll \Gamma^{-1}) \rangle \simeq s_0^2 + \frac{k_B T}{m} t^2 = s_0^2 + v_{th}^2 t^2, \quad (5.3a)$$

characterized by the thermal velocity $v_{th} = \sqrt{\frac{k_B T}{m}}$. On the other hand, in the long time limit $\tau_B \gg 1$ one finds

$$\langle x^2(t \gg \Gamma^{-1}) \rangle \simeq s_0^2 + 2 \frac{k_B T}{m \Gamma} t = s_0^2 + 2 \frac{v_{th}^2}{\Gamma} t, \quad (5.3b)$$

i.e. a result analogous to Eq. (5.1), with diffusion coefficient given by

$$D_1 = \frac{k_B T}{m \Gamma} = \frac{v_{th}^2}{\Gamma}. \quad (5.4)$$

It is important to keep in mind that both Einstein's and Langevin's models describe *normal diffusion* processes of an ensemble of particles within a *homogeneous medium*, and in the absence of any *external force*.

By contrast, diffusion in harmonic traps introduces additional complexities compared to free space, as particles experience a restoring elastic force toward the trap center. The confinement somehow alters the nature of diffusion, and ultimately leads to saturation of the MSD at long times. The first description of a particle undergoing *normal diffusion* within a harmonic trap was provided by Smoluchowski [199]. His result for the MSD can be written as [193]:

$$\langle x^2(t) \rangle = s_\infty^2 + (s_0^2 - s_\infty^2) e^{-2(\frac{\omega}{\Gamma})^2 \Gamma t}, \quad (5.5)$$

where ω is the trap frequency, and $s_\infty^2 = k_B T / (m \omega^2)$ is the final variance reached at thermal equilibrium. It can be readily shown that, in the *force-free limit* $\omega \rightarrow 0$, Eq. (5.5) reduces to Einstein's result Eq. (5.1), see Fig. 5.3. However, as pointed out in Ref. [193], Smoluchowski's Eq. (5.5) is only valid for $\Gamma t \gg 1$ [similarly to Eq. (5.1)] and $\Gamma \gg \omega$, i.e. for sufficiently long (Brownian) times and when the particle's oscillatory motion is overdamped. Uhlenbeck and Ornstein [193] provided generalization to Eq. (5.5), valid at all observation times and under any interaction strength:

$$\langle x^2(t) \rangle_{ud} = s_\infty^2 + (s_0^2 - s_\infty^2) e^{-\Gamma t} \left[\cos(\Omega_{ud} t) + \frac{\Gamma}{2\Omega_{ud}} \sin(\Omega_{ud} t) \right]^2, \quad (5.6a)$$

$$\langle x^2(t) \rangle_{cd} = s_\infty^2 + (s_0^2 - s_\infty^2) e^{-\Gamma t} \left(1 + \frac{\Gamma t}{2} \right)^2, \quad (5.6b)$$

$$\langle x^2(t) \rangle_{od} = s_\infty^2 + (s_0^2 - s_\infty^2) e^{-\Gamma t} \left[\cosh(\Omega_{od} t) + \frac{\Gamma}{2\Omega_{od}} \sinh(\Omega_{od} t) \right]^2, \quad (5.6c)$$

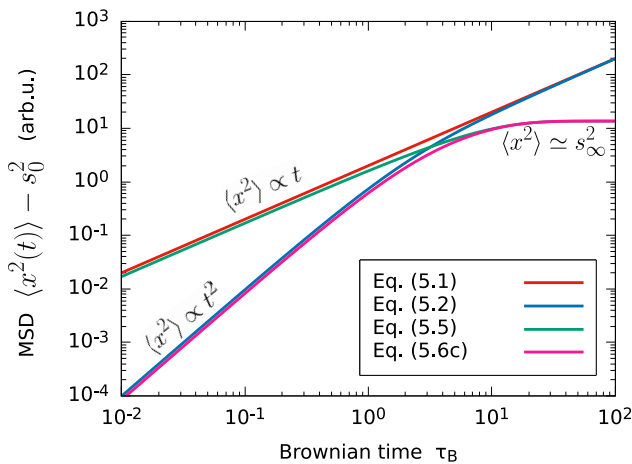


Figure 5.3 – Time evolution of the mean square displacement for different models of *normal diffusion*, see legend and axes. With respect to Einstein's model Eq. (5.1), the Langevin Eq. (5.2) captures the progressive transition from ballistic to diffusive dynamics. Smoluchowski's model Eq. (5.5) includes the effects of an external harmonic confinement, which causes the MSD to saturate at long times. Finally, the more general Uhlenbeck-Ornstein Eq. (5.6c) extends Smoluchowski's model and captures the ballistic-to-diffusive crossover.

with $\Omega_{\text{ud}}^2 = \omega^2 - \Gamma^2/4 = -\Omega_{\text{od}}^2$. Eqs. (5.6a), (5.6b), and (5.6c) hold for underdamped, critically-damped, and overdamped motion, respectively. In particular, it is worth noting that, for $\Gamma \rightarrow 0$, Eq. (5.6a) simplifies to

$$\langle x^2(t) \rangle = s_0^2 \left[\cos^2(\omega t) + \frac{s_\infty^2}{s_0^2} \sin^2(\omega t) \right], \quad (5.7)$$

which precisely coincides with the result reported (e.g.) by Ketterle and Zwierlein in Ref. [168], describing the breathing mode triggered by releasing an ultracold atomic cloud from a tighter (ω_0) to a weaker ($\omega < \omega_0$) harmonic trap, see again Fig. 5.2. If the sample is initially at equilibrium in the tighter trap, i.e. with initial size $s_0^2 = k_B T / (m\omega_0^2)$, the relative amplitude of the oscillation is set by the ratio of the trap frequencies, $A^2 = s_\infty^2/s_0^2 = \omega_0^2/\omega^2$.

The motion of particles in complex disordered systems is generally no longer Brownian, exhibiting instead a so-called *anomalous diffusion* behavior [194,200,201]. Broadly speaking, anomalous diffusion describes any departure from the standard linear relation between mean square displacement and time. Unlike normal diffusion, anomalous processes are characterized by a MSD scaling as $\propto t^\alpha$, indicating either enhanced ($\alpha > 1$) or suppressed ($\alpha < 1$) transport. This phenomenon often arises in systems with obstacles, complex interactions, or spatial heterogeneity. In the absence of external forces, anomalous diffusion processes are typically described in terms of a generalized power law of the form [194,200,201]:

$$\langle x^2(t) \rangle = s_0^2 + 2D_\alpha t^\alpha, \quad (5.8)$$

where D_α is a generalized diffusion coefficient (in units $\text{m}^2/\text{s}^\alpha$), and the exponent α , as anticipated, characterizes the nature of the anomalous process: $\alpha > 1$ indicates a faster-than-diffusion dynamics (*superdiffusion*), whereas $\alpha < 1$ is a signature of *subdiffusion*. Additionally, $\alpha = 2$ ($\alpha > 2$) represents (*super-*)*ballistic* motion, and the extreme case $\alpha = 0$ can be interpreted as perfect *localization*.

Eq. (5.8) can be derived starting from the fractional Fokker-Planck equation, see Refs. [194,201] for details. Without diving into the heavy mathematical machinery needed to tackle the problem, it can be shown that the generalized diffusion coefficient is given by [194,201]:

$$D_\alpha = \frac{k_B T}{m \eta_\alpha \gamma(1 + \alpha)}, \quad (5.9)$$

where $\gamma(x)$ is the gamma function, and η_α (units $\text{s}^{\alpha-2}$) is a generalized friction.

Furthermore, in Ref. [194] the authors also discuss the case of a particle undergoing anomalous diffusion within a harmonic trap. In this case, the MSD reads

$$\langle x^2(t) \rangle = s_\infty^2 + (s_0^2 - s_\infty^2) E_\alpha^{\text{ML}} \left(-2 \frac{\omega^2}{\eta_\alpha} t^\alpha \right), \quad (5.10)$$

where $E_\alpha^{\text{ML}}(x)$ is the Mittag-Leffler function, defined as

$$E_\alpha^{\text{ML}}(x) = \sum_{n=0}^{\infty} \frac{x^n}{\gamma(1 + n\alpha)}. \quad (5.11)$$

From the properties of the gamma function [202], it can be shown that

$$E_2^{\text{ML}}(x) = \cosh(\sqrt{x}), \quad (5.12a)$$

$$E_1^{\text{ML}}(x) = e^x, \quad (5.12b)$$

$$E_{1/2}^{\text{ML}}(x) = e^{x^2} (1 + \text{erf}(x)). \quad (5.12c)$$

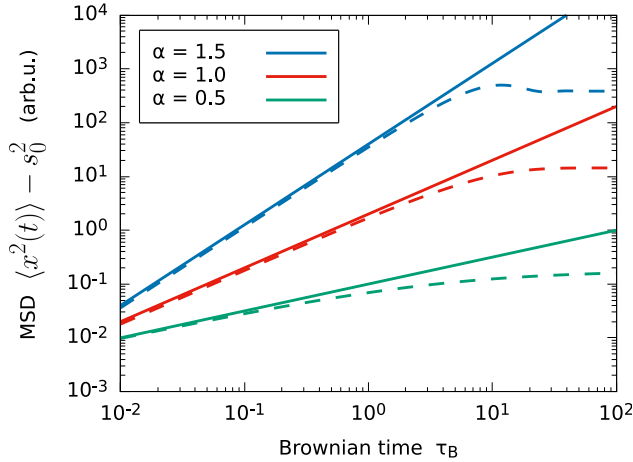


Figure 5.4 – Time evolution of the mean-squared displacement in the case of *anomalous diffusion*, for different exponents α , see legend. Solid lines represent the generalized power law Eq. (5.8), while dashed lines are obtained from Eq. (5.10), with matching color code for the anomalous exponent α . The case of $\alpha = 1$ (red color) corresponds to normal diffusion, equivalently described by Eq. (5.1) (for $\omega = 0$) and Eq. (5.5) ($\omega \neq 0$), respectively. None of the curves captures the short-time ballistic crossover.

Therefore, for $\alpha = 1$, Eq. (5.10) reduces to Smoluchowski’s result Eq. (5.5), with $\eta_1 = \Gamma$. Moreover, in the force-free limit $\omega \rightarrow 0$, Eq. (5.10) (truncating the sum at $n = 1$) reduces to the generalized power law Eq. (5.8), with D_α given by Eq. (5.9). I also explicitly remark here that, for $\alpha = 1$, Eq. (5.9) simplifies to Eq. (5.4).

In Fig. 5.4, I show illustrative plots of Eq. (5.9) (solid lines) and Eq. (5.10) (dashed lines), for different values of the anomalous exponent α (see legend). I stress the fact that, compared to the curves shown Fig. 5.3 for normal diffusion, none of those plotted in Fig. 5.4 exhibits the crossover with the ballistic regime at short times. In other words, Eq. (5.10) generalizes Smoluchowski’s result Eq. (5.5) to anomalous diffusion, but it does *not* provide a generalization to the Uhlenbeck-Ornstein Eqs. (5.6), which (to the best of our knowledge) does not exist in the (incredibly vast) literature on the topic.

I anticipate here that, in our data analysis, we have tested all models discussed above against the experimentally measured MSD of our expanding lithium cloud. However, it should be reminded that none of these models accounts for the case of a non-homogeneous medium, which is instead the scenario corresponding to our experiments, due to the Gaussian spatial density distribution of the chromium bath. Therefore, in general, we decided to limit our fitting region to the data points for which $\langle x^2(t) \rangle_{\text{Li}} \leq \langle x^2 \rangle_{\text{Cr}}$.

Another complication arises from the presence of the external magnetic confinement, which, despite being relatively weak, could in principle affect the expansion dynamics of the Li cloud, as it surely does for $t \rightarrow \infty$. In this regard, the Uhlenbeck-Ornstein Eqs. (5.6) should be valid – at all times and for any interaction strength – for particles undergoing normal diffusion within a harmonic trap. In fact, we found that they provided a satisfactory description of the high temperature data (see Sec. 5.4), although some care is needed to determine the asymptotic value s_∞^2 from the short-time dynamics, especially for weak interactions. However, Eqs. (5.6) yielded unsatisfactory results when fitted to the low temperature datasets exhibiting *strong subdiffusion* ($\alpha \lesssim 0.7$). For these latter, the Metzler-Klafter Eq. (5.10) should be applicable, and we indeed obtained fairly good fits, provided that s_∞^2 was fixed to $k_B T_{\text{Cr}} / (m_{\text{Li}} \omega_{\text{Li}}^2)$, i.e. to the value estimated by (reasonably) assuming plain asymptotic thermalization with the Cr bath. Yet, in the fitting region we considered, the results obtained by employing Eq. (5.10) were, within error bars, indistinguishable from those retrieved from the (much simpler) fit with the generalized power law Eq. (5.8).

Indeed, the main limitation of Eq. (5.8), besides not accounting for the inhomogeneous medium, is to ignore the external confinement. Nonetheless, for short times $t \ll 1/\omega$, the effect of the trapping potential can be safely neglected, as it can be proved mathematically by taking the force-free limit of Eq. (5.10). Moreover, a more careful thinking of the physical effects of an external trapping potential provides further insights into its possible

impact on the dynamics of the diffusing particles: The key point is that the external trap, in practice, acts by “subtracting” kinetic energy from the particles moving away from the trap center, as they climb up the potential hill. Therefore, in general, one should expect a (non-negligible) slowdown of the expansion due to the trap to take place only after a certain *spatial extension* of the cloud has been reached – rather than after a certain *time evolution*, regardless of the cloud size. In other words, in the strongly-interacting regime, where the observed expansion is significantly slower than the non-interacting case, one can arguably neglect the effects of the external trap even for relatively long times $t > 1/\omega$, provided that the cloud size remains sufficiently small.

On top of that, as I will show later, under strong interactions the mean collision rate per Li atom is found to be considerably large, with values exceeding 20 kHz. Since typically ~ 10 collisions are needed to thermalize, i.e. to reach thermal equilibrium between the Li and Cr *velocity distributions* ($m_{\text{Li}} v_{\text{th,Li}}^2 = M_{\text{Cr}} v_{\text{th,Cr}}^2$),¹ this implies that, for strong interactions, the mean kinetic energy per Li atom is always at equilibrium with that of Cr. In other words, as lithium atoms lose kinetic energy by climbing the potential hill, they rapidly reacquire it by collisions with the surrounding chromium gas. Consequently, for sufficiently large collision rates, the effects of our weak magnetic confinement are potentially negligible for the entire observation time.

By contrast, in the opposite regime of weak interactions, where the above considerations do not apply, Eq. (5.8) can be used to fit the data only for short times $t \ll 1/\omega$, and as long as $\langle x^2(t) \rangle_{\text{Li}} \leq \langle x^2 \rangle_{\text{Cr}}$. This is the case of datasets taken far from the resonant region, where the MSD of the Li cloud scales essentially as in Eq. (5.7) [or, more generally, as in Eq. (5.6a) for small but non-negligible interactions]. For these datasets, we impose an additional constraint on the selected fitting region: namely, for $|\delta B| \gtrsim 50$ mG, we only consider points at $t < 6$ ms.

Overall, we found that the generalized power law Eq. (5.8), with the prescriptions discussed above, can be effectively used to describe the entire set of our measurements, while also minimizing the number of free parameters. This allowed us to apply the same fitting procedure to every dataset, greatly simplifying the comparison between the different temperature and interaction regimes experimentally explored. The simple functional form of Eq. (5.8) is indeed quite convenient, as it turns into a purely linear fit, once the initial value is subtracted and the double log scale is taken, namely:

$$\log \left[\langle x^2(t) \rangle - s_0^2 \right] = \log \left(2 D_\alpha \right) + \alpha \log(t) \implies Y(X) = q + \alpha X, \quad (5.13)$$

with linear coefficient α and y -intercept connected to D_α . For these reasons, Eq. (5.13) represents a first, rather robust method to analyze our experimental data.

To conclude this Section, I briefly describe how we extracted the MSD $\langle x^2(t) \rangle$ of our atomic clouds from absorption images.² In general, our main interest concerns the axial (\hat{x}) direction, as the radial ones do not exhibit any significant dynamics. For the measurements at high temperatures, the effects of quantum degeneracy are essentially negligible, and the cloud profiles are well fitted by Maxwell-Boltzmann distributions. In this case, we simply performed 2D Gaussian fits on the recorded column density profiles $n_{\text{OD}}(x, z)$, over the entire clouds. More explicitly, to clarify the notation used for the parameters, the fitting

¹This statement is supported by the numerical simulator of Sec. 5.3.

²Our absorption imaging beam propagates in the horizontal \hat{x}, \hat{y} plane, forming an angle of about 22.5° with the \hat{y} direction. As such, the recorded axial (\hat{x}) size of the atomic clouds appears smaller than the real one by a factor $1/\cos(22.5^\circ) \simeq 1.08$. This systematic error is taken into account in our analysis.

function, when “projected” onto the \hat{x} axis, has the form:

$$G(x) = A \cdot \exp \left[-\frac{1}{2} \left(\frac{x - x_0}{s_x} \right)^2 \right], \quad (5.14)$$

with amplitude A , cloud barycenter x_0 , and $1/\sqrt{e}$ -size s_x as free parameters. In this case, the MSD of the atomic cloud is directly given by $\langle x^2 \rangle = s_x^2$.

On the other hand, for the low-temperature measurements exhibiting subdiffusive behavior, we found that Gaussian fits were not able to properly capture the Li density profiles. This was particularly clear when restricting the vertical fitting boundaries to the high-density, central region of the clouds. In this case, we found satisfactory results by employing a “generalized” Gaussian function of the form

$$G_\beta(x) = B \cdot \exp \left[-\frac{1}{2} \left| \frac{x - x_0}{\sigma_x} \right|^\beta \right], \quad (5.15)$$

with amplitude B , cloud barycenter x_0 , $1/\sqrt{e}$ -size σ_x , and exponent β as free parameters. In this case, the MSD is given by the generalized formula

$$\langle x^2 \rangle_\beta = 4^{1/\beta} \frac{\gamma(3/\beta)}{\gamma(1/\beta)} \sigma_x^2, \quad (5.16)$$

where $\gamma(x)$ is the gamma function. Finally, for the measurements of Sec. 5.6, we also employed the fitting function

$$F(x) = C \cdot \left\{ \frac{(1 - f_{\text{loc}})}{\sqrt{2\pi} s_x} \cdot \exp \left[-\frac{1}{2} \left(\frac{x - x_0}{s_x} \right)^2 \right] + \frac{f_{\text{loc}}}{4\sigma_x} \cdot \exp \left[-\frac{1}{2} \left| \frac{x - x_0}{\sigma_x} \right| \right] \right\}, \quad (5.17)$$

see the discussion there for details.

5.2 Sample preparation

As anticipated in the introduction of this Chapter, our transport experiments consist in studying the (one-dimensional) axial expansion of a small lithium cloud surrounded by a larger thermal bath of Cr atoms, see sketch in Fig. 5.1(a). In this Section, I describe our experimental protocol to prepare the initial sample, underlining its possible subtleties, and I present two different data acquisition methods.

The starting point of our transport experiments is represented by the ultracold ${}^6\text{Li}$ - ${}^{53}\text{Cr}$ mixture that we obtain at the end of the evaporation stage in the sole main bODT (see Sec. 2.6). As such, initially the sample is composed by Li|1>, Li|2>, and Cr|1> atoms, prepared at high-fields above 1.4 kG at temperatures around 200 nK. The axial confinement is provided by the magnetic-field curvature of the BIAS coils, of about 12 G/cm² at 1.4 kG, resulting in a trap frequency $\omega_{x,\text{Li}} = 2\pi \times 17$ Hz ($\omega_{x,\text{Cr}} = 2\pi \times 14$ Hz) for Li (Cr) atoms. On top of that, a magnetic-field gradient of 1.5 G/cm is employed to cancel the relative gravitational sag of the two clouds. As discussed in Sec. 2.6, under these typical conditions the Li gas is deeply degenerate, with $T_{\text{Li}}/T_{\text{F,Li}} \sim 0.2$, while the Cr component only features a mild degeneracy, with reduced temperatures of about $T_{\text{Cr}}/T_{\text{F,Cr}} \sim 0.5 \div 1$. The final temperatures T_{Li} and T_{Cr} can be adjusted, to some extent independently, by modifying the endpoint of the evaporation ramps and/or the sympathetic cooling efficiency of the *Feshbach cooling* stage (see Sec. 2.7). In particular, we started to explore transport phenomena in our system at relatively high temperatures of about $0.5 \div 1$ μK , in order to intentionally avoid possible effects of fermionic quantum degeneracy. This choice seemed particularly

convenient also for what concerns the chromium bath: On the one hand, a higher Cr temperature results in a larger axial extent of the Cr cloud, which ideally enlarges the observation time window where $\langle x^2(t) \rangle_{\text{Li}} \lesssim \langle x^2 \rangle_{\text{Cr}}$. On the other hand, more energetic Cr atoms are less perturbed by the application of the vertical 1560-nm beam that squeezes the Li cloud (see below), thus minimizing possible excitations of the chromium gas.

In the initial trap provided by the combination of main bODT and magnetic-field curvature, the Li axial (\hat{x}) size typically exceeds the Cr one by about a factor of 2 [see, e.g., the sketch in Fig. 3.6(a)], while radially the two clouds have similar extensions. To shrink the lithium cloud along the \hat{x} direction, i.e. in order to make it significantly smaller than the Cr one, we introduced an additional, almost species-selective axial confinement. This is realized by means of a (nearly) vertical ODT beam at 1560 nm with a circular beam waist of about 100 μm , which crosses the main bODT with an angle of about 17° from the \hat{z} direction,³ see again Fig. 5.1(a) [and Sec. 6.3 for details about the optical setup]. At such wavelength, the Cr polarizability is about 2.4 times lower than the Li one: This asymmetry between the two species, combined with the typically higher temperatures of the Cr bath, compared to T_{Li} , has allowed us to find an experimental protocol, detailed below, with which we manage to load a small number of lithium atoms in the crossed trap, without causing significant perturbations of the chromium density profile.

Before detailing our preparation procedure, it is important to remind that, besides squeezing the Li cloud in the axial direction, we also desire to control the Li-Cr scattering length, in order to explore different interaction regimes. This can be done by exploiting a set of high-field *s*-wave FRs, as shown previously in Sec. 3.3. In particular, for the measurements discussed in this Chapter, we selected the $|\text{Li}|1\rangle\text{-Cr}|1\rangle$ FR at about 1414 G. Clearly, however, some care must be taken in order to safely approach the target magnetic-field detuning: First, since we typically prepare our samples on the attractive (“BCS”) side of the FR (corresponding to $\delta B = B - B_0 > 0$ in our case), ramping the field below the resonance pole (“BEC” side) with an interacting mixture would unavoidably cause molecule formation, as discussed in Sec. 4.3. Second, employing fast ramp rates – which would somewhat decrease the molecule conversion efficiency – may trigger collective excitations in both the Li and Cr clouds, due to the rapid (non-adiabatic) change of the interactions. Third, due to three-body recombination processes, close to the resonance pole the lifetime of our samples is limited to a few tens of ms at our typical densities (see Sec. 3.4). This implies that our measurements must necessarily start shortly after (strong) interactions are switched on. Finally, our COMP coils, with which we accurately tune the magnetic field around the FR, have an overshoot issue with magnetic field ramps exceeding 100 \div 200 mG of span. While these overshoots can be partially mitigated by optimizing the parameters of the PID controller employed for the COMP coils stabilization (see Sec. 6.1), we found it rather challenging to completely eliminate them, without considerably losing in the capability to perform fast ramps. To circumvent these problems, in our protocol we use a combination of RF transfers and spin-selective optical blasts, with which we safely reach the target magnetic field detuning with a spin-polarized, non-interacting mixture.

More specifically, with general reference to the three panels of Fig. 5.5, we first set δB to an off-resonant value of about +150 mG, where Li and Cr are essentially not interacting over the preparation timescales. At such field, through a 20-ms-long linear ramp, we increase the power of the 1560-nm cross beam up to a variable value of typically 0.5 \div 2 W, adjusted day-by-day in order to optimize the final lithium sample. Indeed, this causes a (first) loss in the Li atom number, similarly to what shown in Fig. 2.11(b) for the

³This is the same optical path of the bichromatic crossed trap exploited in Sec. 2.8 to tune the relative density and degree of degeneracy of Li and Cr atoms.

bichromatic crossed (see first column at $P_{532} = 0$). At the end of the cross ramp, we apply a π -pulse on the $\text{Cr}|1\rangle \leftrightarrow \text{Cr}|2\rangle$ RF transition, transferring Cr atoms to a non-interacting state (the actual timing of this pulse is irrelevant, as long as it is performed at the initial detuning of $\sim +150$ mG). The RF pulse is followed by an optical blast with Cr|1) resonant light to remove any remaining non-transferred atom. After a hold time of 50 ms, during which the Li component – via intraspecies collisions characterized by a scattering length of about $-2500 a_0$ [138] – is allowed to thermalize and reorganize itself within the new trap configuration, we optically remove Li|2) atoms, obtaining a polarized, non-interacting Li|1)-Cr|2) mixture (see Fig. 5.5(c)). I anticipate here that the removal of the Li|2) component has two main consequences: First, a fraction of Li|1) atoms is lost from the sample, owing to collisions with relatively hot Li|2) atoms in the process of leaving the trap, after excitation by the resonant optical pulse. This is not necessarily a drawback – provided a sufficiently large signal-to-noise ratio for absorption imaging is preserved – since, as anticipated, our goal is to realize a small cloud of Li impurities embedded within a Cr bath. Indeed, the condition $N_{\text{Li}} \ll N_{\text{Cr}}$ allows us to neglect any effect of the Li cloud onto the Cr one, at least to a first approximation. In particular, as I will discuss in Sec. 5.3, this assumption greatly simplifies the computational effort needed for the Monte Carlo simulation. The second consequence is the fact that, after removal of Li|2), Li|1) atoms represent an ideal, non-interacting Fermi gas, since also chromium is already prepared in the spin state Cr|2) at this stage. Therefore, lithium loses its ability to thermalize, and subsequent changes in the trap configuration may result in plain spilling of most-energetic atoms, and more

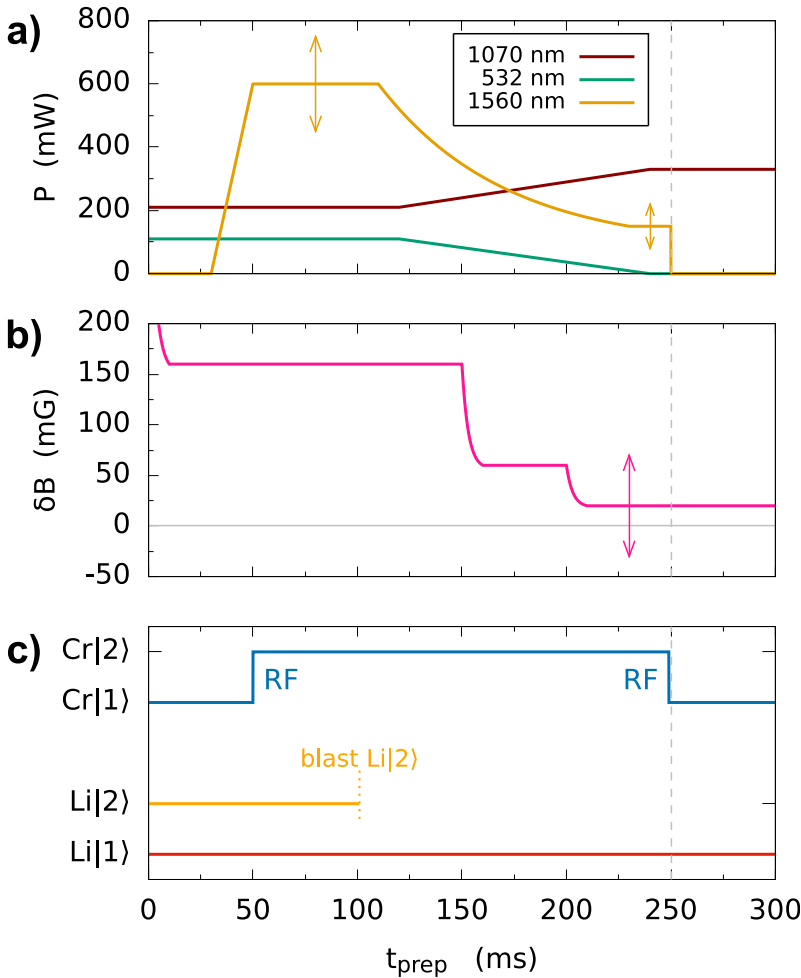


Figure 5.5 – Sketch of the experimental sequence we follow to prepare the initial sample for the transport measurements, see text for details. (a) Optical power in the trap beams at 1070 (red), 532 (green), and 1560 nm (yellow), respectively. (b) Magnetic field steps to approach the target detuning. (c) Population of the Zeeman states Li|1) (red), Li|2) (orange), and Cr|1, 2) (blue). In panels (a) and (b), vertical double-headed arrows indicate values that are adjusted either to access different temperature and interaction regimes, or during day-by-day optimizations of the final sample.

Table 5.1 – Typical starting conditions for the transport measurements, obtained after the procedures detailed in the main text, encompassing both the regimes of “high” and “low” temperatures. Atom numbers and cloud sizes are extracted from *in situ* absorption images by fitting the density profiles with 2D Gaussian functions. The parameters are defined similarly to Eq. (5.14). For the “blind” \hat{y} direction, we use estimates obtained from knowledge of the trapping frequencies. Effective temperatures are instead obtained from time-of-flight measurements. Strictly speaking, these should be intended as estimates of the width of the corresponding velocity distribution. The unequal values measured along the axial and radial directions are a consequence of the preparation protocol, in the final part of which atoms cannot thermalize.

Species	N (10^3)	s_x (μm)	$s_{y,z}$ (μm)	T_x (nK)	$T_{y,z}$ (nK)
Li	20 \div 40	15 \div 40	5 \div 7	50 \div 700	300 \div 400
Cr	100 \div 150	80 \div 150	8 \div 10	350 \div 1000	200 \div 400

generally in strongly out-of-equilibrium velocity distributions, characterized by unequal “effective temperatures” along the three directions. As I will discuss in Sec. 5.5, this “cross-dimensional non-thermalization”, combined with a general temperature mismatch between Li and Cr, causes “strange features” to appear in some of our measurements.

Once the non-interacting $\text{Li}|1\rangle\text{-Cr}|2\rangle$ mixture is prepared, we start to ramp down the power in the cross arm, in order to reach the target value for the measurement. As discussed later, this value essentially determines both the Li initial size and its release energy. This is accomplished by a 120-ms-long exponential ramp with characteristic time constant of 60 ms, see Fig. 5.5(a). Roughly simultaneously, we extinguish the green light in our bODT, and increase the 1070-nm power accordingly to maintain the same trap depth for Cr atoms. This passage from a bichromatic to a purely IR optical dipole trap improves the radial overlap of the atomic clouds, with Li experiencing a stronger confinement than Cr. Parallel to that, as shown in Fig. 5.5(b), we progressively bring the magnetic field detuning to the final target value for the measurement, allowing for a sufficiently long waiting time after each step in order to extinguish the transient overshoot of the COMP coils.

At the end of the preparation sequence, lasting about 250 ms overall, we obtain a small $\text{Li}|1\rangle$ cloud confined at the center of a larger $\text{Cr}|2\rangle$ gas [see the sketch in Fig. 5.1(a) for $t < 0$], with typical parameters reported in Tab. 5.1. The actual experiment then starts by applying a 0.9-ms-long RF π -pulse on Cr, transferring its population to the interacting $\text{Cr}|1\rangle$ state, at the end of which we abruptly switch off the vertical cross beam, thereby allowing Li to expand along the x direction; see sketch of Fig. 5.1(a) for $t > 0$. We subsequently monitor the expansion of the Li gas through *in situ* absorption imaging, with a typical observation time of 20 ms.

Data acquisition

To conclude the introduction to our transport measurements, I briefly discuss here two complementary approaches to data acquisition that, while being absolutely equivalent in the “ideal world”, result in fact distinct when applied to practical scenarios, where one has to deal with medium- and long-term instabilities and drifts, which make prolonged measurements technically challenging in our setup.

To be more specific, in order to obtain a comprehensive picture of the transport dynamics in a given temperature regime, we decided to characterize the expansion of the Li cloud for different interaction strengths, i.e. for different magnetic field detunings. A first, “brute-force” approach consists then in acquiring a time trace of $\langle x^2(t) \rangle$ for each selected δB value, as pictorially represented in Fig. 5.6(a) [horizontal blue arrows]. This is

the preferred approach to perform any quantitative data analysis, and thus to precisely extract physical quantities (α , D_α) from the experimental traces. However, it results rather time consuming, and the outcome of the measurement generally starts to be clear only after the analysis has been carried out, and when the entire dataset is considered. An example of experimental data obtained with this first method is shown in Fig. 5.6(b) [and in Fig. 5.6(d) from a different perspective].

The second approach is, conceptually, “orthogonal” to the first one: In this case, for different *fixed* evolution times t_{fix} , we acquire a “spectrum” of $\langle x^2(t_{\text{fix}}, \delta B) \rangle$ by scanning the magnetic field detuning, see Fig. 5.6(a) [vertical green arrows]. This allows us to obtain a clear qualitative picture more rapidly, see example in Fig. 5.6(c), although we found it not trivial to *reliably* extract the time evolutions at each field with this method, which are required for quantitative data analysis. Despite this limitation, this second method results

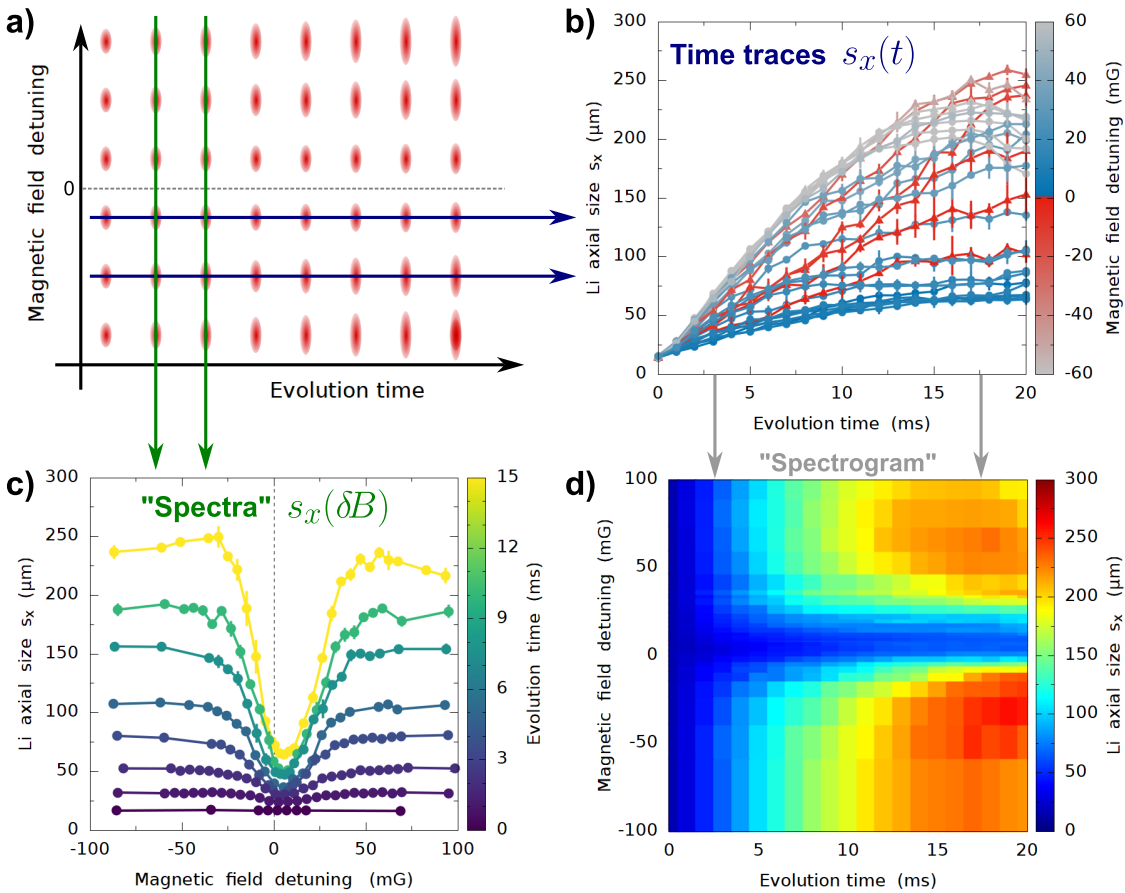


Figure 5.6 – (a) Illustrative sketch of the expansion dynamics of the Li cloud (red ellipses) within the Cr bath (not shown), for different evolution times and magnetic field detunings. Blue and green arrows represent the two “conceptually orthogonal” approaches to data sampling and acquisition, see text. (b) Example of a (high-temperature) transport dataset obtained with the “brute-force” approach: for each selected detuning value (see color scale), a time trace of $s_x(t)$ is recorded. This time-consuming method allows for quantitative data analysis, but it is not optimum for exploratory surveys. (c) Example of transport dataset analogous to that of panel (b), but obtained the “fixed times” sampling method: In this case, for a set of fixed hold times, we acquire a “spectrum” of the Li axial size by scanning δB . This approach offers an immediate way to pinpoint the magnetic field detuning that yields the slowest expansion (e.g., by looking directly at long evolution times), but it results not suitable for quantitative data analysis. (d) Same data as in panel (b), but plotted as a pixelated heat/color map. This perspective offers a qualitative overview of the entire dataset.

quite convenient for exploratory measurements, or to quickly pinpoint the optimum δB value that yields the slowest expansion, in a given temperature regime. Moreover, as shown later, it can also be used as a first direct comparison either between experimental datasets at different temperatures or between experiments and numerical simulations, with no strict need for data analysis, thereby considerably shortening and simplifying the exploration of parameter spaces (both in terms of experiments and simulations).

Finally, I also mention that, similarly to what was done in the experiment to determine the K_3 coefficient [see Sec. 3.4], also here we monitor the magnetic field, before and after each measurement, by performing RF spectroscopy on the $\text{Li}|1\rangle \longleftrightarrow \text{Li}|2\rangle$ transition. The location of the FR pole is pinpointed through a sharp molecular loss signal, similar to those shown in Fig. 4.2(a), to which all the other fields are referenced. We decided to discard measurements showing a B -field drift larger than 4 mG.

5.3 Semi-classical Monte Carlo simulator

As already anticipated, in order to help and support the understanding of our experimental observations, I developed a conceptually simple (yet to some extent physically accurate) semi-classical Monte Carlo simulator, which attempts to replicate numerically the microscopic mechanisms at play within our experimental setup. Honestly, this started as a somewhat playful side project of mine, in a moment while we were still trying to figure out how to properly (and quantitatively) analyze our data in the lab. However, already the first results of the simulations were quite promising and encouraging, strongly motivating me to invest more time in the development of the code.

In general, from a physical point of view, several factors possibly concur to make the diffusion of ultracold Li impurities in a Cr bath a rather non-trivial phenomenon: First, the comparably large mass asymmetry $M_{\text{Cr}}/m_{\text{Li}} \simeq 8.8$ could play a significant role here, with respect to the widely-investigated homonuclear case [90, 188–190]. Roughly speaking, even a single collision with a (nearly ten times heavier) Cr atom can significantly impact the trajectory of a Li impurity.⁴ Second, compared to homonuclear ${}^6\text{Li}$ mixtures near broad Feshbach resonances, the narrow character of ${}^6\text{Li}$ - ${}^{53}\text{Cr}$ FRs could also affect the transport properties of our system, since, as discussed in Sec. 1.5, for large R^* values the various (relative) momentum classes reach the unitary-limited condition at different magnetic field detunings. Third, in contrast with the basic assumptions of most theoretical models, in our experiment the density of the “medium” (i.e. the chromium bath) is not homogeneous, but features a Gaussian envelope due to the nature of harmonically trapped (thermal) gases. Finally, the effects of the magnetic trap itself – which also confines Li atoms, albeit weakly – should be taken into account as well.

As I pointed out in Sec. 5.1, none of the (most common) analytical models existing in the literature incorporates all these effects, in particular the last two, potentially making the interpretation of our experimental observations unclear, and surely not straightforward. In this Section, I describe how they are instead taken into account in my simulations, providing a summary of the algorithm and of the most relevant equations employed. The code, written in Python, is available at the link in Ref. [203].

5.3.1 Numerical simulator: basic form

A first, fundamental approximation of the simulator is based on the fact that, for the transport experiments of this Chapter, the condition $N_{\text{Li}} \ll N_{\text{Cr}}$ generally holds: Namely, the lithium cloud is considered as a statistical ensemble of thermal impurities, which do not cause any (macroscopic) effect on the larger chromium bath. This assumption considerably reduces the computational effort required for the simulation, as only the trajectories of (a few $10^3 \div 10^4$) Li particles have to be computed, whereas the Cr gas is treated within a sort of *local-density approximation*. Secondly, the external confinement is incorporated through the harmonic approximation: This implies that, in the absence of collisions, the unperturbed motion of lithium atoms within the trap has an *exact analytical solution*, which does not require numerical integration of the equations of motion. Thirdly, as shown in Sec. 1.7, the coupled-channel model of A. Simoni (see Sec. 3.2) provides us with essentially complete knowledge of the two-body collisional properties of our mixture, which can be described – with remarkable accuracy – in terms of the simple analytic formulae of the *zero-range approximation*. This allows for a physically accurate modeling of (low-energy and pairwise) elastic *s*-wave collisions, including the effects of the mass imbalance, by employing the parameters characterizing the selected $|\text{Li}|1\rangle$ - $|\text{Cr}|1\rangle$ Feshbach

⁴Note that this is also in stark contrast to the “historical” standard scenario of Brownian motion, where the diffusing particle is typically orders of magnitude heavier than the surrounding fluid molecules.

resonance. Lastly, both Li and Cr atoms are always assumed to be *classical particles*, with well-defined positions and velocities, neglecting any effect of fermionic statistics nor quantum interference.

Before discussing the practical implementation of the program, an important remark should be made: The algorithm is essentially a discrete-time simulation, where the temporal axis is broken up into small time slices of equal length dt_{step} , and the state of the system is updated only after each step, according to the events happening in that time slice. Intuitively, the choice of dt_{step} may play an important role, and one generally expects a requirement for dt_{step} to be “sufficiently small”, although a compromise must be found in order to avoid exceedingly long computation times. This holds true also for my program (which is rather naive in terms of computational efficiency), albeit in a slightly subtle way: In fact, in most discrete-time physical simulations, the concerns about the optimal time step are mainly due to possible energy-conservation issues, especially when performing numerical integration of the equations of motion. However, the analytic solution of the harmonic oscillator, used in the basic form of the simulator (see below), ensures energy conservation (and exact results for the unperturbed motion) regardless of the choice of dt_{step} .

The main issue is instead connected with the evaluation of collision events: As better detailed in the following, in each time slice the probability that a given Li atom undergoes a collision is estimated from a *local* elastic scattering rate, evaluated from Eq. (1.6) as

$$\Gamma_{\text{el}}(x, y, z, k_{\text{rel}}) = n_{\text{Cr}}(x, y, z) \cdot \sigma_{\text{el}}(k_{\text{rel}}) \cdot \frac{\hbar k_{\text{rel}}}{m_{\text{red}}}, \quad (5.18)$$

where $n_{\text{Cr}}(x, y, z)$ is the local density of the chromium gas at the position of the Li atom, and $k_{\text{rel}} = m_{\text{red}}v_{\text{rel}}/\hbar$ is computed by randomly sampling a Cr atom from its velocity distribution. In the simulation, the dimensionless product $\Gamma_{\text{el}}(x, y, z, k_{\text{rel}}) \cdot dt_{\text{step}}$ quantifies then the collision probability for a Li atom during a given time slice. Importantly, to avoid underestimation of the number of collision events, the condition $\Gamma_{\text{el}}(x, y, z, k_{\text{rel}}) \cdot dt_{\text{step}} \leq 1$ must always be satisfied. This turns out to be the most stringent constraint on the choice of dt_{step} , which – for simulations at low temperatures and small magnetic field detunings, where the average Γ_{el} can reach $50 \div 100$ kHz – may need to be as small as $1 \div 2$ μs . On the other hand, for higher temperatures and relatively large $|\delta B| \gtrsim 20 \div 30$ mG (i.e. generally lower Γ_{el} values), satisfying the condition $\Gamma_{\text{el}}(x, y, z, k_{\text{rel}}) \cdot dt_{\text{step}} \leq 1$ results in much less stringent requirements, with suitable dt_{step} values of even $50 \div 100$ μs . In practice, to optimize the computation time, the program employs different time steps depending on the selected magnetic field detuning, with smaller dt_{step} for smaller $|\delta B|$, and vice versa.

Initialization

The program accepts as input the main parameters characterizing the initial atomic samples (see, e.g., those reported in Tab. 5.1), such as atom numbers, axial and radial *in situ* sizes of the two clouds, trap frequencies, and effective temperatures (where the latter are intended as measurements of the variance of the corresponding velocity distributions, $\sigma_v^2 = k_B T/m$). As anticipated, Li and Cr atoms are generally treated as classical particles, characterized by Maxwell-Boltzmann (i.e. Gaussian) distributions both in position and in momentum space. Further, only the trajectories of Li impurities are effectively computed, with the Cr gas essentially acting as an unperturbed thermal reservoir of particles.

The first step consists in generating the initial position and velocity distributions of the Li atoms. This is accomplished by exploiting an internal random-number generator (RNG) that directly returns Gaussian-distributed (pseudo-)random numbers. Specifically, for each simulated atom, six (pseudo-)random numbers are generated (based on the

sample parameters given in input), representing the initial values of the spatial coordinates ($x_0; y_0; z_0$) and velocities ($v_{0,x}; v_{0,y}; v_{0,z}$), respectively. These numbers are stored in arrays and then passed to the subsequent stage of the program, where they are used as the initial conditions to determine the solutions for the harmonic motion.

Unperturbed harmonic motion

The external (optical and magnetic) confinement is taken into account in the program within the harmonic approximation, with knowledge of the trap frequencies from previous experimental characterization. This implies that, without collisions, the particles move as harmonic oscillators, according to the laws of motion (e.g., for the \hat{x} direction):

$$x(t) = A_x \sin(\omega_x t + \phi_x), \quad (5.19a)$$

$$v_x(t) = A_x \omega_x \cos(\omega_x t + \phi_x), \quad (5.19b)$$

where ω_x is the trap frequency (in rad/s). In Eqs. (5.19), the constants A_x and ϕ_x are initially determined from the boundary conditions at $t = 0$, namely:

$$\phi_x = \arctan\left(\frac{\omega_x x_0}{v_{0,x}}\right), \quad (5.20a)$$

$$A_x = \frac{1}{\omega_x} \sqrt{v_{0,x}^2 + \omega_x^2 x_0^2}. \quad (5.20b)$$

The temporal axis is divided into small slices of equal length dt_{step} . At each time step, the positions and velocities of the lithium atoms are updated according to Eqs. (5.19), with analogous equations for the radial \hat{y} and \hat{z} directions.

The program keeps internal memory of the previously evaluated coordinates and velocities, and saves them (with a sampling of 0.5 ms) in a set of output files. However, it should be stressed that the propagation given by Eqs. (5.19) does not strictly rely on the knowledge of the coordinates at the previous step(s): Once A_x and ϕ_x are known, $x(t)$ and $v_x(t)$ can be evaluated for any t (assuming no collisions). In this sense, the choice of dt_{step} does not affect the “free” propagation. The previous coordinates (and velocities) are instead kept in memory for subsequent statistical analysis, such as evaluation of mean free path, mean free time, and autocorrelation functions.

In Fig. 5.7 I show the outcome of two different numerical simulations performed with collisions artificially disabled. For each dataset, the output files containing the x coordinates of all simulated Li atoms (sampled every 0.5 ms), are used to build histograms, out of which the cloud size s_x is extracted through Gaussian fits [with same conventions as in Eq. (5.14)]. The resulting time evolutions $s_x(t)$ show purely undamped breathing oscillations, perfectly described by the theory expectations of Eq. (5.7), given the relevant input parameters of each simulation (see caption), with no need for a fit. This excellent agreement between numerical simulations and theory represents a first, preliminary benchmark of the program, testifying that the unperturbed harmonic motion in the trapping potential is properly taken into account.

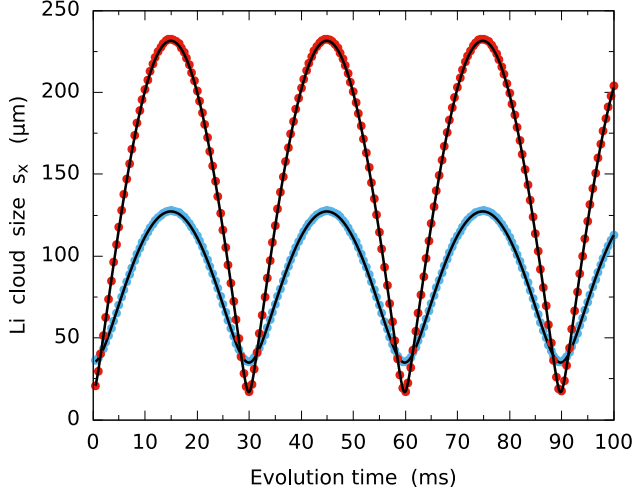


Figure 5.7 – Outcome of numerical simulations with collisions artificially disabled. The trajectory of each Li atom is computed according to Eqs. (5.19). Overall, the Li cloud undergoes purely undamped breathing oscillations, perfectly described by Eq. (5.7). Red (blue) points are obtained for $s_{0,x} = 17 \mu\text{m}$, $T_{0,x} = 430 \text{ nK}$ ($s_{0,x} = 35 \mu\text{m}$, $T_{0,x} = 130 \text{ nK}$), and $\omega_x = 2\pi \times 17 \text{ Hz}$. The black curves are simply plots of Eq. (5.7), with the nominal parameters of each dataset and no fitting performed. The excellent agreement between simulation and theory testifies that the unperturbed harmonic motion in the trap is properly taken into account.

Collision probability

For each time step, and for each simulated atom, after the “free” propagation given by Eqs. (5.19) has been carried out, the program checks for the probability of a collision to occur. As anticipated [see Eq. (5.18)], the algorithm first computes a *local* scattering rate

$$\Gamma_{\text{el}}(x, y, z, k_{\text{rel}}, \delta B) = n_{\text{Cr}}(x, y, z) \cdot \sigma_{\text{el}}(k_{\text{rel}}, \delta B) \cdot \frac{\hbar k_{\text{rel}}}{m_{\text{red}}}, \quad (5.21)$$

at the *current* position (x, y, z) of the selected Li atom. Specifically, in Eq. (5.21), the density profile of the chromium gas is described by the Gaussian envelope

$$n_{\text{Cr}}(x, y, z) = \frac{N_{\text{Cr}}}{(2\pi)^{3/2} s_{x,\text{Cr}} s_{y,\text{Cr}} s_{z,\text{Cr}}} \cdot \exp \left[-\frac{x^2}{2 s_{x,\text{Cr}}^2} - \frac{y^2}{2 s_{y,\text{Cr}}^2} - \frac{z^2}{2 s_{z,\text{Cr}}^2} \right], \quad (5.22)$$

with atom number N_{Cr} and $1/\sqrt{e}$ -radii $s_{\{x,y,z\},\text{Cr}}$ taken from the input parameters.

The *s*-wave elastic scattering cross section $\sigma_{\text{el}}(k_{\text{rel}}, \delta B)$ is evaluated from Eq. (1.13) as

$$\sigma_{\text{el}}(k_{\text{rel}}, \delta B) = \frac{4\pi a^2(\delta B)}{\left[1 + k_{\text{rel}}^2 R^*(\delta B) a(\delta B) \right]^2 + k_{\text{rel}}^2 a^2(\delta B)}, \quad (5.23)$$

with $a(\delta B)$ and $R^*(\delta B)$ given by Eqs. (1.18) and (1.21), respectively, and using the best-fitted parameters reported in Sec. 1.7.

Finally, the relative velocity v_{rel} , which determines the relative momentum $k_{\text{rel}} = m_{\text{red}} v_{\text{rel}}/\hbar$, is computed by randomly sampling a Cr atom from its thermal velocity distribution: In practice, the program generates three Gaussian-distributed (pseudo-)random numbers $v_{i,\text{Cr}}$ (with $i = x, y, z$), centered around zero and with variance $\sigma_{v_{i,\text{Cr}}}^2 = k_{\text{B}} T_{i,\text{Cr}}/M_{\text{Cr}}$ given by the input (effective) temperatures $T_{i,\text{Cr}}$. The relative velocity is then obtained as $v_{\text{rel}} = |\vec{v}_{\text{Li}} - \vec{v}_{\text{Cr}}|$.

Given the local scattering rate from Eq. (5.21), the collision probability is evaluated as $P_{\text{coll}} = \Gamma_{\text{el}}(x, y, z, k_{\text{rel}}, \delta B) \cdot dt_{\text{step}}$, which is a dimensionless positive number. In practice, the program generates a uniformly-distributed (pseudo-)random number $R_{\text{coll}} \in [0, 1]$, and compares it with P_{coll} : if $R_{\text{coll}} \leq P_{\text{coll}}$ the collision takes place, otherwise the algorithm goes directly to the next iteration.

Before discussing how the nature of *s*-wave collisions is taken into account, I stress the fact that, in order not to underestimate the number of scattering events, the time increment

dt_{step} must be chosen small enough to ensure that P_{coll} – each time is evaluated – is *always* less than 1, and thus it can be effectively used as a probability. In fact, *if*, during a given iteration, it happens that $P_{\text{coll}} > 1$, a collision will surely happen in that time step, since by definition $R_{\text{coll}} \leq 1$. However, the “excess probability” $\Delta P_{\text{coll}} = \max[(P_{\text{coll}} - 1), 0]$, in the current implementation, is not taken into account, ultimately resulting in (possibly large numbers of) missed collisions. While different solutions can in principle be conceived (e.g., carrying the excess probability to the next iteration step, or allowing for the possibility of consecutive collisions with probability given by ΔP_{coll}), I opted for the “brutal” strategy of reducing dt_{step} when needed, as it seemed to me the least ambiguous one.

The resulting requirement of $P_{\text{coll}} \leq 1$ to hold under any circumstance actually represents the most stringent constraint on the choice of dt_{step} . To clarify, P_{coll} also depends on the magnetic field detuning, which is known and fixed for every simulation, and – in a somewhat uncontrolled way – on the relative momentum k_{rel} , which is essentially a random quantity. Therefore, in principle, no predictions can be made *a priori* for the optimum dt_{step} , and one has to rely on a trial-and-error approach. In practice, the program keeps track of *all* the computed P_{coll} values and, for each magnetic field detuning, at the end of the simulation provides the maximum value $P_{\text{coll,max}}$, the average value $P_{\text{coll,avg}}$, and the number of occurrences in which the condition $P_{\text{coll}} \geq 1$ has been encountered (N_{flags}). From these values, one can optimize the choice of the time step for each simulated δB . Namely, dt_{step} is reduced until $P_{\text{coll,max}} < 1$ (and thus $N_{\text{flags}} = 0$). Moreover, a general rule of the thumb for a “safe” dt_{step} choice is to keep also $P_{\text{coll,avg}} \lesssim 0.1$. Typical values range from $dt_{\text{step}} = 50 \div 100 \mu\text{s}$ (far from resonance), down to $dt_{\text{step}} = 1 \div 2 \mu\text{s}$ (very close to resonance and for low temperatures).

Modeling of *s*-wave collisions

If the condition $R_{\text{coll}} \leq P_{\text{coll}}$ is satisfied, a collision event occurs. Collisions are modeled as elastic *s*-wave scattering, conserving the modulus of the relative momentum k_{rel} (i.e. of the relative velocity v_{rel}), while changing its spatial orientation with uniform probability across the solid angle. This is accomplished by generating two random angles θ^* and ϕ^* according to:

$$\theta^* = \arccos(\text{Rand}[-1, 1]) , \quad (5.24a)$$

$$\phi^* = \text{Rand}[0, 2\pi] , \quad (5.24b)$$

which in turn determine the new components of the relative velocity

$$v'_{\text{rel},x} = v_{\text{rel}} \cdot \sin(\theta^*) \cos(\phi^*) , \quad (5.25a)$$

$$v'_{\text{rel},y} = v_{\text{rel}} \cdot \sin(\theta^*) \sin(\phi^*) , \quad (5.25b)$$

$$v'_{\text{rel},z} = v_{\text{rel}} \cdot \cos(\theta^*) , \quad (5.25c)$$

with the prime used hereinafter to denote quantities evaluated after the collision. In Eqs. (5.24), the function $\text{Rand}[a, b]$ returns a uniformly-distributed (pseudo-)random number in the range $[a, b]$. It is important to realize that, since the element of solid angle is $d\Omega = d\cos\theta d\phi$, the correct way of generating the polar angle θ^* is indeed that given by (5.24a). By contrast, writing $\theta^* = \text{Rand}[0, \pi]$ would result instead in a non-spherically-symmetric distribution of the outgoing \vec{v}'_{rel} directions, even in the center-of-mass frame. By requiring (three-dimensional) momentum conservation in the lab frame, i.e.

$$m_{\text{Li}}\vec{v}_{\text{Li}} + M_{\text{Cr}}\vec{v}_{\text{Cr}} = m_{\text{Li}}\vec{v}'_{\text{Li}} + M_{\text{Cr}}\vec{v}'_{\text{Cr}} , \quad (5.26)$$

with $\vec{v}'_{\text{Cr}} = \vec{v}'_{\text{Li}} - \vec{v}'_{\text{rel}}$ and knowledge of \vec{v}'_{rel} from Eq. (5.25), one finds that the exit velocity \vec{v}'_{Li} of the Li atom is given by (e.g. for the x direction):

$$v'_{\text{Li},x} = \frac{\widetilde{M}(v'_{\text{rel},x} + v_{\text{Cr},x}) + v_{\text{Li},x}}{1 + \widetilde{M}}, \quad (5.27)$$

where $\widetilde{M} = M_{\text{Cr}}/m_{\text{Li}}$. From Eq. (5.27), one realizes that, even in the lab frame, the outgoing velocity of the lithium atom is essentially set by $\vec{v}'_{\text{rel}} + \vec{v}_{\text{Cr}}$, with “memory” of the previous \vec{v}_{Li} nearly entirely lost already after one collision.

Finally, before moving to the propagation for the next time step, the constants of motion A_x and ϕ_x are updated according to (and analogous for \hat{y} and \hat{z}):

$$\phi'_x = \arctan\left(\frac{\omega_x x'}{v'_{\text{Li},x}}\right) - \omega_x t^*, \quad (5.28a)$$

$$A'_x = \frac{1}{\omega_x} \sqrt{v'^2_{\text{Li},x} + \omega_x^2 x'^2}, \quad (5.28b)$$

where t^* is the time at which the collision happened, and $x' = x$. In other words, collisions are treated as *local and instantaneous events* that do not change the coordinates of the particles, but only their velocities.

The new values of A'_x and ϕ'_x (as well as those obtained for the other two directions) are then used in Eqs. (5.19) for the subsequent propagation, until a new collision occurs.

5.3.2 Wigner’s retardation time

Besides properly accounting for the unperturbed oscillatory motion (see again Fig. 5.7), the numerical simulator in its basic form (i.e., as described in the previous Sec. 5.3.1), reproduces our high-temperature experimental data almost perfectly, as I will show in Sec. 5.4. However, when tested against low-temperature datasets, the agreement becomes poorer, especially close to the resonance pole: In particular, the simulator never yields anomalous exponents $\alpha < 1$, i.e. it does not account for the experimentally observed *subdiffusive* behavior. This discrepancy motivated me to attempt the implementation of new features, mainly trying to introduce some “quantumness” in my (otherwise basically classical) program. Following a suggestion from D. Petrov, the first implemented “quantum correction” was *Wigner’s retardation time* [204]. In this Section, I briefly recall this concept, and discuss its implementation within my code.

Following Eisenbud’s idea [204], a nonzero energy derivative of the scattering phase shift can be interpreted as a *time delay*. Building on this concept, Wigner described the retardation time experienced by a *free particle* scattering off a *fixed* scattering center [204]. If the particle moves with velocity v (momentum $\hbar k$), and undergoes elastic scattering, its trajectory after the collision is “delayed” by a quantity [205]

$$\Delta t_{\text{ret}} = \frac{1}{v} \frac{d\delta(k)}{dk}, \quad (5.29)$$

where $\delta(k)$ is the scattering phase shift. Note that Δt_{ret} can take either positive or negative values: The former case represents situations in which the particle gets “trapped” by the scatterer, whereas the latter one describes scenarios where the particle hardly enters the scattering region. There is no upper bound for Δt_{ret} (i.e. the trapping time can be arbitrarily long), however, since causality must hold, there exists a lower bound set by the “effective radius” R_a of the scatterer: $\Delta t_{\text{ret}} \geq -2R_a/v$.

In the case of a narrow s -wave Feshbach resonance, for low-energy collisions one has [see Eq. (1.11)]:

$$\cot(\delta_0(k_{\text{rel}})) = -\frac{1}{k_{\text{rel}} a} - k_{\text{rel}} R^*, \quad (5.30a)$$

$$\frac{d\delta_0(k_{\text{rel}})}{dk_{\text{rel}}} = a \frac{(k_{\text{rel}}^2 R^* a - 1)}{(1 + k_{\text{rel}}^2 R^* a)^2 + k_{\text{rel}}^2 a^2}. \quad (5.30b)$$

By generally defining the scatterer “effective radius” from the elastic cross section as [see Eq. (1.13)]:⁵

$$R_a = \sqrt{\frac{\sigma_{\text{el}}}{4\pi}} = \frac{|a|}{\sqrt{(1 + k_{\text{rel}}^2 R^* a)^2 + k_{\text{rel}}^2 a^2}}, \quad (5.31)$$

one can see that causality is automatically never violated. Figure 5.8 shows a two-dimensional plot of Δt_{ret} , obtained by inserting Eq. (5.30b) in Eq. (5.29) and using the parameters characterizing the selected Li|1)-Cr|1) FR. As one can notice, for low relative momenta, $|\Delta t_{\text{ret}}|$ can assume fairly large values exceeding 100 μs . In general, the retardation time is *positive* ($\Delta t_{\text{ret}} > 0$) when either $a < 0$ or $a > 1/(k_{\text{rel}}^2 R^*)$, and *negative* ($\Delta t_{\text{ret}} < 0$) for $0 < a < 1/(k_{\text{rel}}^2 R^*)$; see the black curve in Fig. 5.8.

Given Eqs. (5.29) and (5.30b), the implementation of the retardation time for a free particle bouncing off a fixed scatterer is rather straightforward. However, in my numerical simulator the particles (i.e. Li atoms) are trapped in a harmonic potential, and the scattering centers (i.e. Cr atoms) are generally moving, thus more careful considerations are required. My approach to include retardation effects starts from the fact that scattering theory, by construction, provides meaningful information solely in the “far-field” (i.e., for $r \rightarrow \infty$), absorbing all the short-range dynamics in the phase shift(s). From this viewpoint, Wigner’s retardation effects are equivalent to a model where the particle, undergoing the scattering event at $t = t^*$, is *destroyed*, and a *new particle* is created somewhere in the vicinity of the scattering center, such that the new particle’s trajectory passes from the scatterer’s position at $t' = t^* + \Delta t_{\text{ret}}$; see the sketches in Figs. 5.9(a) and 5.9(b).

In the simpler case of a harmonically-trapped Li atom colliding with a *fixed* Cr scatterer (i.e. not moving and not recoiling), it is immediate to see that, after having computed the

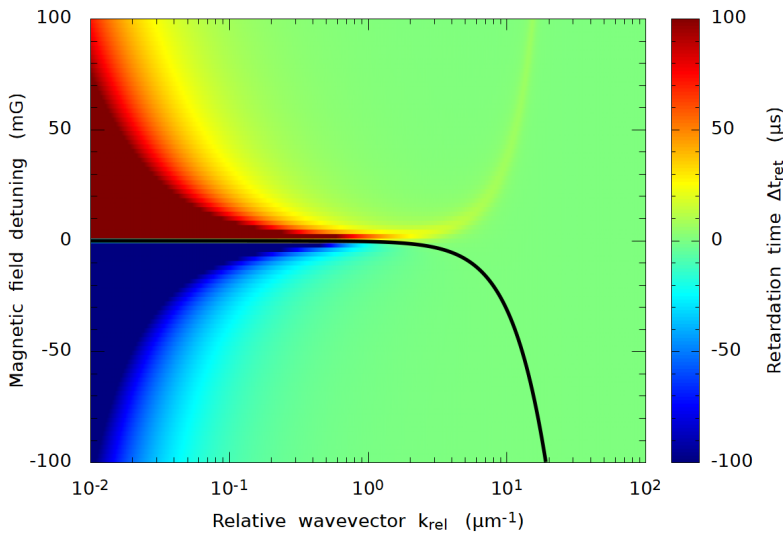


Figure 5.8 – 2D plot of the retardation time Δt_{ret} , as a function of k_{rel} and δB . The plot is obtained by using Eq. (5.30b) in Eq. (5.29), with the specific $a(\delta B)$ and R^* characterizing the selected Li-Cr FR, and an average density of 10^{12} cm^{-3} . The black curve represents the condition $k_{\text{rel}}^2 R^* a = 1$, and separates positive (above) from negative (below) values of Δt_{ret} .

⁵Note that, far from resonance, one retrieves the textbook result $R_a \simeq |a|$.

constants A'_x and ϕ'_x according to Eqs. (5.28) (i.e. *without* the effect of the retardation time), one can simply use

$$\phi'_{x,\text{ret}} = \phi'_x - \omega_x \Delta t_{\text{ret}} \quad (5.32)$$

in place of ϕ'_x to obtain the desired far-field effect of Δt_{ret} . Interestingly, in this case a “retarded” collision causes a phase shift of the phase-space trajectory, see Fig. 5.9(c) and Fig. 5.9(d).

More generally, if the Cr scatterer is allowed to move, all the above considerations should instead be applied to the *relative particle*, which should pass from the center of mass (c.o.m.) position at time $t' = t^* + \Delta t_{\text{ret}}$. In this case, *assuming that the c.o.m. motion is not affected by the collision*,⁶ the program first computes the Li and Cr outgoing trajectories *without* the effect of the retardation time, i.e. using Eqs. (5.28) and analogue ones for Cr. From these, one obtains the c.o.m. position and velocity at time t' :

$$x_{\text{com}}(t') = \frac{m_{\text{Li}}x'_{\text{Li}}(t') + M_{\text{Cr}}x'_{\text{Cr}}(t')}{m_{\text{Li}} + M_{\text{Cr}}}, \quad (5.33a)$$

$$v_{\text{com},x}(t') = \frac{m_{\text{Li}}v'_{\text{Li},x}(t') + M_{\text{Cr}}v'_{\text{Cr},x}(t')}{m_{\text{Li}} + M_{\text{Cr}}} = \frac{m_{\text{Li}}v^{\text{ret}}_{\text{Li},x}(t') + M_{\text{Cr}}v^{\text{ret}}_{\text{Cr},x}(t')}{m_{\text{Li}} + M_{\text{Cr}}}. \quad (5.33b)$$

Then, by further assuming that – at the time $t' = t^* + \Delta t_{\text{ret}}$ – the relative particle emerges from the c.o.m. position with the *same* (relative) velocity \vec{v}'_{rel} it would have had (at the time

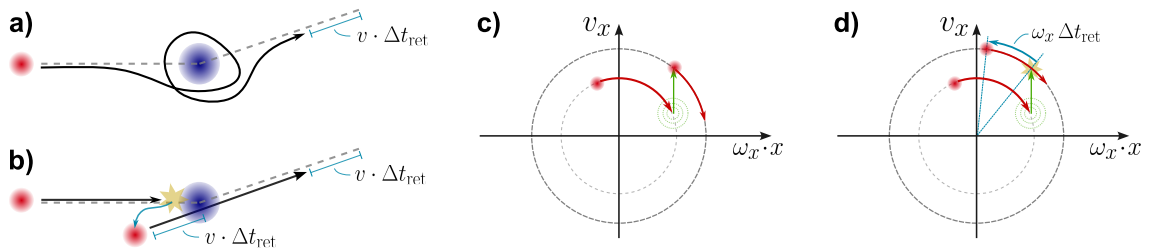


Figure 5.9 – Implementation of Wigner’s retardation time in the numerical simulation. (a) Sketch of a “retarded” collision in free space (with $\Delta t_{\text{ret}} > 0$), according to Wigner’s picture. The particle remains “trapped” around the scattering center for a finite time Δt_{ret} and then leaves, following its “unretarded” trajectory but carrying an overall delay. (b) In the far-field, the above situation is equivalent to a process in which the initial red particle is destroyed by the collision, and a new particle is created at a different position near the scattering center, such that the new particle’s trajectory reproduces the delay effect. (c) Representation of a basic (“unretarded”) s -wave collision in the phase-space cut (\hat{x}, \hat{v}_x) . As discussed in Sec. 5.3.1, standard collision events are assumed to be instantaneous, and to leave the position of the particles unchanged. In the c.o.m. frame, the modulus of the relative velocity is conserved. In the lab frame, the velocities of the colliding particles generally change. This is represented by the “jump” of the red particle from one orbit to another, in this case increasing the v_x component of its velocity. (d) Phase-space representation of the implementation of a “retarded” s -wave collision, in the simpler case in which the scattering center is fixed. The red particle first jumps to a different orbit similarly to panel (c), but its new trajectory is delayed by a phase $\omega_x \Delta t_{\text{ret}}$, in analogy with the sketch of panel (b).

⁶An important remark should be made here: Strictly speaking, in the two-body scattering problem, separation of center of mass and relative motion is only valid in free space, or for $\omega_1 = \omega_2$ in a harmonic trap. Here ω_1 and ω_2 are the trap frequencies of the two particles. In the general case $\omega_1 \neq \omega_2$, c.o.m. and relative degrees of freedom are coupled, see e.g. Refs. [206, 207]. In particular, this holds true also in our system, as generally $\omega_{\text{Li}} \neq \omega_{\text{Cr}}$. However, the effects of the coupling between c.o.m. and relative motion are typically relevant only for extremely tight traps, such as optical lattice sites or tweezers. In our case, instead, both ω_{Li} and ω_{Cr} , as well as their difference, are typically less than $2\pi \times 500$ Hz, and thus for simplicity I decided to neglect any coupling effect between c.o.m. and relative particle. This was implicit also in the “basic” implementation of s -wave collisions described in the previous Sec. 5.3.1.

t^* of the collision) *without* the effect of the retardation time [i.e., as given by Eqs. (5.25)], one finds that the outgoing “retarded” trajectory of the Li atom should satisfy:

$$x_{\text{Li}}^{\text{ret}}(t') = x_{\text{com}}(t'), \quad (5.34a)$$

$$v_{\text{Li},x}^{\text{ret}}(t') = v_{\text{com},x}(t') + \frac{\widetilde{M}}{1 + \widetilde{M}} v'_{\text{rel},x}. \quad (5.34b)$$

From these two conditions, in complete analogy to Eqs. (5.28), one obtains the new constants of motion

$$\phi_x^{\text{ret}} = \arctan\left(\frac{\omega_x x_{\text{Li}}^{\text{ret}}(t')}{v_{\text{Li},x}^{\text{ret}}(t')}\right) - \omega_x t', \quad (5.35a)$$

$$A_x^{\text{ret}} = \frac{1}{\omega_x} \sqrt{(v_{\text{Li},x}^{\text{ret}}(t'))^2 + (\omega_x x_{\text{Li}}^{\text{ret}}(t'))^2}. \quad (5.35b)$$

In summary, according to this receipt, the Li atom – which undergoes a collision event at time t^* , happening at position x_{Li} , with initial velocity $v_{\text{Li},x}$ – emerges *instantaneously* from the collision (i.e. at the same time $t = t^*$), but with new position and velocity given by

$$x_{\text{Li}}^{\text{ret}}(t^*) = A_x^{\text{ret}} \sin(\omega_x t^* + \phi_x^{\text{ret}}), \quad (5.36a)$$

$$v_{\text{Li},x}^{\text{ret}}(t^*) = A_x^{\text{ret}} \omega_x \cos(\omega_x t^* + \phi_x^{\text{ret}}); \quad (5.36b)$$

i.e., those obtained by using Eqs. (5.35) in the laws of motion Eqs. (5.19). Note that, contrarily to the case of fixed scattering centers [see again Eq. (5.32)], here the effect of the retardation time is not a simple delay of the new phase-space trajectory (although this remains true for the relative particle), since generally also the amplitude A_x changes.

Evaluation of Eqs. (5.35) essentially concludes the procedure to implement retardation effects, and also the part of the code related to collisions in general. From this point on, the program goes to the next iteration, i.e. the propagation of the harmonic motion given by Eqs. (5.19) for the subsequent dt_{step} , using the new constants A_x^{ret} and ϕ_x^{ret} and analogous ones for the other two directions.

I conclude this Section by briefly mentioning that retardation effects can be enabled or disabled with a global option found in the initial settings. Moreover, a slightly different implementation is available: In the case of *positive* retardation times $\Delta t_{\text{ret}} > 0$, one can choose to disable further collisions for the entire duration of the “trapping time”, i.e. in the time interval $t^* < t < t^* + \Delta t_{\text{ret}}$. This variation was proposed as an attempt to “mimic” the formation of a temporary, metastable dimer state [see qualitative sketch in Fig. 5.9(a)], forcing the complete blocking of atom-dimer collisions for simplicity. The two implementations differ only slightly in terms of the resulting evolution of the MSD, but the second one (by construction) causes a noticeable decrease of the number of collision events.

5.4 The “high-temperature” regime

As anticipated in the introduction, our transport experiments were initially aimed at measuring the diffusion coefficient D_1 by focusing, in particular, on the regime of high temperatures (and strong interactions). This seemed a reasonable starting point for the investigation of transport phenomena in our system: First, the thermal regime appears intuitively easier to understand than the quantum-degenerate one, as fermionic statistics is expected to play a minor role and the atomic clouds are well described by Maxwell-Boltzmann distributions. Second, from a practical point of view, one desires to maximize the observation time, in order to get more reliable information on the transport coefficients. In our experimental configuration, the effective observation time is limited by the finite axial extension of the chromium cloud, which acts as a medium for the “diffusing” (broadly speaking) lithium atoms. Indeed, once these latter reach the tails of the Cr density distribution, they are essentially free to escape along the axial direction, subsequently moving ballistically within the external trapping potential. Consequently, to extend the observation time window, we decided both to enlarge the size of the chromium cloud, finding a compromise with the corresponding density drop, and to significantly compress the initial Li gas along the axial direction, employing high optical powers in the 1560-nm vertical beam.

In practice, to obtain larger axial sizes of the Cr cloud, we lowered the efficiency of the “Feshbach cooling” stage (see Sec. 2.7). This can be easily done by increasing the magnetic field detuning with respect to the optimum one that yields the maximum Cr PSD, see Fig. 2.9(c). As shown in Figs. 2.9(a) and 2.9(b), a decreased sympathetic cooling efficiency results in higher final temperatures of the Cr gas (and thus larger axial extensions of the Cr cloud, albeit not shown there), but also in larger atom numbers. In terms of particle density, these two effects nearly compensate each other, such that the average n_{Cr} remains roughly constant. Such a non-optimal sympathetic cooling stage generates (non-fully-thermalized) chromium samples that exhibit different velocity distributions along the radial and the axial directions, with typical “effective axial temperatures” of about $T_{x,\text{Cr}} \sim 0.7 \div 1$ μK .

On the other hand, to better clarify the meaning of “high temperatures” for what concerns the Li component – as well as the effects of an increased initial axial confinement on the subsequent dynamics – it is instructive to have a closer inspection of Eq. (5.7), i.e. the formula that describes the undamped breathing mode triggered by the sudden switch off of the vertical beam, which for convenience I report here in the form

$$s_x(t) = s_0 \cdot \sqrt{\cos^2(\omega_x t) + A^2 \sin^2(\omega_x t)}, \quad (5.37)$$

with $A = \omega_0/\omega_x$, where ω_0 and ω_x are the initial and final trap frequencies, respectively. In our case, for Li atoms, $\omega_x \simeq 2\pi \times 17$ Hz (from the magnetic confinement) and $\omega_0^2 = \omega_x^2 + \omega_{1560}^2$, with ω_{1560} being the trap frequency induced by the vertical beam. In the limit $\omega_x t \ll 1$, we can approximate Eq. (5.37) with

$$s_x(t) \simeq \sqrt{s_0^2 + s_0^2 \omega_x^2 (A^2 - 1) t^2}, \quad (5.38)$$

which has the familiar form of ballistic time of flight, where the quantity $s_0^2 \omega_x^2 (A^2 - 1) = s_0^2 (\omega_0^2 - \omega_x^2)$ plays the role of the variance of the velocity distribution, with a corresponding “release temperature”

$$T_{x,\text{rel}} = \frac{m_{\text{Li}}}{k_{\text{B}}} s_0^2 (\omega_0^2 - \omega_x^2). \quad (5.39a)$$

At the same time, for Maxwell-Boltzmann gases, the “real” temperature T_0 of the system is connected to the initial size and trap frequency by $s_0^2 = k_B T_0 / (m_{\text{Li}} \omega_0^2)$, implying that

$$T_{x,\text{rel}} = T_0 \cdot \left(1 - \frac{\omega_x^2}{\omega_0^2} \right). \quad (5.39b)$$

Note that, from Eqs. (5.39), for $\omega_0 \gg \omega_x$ (strong trap frequency mismatch) one has $T_{x,\text{rel}} \simeq T_0$, whereas in the opposite limit $\omega_0 \simeq \omega_x$ (negligible mismatch) one finds $T_{x,\text{rel}} \simeq 0$, regardless of T_0 . In other words, in the absence of Li-Cr interactions, $1/2 k_B T_{x,\text{rel}}$ quantifies the “release energy” of the Li gas, which drives the axial breathing mode caused by the sudden change in the trap frequency. This can be easily realized by backward reasoning, noticing that, for $\omega_0 = \omega_x$ (i.e. $A = 1$), Eq. (5.37) yields a steady $s_x(t) = s_0$, i.e. no dynamics.⁷ For the “high-temperature” dataset discussed in this Section, the initial Li axial trap frequency (size) was around $\omega_0 \simeq 2\pi \times 220$ Hz ($s_0 \simeq 17$ μm), yielding a release temperature of about $T_{x,\text{rel}} \simeq 400$ nK. By contrast, for the “low-temperature” dataset of the next Sec. 5.5, with initial axial trap frequency $\omega_0 \simeq 2\pi \times 60$ Hz and *in situ* size $s_0 \simeq 30 \div 35$ μm , the release temperature was on the order of $T_{x,\text{rel}} \simeq 100(20)$ nK, i.e. about three-to-four times lower.⁸ Importantly, however, I anticipate here that, somehow contrarily to what we originally expected, the *initial* temperature of the lithium gas was found to play only a minor (if not negligible) role in our transport experiments, especially in the “interesting” (i.e. strongly-interacting) region close to the FR pole. The reason is that, for very small detunings, the average elastic scattering rate per Li atom can reach values on the order of tens of kHz, implying a nearly instantaneous thermalization with the surrounding Cr particles. The large number imbalance $N_{\text{Cr}} \gg N_{\text{Li}}$ ensures that the Cr bath remains essentially unaffected by the energy exchanged with the Li impurities, and thus the equilibrium temperature of the system is entirely set by T_{Cr} . In this sense, for the “high temperature” dataset of this Section, the mean Cr temperature $\bar{T}_{\text{Cr}} = 1/3(T_{x,\text{Cr}} + T_{y,\text{Cr}} + T_{z,\text{Cr}})$ was around 600 nK, with a density-averaged density $\langle n_{\text{Cr}} \rangle_{\text{Li}} \simeq 0.4 \times 10^{12}$ cm^{-3} . For the “low temperature” dataset presented in the next Sec. 5.5, instead, the Cr bath was characterized by $\bar{T}_{\text{Cr}} \sim 400$ nK and $\langle n_{\text{Cr}} \rangle_{\text{Li}} \simeq 0.6 \times 10^{12}$ cm^{-3} . While at first glance the difference may not appear substantial, in the next Sections I will discuss its importance more quantitatively.

After this premise on the meaning of “low” and “high” temperatures in the context of our transport measurement, I now move to present our experimental observations for the high- T dataset. We prepared our samples following the procedure detailed in Sec. 5.2, and we subsequently monitored the first 20 ms of the lithium expansion for different magnetic field detunings. We mainly focused on the root-mean-square displacement of the Li cloud, $s_x = \sqrt{\langle x^2 \rangle}$, extracted from the absorption images through two-dimensional Gaussian fits with the conventions of Eq. (5.14). For this dataset, we tested and employed both the data acquisition approaches sketched in Fig. 5.6(a). First, to give an overall picture, in Fig. 5.10 I show the “spectra” of $s_x(\delta B)$ recorded at fixed evolution times t_{fix} (filled circles). For $|\delta B| \gtrsim 50$ mG, i.e. far from resonance, the MSD grows ballistically in time, showing no significant trend with the magnetic field detuning. By contrast, for smaller detunings $|\delta B| \lesssim 30$ mG, we observe a considerable slowdown of the Li expansion, with

⁷An alternative and more rigorous approach, not reported here for sake of conciseness, is based on the comparison between the total mechanical energies before and after the instantaneous change of the trap frequency. Basically, when this happens, the sample is (possibly strongly) out of equilibrium in the new trap configuration. This can be seen as an *excess* kinetic energy ΔE_{kin} (even though energy is effectively *subtracted* from the system!), and it can be easily shown that $\Delta E_{\text{kin}} = 1/2 k_B T_{x,\text{rel}}$, with $T_{x,\text{rel}}$ given by Eqs. (5.39).

⁸Note that, given the functional form of Eq. (5.37), the initial trap frequency ω_0 – and thus the “release temperature” $T_{x,\text{rel}}$ – can be readily derived from a measurement of s_0 and $s_x(t = \pi/2\omega_x) = s_0 A$, provided ω_x is already known.

$s_x(\delta B)$ exhibiting a pronounced minimum at a small, positive detuning of about $+7(2)$ mG. As discussed in Sec. 1.5, this owes to the narrow character of the s -wave FRs at our disposal, which (for all finite relative momenta) shifts the peak of the elastic scattering cross section to the attractive side of the resonance [see Eq. (1.22) and Fig. 1.1], in our case corresponding to $\delta B > 0$. Remarkably, our observation matches the theoretical results of Sec. 1.5 quantitatively well: For a narrow resonance, a (relative) momentum class k_{rel} reaches the unitary-limited condition when $k_{\text{rel}}^2 = -1/(a R^*)$. Given the trend of $a(\delta B)$ [see Eq. (1.18)], for small detunings $\delta B \ll \Delta_B$ we have $k_{\text{rel}}^2 \simeq \delta B / (R^* a_{\text{bg}} \Delta_B)$ [or, in other terms, $\hbar^2 k_{\text{rel}}^2 / (2 m_{\text{red}}) = \delta \mu \delta B$, using Eq. (1.20)]. This means that, for atom pairs colliding with relative momentum k_{rel} , the “optimum” detuning that yields the maximum scattering

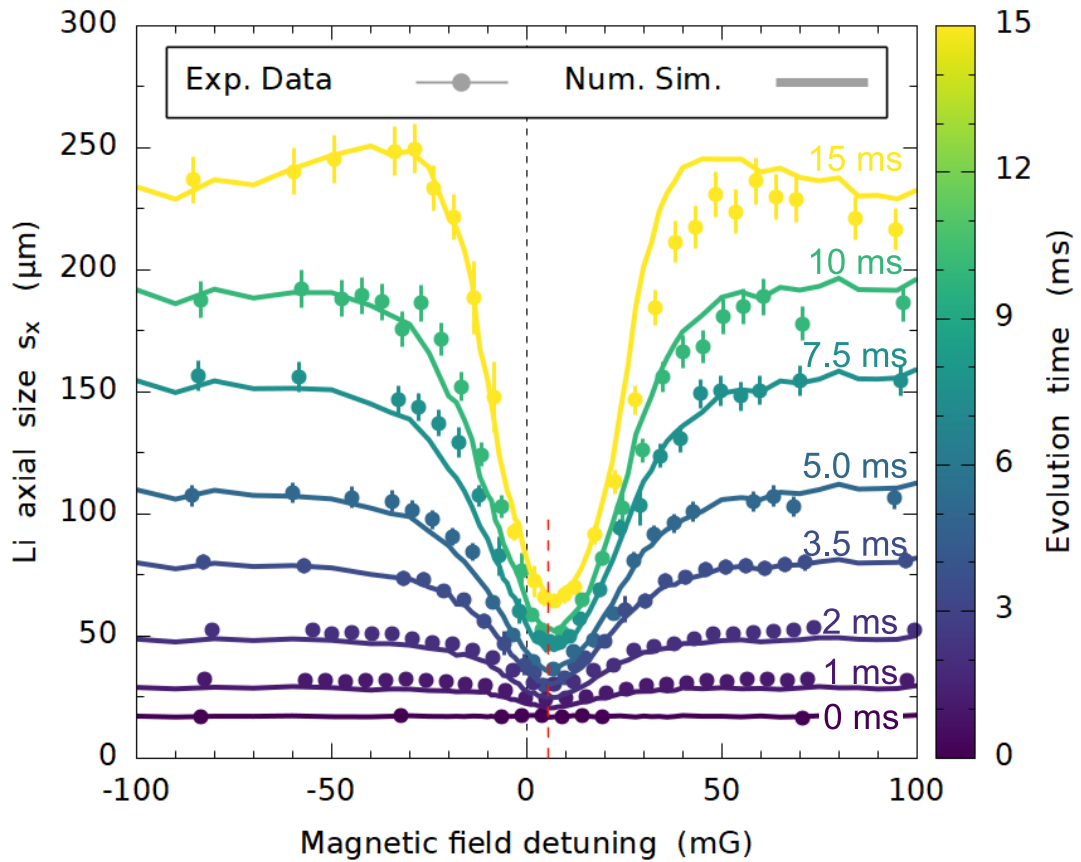


Figure 5.10 – High-temperature dataset: Axial root-mean-square size s_x of the Li cloud as a function of the magnetic field detuning, for different (fixed) evolution times t_{fix} , see the color scale. The filled circles are the experimental results. Each point represents the average of at least three independent measurements, with the error bars indicating the standard deviation of the mean. The red dashed arrow marks the position of the optimum detuning δB_{opt} , estimated from Eqs. (5.40) and (5.41b) with $\bar{T}_{\text{Cr}} = 600$ nK, which quantitatively matches our experimental observation. The solid lines represent instead the outcome of my simulation, run with the sole “basic ingredients” described in Sec. 5.3.1, with the input parameters reported in Tab. 5.2. Here inclusion of retardation effects and mean-field interactions does not change appreciably the simulation results. Importantly, the almost perfect agreement between simulation and experiment constitutes the first meaningful benchmark for my numerical model, and indicates that our experimental observations in this temperature regime can be explained and understood in terms of elastic two-body s -wave collisions only.

cross section is

$$\delta B_{\text{opt}} \simeq R^* a_{\text{bg}} \Delta_B k_{\text{rel}}^2. \quad (5.40)$$

At the same time, for a (thermal) heteronuclear mixture in a harmonic trap, the thermally-averaged modulus of relative velocity is given by [208]

$$\langle v_{\text{rel}} \rangle = \sqrt{\frac{8 k_B}{\pi} \left(\frac{T_1}{m_1} + \frac{T_2}{m_2} \right)}, \quad (5.41a)$$

where T_i and m_i are, respectively, the temperatures and masses of species 1 and 2. In our case, as discussed above, at small detunings the fast thermalization rates and large number imbalance imply that $T_{\text{Li}} = T_{\text{Cr}}$ essentially already from the start of the measurement, regardless of the initial T_{Li} . Therefore we have

$$\langle v_{\text{rel}} \rangle = \sqrt{\frac{8 k_B}{\pi} \left(\frac{T_{\text{Cr}}}{m_{\text{Li}}} + \frac{T_{\text{Cr}}}{M_{\text{Cr}}} \right)}. \quad (5.41b)$$

For $T_{\text{Cr}} = \bar{T}_{\text{Cr}} = 600$ nK, from Eq. (5.41b) one finds $\langle k_{\text{rel}} \rangle = m_{\text{red}} \langle v_{\text{rel}} \rangle / \hbar \simeq 4 \mu\text{m}^{-1}$. Inserting this value in Eq. (5.40), together with the parameters characterizing the selected Li|1>-Cr|1) FR ($a_{\text{bg}} = 41.5 a_0$, $R^* = 6020 a_0$, $\Delta_B = 477$ mG), one obtains $\delta B_{\text{opt}} \simeq +6$ mG, nicely matching the position of the observed minimum of $s_x(\delta B)$, see the red dashed line in Fig. 5.10.

I anticipate here that, as it can be noticed in Fig. 5.10 (solid lines, with same color code as the experimental points), the numerical simulator I developed – with the sole basic ingredients described in Sec. 5.3.1, and with input parameters fixed to those measured on the atomic clouds (see Tab. 5.2) – is able to reproduce *quantitatively* our experimental results in this temperature regime, with an almost perfect agreement at all times and magnetic field detunings explored. This already suggests that, at these temperatures, the sole mechanism of two-body elastic *s*-wave collisions (at a narrow resonance) suffices to account for our experimental observations.

A more quantitative analysis of the experimental data acquired as in Fig. 5.10 is difficult to obtain. In fact, as discussed in Sec. 5.1, diffusion processes are better characterized in the time domain, i.e. from the temporal evolution of the MSD. However, we found it rather challenging to extract $s_x^2(t)$ from the spectra of Fig. 5.10, owing to the extreme sensitivity of the outcome to small (\sim mG level) relative shifts of the horizontal axes between different datasets, in particular in the region where $s_x(\delta B)$ is steeply decreasing. We therefore acquired another set of measurements in this temperature regime, following the “brute-force” approach depicted in Fig. 5.6(a). The experimentally measured time traces $s_x(t)$ are shown in Fig. 5.11(a) for various δB values (see color scale). As one can notice, the slowest expansions are observed for small positive detunings (darker blue circles), in complete analogy to the data of Fig. 5.10. Moreover, small negative detunings (darker red triangles) generally feature significantly higher expansion rates compared to positive ones. Finally, time evolutions acquired at large detunings (gray symbols), either positive or negative, show a decrease of $s_x(t)$ for $t > 15$ ms, which is the expected behavior for vanishing interactions, according to Eq. (5.37) or, more generally, to Eq. (5.6a). Indeed, in the absence of collisions, $s_x(t)$ reaches its maximum value for $\tau = \pi/(2\omega_x)$ (and any other odd multiple of τ), corresponding in our case to 14.7 ms.

In order to better characterize the observed dynamics, as well as to obtain quantitative estimates of the transport coefficients, we fitted the data of Fig. 5.11(a) with the generalized power law model Eq. (5.8). Examples of best fits are shown in Fig. 5.11(c), plotted in double log scale after subtraction of the initial size to emphasize their temporal scaling

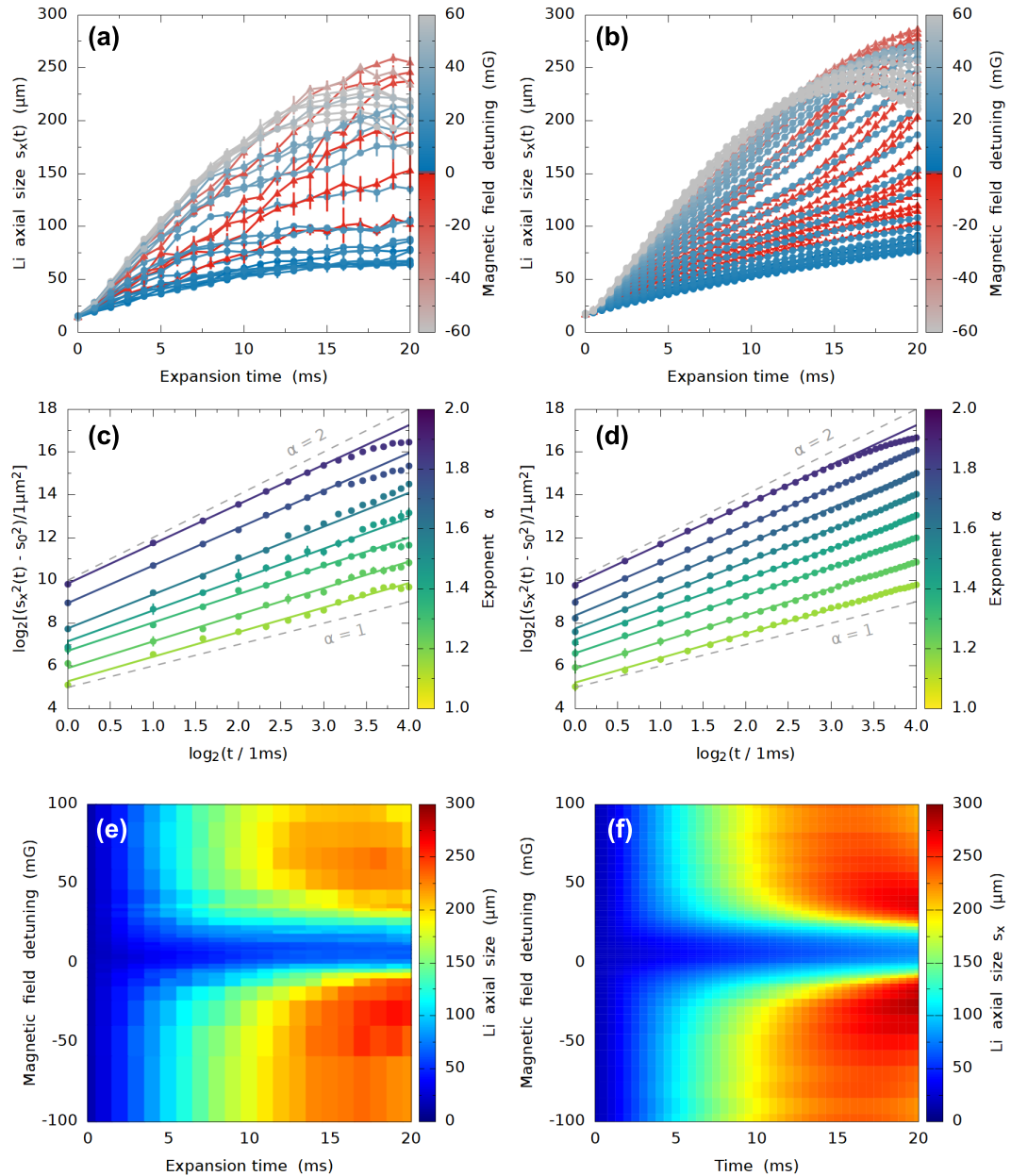


Figure 5.11 – Experimental and numerical results for the high-temperature dataset. (a) Experimental time evolutions of the Li axial size $s_x(t)$, acquired for different magnetic field detunings (see color scale). The lines connecting the points here are merely guides to the eye. (c) Examples of best fits with the generalized power law model Eq. (5.8), with the anomalous exponent α setting the color scale. The data show the transition from the ballistic ($\alpha \simeq 2$) to the diffusive ($\alpha \simeq 1$) regime. Each trace is arbitrarily displaced on the vertical direction for display purposes. The gray dashed lines are guides to the eye showing the expected slopes for $\alpha = 1$ and $\alpha = 2$. (e) Same data of panel (a), but plotted as a 2D heat map (“spectrogram”) to provide an alternative visualization of the temporal evolution $s_x(t, \delta B)$ for different detunings. Panels (b), (d), and (f) are the analogous of panels (a), (c), and (e), respectively, but for the numerical data obtained with my simulator. The input parameters, reported in Tab. 5.2, correspond to those measured on the atomic samples, within experimental uncertainty. As for the spectra shown in Fig. 5.10, the remarkable agreement between simulation and experiment let us conclude that, in this regime, our observations can be understood on the basis of the sole “basic ingredients” described in Sec. 5.3.1. The numerical data shown here are obtained from the same simulation run that yielded those presented previously in Fig. 5.10.

(set by the anomalous exponent α , see color scale). Notably, Eq. (5.8) provides fairly good fits to our experimental data, in particular when $\alpha \lesssim 1.5$. Time traces featuring $\alpha > 1.5$ (obtained for large $|\delta B|$ values) show instead deviations from the trend of Eq. (5.8) at long observation times [$t > 8$ ms, corresponding to abscissa values $x > 3$ in Fig. 5.11(c)]. For these latter, we restricted the fitting region to $t \leq 8$ ms. Moreover, a vertical limit was also applied to exclude points where the root-mean-square axial size of the Li cloud exceeded that of the Cr one, which for this high-temperature dataset was constantly around $s_{x,\text{Cr}} \simeq 130$ μm .

According to the characterization provided by Eq. (5.8), in the time window of our measurements and in terms of the anomalous exponent α , we observe a progressive transition from a ballistic ($\alpha \simeq 2$) to a diffusive ($\alpha \simeq 1$) dynamics, signaled in Fig. 5.11(c) by the logarithmic slope gradually changing between these two boundaries (see gray dashed lines). The complete results of the fits with the generalized power law Eq. (5.8), in terms of the exponent α and the generalized diffusion coefficient D_α , are shown in Figs. 5.12 and 5.12, respectively, where they are plotted as a function of the magnetic field detuning (colored circles). Qualitatively, both trends strongly resemble those obtained for the “spectra” of Fig. 5.10: As the resonance region is approached, and thus the Li-Cr scattering rate is enhanced, the early-time evolution of the MSD gradually changes from ballistic to diffusive, as quantified by the anomalous exponent α . In parallel, at first glance surprisingly, the generalized diffusion coefficient is found to drop by more than two orders of magnitude. Such a large dynamic range is strictly related to the unconventional units of D_α : In fact, as one can notice from Eq. (5.8), the SI units of the generalized diffusion coefficient are $[D_\alpha] = \text{m}^2/\text{s}^\alpha$. In our experiments, we measure the MSD in μm^2 and the evolution time in ms, such that $[D_{\alpha,\text{exp}}] = \mu\text{m}^2/\text{ms}^\alpha$. However, in the literature [209], D_α is typically normalized to the “quantum of diffusion” \hbar/m , where m is the mass of the particle, and thus expressed in $[\tilde{D}_\alpha] = [D_\alpha/(\hbar/m)] = \text{s}^{1-\alpha}$. Note that, for $\alpha = 1$ (normal diffusion), \tilde{D}_1 is a dimensionless quantity. In our case, the conversion from $\mu\text{m}^2/\text{ms}^\alpha$ to $\text{s}^{1-\alpha}$ reads

$$\tilde{D}_\alpha [\text{s}^{1-\alpha}] = \frac{D_\alpha [\text{m}^2/\text{s}^\alpha]}{\hbar/m_{\text{Li}}} = 10^{3\alpha} \cdot \frac{10^{-12} D_{\alpha,\text{exp}} [\mu\text{m}^2/\text{ms}^\alpha]}{\hbar/m_{\text{Li}}}. \quad (5.42)$$

The multiplicative factor $10^{3\alpha}$, arising from the “fractional units” of D_α , is indeed the fundamental reason behind the huge dynamical range: For instance, a change in the anomalous exponent of $\Delta\alpha = 1$ (i.e., as in the ballistic-to-diffusive crossover) generates a factor 10^3 in the unit conversion given by Eq. (5.42). In this respect, it is important to realize that Fig. 5.12(b) constitutes a rather “strange” and unusual plot, since nominally each point has a different unit of measurement from the others, according to the respective values of α : this is the reason why each data point is represented with a different color.⁹

Importantly, however, for the slowest expansion dynamics recorded in this high- T dataset, which features $\alpha = 1.15(5)$ (i.e. close to normal diffusion), the (generalized) diffusion coefficient is found to be $D_{1.15} = 30(10) \text{ s}^{-0.15} \hbar/m_{\text{Li}}$. Albeit, for the reasons just discussed, a direct quantitative comparison is somehow questionable, the low value of D_α measured in this experiment is “not too far” from the value of D_1 measured for homonuclear ${}^6\text{Li}$ unitary Fermi gases around broad Feshbach resonances [190], of about $D_1 \simeq 6 \hbar/m_{\text{Li}}$. The seeming proximity of our minimum D_α to the “universal” value of Ref. [190] strongly encouraged and motivated us to perform analogous measurements at lower temperatures.

⁹The color scale in Fig. 5.12(a), instead, does not carry the same meaning, as α is anyway a dimensionless quantity, i.e. a (positive) number. It is introduced mainly to facilitate the comparison between the two panels.

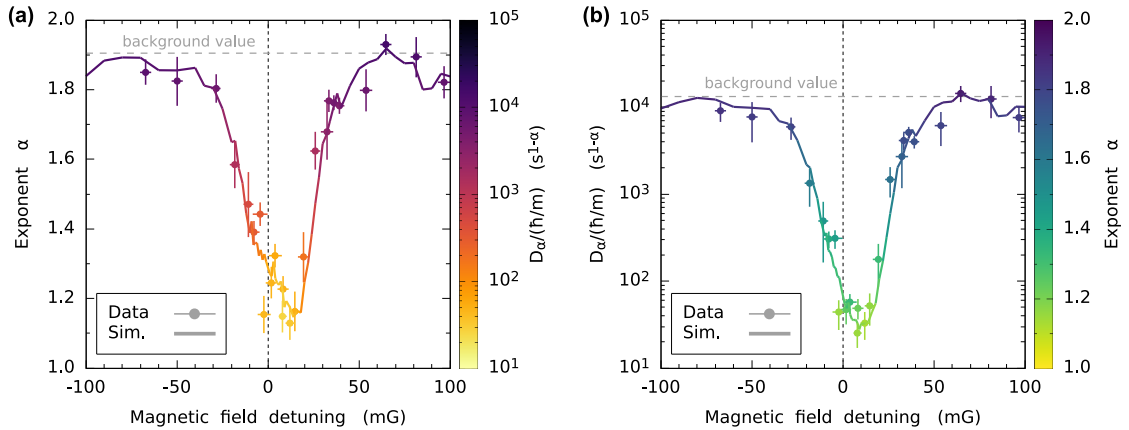


Figure 5.12 – Fit results of the generalized power-law model Eq. (5.8). (a) Fitted exponent α , as a function of the magnetic field detuning δB . The color scale encodes the generalized diffusion coefficient D_α , normalized to \hbar/m_{Li} . (b) Fitted D_α , normalized to \hbar/m_{Li} , as a function of δB . Note that the units of D_α depend on the associated exponent α , encoded in the color scale. In both panels, points with error bars refer to the fits performed on experimental data, while solid lines show the results of the same analysis conducted on the numerical data, which also in these terms reproduces our observations remarkably well. Finally, the horizontal dashed lines represent the experimental values obtained in the non-interacting regime, setting $\delta B \simeq 0.5$ G, i.e. close to the zero crossing of the scattering length.

Before moving to the (more interesting) regime of lower temperatures, a few important remarks should be made. The right panels in Fig. 5.11 are the equivalent of the corresponding left ones, but for the numerical data obtained with my simulator. The simulation run that produced these figures is exactly the same from which the spectra of Fig. 5.10 were obtained, i.e. with the sole core ingredients described in Sec. 5.3.1, and input parameters fixed to the experimentally measured values, see Tab. 5.2. Also in this case, the simple numerical “s-wave collider” reproduces the experimental observations almost perfectly. The slightly larger values of s_x obtained by the simulation for long observation times and intermediate-to-large detunings, compared to the experimentally measured ones [see the red lobes in Figs. 5.11(f) and 5.11(e), respectively], could be ascribed to possible underestimation of s_x in the experiment, when the signal-to-noise ratio is considerably lowered by the fast expansion of the Li cloud. A more quantitative comparison between experimental and numerical results is represented by the solid lines in Figs. 5.12(a) and 5.12(b), which show the fit results of the power law model Eq. (5.8) obtained from the simulated data, following the same procedures adopted for the analysis of the experimental ones. Once again, I stress the excellent agreement between my simple simulator and the real-world experiment, letting us conclude that, at least in this regime, the numerical model effectively embodies all relevant microscopic processes at play in our system.

Finally, I remark that the “superdiffusive” dynamics, encoded in $1 < \alpha < 2$ values should not be interpreted as a persistent feature of the system, which is expected to become normally diffusive if the observation time was sufficiently long.¹⁰

¹⁰This statement is supported both by theoretical arguments [see, e.g., Eq. (5.2)], and by numerical simulations run with long final times and infinitely-extended chromium bath.

Table 5.2 – Input parameters for high-temperature simulation. A part from the number of simulated Li atoms – which only affects the “noise” in the simulation, and was chosen to be 10^4 in order to keep reasonable computation times (here about 40 minutes on my laptop) – all the other values are fixed to those experimentally measured for the high-temperature dataset presented in this Section. The real number of Li atoms in the experiment was $N_{\text{Li}} = 20(5) \times 10^3$. The effective temperatures and the trap frequencies have a common relative error of about 15% (besides the two ν_x , which are known precisely), while the *in situ* radii share an error of less than 5%. Day-to-day fluctuations of the experimental parameters are on the order of these uncertainties at maximum.

Species	N	$T_x; T_y; T_z$ (nK)	$s_x; s_y; s_z$ (μm)	$\nu_x; \nu_y; \nu_z$ (Hz)
Li	1×10^4	400; 400; 400	17; 7.5; 6.5	17; 450; 580
Cr	1.3×10^5	1000; 370; 370	110; 11.0; 10.0	14; 88; 112

5.5 The “low-temperature” regime

Following the promising results of the previous Sec. 5.4, we decided to lower the temperature of the system and repeat the same kind of measurements. According to our initial expectations, this should have allowed us to observe more clearly the diffusive regime, i.e. a purely $\alpha = 1$ temporal scaling of the MSD (compared to the minimum α value measured at high temperatures, of about 1.15), and thus to obtain a more straightforward estimate of the diffusion coefficient D_1 . Experimentally, we lowered the effective temperatures of both Cr and Li atoms: For chromium, we increased the efficiency of the “Feshbach cooling” stage, obtaining final samples with $\bar{T}_{\text{Cr}} \simeq 400$ nK and a density-averaged density $\langle n_{\text{Cr}} \rangle_{\text{Li}} \simeq 0.6 \times 10^{12} \text{ cm}^{-3}$. For lithium, we decreased the optical power in the vertical beam, i.e. the initial trap frequency and release energy, which for this dataset were about $\omega_0 \simeq 2\pi \times 60$ Hz and $T_{x,\text{rel}} \simeq 80$ nK, respectively. Correspondingly, the initial (average) axial size of the Li (Cr) cloud was around ~ 30 μm (~ 100 μm). However, due to the small lithium atom number, and the generally low (axial) trap frequencies of both species (especially after removal of the vertical beam), neither Li nor Cr was below $T/T_{\text{F}} = 1$.

Also for this dataset, we acquired complementary measurements following the two schemes of Fig. 5.6. The “spectra” of $s_x(\delta B)$ recorded at fixed evolution times are shown in Fig. 5.13 (colored circles). For large detunings ($|\delta B| \rightarrow 100$ mG), the expansion of the Li cloud tends to the ballistic one, measured for vanishing interactions close to the zero-crossing of the scattering length (out of scale in Fig. 5.13). Close to the FR pole ($-20 \lesssim \delta B \lesssim +30$), instead, $s_x(\delta B)$ features a pronounced “dip” that signals a considerably slower expansion, similarly to the high- T data shown in Fig. 5.10, but with an appreciably lower minimum value (here around 50 μm at $t_{\text{fix}} = 15$ ms, see the yellow points) – still found on the $a < 0$ side of the FR [see red dashed arrow with prediction based on Eqs. (5.40) and (5.41b)]. However, for intermediate (positive and negative) detunings around $|\delta B| \sim 30 \div 50$ mG, a “faster-than-ballistic” dynamics seemingly appears, signaled by the peculiar “shoulders” exhibited by the spectra acquired at long evolution times.

On the basis of the data shown in Fig. 5.13, my numerical simulator seems (at first) to perform decently well also in this temperature regime, see the colored lines. In particular, it is able to qualitatively (and semi-quantitatively) capture the “strange shoulders” observed at intermediate detunings, which – just to provide some context – were initially causing some puzzlement in the interpretation of our measurements. I anticipate here that, according to my simulations, these features basically originate from the temperature mismatch between Li and Cr atoms.¹¹ More specifically, this occurs whenever the effective “axial temperature” $T_{x,\text{Li}}$ of lithium, essentially set by its initial axial trap frequency [see Eqs. (5.39)], is considerably lower than the average \bar{T}_{Cr} (and/or of the average \bar{T}_{Li}). In this case, there exists an intermediate “few-collision regime”, where the average scattering rate per Li atom is on the order of $100 \div 200$ Hz, corresponding to $\sim 2 \div 4$ collisions in 20 ms of evolution time: Such a low number of collision events is somewhat too small to effectively slow down the axial expansion of the lithium cloud, but, at the same time, it causes a partial inter-species thermalization and, loosely speaking, a general “scrambling” of the initial 3D velocity of each Li atom that underwent (even a few) scattering events, owing to the nature of s -wave collisions; see, e.g., Eq. (5.27). Consequently, under these conditions, on average the \hat{x} component of the Li atoms velocity is effectively increased in modulus compared to the initial one, yielding an overall axial expansion of the cloud which “overtakes” that observed in the background, i.e. for ~ 0 collisions per atom. However, the experimental data in Fig. 5.13 show an asymmetry between the “left” and the “right”

¹¹And, partially, from the “internal cross-dimensional mismatch” of the effective temperatures $T_x, T_{y,z}$ of Li atoms after the preparation with the protocol of Sec. 5.2, see the parameters in Tab. 5.3.

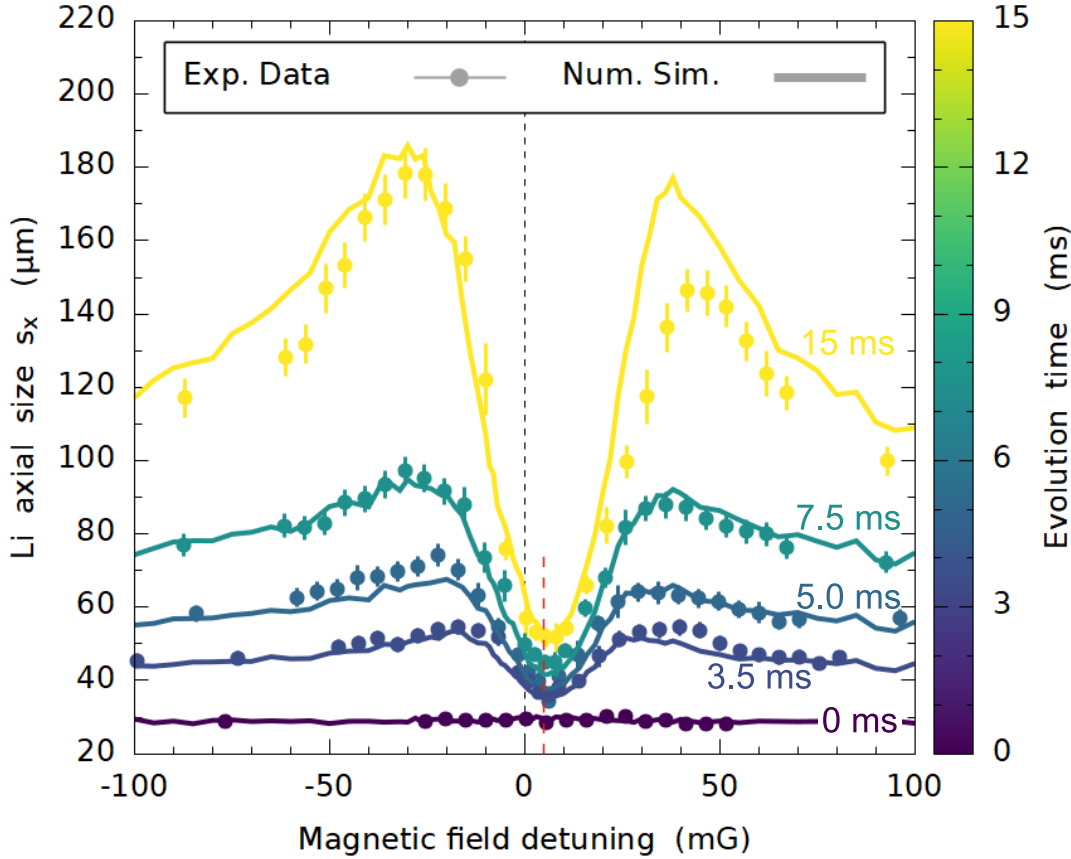


Figure 5.13 – Low-temperature dataset: Axial root-mean-square size s_x of the Li cloud as a function of the magnetic field detuning, for different (fixed) evolution times t_{fix} , see the color scale. The filled circles are the experimental results. Each point represents the average of at least three independent measurements, with the error bars indicating the standard deviation of the mean. The solid lines represent instead the outcome of my simulation, run with the sole “basic ingredients” described in Sec. 5.3.1, with the input parameters reported in Tab. 5.3.

shoulder, respectively corresponding to positive and negative (weak) interactions, which is not captured by the semi-classical simulation with the basic ingredients of Sec. 5.3.1, nor with the inclusion of retardation effects (see Sec. 5.3.2), not shown in Fig. 5.13. A possible origin could be ascribed to the effect of mean-field interactions, see Eq. (1.7). These are generally not straightforward to include in my simulation, owing to their non-trivial dependence on the relative momentum k_{rel} in the case of a narrow FR [see Eq. (1.12)]. I briefly mention here that a tentative, preliminary approach to incorporate these effects (not discussed in Sec. 5.3 because not fully rigorous), which starts from a mean-field Hamiltonian and numerically integrates the equations of motion with the Runge-Kutta method, indeed provides an asymmetry between left and right shoulders, not too far from the observed one.

As for the previous dataset, further insights into the expansion dynamics is gained from a quantitative analysis of the time evolution of the MSD, obtained from the time traces $s_x(t)$ acquired for different detunings (i.e., the first method of Fig. 5.6). The raw experimental data are shown in Fig. 5.14(a), and the corresponding outcome of the numerical simulation in Fig. 5.14(b). Qualitatively, the general trend appears similar to that observed for higher temperatures (cf. Fig. 5.11): The slowest expansion rates are observed for small positive

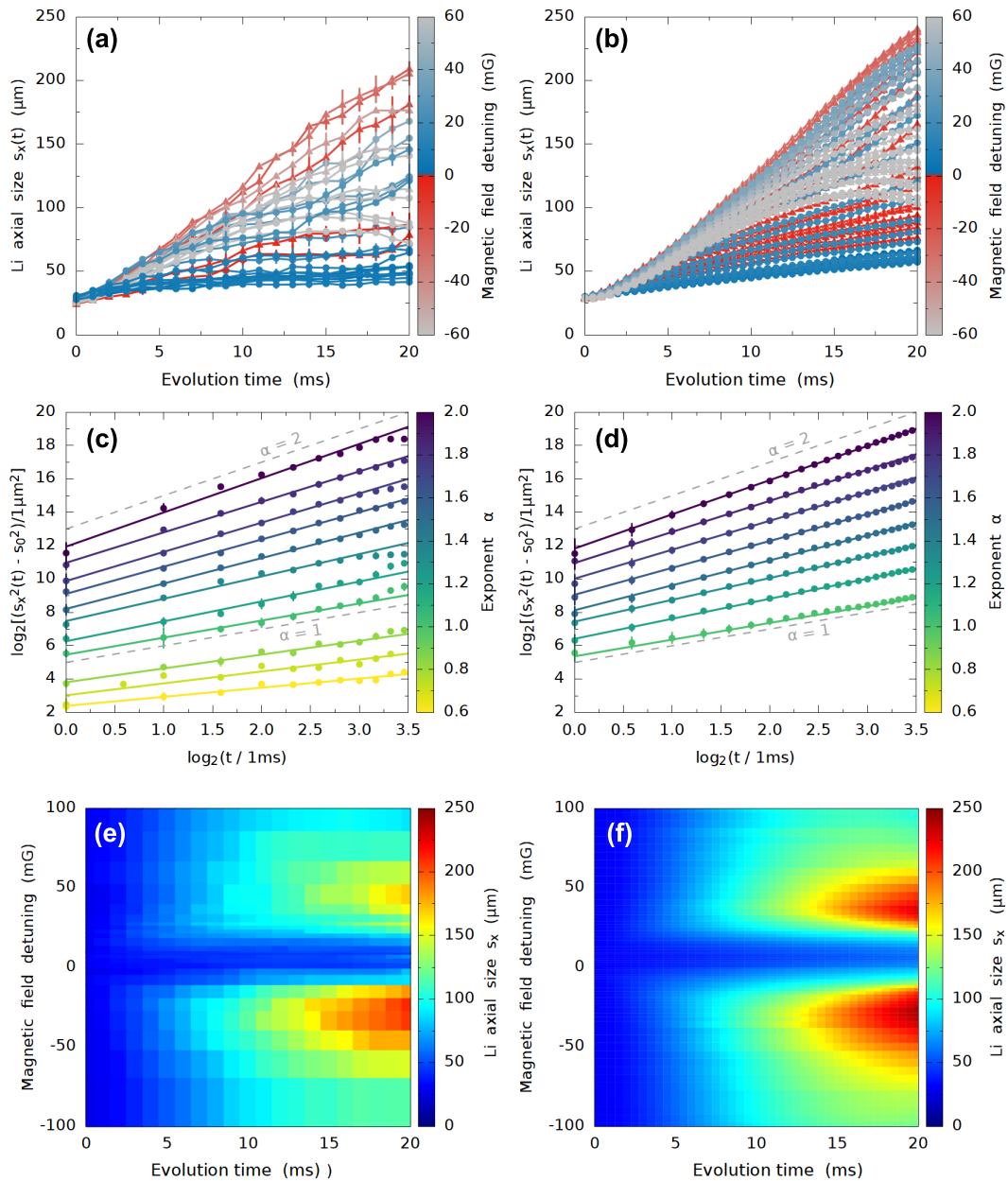


Figure 5.14 – Experimental (left) and numerical (right) results for the low-temperature dataset. (a),(b) Time evolutions of the Li axial size $s_x(t)$, for different magnetic field detunings (see color scale). Here the lines connecting the points are merely guides to the eye. Note that the lowest traces in panel (a) [experiment] appear “flatter” than the corresponding ones in panel (b) [simulation]. (c),(d) Examples of best fits with the generalized power law model Eq. (5.8), with the anomalous exponent α setting the color scale. Here, besides observing the full crossover from ballistic-to-diffusive dynamics, the experimental data in panel (c) show strong signatures of *subdiffusive* dynamics, with α values as low as 0.6. In stark contrast, the numerical data of panel (d) show a minimum value of $\alpha = 1$. In other words, the observed subdiffusive-like expansion is not accounted for by the simulation. In both panels, each trace was arbitrarily displaced on the vertical direction for display purposes, and the gray dashed lines are guides to the eye showing the expected slopes for $\alpha = 1$ and $\alpha = 2$. (e),(f) Same data of panels (a) and (b), respectively, but plotted as a 2D heat map (“spectrogram”) to provide a simultaneous visualization of the temporal evolution $s_x(t, \delta B)$ for different detunings. In both panels, the red regions correspond to the “shoulders” in the spectra of Fig. 5.13.

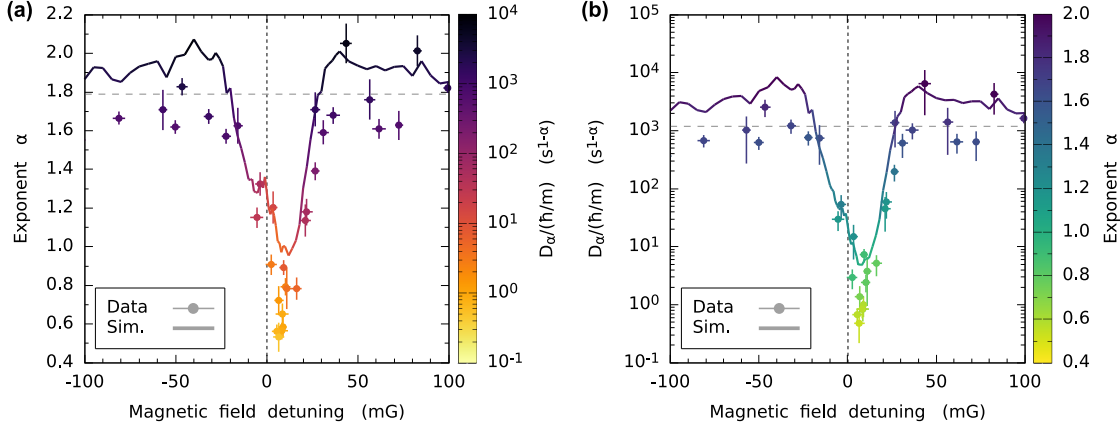


Figure 5.15 – Fit results of the generalized power-law model Eq. (5.8) for the low- T dataset. (a) Fitted exponent α , as a function of the magnetic field detuning δB , with color scale set by $D_\alpha/(\hbar/m_{\text{Li}})$. (b) Fitted coefficient $D_\alpha/(\hbar/m_{\text{Li}})$ as a function of δB . Note that the units of D_α depend on the associated exponent α , encoded in the color scale. In both panels, points with error bars refer to the fits performed on experimental data, while solid lines show the results of the same analysis conducted on the numerical data. Error bars represent the error returned from the fit. Horizontal dashed lines represent the experimental values obtained in the non-interacting regime, setting $\delta B \simeq 0.5$ G, i.e. close to the zero crossing of the scattering length. Compared to the high- T results shown previously in Fig. 5.12, here the agreement between simulation and experiment is less satisfying. In particular, this is true in the interesting region of small positive detunings, where the semi-classical simulation clearly fails to reproduce the experimentally observed $\alpha < 1$ values.

detunings (darker blue), small negative detunings (darker red) generally feature faster expansions, and for large detunings (grayish) the Li cloud expands nearly ballistically. This holds true for both experimental and the numerical data, and one can also appreciate that points at intermediate detunings feature s_x values that exceed the background ones at long evolution times, corresponding to the “shoulders” in the data of Fig. 5.13. However, a closer inspection already reveals a key difference between experiments and (semi-classical) simulations: In fact, the slowest measured expansions in Fig. 5.14(a) appear somewhat “flatter” than the corresponding simulated ones in Fig. 5.14(b). The distinction is subtle at first because, somehow deceptively, the final values of s_x obtained at long times are *quantitatively* similar, but the temporal evolutions with which they are reached are in fact *qualitatively* different. This discrepancy is better quantified in terms of the anomalous exponent α , obtained by fitting our data with the power law model Eq. (5.8); see examples in Figs. 5.14(c) [experiment] and 5.14(d) [simulation]. Here, the striking feature is the presence, in panel (c), of time traces that are well described by power laws with exponents α significantly lower than the diffusive one ($\alpha = 1$) – which lack instead in the simulated data shown in panel (d), where the minimum obtained α is indeed 1.

The complete fit results in terms of the parameters α and D_α are shown in Figs. 5.15(a) and 5.15(b), respectively, with the usual convention that filled colored circles represent the experimentally obtained ones, while solid colored lines are extracted from the simulations. Compared to the high-temperature dataset shown previously in Fig. 5.12, here the agreement between (semi-classical) numerical simulations and experimental results is generally less satisfying. In particular, while at large and intermediate detunings the minor discrepancies are perfectly acceptable within (more) reasonable error bars (i.e., slightly larger than those displayed in the figure, obtained from the fit algorithm) and uncertainties on the experimental parameters, the simulation *clearly fails* (out of error bars) to reproduce the (many) experimental observations of $0.5 \lesssim \alpha < 1$ in the magnetic field region

Table 5.3 – Input parameters for low-temperature simulation. The values reported here correspond to those measured experimentally for the dataset presented in this Section, a part from the number of simulated Li atoms (which is irrelevant in this sense, as in the simulation they are treated as independent particles). Anyway, the real N_{Li} in these experiments was not too different, $N_{\text{Li}} = 15(5) \times 10^3$. The effective temperatures and the trap frequencies have a common relative error of about 20% (besides the two ν_x , which are known precisely), while the *in situ* radii share an error of less than 5%. Day-to-day fluctuations of the experimental parameters are on the order of these uncertainties.

Species	N	$T_x; T_y; T_z$ (nK)	$s_x; s_y; s_z$ (μm)	$\nu_x; \nu_y; \nu_z$ (Hz)
Li	1×10^4	75; 300; 300	30; 7.5; 6.0	17; 530; 680
Cr	1.5×10^5	700; 240; 240	100; 11.0; 9.0	14; 88; 112

$0 < \delta B < +20$ mG, i.e. for strong attractive interactions.¹² Such a discrepancy between numerical and experimental results was not resolved by switching on retardation effects in my simulator. Interestingly, these affect the outcome of the simulation at *small positive detunings*, but solely in terms of a reduced value of the root-mean-square displacement $s_x(t)$ reached at long times. However, the slowest dynamics in the simulations remain always characterized by $\alpha = 1$, even by (artificially) lowering further the temperature of the system, within reasonable physical ranges. I also mention here that none of the other models discussed in Sec. 5.1 seemed to provide acceptable fits to our data showing $\alpha \ll 1$, besides the (quite involved) one of Eq. (5.10), which anyway returned results completely analogous to those obtained with Eq. (5.8) (see again the plots in Fig. 5.4), at the expense of a more complicated (and more susceptible) data analysis.

By also confronting ourselves with our theory collaborators for these transport measurements, namely Dr. Dmitry Petrov (LPTMS, University of Paris-Saclay) and Prof. Tilman Enss (University of Heidelberg), we experimentally addressed the possibility that our observations could have been ascribed to “trivial” thermalization dynamics: In fact, since for thermal gases the diffusion coefficient is generally T -dependent, a strong initial temperature mismatch between Li and Cr atoms could indeed yield an effective time-dependent $D(t)$ during our (not infinitely long) observation time. For instance, this is essentially what happens in the “few-collision regime” that yields the shoulders in the spectra of Fig. 5.13. In this regard, before discussing our experimental test, I note here that, for the temperature regime investigated in this Section, at small positive detunings my numerical simulator returns average scattering rates on the order of $10 \div 20$ kHz (per Li atom). Moreover, by keeping track in the simulations of the mean kinetic energies, one sees that an average number of $10 \div 20$ collisions is sufficient for the two species to thermalize, i.e. to reach the condition $m_{\text{Li}} v_{\text{th,Li}}^2 = M_{\text{Cr}} v_{\text{th,Cr}}^2$,¹³ even for strong temperature mismatches. In other words, this means that, according to the simulations, after 1 ms from the start of the experiment (at maximum), the average kinetic energy of Li atoms has equilibrated with that of Cr atoms, which remains unaffected due to the experimental condition $N_{\text{Cr}} \gg N_{\text{Li}}$. As such, unlike the seeming super-diffusion obtained at intermediate detunings, fully ascribable to the transient early-time dynamics accessed in the experiment, the sub-diffusive dynamics revealed near the resonance pole does not appear reconcilable with such “out-of-equilibrium”, transient effects.

¹²Note that, in correspondence of $0.5 \lesssim \alpha < 1$, the experimentally extracted (normalized) generalized diffusion coefficient also reaches particularly low values.

¹³The distinction is subtle but important: what is reached rapidly is thermal equilibrium in terms of *kinetic energy*, but the spatial extent of the Li cloud remains much smaller than its equilibrium one, as shown below in Fig. 5.16, see text.

In order to exclude possible thermalization-induced transients in our measurements at low detunings ($|\delta B| < 10$ mG), we performed the following experiment: We prepared the lithium cloud with $T_{x,\text{rel}} \simeq 60$ nK, and the chromium bath with $\bar{T}_{\text{Cr}} \simeq 270$ nK, i.e. a more-than-fourfold mismatch between the axial release temperature of Li and the average effective temperature of Cr. First, we traced the undamped breathing oscillations obtained by releasing Li into a non-interacting gas of Cr $|2\rangle$ atoms, obtained simply by not performing the final RF transfer in the protocol of Sec. 5.2. The recorded dynamics is shown in Fig. 5.16, gray squares, and follows the expected oscillatory trend given by Eq. (5.37) (not shown). In the absence of collisions, the maximum value of $s_x(t)$ is related to the width of the initial velocity distribution (i.e. to the initial effective temperature) through Eqs. (5.39), and it is firstly reached after an evolution time $\tau = \pi/(2\omega_x)$ ($\simeq 15$ ms in our setup) from the release into the (weaker) final trap. In this case, we obtain $s_x(\tau) \simeq 80$ μm (with initial size $s_0 \simeq 27$ μm), corresponding to $T_{x,\text{rel}} \simeq 60$ nK,¹⁴ see gray dashed line. Secondly, we repeated the same measurement, but switching on strong Li-Cr interactions, i.e. applying the final RF transfer of our standard preparation scheme at a small positive detuning of a few mG. We traced the time evolution of $s_x(t)$ for 30 ms, out of which we extracted an exponent $\alpha = 0.67(7)$ from the fit to Eq. (5.8), see blue circles in Fig. 5.16. This passage was done to check that our experimental conditions were indeed within the range that yields subdiffusive-like expansions, although the value of the exponent was not the lowest-recorded one. As a third step, we acquired a trace that started under the same strongly-interacting conditions of the blue data, but after 8 ms of evolution we applied a strong π -pulse on the Li $|1\rangle \longleftrightarrow$ Li $|2\rangle$ RF transition – thereby effectively switching off Li-Cr interactions – and we subsequently followed the dynamics of the transferred Li $|2\rangle$ atoms. The resulting overall trace is shown by the red points in Fig. 5.16, and it should be read in the following way: In the first 8 ms, the red points show a subdiffusive expansion of the Li $|1\rangle$ cloud that is entirely equivalent to that of the blue points. At 8 ms, interactions are switched off (see red dashed arrow), and from that point on the non-interacting Li $|2\rangle$ cloud starts an oscillatory dynamics totally analogous to that of the (non-interacting) gray data, but with a significantly larger amplitude, corresponding to a higher temperature of about 250(20) nK. In other words: this is a measurement of the axial momentum distribution of the blue data at $t = 8$ ms, which shows that Li and Cr were essentially thermalized. In the last (and most important) step, we acquired a measurement similar to the previous one, but applying the Li $|1\rangle \longrightarrow$ Li $|2\rangle$ π -pulse after just 1 ms of (strongly-interacting) evolution time. The outcome, shown by the green points in Fig. 5.16, is at this point clear to interpret: Since the maximum reached $s_x(t)$ value during the free breathing oscillations is essentially the same for the red and green data points, lithium atoms were already thermalized after 1 ms during the measurement that yielded the (subdiffusive) blue data.

To summarize, the overall characterization shown in Fig. 5.16 is a strong experimental evidence against possible thermalization-induced transients for our low- T measurements in the strongly-interacting regime. The thermalization rate, although not precisely quantified here, is compatible at least in order of magnitude with the expectations from the numerical simulations. Furthermore, another important remark should be made: On the one hand, it is undoubted that a thermalization timescale similar to the observation time would lead to a time-dependent diffusion coefficient $D_1(t)$. On the other hand, however, since for thermal gases one has $D_1(T) \propto T^{3/2}$ [210], a *subdiffusive*-like trend could only originate from a temperature *effectively decreasing* during the evolution. This is surely not the case in our experimental configuration, where Li atoms, initially, are typically much colder than Cr ones.

¹⁴This is essentially the way in which we measure the axial velocity distribution of Li.

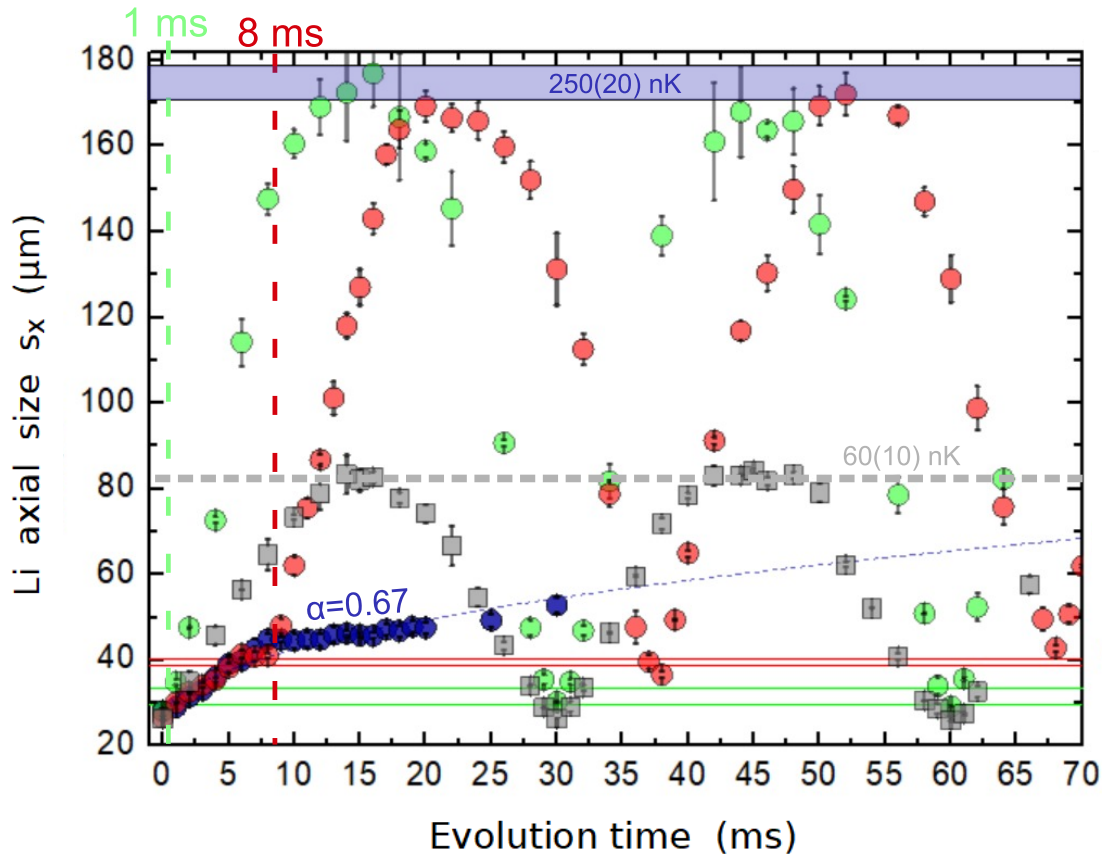


Figure 5.16 – Experimental checks to exclude thermalization-induced transients for the experimental data showing subdiffusive-like expansion. Gray squares are obtained by releasing a cold Li cloud within a non-interacting Cr[2] bath. The maximum axial size is connected to the width of the initial velocity distribution, here around 60 nK (see gray dashed line). Blue circles are instead obtained by switching on interactions, and show a subdiffusive-like expansion characterized by $\alpha = 0.67(7)$. Red circles are obtained from a measurement that started under the same conditions of the blue data, but at $t = 8$ ms interactions were switched off, allowing Li atoms to perform breathing oscillations. The maximum s_x value corresponds to an axial temperature of about 250(20) nK, which coincides with the average Cr temperature \bar{T}_{Cr} , thereby indicating that thermal equilibrium (in terms of velocity distributions) was reached at the time interactions were turned off. Finally, and most importantly, green data are obtained similarly to red ones, but switching off Li-Cr interactions after just 1 ms of evolution time. The maximum s_x value, entirely compatible with that measured for red points, testifies that thermal equilibrium was already reached essentially from the start of the measurement. This represents a strong experimental evidence against possible thermalization-induced, transients effects affecting the blue data and, more generally, our measurements that exhibit subdiffusive-like behavior.

Before moving to the next Section, I remark that, although not shown in Fig. 5.16 for sake of clarity, we have also checked that the observed dynamics is not trivially originated by “classical trapping” of the lithium atoms binding chromium into LiCr molecules: Indeed, if present, these could be revealed by the atomic imaging lights (see Sec. 4.8), and thus contribute to the cloud density profiles. Owing to their ten-fold enhanced mass, relative to the Li one, the possible presence of LiCr dimers could indeed result in an anomalous behavior and a considerable slowing down of the whole cloud expansion within the resonance region. However, while near narrow resonances metastable “closed-channel” molecules could in principle be created also for $a < 0$ ($\delta B > 0$ in our case), where the anomalous dynamics is revealed in our system, from the studies of Chapter 4 we have no experimental

evidence that dimer formation plays a role in our system on the attractive side of the FR. Moreover, a dimer cloud would exhibit an equilibrium axial size nearly identical to the chromium one (of about 90 μm in the measurements of Fig. 5.16), thus much larger than the observed one reached by the Li cloud at our longest expansion times. Finally, if this “trapping” mechanism was at play, we would expect it to be more prominent for $\delta B < 0$ values, rather than for $\delta B > 0$ ones, where real Feshbach dimers could be efficiently created by three-body recombination processes. In any case, to unambiguously exclude their presence, we acquired a further measurement under the same conditions of the blue data in Fig. 5.16, but adding a small amount of green light in our main bODT. The green power employed, of about 30 mW, was not dramatically perturbing the overall trap depth, essentially set by 330 mW of IR light. Nonetheless, owing to the fast photo-excitation loss rate induced by 532-nm light on our Feshbach dimers (see Sec. 4.5) it was sufficient to introduce a species-dependent loss rate of about 300 Hz solely for LiCr. The observed dynamics was also in this case compatible with that exhibited by the blue data in Fig. 5.16, and we could thus definitively rule out that the observed sub-diffusive dynamics trivially originated from dimer formation.

5.6 Temperature dependence of the subdiffusive dynamics

The failure of the semi-classical simulator and, most importantly, our experimental ruling-out of possible thermalization effects and dimer formation (and, to the best of our possibilities, of systematic errors), led us toward the conclusion that, for sufficiently low temperatures and strong interactions, some additional physical mechanism could be at play in our system – ultimately resulting in an anomalous slowing down of the lithium expansion, and causing the departure from (slow but) normal diffusive transport. We therefore decided to characterize systematically how the emergence of the anomalous dynamics depends upon the mixture temperature. In practice, we focused on the “interesting” region of small positive detunings and, once the optimum δB value leading the slowest dynamics was identified under several different temperature regimes, we investigated the lithium expansion.

Before presenting and discussing our observations, however, an important premise should be made: Even among ourselves, it was initially not entirely clear how to properly compare results obtained from our analysis for datasets corresponding to (rather) different experimental conditions. In fact, changing the temperature of the harmonically trapped mixture, and in particular of the chromium component, also causes a variation of particle densities (and density-averaged densities), which at some point could become significant. Moreover, in our investigation we also included exploratory measurements where we probed regions of the parameter space that differed considerably from one another. The characterization of the expansion dynamics in terms of Eq. (5.8) was always found satisfying across all the various explored regimes, and we could indeed obtain for each dataset the corresponding α and D_α parameters, as shown in the following. However, a rather practical question soon arose in the lab, in particular when discussing and presenting our experimental findings to our theory collaborators. Simply put: “*What is the most proper ‘x axis’ to present (and understand) our results?*”.

A key point, that was realized while discussing our anomalous transport data with D. Petrov, is the strong similarity between our observation and those reported in a variety of studies on matter-wave transport in disordered potentials close to a metal-to-insulator transition, see e.g. [211–214]. Also there, anomalously slow expansion and subdiffusive dynamics were experimentally unveiled, arising from quantum interference effects and multiple scattering events in collisionally dense media: either precursing a localized regime

approached from the “metallic” phase, or arising from the competition between disorder and non-linear interactions. This strong similarity suggested us to consider the anomalous behavior of our system from the viewpoint of quantum interference effects originating from multiple scattering of lithium atoms in the “disordered landscape” constituted by the chromium bath. In this picture, the Cr gas should be viewed as a random potential landscape of point-like scatterers for the lithium impurities. Indeed, if chromium was *perfectly static*, our setup would realize the so-called random Lorentz gas of point-like resonant scatterers [215]. Interestingly, a scalar matter wave propagating in such a three-dimensional disordered medium is predicted to exhibit a transition from a delocalized metallic state (for weak interactions and/or high energy) to an Anderson-like localized state [216], for sufficiently strong interactions and low enough energies [215,217]. On the other hand, if the point-like scatterers exhibit a sufficiently fast thermal motion, the disruptive quantum interference leading to particle localization could be rapidly washed out due to decoherence induced by thermal fluctuations – thus re-establishing normal diffusion. These two opposite regimes should somehow connect when the disorder potential is moving only very slowly.

Building on this idea (that would make little sense in case of homonuclear Fermi mixtures, but that sounds reasonable in our mass-imbalanced system), we tentatively considered a Ioffe-Regel-like criterion for our system, neglecting for the moment the thermal motion of Cr atoms. Roughly speaking, for a quantum particle propagating with momentum $\hbar k$ through a static random medium, according to this criterion one should expect (strong) localization effects to occur whenever the mean free path λ_{free} becomes smaller than the wavelength of the scattered wave. Namely, this happens when $k \lambda_{\text{free}} < 1$ [215]. To make a rough estimate, a particle that moves with velocity v in a medium of density n has an average scattering rate $\Gamma \sim n \sigma v$, corresponding to a mean free time $\tau_{\text{free}} \sim 1/\Gamma$, and to a mean free path $\lambda_{\text{free}} \sim v/\Gamma \sim 1/(n\sigma)$. Moreover, for unitary-limited (*s*-wave) collisions one has $\sigma = 4\pi/k^2$, and thus $\lambda_{\text{free}} \sim k^2/(4\pi n)$. Therefore, the Ioffe-Regel criterion in such resonant regime would be given by the condition $k^3/(4\pi n) \leq 1$.

Inspired by this simple consideration, we tentatively identified the quantity $k_{\text{Li}}/n_{\text{Cr}}^{1/3}$ as a reasonable x axis for our data. To test if this could indeed be a good dimensionless control parameter in our system, let us consider the typical parameters of the two datasets presented in Secs. 5.4 and 5.5. We estimate k from the thermal momentum of Li assuming instantaneous thermal equilibrium with Cr, i.e. $k \sim \sqrt{m_{\text{Li}} k_{\text{B}} \overline{T}_{\text{Cr}}}/\hbar$, and we take n to be the density-averaged density $\langle n_{\text{Cr}} \rangle_{\text{Li}}$. For the high- T dataset we get $k^3/(4\pi n) \sim 4$, whereas for the low- T one we obtain $k^3/(4\pi n) \sim 1.5$. Besides numerical factors, the important point here is that the dimensionless quantity $\sim k_{\text{Li}}^3(\overline{T}_{\text{Cr}})/n_{\text{Cr}}$ seems indeed to provide a quantitative distinction between “high” and “low” temperatures regimes, and it has the advantage of encoding, together with the temperature change, the corresponding one in the (density-weighted) Cr density of our trapped samples.

After this premise, I now move to present our experimental results, together with our current interpretation and understanding, which is still ongoing at the time of the submission of my Thesis. As anticipated, in order to gain more insights into the anomalous behavior observed at low temperatures, we performed a systematic study of the system evolution for varying T , focusing each time on the optimum $\delta B > 0$ value where the slowest dynamics was observed. For each investigated experimental condition, we recorded the time trace of $s_x(t)$, and extracted the parameters α and D_α through fits with the generalized power law Eq. (5.8). Our results are presented in Figs. 5.17(a) and 5.17(b) [filled colored circles] as a function of the parameter $\chi = k_{\text{Li}}(\overline{T}_{\text{Cr}})/\sqrt[3]{\langle n_{\text{Cr}} \rangle_{\text{Li}}}$. As discussed above, this dimensionless quantity essentially combines information on both the characteristic thermal wave-vector and the Cr average density. In practice, for each acquired trace we estimated

the corresponding χ value, obtained on the basis of the measured \bar{T}_{Cr} and the estimated $\langle n_{\text{Cr}} \rangle_{\text{Li}}$, by averaging over the whole time window experimentally explored (typically 20 ms). From Fig. 5.17(a), one can notice how the expansion dynamics gradually changes character: From weakly super-diffusive at high temperatures (large χ values), to normal diffusion in an intermediate range ($\chi \sim 3.5$), to a sub-diffusive one at the lowest temperatures, where α exponents as low as 0.3 are detected. Parallel to a decreasing α , we also observed a monotonous drop of the (generalized) diffusion constant D_α , see Fig. 5.17(b). The empty

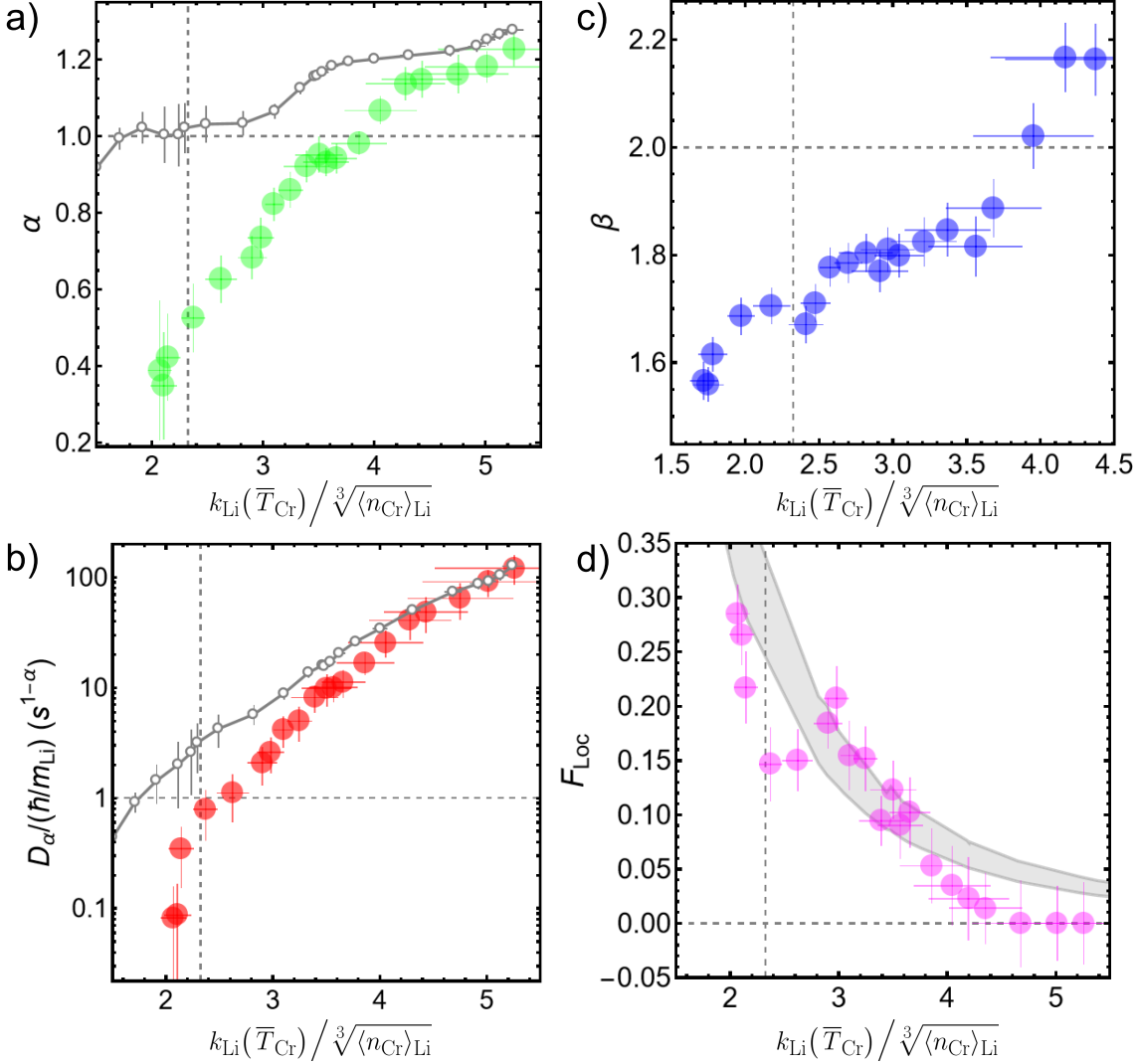


Figure 5.17 – Characterization of the slowest dynamics across different temperature regimes, expressed in terms of the dimensionless quantity $\chi = k_{\text{Li}}(\bar{T}_{\text{Cr}}) / \sqrt[3]{\langle n_{\text{Cr}} \rangle_{\text{Li}}}$, obtained by averaging over the entire observation time. (a) Exponent α extracted from the power law model Eq. (5.8). Filled green circles represent the experimental values, while empty gray circles are obtained from the semi-classical simulation. (b) Same as above, but for the generalized diffusion coefficient D_α , plotted in normalized fractional units. Here the experimental values are colored red. (c) Exponent β of the “generalized Gaussian” Eq. (5.15) (FIT A) used to describe the experimentally observed density profiles. Each value is obtained by averaging over the entire recorded dynamics. (d) Exponential weight f_{loc} obtained from fitting the density profiles to Eq. (5.17) (FIT B). Each value is obtained by averaging over the entire recorded dynamics. The gray shaded area is obtained by tentatively applying the Ioffe-Regel-like criterion while considering the finite momentum distributions, see text for details. The profiles obtained from the semi-classical Monte Carlo simulation do not exhibit deviations from the Gaussian shape, i.e. $\beta \simeq 2$ and $f_{\text{loc}} \simeq 0$.

gray circles in Figs. 5.17(a) and 5.17(b) show instead the corresponding α and D_α values obtained from the semi-classical simulations, with parameters tuned to those measured on the atomic samples. As one can notice, they also show a progressive and monotonous decrease of α and D_α as χ is lowered, but the diffusive threshold $\alpha = 1$ (interestingly, with a corresponding $D_1 \sim 1 \hbar/m_{\text{Li}}$) is essentially never crossed. It is also interesting to note how the data exhibiting the slowest subdiffusive dynamics are found at χ values below $(4\pi)^{1/3} \simeq 2.32$, see dashed vertical line in Fig. 5.17 panels. Namely, in that regime, the Ioffe-Regel criterion for unitary-limited scattering, discussed at the beginning of this section, appears to be satisfied by the Li thermal wave-vector: $k_{\text{Li}}^3 \langle \bar{T}_{\text{Cr}} \rangle / \langle n_{\text{Cr}} \rangle_{\text{Li}} < 4\pi$.

Besides $\alpha < 1$ values, another feature exhibited by the low- T experimental data – and not accounted for by the simulator – is represented by *non-Gaussian* density profiles of the Li cloud, which appear to be strongly connected with the subdiffusive expansion of $s_x(t)$. Deviations from a standard Gaussian distribution, which is the expected one for both ballistic and diffusive thermal clouds, are unveiled by the two complementary fitting functions Eqs. (5.15) and (5.17), respectively. The former one (denoted “FIT A”) is a generalized “stretched” Gaussian that interpolates between the standard Gaussian function ($\beta = 2$), which characterizes density distributions under *normal diffusion*, and an exponential decaying envelope ($\beta = 1$), characteristic of Anderson-localized single-particle states. The latter one (“FIT B”) has a similar purpose, but the interpolation between these two distinct regimes is obtained by means of mutually dependent amplitudes: $f_{\text{loc}} \rightarrow 0$ returns a Gaussian, while $f_{\text{loc}} \rightarrow 1$ gives an exponentially-decaying density profile.

It is interesting to see how both the generalized Gaussian exponent β and the exponential weight f_{loc} , averaged over the entire observation time, gradually evolve as a function of χ , see Figs. 5.17(c) and 5.17(d), respectively. One can also notice a strong correlation between the trends of these parameters and those featured by α and D_α in Figs. 5.17(a) and 5.17(b), a decrease of the diffusion parameters being reflected both by a decreased β (FIT A) and by an increased f_{loc} (FIT B). Yet, as long as $\alpha \gtrsim 1$, the profiles obtained with FIT A and FIT B appear compatible with a single Gaussian envelope, signaled by $\beta \sim 0$ and $f_{\text{loc}} \sim 0$, respectively. The slightly-above-Gaussian values of β obtained for the largest χ values (highest temperatures) can be ascribed to the time averaging over the ballistic-to-diffusive transient dynamics in that regime.

When FIT B is applied to the experimental profiles, we also reveal a rather distinct dynamics for the Gaussian and exponential components of the density envelopes. This is illustrated in Fig. 5.18, where I show radially-integrated density profiles (gray circles) recorded at short (2 ms, left panels) and long (19 ms, right panels) evolution times in the diffusive [(a) and (b)] and deep sub-diffusive [(c) and (d)] regimes, respectively. Blue solid lines in the figures are best fits of Eq. (5.15) to the data. Magenta and dashed gray lines are instead the best-fitted exponential and Gaussian contributions from the FIT B analysis. One can see that, in the diffusive case, a single Gaussian nicely reproduces the distributions both at short and long times, as signaled by the small (and unphysically negative) exponential weight, and by the fact that the Gaussian contribution of Eq. (5.17) is indistinguishable from the generalized one based on Eq. (5.15), implying that $\beta \simeq 2$. In the sub-diffusive case, instead, FIT B reveals a sizable exponential component ($f_{\text{loc}} \sim 0.3$) that does not exhibit any appreciable drop nor expansion over time, whereas the Gaussian component exhibits a subdiffusive expansion, leading to α and D_α values essentially identical to those extracted when FIT A was employed to evaluate the second moment of the density distributions. Correspondingly, in such regime strong deviations from the Gaussian envelope are signaled by FIT A results, yielding stretched Gaussian exponents as low as $\beta = 1.5$.

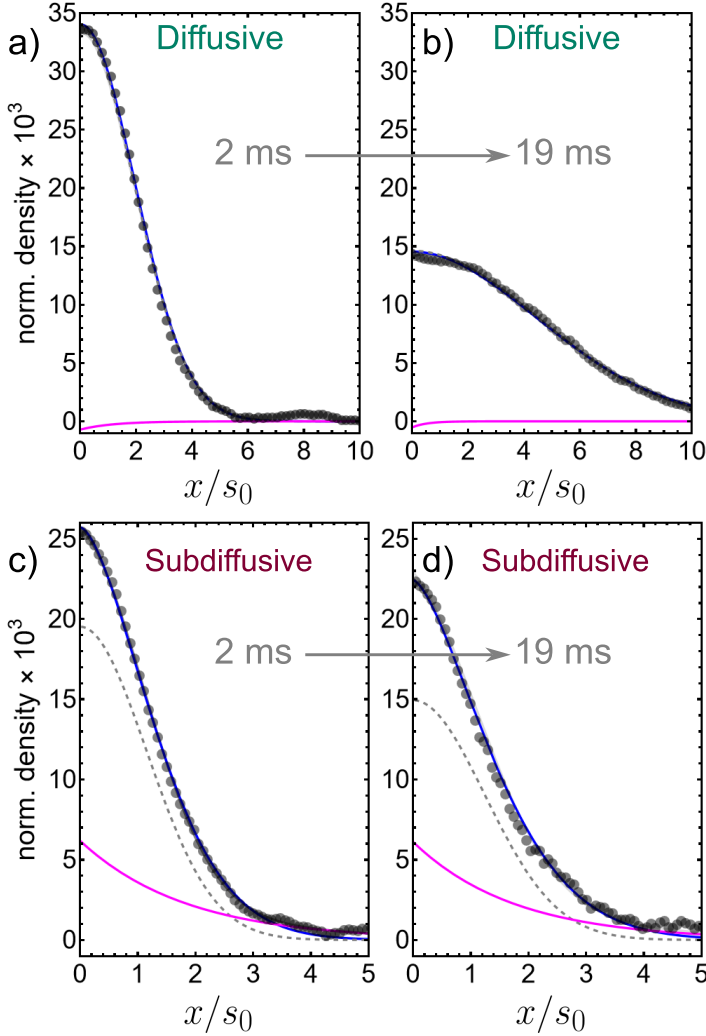


Figure 5.18 – Radially-integrated density profiles of expanding Li clouds. Panels (a) and (b) show a comparison of the cloud shape at short (2ms) and long (19ms) observation times, in the case of a slightly-super-diffusive expansion ($\alpha \gtrsim 1$). In both cases, the profiles are well described by a standard Gaussian function. Note also the difference in the cloud size between long and short times. Panels (c) and (d) are the analogous of the former two, but for a strongly-subdiffusive expansion with $\alpha \simeq 0.5$. Here, in both cases, the density profiles deviate from purely Gaussian ones, as it can be noticed by the comparably longer tails. This is signaled by an exponent $\beta < 2$ (FIT A), or by a nonzero exponential weight f_{loc} (FIT B). Importantly, note that, from the FIT B analysis, we obtain an exponentially-decaying component that does not evolve within the observation time window (see magenta lines). By contrast, the Gaussian component (gray dashed line) exhibits a subdiffusive growth.

Finally, it is interesting to compare the experimentally-determined behavior of f_{loc} versus χ , with the localized fraction that one would expect for a thermal distribution in case of purely static (three-dimensional) disorder. A rigorous determination of such quantity is still missing for our specific system, and calculations are currently being pursued by our collaborator D. Petrov. Nonetheless, we can easily make a rough estimate of f_{loc} by assuming that the Ioffe-Regel criterion $k_c \cdot \lambda_{\text{free}}(k_c) = 1$ determines the critical wave-vector k_c that separates localized states ($k < k_c$) from delocalized ones ($k > k_c$). This assumption appears indeed to be rather accurate in the case of a low-density gas of resonant point-like scatterers, based on the numerical study reported in Ref. [215]. We thus attempted to evaluate f_{loc} as it follows: For a given bath density $\langle n_{\text{Cr}} \rangle_{\text{Li}}$ and different magnetic field detunings, i.e. scattering cross sections, we determined the $k_c(\delta B)$ that satisfies the Ioffe-Regel criterion. Subsequently, assuming that Li atoms feature a thermal momentum distribution at temperature \bar{T}_{Cr} , we estimated the fraction of localized particles as:

$$f_{\text{loc}} = 4\pi \int_0^{k_c} n_{\text{Li}}(k) k^2 dk. \quad (5.43)$$

This results in a trend of f_{loc} as a function of the B -field detuning, i.e. as a function of R^*/a , as the one shown in Fig. 5.19 below. For this specific example, we assumed a bath temperature of $\bar{T}_{\text{Cr}} = 280$ nK, and evaluated f_{loc} for two density values of $1.45 \times 10^{12} \text{ cm}^{-3}$ (black line) and $0.9 \times 10^{12} \text{ cm}^{-3}$ (blue line), respectively. In both cases, one can see how

a clear optimum value of detuning exists, where f_{loc} is maximized. By thus assuming that we indeed performed the measurement at such optimum point, we can build up a theoretical estimate for f_{loc} , expected for the case of static disorder, under the various χ values explored in the experiment. The result of such simple theoretical analysis is shown in Fig. 5.17(d) as the gray shaded region, the extremes of which correspond to the estimated f_{loc} assuming either the peak chromium density (upper gray curve) or its value averaged over the Li distribution (lower gray curve). One can notice how this simple estimate qualitatively matches the trend of f_{loc} revealed experimentally. In particular, it is interesting to see how the theoretical curves systematically lay *above* the experimental values, with a theory-experiment mismatch that is gradually reduced when the system temperature is lowered, i.e. for lower χ values in Fig. 5.17(d). This is somewhat reasonable, in light of the fact that our Cr atoms have in reality a finite thermal motion: At high temperatures, this may act as a source of rapid decoherence – reasonably destroying any quantum interference effect, thus impeding the emergence of any localized regime. In contrast, as the thermal motion of the heavy chromium scatterers is reduced by lowering the system temperature, a non-zero localized fraction of the Li sample can emerge.

While this first attempt of a theory-experiment comparison is somewhat hand-waving, and it cannot be at all considered as a conclusive explanation of our findings, the semi-quantitative agreement shown in Fig. 5.17(d) strongly suggests that the anomalous dynamics of our system is indeed connected to the physics of matter waves propagating in random media. The rigorous establishment of such a link, and a clear understanding of the interplay between disorder-induced localization and thermal-induced decoherence, are to date missing, and they represent our current main task, in collaboration with D. Petrov. If our current interpretation of the anomalous transport dynamics will be confirmed, a wealth of exciting further experiments awaits to be performed in our setup. For instance, a rather simple upgrade of the Li-Cr machine could enable us to investigate the effect of a reduced system dimensionality, which is known to have a strong impact on localization phenomena. Thanks to the rather distinct polarizabilities of our mixture components over

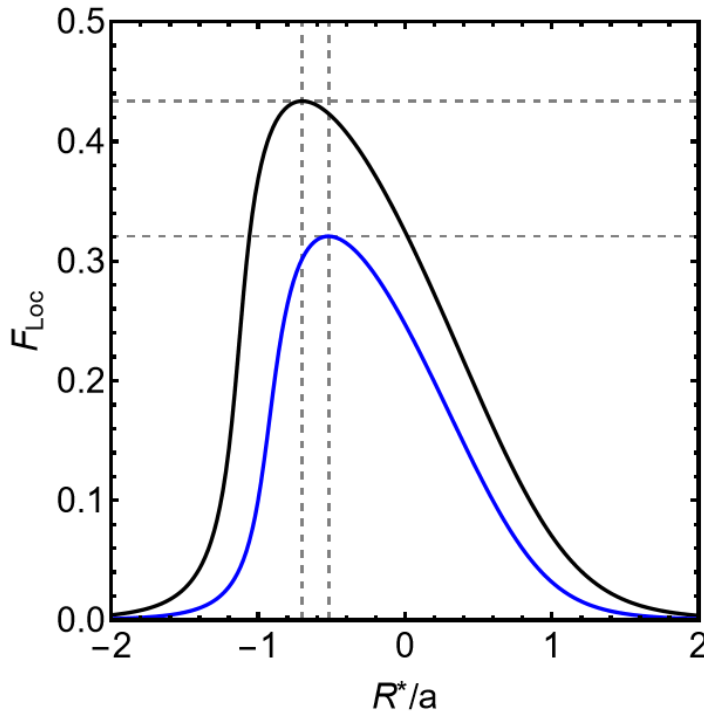


Figure 5.19 – Estimation of f_{loc} based on Eq. (5.43), as a function of the dimensionless quantity R^*/a (which, close to resonance, is proportional to the magnetic-field detuning). The calculation is performed by taking an average bath temperature $\bar{T}_{\text{Cr}} = 280$ nK, for two different values of the (density-averaged) density $\langle n_{\text{Cr}} \rangle_{\text{Li}}$: $1.45 \times 10^{12} \text{ cm}^{-3}$ (black line) and $0.9 \times 10^{12} \text{ cm}^{-3}$ (blue line), respectively.

a wide spectral range, species-selective optical lattices could be devised and employed to control the relative mobility of lithium and chromium atoms. Finally, an appealing measurement already planned for the next future in our lab, which can be performed almost straightforwardly with the current setup, consists in the inverting the role of heavy and light particles – namely the investigation of heavy impurity transport within a Fermi gas of light atoms.

Chapter 6

Technical upgrades of the experimental setup

As anticipated in the introduction of Chapter 2, the build-up of the Li-Cr machine was essentially finalized, at least in its core parts, during my Master Thesis, i.e. before the start of my Ph.D.; see Refs. [102, 121–123]. Yet, the subsequent knowledge acquired over the Li-Cr system stimulated us to further optimize and upgrade the existing setup.

In particular, the narrow character of the Li-Cr s -wave FRs, combined with their high-field location above 1.4 kG (see Chapter 3), required us to significantly improve our magnetic field stability, and to implement optical schemes to prepare the lights for (spin-selective) high-field absorption imaging.

Further, the realization that LiCr Feshbach dimers suffered from sizeable photo-excitation losses induced by the lights in our bODT motivated us to test a different (more infrared) trapping wavelength, viz. 1560 nm, following promising results from the Dy-K experiment in Innsbruck.

Additionally, I briefly discuss a recent upgrade of the experimental routine, namely the simultaneous loading of two independent optical dipole traps, that allows us to perform a double-loading of the Li component. Such a simple trick is in principle exploitable in any ultracold atom experiment, especially single-species ones, to boost the final atom number.

The Chapter is organized as it follows:

- In Sec. 6.1, I describe our setup to generate very stable magnetic fields on the order of ~ 1.5 kG, with residual B -field noise on the few-mG level;
- In Sec. 6.2, I illustrate our new high-field imaging setups for Li and Cr atoms, with which we produce the absorption imaging beams resonant either at 1414 G or at 1461 G;
- In Sec. 6.3, I outline the optical setup for the far-off-resonant trap (FORT) at 1560 nm, with which we realize two additional ODT beams; one counter-propagating with the main bODT, the other employed as a vertical cross arm;
- In Sec. 6.4, I present our recently developed double-loading scheme for Li, with which we load a secondary IR dipole trap simultaneously to the main bODT. This secondary trap can be used either to improve final sample, or as a reference for magnetic-field sensitive measurements.

6.1 Magnetic field stabilization

Most of the experimental studies conducted in this Thesis, in particular those reported in Chapters 4 and 5, require excellent stability of the magnetic field bias, and an accurate dynamic tuning of it within the experimental cycle, in light of the comparably narrow width of the available Li-Cr FRs, combined with their high-field location exceeding 1.4 kG. In our setup, a highly stable B field along the vertical direction is produced by means of four different sets of coils, denoted BIAS, GRAD, COMP, and AC-COMP coils, respectively.

The main BIAS coils can produce magnetic fields of up to 1.5 kG, corresponding to a DC current of about 200 A. This is generated by a 15-kW programmable power supply (TDK-Lambda GSP-80-195). The BIAS current, measured with a current transducer (LEM ITN 600-S ULTRASTAB), is actively stabilized via a proportional-integral controller acting on the voltage programming input of the power supply. This ensures reproducibility and medium-term stability of the applied bias field. The (smaller) GRAD coils, powered by a Delta Elektronika SM 30-200 power supply, can in principle produce fields up to ~ 1 kG with a 200 A current. However, in our experiments these coils are usually employed in anti-Helmholtz configuration, generating the magnetic field gradients both for the (C)MOT and for the gravitational sag compensation in the bODT (see Chapter 2). For this latter purpose, we typically work with levitating gradients of about 1.5 G/cm, obtained with 1.5 A of current. In this configuration, the intrinsic stability of the GRAD coils power supply, of a few parts in 10^5 , suffices to guarantee a negligible noise contribution to the overall bias field. The (much smaller) COMP coils can produce fields of about 2.5 G at the maximum employed current of 5 A. They are used, in combination with the BIAS ones, to finely tune the magnetic field around a FR. The COMP coils current is also actively stabilized by means of a setup analogous to the BIAS coils one, with a second controller and current transducer set of the same type.

As the COMP setup is concerned, active stabilization of the current allows us to reduce the noise of the generated magnetic field well below 1 mG. The BIAS coils, instead, that are driven with a significantly higher current, exhibit a larger residual closed-loop noise synchronous with the 50-Hz mains. This is characterized by a peak-to-peak amplitude of about 40 mG at 1.4 kG, and by Fourier components at 50 Hz and a few higher harmonics; see the blue squares and the blue curve in Fig. 6.1(a). This behavior is revealed by synchronizing the experimental sequence with the 50-Hz mains. Since the line carrier frequency can vary appreciably within the duration of the experiment, we not only synchronize the start of the experiment with the AC line, but also before the execution of field-sensitive measurements. This allows us to trace the magnetic field fluctuations via RF spectroscopy on the $\text{Cr}|1\rangle \leftrightarrow \text{Cr}|2\rangle$ Zeeman transition, more sensitive than the $\text{Li}|1\rangle \leftrightarrow \text{Li}|2\rangle$ one by a factor ~ 8 at 1414 G.¹ Specifically, we adjust the RF power and pulse duration to achieve a π -pulse on resonance, and then detune the frequency to yield a 50% transferred fraction. This side-of-fringe configuration yields the maximum sensitivity to magnetic field variations and, for Fourier-limited pulse widths exceeding noise-induced frequency shifts, it can be used to unambiguously retrieve the time evolution of the B field from the transfer efficiency.

In order to do so, we initially employ a 1.8-ms-long pulse to characterize the noise of our coil setup, and only at a later stage we extend it to 3.6 ms to gain in sensitivity at the expense of a reduced bandwidth. A typical magnetic field trace obtained with the initial 1.8-ms-long pulse is presented in Fig. 6.1(a) (blue squares). As anticipated, the observed trend is well fitted by a sum of sinusoidal functions with a main 50-Hz component and a few higher harmonics (mainly the odd ones, in particular 150 and 250 Hz) of progressively smaller amplitudes; see the solid blue line. The best-fit function to the experimental data is then reversed and used to drive the additional AC-COMP coils setup to implement the feed forward to compensate field fluctuations. A second iteration with the 3.6-ms-long pulse allows us to further refine the signal sent to the AC-COMP coils.

Through this active compensation procedure, we are finally left with residual 5-mG peak-to-peak fluctuations synchronous with the 50-Hz mains; see the green circles in Fig. 6.1(a).

¹At this field, the differential magnetic moment $\delta\mu_{12}$ that characterizes the $\text{Li}|1\rangle \leftrightarrow \text{Li}|2\rangle$ ($\text{Cr}|1\rangle \leftrightarrow \text{Cr}|2\rangle$) RF transition equals 0.78 kHz/G (6.05 kHz/G).

Such a stability, once achieved, is found to be maintained over several weeks, with no need for a day-to-day optimization of the signal sent to the AC-COMP coils.

In order to determine the shot-to-shot noise of the magnetic field, which constitutes the main source for field fluctuations asynchronous with the 50-Hz mains, we acquire statistics of the observed transfer efficiency for variable spectral resolution (i.e. variable pulse lengths) at fixed time of the pulse during the sequence. Figure 6.1(b) shows an example of such a characterization, performed via RF spectroscopy over the $\text{Li}|1\rangle \leftrightarrow \text{Li}|2\rangle$ transition exploiting the same side-of-fringe configuration described above, once the stability shown in Fig. 6.1(a) was achieved. The standard deviation of the transfer efficiency σ_{te} appears linearly correlated with the π -pulse time τ_π over a relatively wide range. The slope is directly connected to the standard deviation of the shot-to-shot noise of the B -field. The nonzero offset extrapolated for $\tau_\pi \rightarrow 0$ suggests instead the presence of an additional, constant noise contribution in our measurements, likely independent from magnetic field fluctuations, that we ascribe to imaging noise. Accordingly, we fit our data with a sum of two uncorrelated contributions:

$$\sigma_{te}(\tau_\pi) = \sqrt{\sigma_{\text{img}}^2 + (K \delta\mu_{\text{rf}} \sigma_{\delta B} \tau_\pi)^2}, \quad (6.1)$$

with $\delta\mu_{\text{rf}} = 0.78$ kHz/G for the employed Li transition, and $K = 1.897$ a numerical factor characteristic of the side-of-fringe scheme. The fit returns a shot-to-shot standard deviation $\sigma_{\delta B} = 2.4(2)$ mG.

Finally, slow thermal effects on the whole coil setup are strongly mitigated by stabilizing the temperature of the sensing resistor in the BIAS coils system. The residual drifts of the bias field, on the order of $5 \div 10$ mG/hour, are manually compensated for by finely adjusting the COMP coils current.

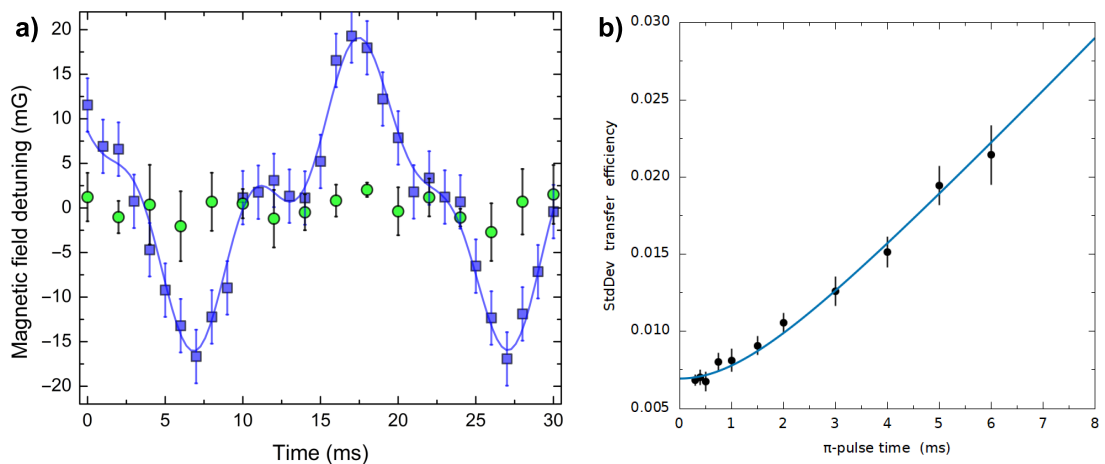


Figure 6.1 – Stability of the bias magnetic field at 1.4 kG. (a) Blue squares show a typical magnetic field trace, obtained through the spectroscopic technique described in the text after synchronizing the experimental sequence with the 50-Hz mains, once the sole active stabilization of the current of the BIAS and COMP coils setups is implemented. The observed trace, synchronous with the mains and characterized by a peak-to-peak amplitude of about 40 mG, is well fitted to a sum of sinusoidal functions with a main Fourier component at 50 Hz plus a few higher harmonics of decreasing amplitude (blue line). Employing the (reversed) fitted trace to drive the AC-COMP coils setup, we strongly mitigate the main noise contribution, being left with a residual (synchronous) noise (green circles) of about 5 mG peak-to-peak. (b) Characterization of the (asynchronous) shot-to-shot noise of the magnetic field. Black circles show the standard deviation of the transfer efficiency as a function of the π -pulse time. Taking into account also an independent constant noise source in our measurements (see text), we extract a shot-to-shot noise standard deviation of $2.4(2)$ mG.

6.2 High-field imaging setups

The lithium and chromium high-field imaging setups have been modified and upgraded compared to those reported in my Master Thesis [102]. After the identification and assignment of ${}^6\text{Li}$ - ${}^{53}\text{Cr}$ Feshbach resonances (see Chapter 3), our interest has been focused on the two magnetic field regions around 1414 and 1461 G, where two among such features – occurring in the $\text{Li}|1\rangle$ - $\text{Cr}|1\rangle$ and $\text{Li}|2\rangle$ - $\text{Cr}|1\rangle$ spin combinations, respectively – were found. We therefore implemented new imaging setups for both Li and Cr atoms, able to deliver resonant light addressing the relevant optical transitions at such high fields, as well as at zero field – which is required to image the MOT clouds, and thus rather helpful to debug and optimize the first stages of the experiment.

Lithium

The new Li high-field imaging setup, sketched in Fig. 6.2, can produce the light frequencies for both the two lowest Zeeman states ($\text{Li}|1\rangle$ and $\text{Li}|2\rangle$), either at 1414 or at 1461 G. In this new scheme, light is initially taken directly from the D2 master laser, which is locked at about -308 MHz from the repumper transition of the MOT [123], ${}^2S_{1/2} |F = 1/2\rangle \rightarrow {}^2P_{3/2} |F' = 3/2\rangle$ (see Fig. 2.2). A series of three double-pass acousto-optic modulators (AOMs) in a cascade configuration is employed to redshift the laser light to the desired frequency. The former two AOMs, driven by a shared controllable driver, are carefully aligned to yield equal diffraction efficiencies for two different frequencies, separated by ~ 18 MHz, thereby introducing the $\text{Li}|1\rangle$ - $\text{Li}|2\rangle$ frequency shift of about 72 MHz after the double-pass through both of them. Specifically, to produce the two lights resonant at 1414 G, AOM1 and AOM2 are both driven either at 191 MHz (for $\text{Li}|1\rangle$) or at 209 MHz ($\text{Li}|2\rangle$). Alternatively, when we desire to work at 1461 G, the first two AOMs are both driven either at 207 MHz (for $\text{Li}|1\rangle$) or at 225 MHz ($\text{Li}|2\rangle$). In both cases, the third AOM operates instead constantly at 392 MHz. The three double-pass stages are all realized in *cat-eye* configuration, such that the optical paths of $\text{Li}|1\rangle$ and $\text{Li}|2\rangle$ lights are spatially overlapped at the end of the cascade. These are then further combined on a polarizing beam-splitter with the zero-field imaging path (not shown in Fig. 6.2), and then injected into the imaging fiber, which finally delivers light to the atoms.

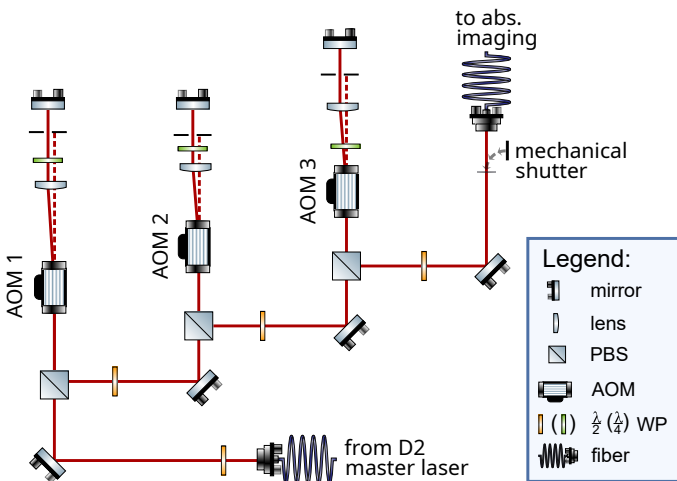


Figure 6.2 – Sketch of the new optical setup to prepare the lights for high-field absorption imaging of Li. Light is initially taken from the output of the D2 master laser, and then downshifted by about ~ 1.5 GHz via three double-pass AOMs in cascade configuration. The first two AOMs can be controllably adjusted in frequency to address either $\text{Li}|1\rangle$ or $\text{Li}|2\rangle$ atoms on demand. At the end of the cascade, the high-field path is combined with the zero-field one (not shown), before being injected into the imaging fiber.

Chromium

The new high-field imaging setup for Cr, sketched in Fig. 6.3, can deliver resonant light only for the lowest Cr spin state ($\text{Cr}|1\rangle$) either at 1414 or at 1461 G. Initially, light is taken from the transverse cooling (TC) AOM path (see details in Ref. [102]): either from the non-diffracted order (for high fields), or from a pickup of the double-pass output (for zero field). These two beams, having orthogonal polarizations, are combined on a polarizing beam-splitter (PBS) and injected into a first fiber, that brings them to the imaging breadboard, sketched in Fig. 6.3. As shown there, at the fiber output they are split by a PBS into two different paths: The former one, transmitted from the PBS, first passes through two consecutive AOMs in a retro-reflected *cat-eye* configuration. A third single-pass AOM further downshifts the frequency to the desired value. When the first two AOMs are driven at 387 MHz (394 MHz) and the third one at 192 MHz (228 MHz), light at the output of this stage is resonant with $\text{Cr}|1\rangle$ atoms at 1414 G (1461 G).

The second path, realizing the zero-field imaging, does not require any additional frequency shifts besides those inherited from the TC AOM. High- and zero-field lights are ultimately combined on a PBS, and coupled to a common fiber which brings them onto the experimental table. Whenever one of the two is not needed, a safety block is placed on its path.

Compared to the Li imaging setup, a limitation of the Cr one is the lack of $\text{Cr}|2\rangle$ resonant light, which is further redshifted by about 190 MHz with respect to the $\text{Cr}|1\rangle$ imaging frequency at the fields of interest. While different schemes can be thought and implemented in the future on the setup, a simple and practical way to image $\text{Cr}|1\rangle$ and $\text{Cr}|2\rangle$ atoms in the same experimental shot – using only $\text{Cr}|1\rangle$ light – is offered by the possibility to drive fast $\text{Cr}|1\rangle \leftrightarrow \text{Cr}|2\rangle$ RF transitions. In practice, one first takes an absorption image of the $\text{Cr}|1\rangle$ state, then applies a fast π -pulse, and finally takes a second image of the $\text{Cr}|1\rangle$ state, which is now populated by atoms that were in $\text{Cr}|2\rangle$ before the RF pulse. We employ this “RF-assisted” imaging protocol whenever we perform RF spectroscopy on Cr atoms (see, e.g., Sec. 6.1), or when we wish to check the polarization degree of Cr. Indeed, the protocol can also be extended to image higher Zeeman states ($\text{Cr}|j \geq 3\rangle$), provided the RF antenna is able to address the corresponding transitions; see Ref. [218] for technical details on the antenna.

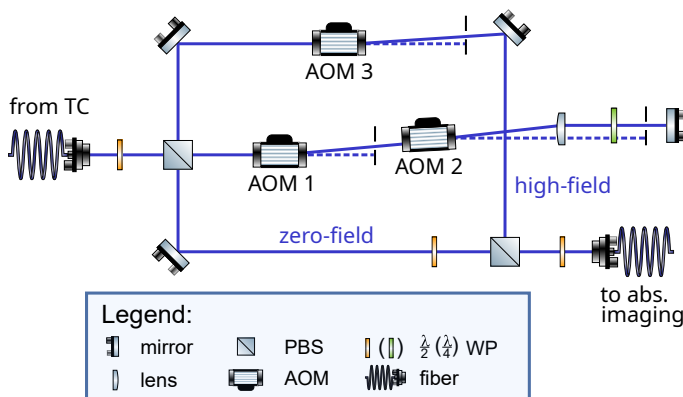


Figure 6.3 – Sketch of the new optical setup to prepare the imaging lights for Cr. The high-field path originates from the non-diffracted order of the TC AOM. On the imaging breadboard, it passes through two consecutive AOMs in a retro-reflected configuration, and subsequently through a third, single-pass AOM. The zero-field path, picked from the resonant TC beam, does not require any frequency shifts. The two paths are combined on a PBS before being injected into the imaging fiber.

6.3 FORT optical setup

As discussed in Chapter 4, Sec. 4.5, by studying the trap-light-induced photoassociation rates of LiCr Feshbach dimers, we found that the two lights in our bODT (1070 and 532 nm) constituted a limiting factor to the molecule lifetime, featuring intensity-dependent loss rates of $\Gamma_{cc,1070} = 5.9(2)$ Hz/(kW cm⁻²) and $\Gamma_{cc,532} = 397(14)$ Hz/(kW cm⁻²), respectively. Namely, given the beam waists of these two trap beams (see Fig. 2.5), such numbers translate into $\Gamma_{cc,1070} = 131(5)$ Hz/W and $\Gamma_{cc,532} = 10.4(4)$ kHz/W. The (much stronger) effect of the green light is detrimental for the lifetime of LiCr Feshbach dimers, even for relatively low powers of a few tens of mW. On the other hand, the (weaker) photo-excitation rate induced by 1070-nm light, for typical employed powers of about $P_{1070} \sim 200 \div 300$ mW, still allows for a sufficiently long lifetime (tens of ms) for several measurements to be performed, albeit it arguably prevents beforehand any possibility to obtain long-lived samples of Feshbach molecules, and to realize a final sympathetic cooling stage of LiCr with either lithium or chromium atoms. For these reasons, borrowing knowledge from the K-Dy experiment in Innsbruck (data still unpublished at the moment of this writing), we decided to test a new trapping wavelength for LiCr dimers, i.e. 1560 nm, with considerably lower energy per photon compared to the 1070-nm one, implementing two new trap beams (“main” and “cross”, see below) on the setup. In particular, the “main” trap at 1560 nm, collinear with the main bODT, has allowed us to obtain long-lived, pure molecular samples with lifetimes exceeding 0.2 s, see Secs. 4.5 and 4.9.

The optical setup implemented for the far-off-resonant trap (FORT) is sketched in Fig. 6.4. Laser light is delivered by an erbium fiber amplifier (Keopsys-CEFA-CBO-HP), seeded by a single-mode master laser (RockTM, NP Photonics), with a total output power of about 16 W. As sketched in Fig. 6.4(a) [to be read from the right to the left], at the amplifier output an optical isolator is employed to avoid back reflections that could damage the laser. The beam is then sent to a first, power-tunable AOM: the first negative diffracted order is employed to realize the “main” 1560-nm trap, and it is directly injected into a high-power photonic-crystal fiber. The non-diffracted order is instead directed toward a second AOM, analogous to the former one, the first positive diffracted order of which realizes the “cross” 1560-nm trap.

Figure 6.4(b) shows instead how the main FORT is overlapped with our bODT, and hence focused on the atomic clouds. At the output of the main fiber, a telescope is used to adjust the waist and divergence of the 1560-nm beam.² A controllable flip mirror directs the main bODT toward a beam dump during the entire evaporation stage (see Sec. 2.6), i.e. when the high optical power of the main bODT could damage the photonic-crystal fiber of the FORT. At the end of evaporation, when we desire to transfer the atoms from the main (b)ODT to the FORT [see, e.g., Sec. 4.9], the flip mirror is opened, and the 1560-nm light is switched on by activating the AOM.

A good starting point to overlap the two beams at the atoms position is found when the 1070-nm light is coupled to the output of the photonic-crystal fiber. From there, to compensate for the residual shifts due to refraction within the optics, we carefully optimize the final alignment by maximizing the transferred atom number in the FORT, reaching nearly 100% efficiency for both species.

The vertical cross beam at 1560 nm, not shown in Fig. 6.4(b), replaces the 1070-nm one in our crossed bODT, see Sec. 2.8. It features a (circular) beam waist of about 100 μm (at the atoms/molecules position). In this Thesis, it is employed mainly for the preparation of the Li cloud in the transport measurements of Chapter 5.

²We tested two different (circular) beam waists: 55 μm and 29 μm (at the atoms/molecules position). The long-lived dimer samples of Sec. 4.9 were obtained with the former beam configuration.

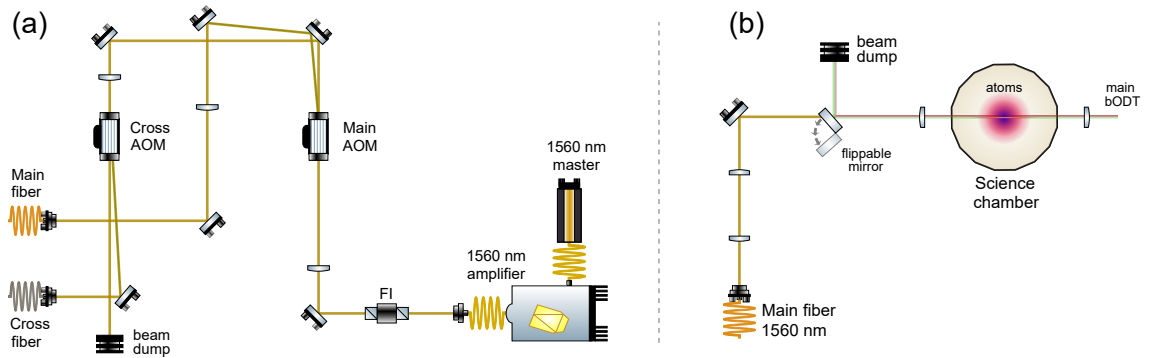


Figure 6.4 – Sketch of the optical setup for the new FORTs at 1560 nm. (a) Laser table: preparation of “main” and “cross” beams. (b) Science table: overlap between the main FORT and the main bODT. See text for description and details.

6.4 Double-loading scheme for lithium

As a very recent development, during the last months of my Ph.D. we implemented a double-loading scheme for lithium, which allows us to significantly increase the number of Li atoms loaded in the bODT (cf. Sec. 2.5). This, in turn, also improves the sympathetic cooling efficiency, ultimately resulting in a sizable gain for both species at the end of the evaporation stage. The idea is to recycle some power from the IR laser source in order to shine a secondary, horizontal ODT beam on the CMOT clouds, thereby simultaneously loading lithium in two different optical traps. Such a secondary beam, containing IR light only, is generated from the non-diffracted order of the main IR AOM,³ and shone on the atoms after passing through an additional, vertically-mounted AOM: this allows us to controllably adjust the vertical displacement from the main bODT, as explained in the following.

To realize two different optical traps, during the loading stage the overall optical power of the IR laser is ramped up to 300 W, while the RF power sent to the main AOM is reduced accordingly in order to still have 130 W on the main beam realizing the bODT, thereby not affecting the loading dynamics of the main optical trap (see Sec. 2.5). With this configuration, considering the secondary AOM peak-efficiency of about 70%, the maximum power available on the additional IR trap is around 120 W. The strategy that we follow consists in carefully aligning the secondary IR beam *below* the main bODT, performing a simultaneous loading of the two traps during the CMOT stage. Clearly, due to the absence of green light in the secondary IR ODT, the Cr component is not loaded into it with this procedure (see Fig. 2.6), resulting in a pure Li sample in the two lowest Zeeman states.

After the double loading, one could perform an evaporative cooling stage in the secondary trap that follows the one of the main bODT (described in Sec. 2.6). In this way, degenerate samples of about 5×10^5 Li atoms (per spin state) at $T_{\text{Li}}/T_{\text{F,Li}} \simeq 0.15$ (with $T_{\text{Li}} \simeq 200$ nK) can be produced in the additional trap, without affecting the evaporation dynamics of the main one. Figure 6.5 shows a typical absorption image obtained by following this procedure. Naively thinking, an overall improvement of the final Li-Cr sample in the main bODT could then be obtained by merging the two traps after this separate evaporation. As anticipated, the possibility to merge the two beams is offered by the vertically-mounted AOM, which can be controllably tuned in frequency, resulting in a vertical displacement of the secondary beam. In principle, a perfect merge with 100%

³This is the beam that we used for the vertical bichromatic cross of Sec. 2.8, now replaced in that role by the 1560-nm cross beam, see Sec. 6.3.

transfer efficiency would constitute a significant gain in the Li atom number, possibly allowing for further evaporation of the Li-Cr mixture.

However, when tested experimentally, such a scheme did not yield any positive effect, regardless of the “gentleness” of the merging frequency-ramp: In fact, in general, we observed a substantial heating of the atoms, accompanied by significant trap losses. We interpret this observation as a direct consequence of the Fermi-Dirac statistics and the Pauli principle: Since the Li samples in both the main and the secondary trap at the end of the evaporation sequence are deeply degenerate, and thus most of the single-particle levels are already occupied, the merging procedure actually promotes many atoms to high-energy states, resulting in overall heating of the final sample, which causes atom losses.

A more efficient scheme to exploit the secondary trap, developed after noticing that the one discussed above was not successful, is based on an adiabatic merge performed shortly after the start of the evaporation stage, when the atoms are still in the thermal regime. Looking at the final sample, we carefully optimized the merging time, the duration of the merging (frequency) ramp, and the duration of the subsequent power ramp employed to extinguish the secondary trap, once overlapped with the main one. We found an optimum in this parameter space when the merging was performed about 1.5 s from the start of the evaporation (when the temperature is around 15 μ K), exploiting a 50-ms-long radiofrequency ramp with the shape of the “minimum-jerk function” [219], followed by a 250-ms-long exponential ramp to remove the secondary IR beam.

Compared to the numbers reported at the end of Sec. 2.6, without the green beam in the main dipole trap (and thus without loading the Cr component), the scheme described above results in a significant gain in the final Li atom number, which increases from 1.9×10^6 up

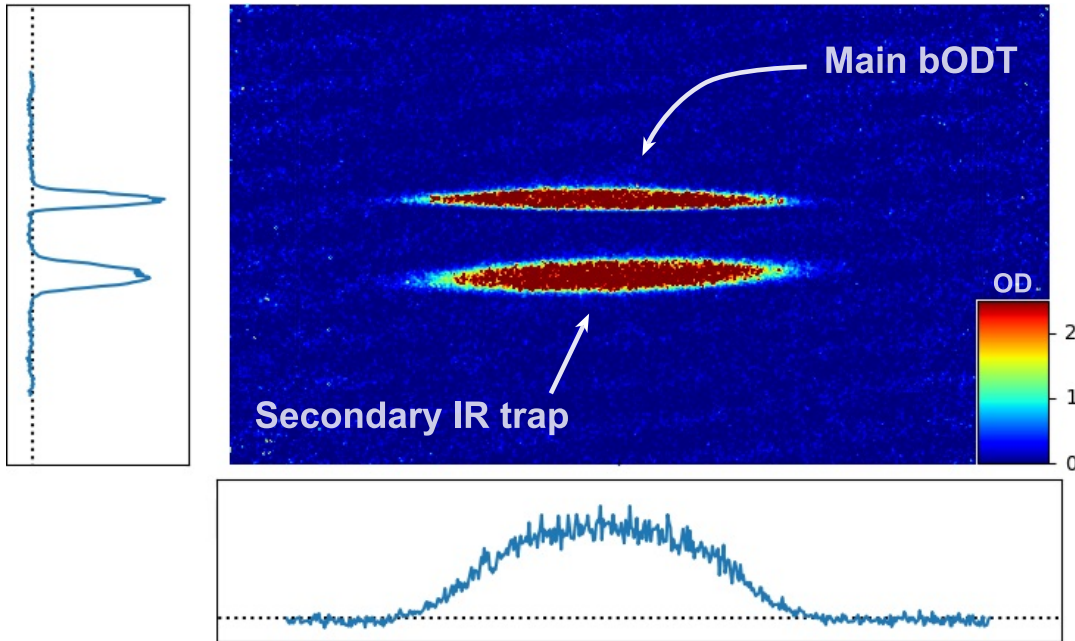


Figure 6.5 – Typical absorption image of a Li sample held in the double trap. The upper cloud is trapped in the main bODT and the bottom one in the secondary IR trap. The image was obtained by following the double-loading scheme described in the text, in the absence of Cr atoms and without merging the two traps. Following an evaporation trajectory analogous to that of the main bODT, we obtain in the secondary trap deeply degenerate Li samples comprising up to 5×10^5 atoms per spin state, with $T_{\text{Li}}/T_{\text{F,Li}} \simeq 0.15$ and $T_{\text{Li}} \simeq 200$ nK. In this picture, the centers of the two clouds are separated by 125 μm .

to 3×10^6 per spin state.⁴ In the presence of the green beam in the main bODT, but still in the absence of Cr atoms, the relative gain is further increased, with N_{Li} passing from 0.5×10^6 to 1×10^6 , per spin state. Most importantly, when the double-loading scheme is applied under our standard evaporation conditions, i.e. also in the presence of chromium, the net gain in N_{Li} results also in an improvement of the Cr component, both in terms of atom number and temperature. Specifically, without applying the “Feshbach cooling” stage in the final part of the evaporation (see Sec. 2.7), we observe N_{Li} (N_{Cr}) increasing from 4×10^5 (2×10^5) up to 6×10^5 (2.5×10^5), with the Cr temperature decreasing from 600 nK down to about 400 nK, thereby reducing the gap displayed in Fig. 2.8(d). Furthermore, when the “Feshbach cooling” stage is performed, the Li|1⟩ (Cr|1⟩) atom number grows from 3.5×10^5 (1×10^5) up to 4.5×10^5 (1.5×10^5), with both species thermalized at about 200 nK. This boost in the atom numbers has allowed us to increase the number of associated ${}^6\text{Li}{}^{53}\text{Cr}$ Feshbach molecules, as well as the density of the Cr bath for the transport measurements of Chapter 5.

As a final remark, I discuss another possible employment of the secondary trap, not tested in the experiment yet. If the merge is not performed, at the end of the evaporation stage one obtains two independent samples, i.e. a Li-Cr mixture and a pure Li cloud, trapped in the main bODT and in the secondary IR beam, respectively, with a vertical displacement of about 125 μm (see Fig. 6.5). The secondary Li sample could then be used as an effective co-magnetometer, in order to measure the *real* magnetic field, on top of drifts and fluctuations, within the very same experimental cycle that performs a field-sensitive measurement on the Li-Cr mixture. For instance, one could carefully block part of the Li imaging beam with a knife-edge, in such a way that the secondary Li sample is not affected by the (destructive) absorption image used to acquire the measurement on the main one. After that, by means of RF spectroscopy schemes, the magnetic field at the position of the secondary trap can be measured, and – knowing the magnetic-field gradient – the field at the position of the main trap can be readily derived. Alternatively, with an imaging beam that only addresses the secondary sample, the actual magnetic field could be even probed *before* performing the field-sensitive measurement on the main (bi)atomic or molecular cloud, and the result could be sent to an active feedback loop that corrects the magnetic field accordingly. For instance, if the main trap contains only Li|1⟩ and Cr|1⟩ atoms (or LiCr molecules formed starting from this parent mixture), the secondary sample could be prepared in the Li|2⟩ state, with RF spectroscopy performed on the Li|2⟩ \longleftrightarrow Li|3⟩ transition, thereby not affecting atoms or molecules in the main trap.

⁴To be more precise, the numbers reported here refer to the Li|1⟩ spin state. Under any circumstances, the Li|2⟩ atom number is found to be constantly about 30% lower, as discussed in Sec. 2.6.

Conclusions and outlook

In conclusion, in this Thesis I described the experimental studies and reported on the main scientific achievements that I obtained during my Ph.D. Starting from an existing setup delivering cold lithium-chromium mixtures in a dual-species magneto-optical trap [121], during the four and a half years from the beginning of my Master Thesis [102] to the end of my doctorate, I contributed to the further development of the Li-Cr machine in terms of key technical upgrades, implementation and refinement of experimental protocols, and, most importantly, general advances in the investigation and understanding of such a novel system. In particular, our main research achievements encompass the first realization of doubly-degenerate mass-imbalanced ${}^6\text{Li}$ - ${}^{53}\text{Cr}$ Fermi mixtures, the exhaustive characterization of their elastic and inelastic scattering properties, the production of high phase-space density gases of bosonic LiCr Feshbach molecules, and the investigation of transport properties of Li impurities embedded in a thermal Cr bath. Our efforts make Li-Cr Fermi mixtures an appealing playground with which to investigate a plethora of yet unexplored phenomena, spanning from the few- and many-body physics of strongly interacting fermionic matter to the formation of ground-state paramagnetic polar molecules in the quantum degenerate regime.

In fact, owing to the special chromium-lithium mass ratio, $M_{\text{Cr}}/m_{\text{Li}} \simeq 8.8$, extremely close to the critical values above which *non-Efimovian* cluster states are predicted to emerge [9, 11, 13, 15, 20, 22], our mixture may provide an exemplary benchmark for a wealth of theoretical predictions, lacking direct experimental observation in any physical system so far. Moreover, the collisional stability predicted for such exotic few-body states [14, 20, 30] makes them appealing also from a many-body perspective. For instance, novel types of quasiparticles could emerge in the light impurity problem: Besides Fermi polarons and dressed dimers [33], lithium impurities embedded in a *deeply degenerate* Cr Fermi gas may indeed exhibit more complex quasiparticles [30, 32, 35], connected with the existence of higher-order few-body states in the vacuum. In this respect, the ability to widely tune both the degree of degeneracy and the relative densities of the Li and Cr components in our crossed bODT (see Fig. 2.11) offers a compelling opportunity to investigate, with the same experimental setup, both heavy and light impurity problems within fermionic media.

Our progress toward double Fermi degeneracy was accompanied by extensive surveys of ${}^6\text{Li}$ - ${}^{53}\text{Cr}$ Feshbach resonances, which allowed us to identify more than 50 of such features, well separated one from the other and displaying a *nonchaotic* pattern. Through a coupled-channel model, our collaborator Prof. A. Simoni was able to unambiguously connect each of these FRs to a LiCr molecular level with well-defined quantum numbers. His task was somewhat simplified by the fact that the interaction between Li (${}^2S_{1/2}$) and Cr (7S_3) atoms, besides featuring only weak magnetic anisotropy, leads to two sole spin multiplicities (sextet and octet), similarly to standard bi-alkali case of singlet and triplet. In particular, we identified and experimentally characterized a pair of strong and isolated high-field *s*-wave FRs, featuring magnetic-field widths of about 0.5 G, with character similar to Li-K ones [129, 130] but immune to two-body losses. Despite their comparatively narrow nature, combined with their high-field location above 1.4 kG, these features allow for the resonant control of Li-Cr interactions in our experiment.

As a direct example, the experiments that I have described in Chapter 5 represent a relevant step forward in the exploitation of our mixture to investigate transport phenomena within mass-asymmetric fermionic matter, and they indeed demonstrate the possibility to employ such Li-Cr FRs to controllably realize strongly-interacting mixtures in the

experiment, despite their rather “scary” magnetic field locations and comparably small B -field widths. As already mentioned in the conclusions of Chapter 5, a wealth of possible extensions of the transport studies presented therein can be envisioned, and rather straightforwardly implemented on our setup. For instance, in the future it will be interesting to investigate how the anomalous transport, and eventually the complete halt of diffusion due to the system localization, may be affected by the trap geometry, or by a reduced dimensionality. It is indeed known that, for static disorder, localization is greatly favored in two- and one- dimensions, with respect to the three-dimensional case. Additionally, the implementation of a species-selective optical lattice could allow for a systematic study of the subtle interplay between the system tendency to localize (for sufficient point-like disorder strength) and the delocalizing effects induced by a slow, incoherent motion of the scatterer centers: By tuning the effective mass of the chromium atoms, one could sizably reduce their mobility, thus enhancing possible quantum interference effects. In this regard, I remark the interesting, yet not fully established, connection between three- (and four-) body universal clusters, expected for the Li-Cr mass ratio to emerge on the molecular side of a FR, and the so-called quantum proximity resonances [220], predicted on the $a < 0$ side of a narrow resonance, in the case of one impurity atom colliding with two fixed scatterer centers via a short range interaction. Another interesting aspect we could address with our setup in the future concerns the investigation of the role played by Pauli blocking and Fermi degeneracy on the anomalous dynamics that we observed, so far, with both impurities and bath particles in the thermal regime. While we expect that a further reduction of the mixture temperature will help enhancing the coherence of the system, once a Fermi gas (or a doubly-degenerate mixture) would emerge, Pauli suppression of scattering events could have a non-trivial impact on the transport and/or localization properties of our system. Finally, an appealing investigation, complementary to those reported in Chapter 5 of this Thesis, is represented by exchanging the impurity-bath roles played by our mixture components, i.e. embedding a few heavy Cr particles within a light Li Fermi gas. In this case, the Li-Cr mixture could be regarded as a “finite mass-imbalance version” of the archetypal system of the so-called Anderson orthogonality catastrophe, realized by an infinitely heavy impurity within an ideal Fermi gas.

The existence of suitable, isolated s -wave Li-Cr FRs provides also an optimal starting point to form bosonic Feshbach dimers. We have successfully produced ultracold gases comprising up to 5×10^4 ${}^6\text{Li}{}^{53}\text{Cr}$ Feshbach molecules, at temperatures around 200 nK and peak phase-space densities exceeding 0.1. Thanks to the immunity to two-body decay and the good stability against three-body recombination of our fermionic mixture, we could perform magneto-association with ramp rates slower than the two-body-adiabatic regime by orders of magnitude. We directly revealed the paramagnetic nature of the LiCr molecule, and demonstrated precise control of the Feshbach state via a novel optical measurement of the open-channel fraction and binding energy. Moreover, through the characterization of the dominant loss mechanisms affecting our Feshbach dimers, we have identified an experimental configuration where their lifetime exceeds 0.2 s.

Parallel to our efforts in the lab, our theory collaborator Prof. M. Tomza and his group developed a cutting-edge, *ab initio* quantum chemical model for LiCr, with which they determined the fundamental properties of this new molecular species. In particular, for the rovibrational X ${}^6\Sigma^+$ ground state, their model predicts a large electric dipole moment of 3.3(2) D, on top of the sizable magnetic one of $5 \mu_B$. Additionally, M. Tomza and colleagues foresee that our Feshbach dimers – which notably are already created in the *least bound* X ${}^6\Sigma^+$ rotationless vibrational level – can be efficiently transferred to the absolute ground state, via STIRAP through an excited (4) ${}^6\Sigma^+$ level, with transitions at

experimentally accessible wavelengths. Conveniently, direct imaging (and possibly even laser cooling schemes!) of ground-state LiCr may be enabled by the presence of strong $X\ ^6\Sigma^+ \rightarrow (2)\ ^6\Pi$ optical transitions.

Our experimental and theoretical results combine synergistically to make ultracold LiCr emerge as an extremely appealing system for a wealth of fundamental studies and future applications. In fact, a high phase-space density sample of $^6\text{Li}^{53}\text{Cr}$ Feshbach dimers, which we have already realized in the lab, opens exciting new routes for the investigation of strongly correlated fermionic matter. For instance, extending the protocols we have developed so far may allow us to Bose-condense our Feshbach dimers, thereby paving the way to studies of the BCS-BEC crossover in the presence of a large mass asymmetry [45, 46, 49]. Moreover, the creation of long-lived LiCr dimers in the presence of a controlled amount of Cr atoms is a fundamental step towards the aforementioned exotic few- and many-body phenomena that are uniquely enabled by the “magic” mass ratio of our atomic Fermi mixture [111]. Besides LiCr₂ fermionic trimers [9, 11, 13], LiCr₃ bosonic tetramers [15, 21, 22], and the related new kinds of quasiparticles within the light-impurity problem [32, 33, 35], exciting prospects are given by the possible emergence of many-body regimes beyond the BCS-BEC crossover scenario, such as trimer Fermi gases [30] or quartet superfluid states [31].

Additionally, from the viewpoint of doubly-polar molecules, the combination of our experimental achievements with the theoretical work of M. Tomza and colleagues suggests that the realization of ground-state $^6\text{Li}^{53}\text{Cr}$ bosonic molecules, with large electric and magnetic dipole moments, is within reach. Clearly, identification of the optimal STIRAP pathway will require extensive laser spectroscopy. However, this task will be greatly facilitated by the predictions of the theoretical *ab initio* model, and also by the long lifetime of Feshbach dimers that we already demonstrated. Interestingly, electric dipole moments as high as 1 D can already be obtained in relatively shallow vibrational levels of LiCr with $v \simeq 37$ and a binding energy as low as 190 cm^{-1} , see Fig. 4.13. Given the relatively simple spectroscopic survey needed to find these states, this possibility represents an attractive, intermediate short-term step. In particular, such vibrationally excited molecules offer high sensitivity to the electron-to-proton mass ratio m_e/m_p [169], surpassing that of alkali and alkaline-earth dimers. This sensitivity could enable precision measurements to detect potential variations of m_e/m_p , providing new insights into fundamental physics.

Ground-state LiCr molecules, pinned in optical lattices or tweezers, will find immediate application in the context of quantum simulation of spin Hamiltonians [66–69] and high-dimensional quantum computing [70, 71], exploiting their internal spin degree of freedom, absent in ground-state bi-alkali dimers. Moreover, bulk gases will be ideal test beds for quantum controlled chemistry: Although ground-state LiCr molecules are chemically unstable against atom-exchange reactions $2\text{LiCr} \rightarrow \text{Li}_2 + \text{Cr}_2$, in their spin-stretched state resulting from STIRAP they are expected to be stabilized, owing to the fact that the decay to deep Cr₂ levels becomes spin-forbidden. The predicted rotational constant and electric dipole moment, incidentally close to those of CaF [221], suggest that collision shielding, via microwave [222] or static electric fields [223, 224], could be applied to stabilize bulk samples and perform evaporative cooling. Additionally, resonant tuning of magnetic [74] and field-linked resonances [225] may be investigated in LiCr. Prospects for precision measurements also appear promising: on top of the measurement of m_e/m_p already mentioned, the observation of the electron’s electric dipole moment may be facilitated by the internal co-magnetometer states offered by long-lived $^4\Delta$ metastable levels [185], unavailable in bi-alkali dimers. Finally, it is worth noting that fermionic isotopologues $^7\text{Li}^{53}\text{Cr}$ and $^6\text{Li}^{52}\text{Cr}$ could also be formed via magneto-association across suitable FRs on our experimental setup. In particular, the first experimental evidence of $^6\text{Li}^{52}\text{Cr}$ molecule formation was obtained in the lab by my colleagues Alessio Ciamei and Beatrice Restivo while this Thesis

was being written. Correspondingly, the magnetic field location of two high-field s -wave ${}^6\text{Li}$ - ${}^{52}\text{Cr}$ has been measured. Interestingly, such a measurement precisely *fixes* the number of bound states in the ground-state sextet potential to $N_6 = 46$, in perfect agreement with the prediction of M. Tomza and colleagues (see Sec. 4.10.1).

Acknowledgments

The list of people I want to acknowledge for their help, guidance, assistance, friendship, and support over these years is, in principle, fairly long, and no finite number of words can fully express my gratitude.

Starting from the scientific part, I would like to sincerely thank Matteo for accepting me into the Li-Cr lab, and for supervising both my Master Thesis and my Ph.D. Besides being always a kind and supportive person, with his incredibly vast and detailed knowledge in our field¹ he constantly guided and directed me during my research activity, one *Feshbach cigarette* after another. Roughly speaking, to make a quick estimate, if I take: two hundred nanokelvins, five in ten to the eleventh, and six thousands a_0 , it turns out that he has been the best supervisor I could have ever wished for. Thanks Matte.

For very similar reasons, the second person I wish to thank is Alessio.² Not only did he teach me everything I know in the lab, but also everything I actually *don't* know in the lab. He has always been a great friend and lab mate, and I will never forget all the successful results that we achieved together, from the long evenings of Feshbach spectroscopy (“*we can't go home unless we find one!*”) to the very first molecular signals, and more or less everything else contained in this manuscript. In particular, I personally am very fond of our optical measurement of the open-channel fraction, which beautifully resulted from the combination of my experimental observations with his theoretical model. I will also treasure all the philosophical discussions that we had while working together on the experiment, especially those metaphorically concerning the stability of a table as a function of the number of its legs. For instance, now I know that somewhat remarkable stability can be achieved with *exactly zero legs*. Jokes aside, the most powerful and meaningful lesson I learned from him, valid both inside and outside of the lab, is that if things seem to get worse on one side – and they also seem to get worse on the other side – it means there is an optimum condition in between.

Continuing on my list, I wish to thank Andreas for being as patient and kind (to me, and more generally to everyone else asking for help) as he is technically skilled. It is rare to find a person that is so gentle with both other humans *and* electronic devices. It is undeniable that – if the standard layman's solution for a generic computer problem is to restart it – the typical solution to any electronics-related issue in our lab (and not only!) starts with «*Sorry, Andi. . .*». Needless to say, the Li-Cr experiment would be nearly impossible without his contribution.

Coming to the “young” Li-Cr people, a special thanks goes to Antonio and Beatrice, who brought a breath of fresh air in the lab during the second half of my Ph.D. It has been both exciting and instructive for me to introduce you to the experiment, to the best of my possibilities, from the first fiber couplings to the most nerdy tricks on the control program. Thanks for all the jokes and all the laughs we had together, for sharing fundamental views and ideals on real-life topics, and for allowing (and often appreciating) my (I would say *moderate*) blasphemy. To conclude this first part, I also thank all the people who worked on the experiment before me, building the core of the apparatus and of the optical setup. In particular, thanks to Elettra, Irene, and Cristiano.

Going out of the lab door, I acknowledge the entire Quantum Gas Group in Florence (+ Pisa branch!) for the uncountable fruitful discussions, the stimulating meetings, and for the persistent, mutual support to lend and borrow lab equipment. In particular, I owe

¹He would cite here a few papers, of which he most likely knows even the DOI by heart.

²A.k.a. the Shaolin Master Cha-Mei.

special thanks to Giovanni Modugno, Marco Fattori (who first introduced me to Matteo), Carlo Sias,³ Leonardo Fallani, and Giacomo Roati.

I am also extremely and warmly grateful to my fellow ultracold Ph.D. students in other labs, especially to Nicolò, Giulio, Luca, Diego, Ludovica, and Tommaso. For those who were there, Varenna 2022 and YAO 2023 are definitely among the best memories I have of these last years.

Stepping outside of Florence and Tuscany, a truly wholehearted, special, mass-imbalanced, resonantly-interacting, fermionic thanks goes to Cosetta and Alberto, whose importance for me as real-life friends, hiking buddies, and fellow scientists is hard to quantify even on a log scale. I consider the fact that we happened to be Ph.D. students (in our respective labs) during the same years as an extremely lucky circumstance. Further, our choice to become close friends, instead of somewhat competitors, is to me one of the most spectacular examples of how science and research should be embraced. Much love guys, thanks.

I take the opportunity to thank here also the rest of the Innsbruck group, in particular Prof. R. Grimm and all the people in his team.

Somehow unluckily, physics is not an entirely experimental field,^[citation needed] and theory is often required. The interaction between experimentalists and theorists is typically one of the most complex in nature, and no efficient communication scheme has been devised yet. Despite this, I really wish to thank Dmitry Petrov multiple times, at least once for each of the (typically rather extended) discussions that we had during these years, as well as for the patience and kindness with which he replied to my scattered emails about scattering theory. In particular, I personally consider the fact that I once made him “moderately interested” about an idea of mine (which unfortunately turned out to be somewhat wrong) one of the greatest accomplishments of my (past, present, and future) career. I also acknowledge our other theory collaborators, Prof. A. Simoni and Prof. M. Tomza, who provided fundamental assistance with their theoretical calculations.

Moving now to my family, the greatest thanks goes to my parents for the everlasting support they had towards me. Studying physics (so many years!) and graduating would not have been possible without their fundamental contribution and presence. Special thanks to my brothers, Davide and Nicola,⁴ who were absolute role models for me when I was younger. A wholehearted thanks also to my grandparents, in particular to my grandma Vera, who raised me as a second mother. I am sure she will completely understand and appreciate these sentences in English, given the cheat sheet I prepared for her when I was a kid. Of course, I cannot avoid mentioning my beloved orange cat, Meo, the cutest and most adorable bunch of atoms in the entire galaxy, out of error bars.

The years I spent in Florence have undoubtedly changed me significantly and, I would say, quite positively. Studying, working and, most importantly, living here has been a great and unforgettable experience mainly thanks to: Sara, Nico (who totally deserves the double mention), Giulia(na), Marianna, Nicoletta, Guido(ne), Diablo, Fungi, Augusto, Raffa, Barb, Tecla, Momo, Cini, Duccio, J, René, Celle, and all the other people from Aula Stud and Circolo.

Last, but absolutely not least, an amazing thanks to all the *regaz* that are friends of mine from a lifetime ago, in particular: Checco, Ismael, Lollo, Iwo, Otti, Fede, Tommi, Richi, Clod, Seppia, Pier, and the whole extended Bologna’s *balotta*.

³Or, should I say, M. O.?!

⁴Dado and Dodo, respectively.

Bibliography

- [1] R. Casalbuoni and G. Nardulli, “Inhomogeneous superconductivity in condensed matter and QCD,” *Rev. Mod. Phys.*, vol. 76, pp. 263–320, Feb 2004.
- [2] O. Andersen and L. Boeri, “On the multi-orbital band structure and itinerant magnetism of iron-based superconductors,” *Annalen der Physik*, vol. 523, no. 1-2, pp. 8–50, 2011.
- [3] H.-W. Hammer, A. Nogga, and A. Schwenk, “Colloquium: Three-body forces: From cold atoms to nuclei,” *Rev. Mod. Phys.*, vol. 85, pp. 197–217, Jan 2013.
- [4] M. Yi, Y. Zhang, Z.-X. Shen, and D. Lu, “Role of the orbital degree of freedom in iron-based superconductors,” *npj Quantum Materials*, vol. 2, p. 57, Oct 2017.
- [5] G. Wang, A. Chernikov, M. M. Glazov, T. F. Heinz, X. Marie, T. Amand, and B. Urbaszek, “Colloquium: Excitons in atomically thin transition metal dichalcogenides,” *Rev. Mod. Phys.*, vol. 90, p. 021001, Apr 2018.
- [6] Y. Jiang, S. Chen, W. Zheng, B. Zheng, and A. Pan, “Interlayer exciton formation, relaxation, and transport in TMD van der Waals heterostructures,” *Light: Science & Applications*, vol. 10, p. 72, Apr 2021.
- [7] C. Chin, R. Grimm, P. Julienne, and E. Tiesinga, “Feshbach resonances in ultracold gases,” *Rev. Mod. Phys.*, vol. 82, pp. 1225–1286, Apr 2010.
- [8] V. Efimov, “Energy levels of three resonantly interacting particles,” *Nuclear Physics A*, vol. 210, no. 1, pp. 157–188, 1973.
- [9] O. I. Kartavtsev and A. V. Malykh, “Low-energy three-body dynamics in binary quantum gases,” *Journal of Physics B: Atomic, Molecular and Optical Physics*, vol. 40, pp. 1429–1441, mar 2007.
- [10] Y. Nishida and S. Tan, “Universal Fermi gases in mixed dimensions,” *Phys. Rev. Lett.*, vol. 101, p. 170401, Oct 2008.
- [11] J. Levinsen, T. G. Tiecke, J. T. M. Walraven, and D. S. Petrov, “Atom-dimer scattering and long-lived trimers in fermionic mixtures,” *Phys. Rev. Lett.*, vol. 103, p. 153202, Oct 2009.
- [12] Y. Castin, C. Mora, and L. Pricoupenko, “Four-body Efimov effect for three fermions and a lighter particle,” *Phys. Rev. Lett.*, vol. 105, p. 223201, Nov 2010.
- [13] S. Endo, P. Naidon, and M. Ueda, “Universal physics of 2+1 particles with non-zero angular momentum,” *Few-Body Systems*, vol. 51, pp. 207–217, Nov 2011.
- [14] J. Levinsen and D. S. Petrov, “Atom-dimer and dimer-dimer scattering in fermionic mixtures near a narrow Feshbach resonance,” *The European Physical Journal D*, vol. 65, pp. 67–82, Nov 2011.
- [15] D. Blume, “Universal four-body states in heavy-light mixtures with a positive scattering length,” *Phys. Rev. Lett.*, vol. 109, p. 230404, Dec 2012.

- [16] D. Blume, “Few-body physics with ultracold atomic and molecular systems in traps,” *Reports on Progress in Physics*, vol. 75, p. 046401, mar 2012.
- [17] S. Endo, P. Naidon, and M. Ueda, “Crossover trimers connecting continuous and discrete scaling regimes,” *Phys. Rev. A*, vol. 86, p. 062703, Dec 2012.
- [18] V. Ngampruetikorn, M. M. Parish, and J. Levinsen, “Three-body problem in a two-dimensional fermi gas,” *EPL (Europhysics Letters)*, vol. 102, p. 13001, apr 2013.
- [19] J. Levinsen and M. M. Parish, “Bound states in a quasi-two-dimensional fermi gas,” *Phys. Rev. Lett.*, vol. 110, p. 055304, Jan 2013.
- [20] B. Bazak and D. S. Petrov, “Five-body efimov effect and universal pentamer in fermionic mixtures,” *Phys. Rev. Lett.*, vol. 118, p. 083002, Feb 2017.
- [21] B. Bazak, “Mass-imbalanced fermionic mixture in a harmonic trap,” *Phys. Rev. A*, vol. 96, p. 022708, Aug 2017.
- [22] R. Liu, C. Peng, and X. Cui, “Universal tetramer and pentamer bound states in two-dimensional fermionic mixtures,” *Phys. Rev. Lett.*, vol. 129, p. 073401, Aug 2022.
- [23] M. Jag, M. Zaccanti, M. Cetina, R. S. Lous, F. Schreck, R. Grimm, D. S. Petrov, and J. Levinsen, “Observation of a strong atom-dimer attraction in a mass-imbalanced fermi-fermi mixture,” *Phys. Rev. Lett.*, vol. 112, p. 075302, Feb 2014.
- [24] P. Naidon and S. Endo, “Efimov physics: a review,” *Reports on Progress in Physics*, vol. 80, p. 056001, mar 2017.
- [25] T. Kraemer, M. Mark, P. Waldburger, J. G. Danzl, C. Chin, B. Engeser, A. D. Lange, K. Pilch, A. Jaakkola, H.-C. Nägerl, and R. Grimm, “Evidence for efimov quantum states in an ultracold gas of caesium atoms,” *Nature*, vol. 440, pp. 315–318, Mar 2006.
- [26] S. Knoop, F. Ferlaino, M. Mark, M. Berninger, H. Schöbel, H.-C. Nägerl, and R. Grimm, “Observation of an efimov-like trimer resonance in ultracold atom–dimer scattering,” *Nature Physics*, vol. 5, pp. 227–230, Mar 2009.
- [27] M. Zaccanti, B. Deissler, C. D’Errico, M. Fattori, M. Jona-Lasinio, S. Müller, G. Roati, M. Inguscio, and G. Modugno, “Observation of an efimov spectrum in an atomic system,” *Nature Physics*, vol. 5, pp. 586–591, Aug 2009.
- [28] F. Ferlaino, S. Knoop, M. Berninger, W. Harm, J. P. D’Incao, H.-C. Nägerl, and R. Grimm, “Evidence for universal four-body states tied to an efimov trimer,” *Phys. Rev. Lett.*, vol. 102, p. 140401, Apr 2009.
- [29] B. Huang, L. A. Sidorenkov, R. Grimm, and J. M. Hutson, “Observation of the second triatomic resonance in efimov’s scenario,” *Phys. Rev. Lett.*, vol. 112, p. 190401, May 2014.
- [30] S. Endo, A. M. García-García, and P. Naidon, “Universal clusters as building blocks of stable quantum matter,” *Phys. Rev. A*, vol. 93, p. 053611, May 2016.
- [31] R. Liu, W. Wang, and X. Cui, “Quartet superfluid in two-dimensional mass-imbalanced fermi mixtures,” *Phys. Rev. Lett.*, vol. 131, p. 193401, Nov 2023.

- [32] C. J. M. Mathy, M. M. Parish, and D. A. Huse, “Trimers, molecules, and polarons in mass-imbalanced atomic fermi gases,” *Phys. Rev. Lett.*, vol. 106, p. 166404, Apr 2011.
- [33] P. Massignan, M. Zaccanti, and G. M. Bruun, “Polarons, dressed molecules and itinerant ferromagnetism in ultracold fermi gases,” *Rep. Progr. Phys.*, vol. 77, no. 3, p. 034401, 2014.
- [34] R. Schmidt, M. Knap, D. A. Ivanov, J.-S. You, M. Cetina, and E. Demler, “Universal many-body response of heavy impurities coupled to a fermi sea: a review of recent progress,” *Reports on Progress in Physics*, vol. 81, p. 024401, jan 2018.
- [35] R. Liu, C. Peng, and X. Cui, “Emergence of crystalline few-body correlations in mass-imbalanced fermi polarons,” *Cell Reports Physical Science*, vol. 3, no. 8, p. 100993, 2022.
- [36] A. Bulgac, M. M. Forbes, and A. Schwenk, “Induced p -wave superfluidity in asymmetric fermi gases,” *Phys. Rev. Lett.*, vol. 97, p. 020402, Jul 2006.
- [37] D. Suchet, Z. Wu, F. Chevy, and G. M. Bruun, “Long-range mediated interactions in a mixed-dimensional system,” *Phys. Rev. A*, vol. 95, p. 043643, Apr 2017.
- [38] A. Camacho-Guardian and G. M. Bruun, “Landau effective interaction between quasiparticles in a bose-einstein condensate,” *Phys. Rev. X*, vol. 8, p. 031042, Aug 2018.
- [39] W. V. Liu and F. Wilczek, “Interior gap superfluidity,” *Phys. Rev. Lett.*, vol. 90, p. 047002, Jan 2003.
- [40] M. M. Forbes, E. Gubankova, W. V. Liu, and F. Wilczek, “Stability criteria for breached-pair superfluidity,” *Phys. Rev. Lett.*, vol. 94, p. 017001, Jan 2005.
- [41] M. Iskin and C. A. R. Sá de Melo, “Two-species fermion mixtures with population imbalance,” *Phys. Rev. Lett.*, vol. 97, p. 100404, Sep 2006.
- [42] M. M. Parish, F. M. Marchetti, A. Lamacraft, and B. D. Simons, “Finite-temperature phase diagram of a polarized fermi condensate,” *Nature Phys.*, vol. 3, pp. 124–128, 02 2007.
- [43] M. A. Baranov, C. Lobo, and G. V. Shlyapnikov, “Superfluid pairing between fermions with unequal masses,” *Phys. Rev. A*, vol. 78, p. 033620, Sep 2008.
- [44] K. B. Gubbels, J. E. Baarsma, and H. T. C. Stoof, “Lifshitz point in the phase diagram of resonantly interacting ${}^6\text{Li}$ – ${}^{40}\text{K}$ mixtures,” *Phys. Rev. Lett.*, vol. 103, p. 195301, Nov 2009.
- [45] A. Gezerlis, S. Gandolfi, K. E. Schmidt, and J. Carlson, “Heavy-light fermion mixtures at unitarity,” *Phys. Rev. Lett.*, vol. 103, p. 060403, Aug 2009.
- [46] J. E. Baarsma, K. B. Gubbels, and H. T. C. Stoof, “Population and mass imbalance in atomic fermi gases,” *Phys. Rev. A*, vol. 82, p. 013624, Jul 2010.
- [47] K. Gubbels and H. Stoof, “Imbalanced fermi gases at unitarity,” *Physics Reports*, vol. 525, no. 4, pp. 255–313, 2013.

- [48] J. Wang, Y. Che, L. Zhang, and Q. Chen, “Enhancement effect of mass imbalance on fulde-ferrell-larkin-ovchinnikov type of pairing in fermi-fermi mixtures of ultracold quantum gases,” *Scientific Reports*, vol. 7, p. 39783, Jan 2017.
- [49] M. Pini, P. Pieri, R. Grimm, and G. C. Strinati, “Beyond-mean-field description of a trapped unitary fermi gas with mass and population imbalance,” *Phys. Rev. A*, vol. 103, p. 023314, Feb 2021.
- [50] C. W. von Keyserlingk and G. J. Conduit, “Itinerant ferromagnetism in an interacting fermi gas with mass imbalance,” *Phys. Rev. A*, vol. 83, p. 053625, May 2011.
- [51] A. Sotnikov, D. Cocks, and W. Hofstetter, “Advantages of mass-imbalanced ultracold fermionic mixtures for approaching quantum magnetism in optical lattices,” *Phys. Rev. Lett.*, vol. 109, p. 065301, Aug 2012.
- [52] A. Sotnikov, M. Snoek, and W. Hofstetter, “Magnetic phases of mass- and population-imbalanced ultracold fermionic mixtures in optical lattices,” *Phys. Rev. A*, vol. 87, p. 053602, May 2013.
- [53] P. Massignan, Z. Yu, and G. M. Bruun, “Itinerant ferromagnetism in a polarized two-component fermi gas,” *Phys. Rev. Lett.*, vol. 110, p. 230401, Jun 2013.
- [54] X. Cui and T.-L. Ho, “Phase separation in mixtures of repulsive fermi gases driven by mass difference,” *Phys. Rev. Lett.*, vol. 110, p. 165302, Apr 2013.
- [55] D. S. Petrov, C. Salomon, and G. V. Shlyapnikov, “Weakly bound dimers of fermionic atoms,” *Phys. Rev. Lett.*, vol. 93, p. 090404, Aug 2004.
- [56] M. Jag, M. Cetina, R. S. Lous, R. Grimm, J. Levinsen, and D. S. Petrov, “Lifetime of feshbach dimers in a fermi-fermi mixture of ${}^6\text{Li}$ and ${}^{40}\text{K}$,” *Phys. Rev. A*, vol. 94, p. 062706, Dec 2016.
- [57] K.-K. Ni, S. Ospelkaus, M. H. G. de Miranda, A. Pe’er, B. Neyenhuis, J. J. Zirbel, S. Kotochigova, P. S. Julienne, D. S. Jin, and J. Ye, “A high phase-space-density gas of polar molecules,” *Science*, vol. 322, no. 5899, pp. 231–235, 2008.
- [58] T. Takekoshi, L. Reichsöllner, A. Schindewolf, J. M. Hutson, C. R. Le Sueur, O. Dulieu, F. Ferlaino, R. Grimm, and H.-C. Nägerl, “Ultracold dense samples of dipolar rbc molecules in the rovibrational and hyperfine ground state,” *Phys. Rev. Lett.*, vol. 113, p. 205301, Nov 2014.
- [59] P. K. Molony, P. D. Gregory, Z. Ji, B. Lu, M. P. Köppinger, C. R. Le Sueur, C. L. Blackley, J. M. Hutson, and S. L. Cornish, “Creation of ultracold ${}^{87}\text{Rb}{}^{133}\text{Cs}$ molecules in the rovibrational ground state,” *Phys. Rev. Lett.*, vol. 113, p. 255301, Dec 2014.
- [60] J. W. Park, S. A. Will, and M. W. Zwierlein, “Ultracold dipolar gas of fermionic ${}^{23}\text{Na}{}^{40}\text{K}$ molecules in their absolute ground state,” *Phys. Rev. Lett.*, vol. 114, p. 205302, May 2015.
- [61] M. Guo, B. Zhu, B. Lu, X. Ye, F. Wang, R. Vexiau, N. Bouloufa-Maafa, G. Quéméner, O. Dulieu, and D. Wang, “Creation of an ultracold gas of ground-state dipolar ${}^{23}\text{Na}{}^{87}\text{Rb}$ molecules,” *Phys. Rev. Lett.*, vol. 116, p. 205303, May 2016.
- [62] H. Son, J. J. Park, W. Ketterle, and A. O. Jamison, “Collisional cooling of ultracold molecules,” *Nature*, vol. 580, pp. 197–200, Apr 2020.

- [63] L. D. Carr, D. DeMille, R. V. Krems, and J. Ye, “Cold and ultracold molecules: science, technology and applications,” *New Journal of Physics*, vol. 11, p. 055049, may 2009.
- [64] M. A. Baranov, M. Dalmonte, G. Pupillo, and P. Zoller, “Condensed matter theory of dipolar quantum gases,” *Chemical Reviews*, vol. 112, no. 9, pp. 5012–5061, 2012.
- [65] J. L. Bohn, A. M. Rey, and J. Ye, “Cold molecules: Progress in quantum engineering of chemistry and quantum matter,” *Science*, vol. 357, no. 6355, pp. 1002–1010, 2017.
- [66] A. Micheli, G. K. Brennen, and P. Zoller, “A toolbox for lattice-spin models with polar molecules,” *Nature Physics*, vol. 2, pp. 341–347, May 2006.
- [67] J. Pérez-Ríos, F. Herrera, and R. V. Krems, “External field control of collective spin excitations in an optical lattice of $^2\Sigma$ molecules,” *New Journal of Physics*, vol. 12, p. 103007, oct 2010.
- [68] N. Y. Yao, M. P. Zaletel, D. M. Stamper-Kurn, and A. Vishwanath, “A quantum dipolar spin liquid,” *Nature Physics*, vol. 14, pp. 405–410, Apr 2018.
- [69] S. L. Cornish, M. R. Tarbutt, and K. R. A. Hazzard, “Quantum computation and quantum simulation with ultracold molecules,” *Nature Physics*, vol. 20, pp. 730–740, May 2024.
- [70] M. Hughes, M. D. Frye, R. Sawant, G. Bhole, J. A. Jones, S. L. Cornish, M. R. Tarbutt, J. M. Hutson, D. Jaksch, and J. Mur-Petit, “Robust entangling gate for polar molecules using magnetic and microwave fields,” *Phys. Rev. A*, vol. 101, p. 062308, Jun 2020.
- [71] M. Karra, K. Sharma, B. Friedrich, S. Kais, and D. Herschbach, “Prospects for quantum computing with an array of ultracold polar paramagnetic molecules,” *The Journal of Chemical Physics*, vol. 144, p. 094301, 03 2016.
- [72] H. Son, J. J. Park, Y.-K. Lu, A. O. Jamison, T. Karman, and W. Ketterle, “Control of reactive collisions by quantum interference,” *Science*, vol. 375, no. 6584, pp. 1006–1010, 2022.
- [73] T. M. Rvachov, H. Son, A. T. Sommer, S. Ebadi, J. J. Park, M. W. Zwierlein, W. Ketterle, and A. O. Jamison, “Long-lived ultracold molecules with electric and magnetic dipole moments,” *Phys. Rev. Lett.*, vol. 119, p. 143001, Oct 2017.
- [74] J. J. Park, Y.-K. Lu, A. O. Jamison, T. V. Tscherbul, and W. Ketterle, “A Feshbach resonance in collisions between triplet ground-state molecules,” *Nature*, vol. 614, pp. 54–58, Feb 2023.
- [75] T. Langen, G. Valtolina, D. Wang, and J. Ye, “Quantum state manipulation and cooling of ultracold molecules,” *Nature Physics*, vol. 20, pp. 702–712, May 2024.
- [76] G. Valtolina, K. Matsuda, W. G. Tobias, J.-R. Li, L. De Marco, and J. Ye, “Dipolar evaporation of reactive molecules to below the Fermi temperature,” *Nature*, vol. 588, pp. 239–243, Dec 2020.
- [77] M. Duda, X.-Y. Chen, A. Schindewolf, R. Bause, J. von Milczewski, R. Schmidt, I. Bloch, and X.-Y. Luo, “Transition from a polaronic condensate to a degenerate Fermi gas of heteronuclear molecules,” *Nature Physics*, vol. 19, pp. 720–725, May 2023.

- [78] N. Bigagli, W. Yuan, S. Zhang, B. Bulatovic, T. Karman, I. Stevenson, and S. Will, “Observation of bose–einstein condensation of dipolar molecules,” *Nature*, vol. 631, pp. 289–293, Jul 2024.
- [79] N. V. Vitanov, A. A. Rangelov, B. W. Shore, and K. Bergmann, “Stimulated raman adiabatic passage in physics, chemistry, and beyond,” *Rev. Mod. Phys.*, vol. 89, p. 015006, Mar 2017.
- [80] V. Barbé, A. Ciamei, B. Pasquiou, L. Reichsöllner, F. Schreck, P. S. Żuchowski, and J. M. Hutson, “Observation of Feshbach resonances between alkali and closed-shell atoms,” *Nature Physics*, vol. 14, pp. 881–884, Sep 2018.
- [81] A. Green, H. Li, J. H. See Toh, X. Tang, K. C. McCormick, M. Li, E. Tiesinga, S. Kotochigova, and S. Gupta, “Feshbach resonances in p -wave three-body recombination within fermi-fermi mixtures of open-shell ${}^6\text{Li}$ and closed-shell ${}^{173}\text{Yb}$ atoms,” *Phys. Rev. X*, vol. 10, p. 031037, Aug 2020.
- [82] T. Franzen, A. Guttridge, K. E. Wilson, J. Segal, M. D. Frye, J. M. Hutson, and S. L. Cornish, “Observation of magnetic Feshbach resonances between Cs and ${}^{173}\text{Yb}$,” *Phys. Rev. Res.*, vol. 4, p. 043072, Oct 2022.
- [83] M. Borkowski, L. Reichsöllner, P. Thekkeppatt, V. Barbé, T. van Roon, K. van Druten, and F. Schreck, “Active stabilization of kilogauss magnetic fields to the ppm level for magnetoassociation on ultranarrow Feshbach resonances,” *Review of Scientific Instruments*, vol. 94, p. 073202, 07 2023.
- [84] M. D. Frye, S. L. Cornish, and J. M. Hutson, “Prospects of forming high-spin polar molecules from ultracold atoms,” *Phys. Rev. X*, vol. 10, p. 041005, Oct 2020.
- [85] E. Soave, A. Canali, Z.-X. Ye, M. Kreyer, E. Kirilov, and R. Grimm, “Optically trapped feshbach molecules of fermionic ${}^{161}\text{Dy}$ and ${}^{40}\text{K}$,” *Phys. Rev. Res.*, vol. 5, p. 033117, Aug 2023.
- [86] D. S. Petrov, “Three-body problem in fermi gases with short-range interparticle interaction,” *Phys. Rev. A*, vol. 67, p. 010703, Jan 2003.
- [87] E. Stoner, “Atomic moments in ferromagnetic metals and alloys with non-ferromagnetic elements,” *Philos. Mag.*, vol. 15, pp. 1018–1034, 1933.
- [88] G.-B. Jo, Y.-R. Lee, J.-H. Choi, C. A. Christensen, T. H. Kim, J. H. Thywissen, D. E. Pritchard, and W. Ketterle, “Itinerant ferromagnetism in a fermi gas of ultracold atoms,” *Science*, vol. 325, no. 5947, pp. 1521–1524, 2009.
- [89] F. Scazza, G. Valtolina, P. Massignan, A. Recati, A. Amico, A. Burchianti, C. Fort, M. Inguscio, M. Zaccanti, and G. Roati, “Repulsive fermi polarons in a resonant mixture of ultracold ${}^6\text{Li}$ atoms,” *Phys. Rev. Lett.*, vol. 118, p. 083602, Feb 2017.
- [90] G. Valtolina, F. Scazza, A. Amico, A. Burchianti, A. Recati, T. Enss, M. Inguscio, M. Zaccanti, and G. Roati, “Exploring the ferromagnetic behaviour of a repulsive fermi gas through spin dynamics,” *Nat. Phys.*, vol. 13, pp. 704–709, Jul 2017.
- [91] A. Amico, F. Scazza, G. Valtolina, P. E. S. Tavares, W. Ketterle, M. Inguscio, G. Roati, and M. Zaccanti, “Time-resolved observation of competing attractive and repulsive short-range correlations in strongly interacting fermi gases,” *Phys. Rev. Lett.*, vol. 121, p. 253602, Dec 2018.

- [92] F. Scazza, G. Valtolina, A. Amico, P. E. S. Tavares, M. Inguscio, W. Ketterle, G. Roati, and M. Zaccanti, “Exploring emergent heterogeneous phases in strongly repulsive fermi gases,” *Phys. Rev. A*, vol. 101, p. 013603, Jan 2020.
- [93] R. Van Zee, C. Baumann, and W. Weltner, “HCr, LiCr, and NaCr molecules: ESR and ground state properties,” *Chemical Physics Letters*, vol. 113, no. 6, pp. 524–529, 1985.
- [94] S. Finelli, A. Ciamei, B. Restivo, M. Schemmer, A. Cosco, M. Inguscio, A. Trenkwalder, K. Zaremba-Kopczyk, M. Gronowski, M. Tomza, and M. Zaccanti, “Ultracold LiCr: A new pathway to quantum gases of paramagnetic polar molecules,” *PRX Quantum*, vol. 5, p. 020358, Jun 2024.
- [95] C. Joachain, *Quantum Collision Theory*. North-Holland Publishing Company, 1975.
- [96] E. Merzbacher, *Quantum Mechanics*. Wiley, 1998.
- [97] B. H. Bransden and C. J. Joachain, *Physics of atoms and molecules*. Pearson Education, Harlow, 2003.
- [98] C. Bertulani and P. Danielewicz, *Introduction to Nuclear Reactions*. Graduate Student Series in Physics, CRC Press, 2019.
- [99] C. Cohen-Tannoudji, B. Diu, and F. Laloë, *Quantum Mechanics*. No. v. 1 in A Wiley - Interscience publication, Wiley, 1977.
- [100] A. Messiah, *Quantum Mechanics*. No. v. 2 in Quantum Mechanics, Elsevier Science, 1961.
- [101] L. Landau and E. Lifshits, *Quantum Mechanics: Non-Relativistic Theory*. A-W series in advanced physics, Oxford: Pergamon Press, 1977.
- [102] S. Finelli, “Ultracold chromium-lithium fermionic mixtures with resonant interactions,” 2021.
- [103] M. Baranger, “Simplified quantum-mechanical theory of pressure broadening,” *Phys. Rev.*, vol. 111, pp. 481–493, Jul 1958.
- [104] M. Baranger, “General impact theory of pressure broadening,” *Phys. Rev.*, vol. 112, pp. 855–865, Nov 1958.
- [105] E. P. Wigner, “On the behavior of cross sections near thresholds,” *Phys. Rev.*, vol. 73, pp. 1002–1009, May 1948.
- [106] D. S. Petrov, “The few-atom problem,” in *Many-Body Physics with Ultracold Gases: Lecture Notes of the Les Houches Summer School: Volume 94*, Oxford University Press, 11 2012.
- [107] H. Bethe and R. Peierls, “Quantum Theory of the Dipole,” *Proceedings of the Royal Society of London Series A*, vol. 148, pp. 146–156, Jan. 1935.
- [108] G. Breit and E. Wigner, “Capture of slow neutrons,” *Phys. Rev.*, vol. 49, pp. 519–531, Apr 1936.
- [109] P. Massignan, “Polarons and dressed molecules near narrow feshbach resonances,” *Europhys. Lett.*, vol. 98, no. 1, p. 10012, 2012.

- [110] P. Naidon, “Closed-channel parameters of Feshbach resonances,” *SciPost Phys.*, vol. 18, p. 036, 2025.
- [111] M. Zaccanti, “Mass-imbalanced Fermi mixtures with resonant interactions,” *arXiv:2306.02736*, 2023.
- [112] K. M. O’Hara, S. L. Hemmer, S. R. Granade, M. E. Gehm, J. E. Thomas, V. Venturi, E. Tiesinga, and C. J. Williams, “Measurement of the zero crossing in a feshbach resonance of fermionic ${}^6\text{Li}$,” *Phys. Rev. A*, vol. 66, p. 041401, Oct 2002.
- [113] S. Jochim, M. Bartenstein, G. Hendl, J. H. Denschlag, R. Grimm, A. Mosk, and M. Weidemüller, “Magnetic field control of elastic scattering in a cold gas of fermionic lithium atoms,” *Phys. Rev. Lett.*, vol. 89, p. 273202, Dec 2002.
- [114] T. Loftus, C. A. Regal, C. Ticknor, J. L. Bohn, and D. S. Jin, “Resonant control of elastic collisions in an optically trapped fermi gas of atoms,” *Phys. Rev. Lett.*, vol. 88, p. 173201, Apr 2002.
- [115] C. A. Regal and D. S. Jin, “Measurement of positive and negative scattering lengths in a fermi gas of atoms,” *Phys. Rev. Lett.*, vol. 90, p. 230404, Jun 2003.
- [116] M. Inguscio, W. Ketterle, and C. Salomon, *Ultracold Fermi gases*, vol. 164. IOS Press, 2007.
- [117] S. Giorgini, L. P. Pitaevskii, and S. Stringari, “Theory of ultracold atomic fermi gases,” *Rev. Mod. Phys.*, vol. 80, pp. 1215–1274, Oct 2008.
- [118] W. Zwerger, ed., *The BCS-BEC Crossover and the Unitary Fermi Gas*, vol. 836 of *Lecture Notes in Physics*. Springer Berlin Heidelberg, 2012.
- [119] L. Radzihovsky and D. E. Sheehy, “Imbalanced feshbach-resonant fermi gases,” *Rep. Progr. Phys.*, vol. 73, no. 7, p. 076501, 2010.
- [120] A. Ciamei, S. Finelli, A. Cosco, M. Inguscio, A. Trenkwalder, and M. Zaccanti, “Double-degenerate fermi mixtures of ${}^6\text{Li}$ and ${}^{53}\text{Cr}$ atoms,” *Phys. Rev. A*, vol. 106, p. 053318, Nov 2022.
- [121] E. Neri, A. Ciamei, C. Simonelli, I. Goti, M. Inguscio, A. Trenkwalder, and M. Zaccanti, “Realization of a cold mixture of fermionic chromium and lithium atoms,” *Phys. Rev. A*, vol. 101, p. 063602, Jun 2020.
- [122] C. Simonelli, E. Neri, A. Ciamei, I. Goti, M. Inguscio, A. Trenkwalder, and M. Zaccanti, “Realization of a high power optical trapping setup free from thermal lensing effects,” *Opt. Express*, vol. 27, pp. 27215–27228, Sep 2019.
- [123] E. Neri, *Mass imbalanced Fermi mixtures with 2- and 3-body resonant interactions*. PhD thesis, University of Florence, 2019.
- [124] F. M. Spiegelhalter, A. Trenkwalder, D. Naik, G. Kerner, E. Wille, G. Hendl, F. Schreck, and R. Grimm, “All-optical production of a degenerate mixture of ${}^6\text{Li}$ and ${}^{40}\text{K}$ and creation of heteronuclear molecules,” *Phys. Rev. A*, vol. 81, p. 043637, Apr 2010.
- [125] R. Chicireanu, A. Pouderos, R. Barbé, B. Laburthe-Tolra, E. Maréchal, L. Vernac, J.-C. Keller, and O. Gorceix, “Simultaneous magneto-optical trapping of bosonic and fermionic chromium atoms,” *Phys. Rev. A*, vol. 73, p. 053406, May 2006.

- [126] B. Naylor, A. Reigue, E. Maréchal, O. Gorceix, B. Laburthe-Tolra, and L. Vernac, “Chromium dipolar fermi sea,” *Phys. Rev. A*, vol. 91, p. 011603, Jan 2015.
- [127] Chicireanu, R., Beaufils, Q., Pouderous, A., Laburthe-Tolra, B., Maréchal, É., Vernac, L., Keller, J.-C., and Gorceix, O., “Accumulation of chromium metastable atoms into an optical trap,” *Eur. Phys. J. D*, vol. 45, no. 2, pp. 189–195, 2007.
- [128] Q. Beaufils, R. Chicireanu, T. Zanon, B. Laburthe-Tolra, E. Maréchal, L. Vernac, J.-C. Keller, and O. Gorceix, “All-optical production of chromium bose-einstein condensates,” *Phys. Rev. A*, vol. 77, p. 061601, Jun 2008.
- [129] E. Wille, F. M. Spiegelhalder, G. Kerner, D. Naik, A. Trenkwalder, G. Hendl, F. Schreck, R. Grimm, T. G. Tiecke, J. T. M. Walraven, S. J. J. M. F. Kokkelmans, E. Tiesinga, and P. S. Julienne, “Exploring an ultracold fermi-fermi mixture: Interspecies feshbach resonances and scattering properties of ^6Li and ^{40}K ,” *Phys. Rev. Lett.*, vol. 100, p. 053201, Feb 2008.
- [130] D. Naik, A. Trenkwalder, C. Kohstall, F. Spiegelhalder, M. Zaccanti, G. Hendl, F. Schreck, R. Grimm, T. Hanna, and P. Julienne, “Feshbach resonances in the 6Li - 40K fermi-fermi mixture: elastic versus inelastic interactions,” *The European Physical Journal D*, vol. 65, pp. 55–65, 2011.
- [131] A. Burchianti, G. Valtolina, J. A. Seman, E. Pace, M. De Pas, M. Inguscio, M. Zaccanti, and G. Roati, “Efficient all-optical production of large ^6Li quantum gases using D_1 gray-molasses cooling,” *Phys. Rev. A*, vol. 90, p. 043408, Oct 2014.
- [132] H. Metcalf, P. Van der Straten, J. Birman, J. Lynn, H. Stanley, M. Silverman, and M. Voloshin, *Laser Cooling and Trapping*. Graduate texts in contemporary physics, Springer, 1999.
- [133] R. Chang, A. L. Hoendervanger, Q. Bouton, Y. Fang, T. Klafka, K. Audo, A. Aspect, C. I. Westbrook, and D. Clément, “Three-dimensional laser cooling at the doppler limit,” *Phys. Rev. A*, vol. 90, p. 063407, Dec 2014.
- [134] P. D. Lett, W. D. Phillips, S. L. Rolston, C. E. Tanner, R. N. Watts, and C. I. Westbrook, “Optical molasses,” *J. Opt. Soc. Am. B*, vol. 6, pp. 2084–2107, Nov 1989.
- [135] A. Frisch, *Dipolar Quantum Gases of Erbium*. PhD thesis, University of Innsbruck, 2014.
- [136] F. P. D. Santos, F. Perales, J. Léonard, A. Sinatra, J. Wang, F. S. Pavone, E. Rasel, C. S. Unnikrishnan, and M. Leduc, “Efficient magneto-optical trapping of a metastable helium gas,” *The European Physical Journal - Applied Physics*, vol. 14, no. 1, p. 69–76, 2001.
- [137] G. Bismut, B. Pasquiou, D. Ciampini, B. Laburthe-Tolra, E. Maréchal, L. Vernac, and O. Gorceix, “Optimized loading of an optical dipole trap for the production of chromium becs,” *Applied Physics B*, vol. 102, pp. 1–9, Jan 2011.
- [138] G. Zürn, T. Lompe, A. N. Wenz, S. Jochim, P. S. Julienne, and J. M. Hutson, “Precise characterization of ^6Li feshbach resonances using trap-sideband-resolved rf spectroscopy of weakly bound molecules,” *Phys. Rev. Lett.*, vol. 110, p. 135301, Mar 2013.

- [139] A. Ciamei, S. Finelli, A. Trenkwalder, M. Inguscio, A. Simoni, and M. Zaccanti, “Exploring ultracold collisions in ${}^6\text{Li}$ – ${}^{53}\text{Cr}$ fermi mixtures: Feshbach resonances and scattering properties of a novel alkali-transition metal system,” *Phys. Rev. Lett.*, vol. 129, p. 093402, Aug 2022.
- [140] M. Lu, N. Q. Burdick, and B. L. Lev, “Quantum degenerate dipolar fermi gas,” *Phys. Rev. Lett.*, vol. 108, p. 215301, May 2012.
- [141] K. Aikawa, A. Frisch, M. Mark, S. Baier, R. Grimm, and F. Ferlaino, “Reaching fermi degeneracy via universal dipolar scattering,” *Phys. Rev. Lett.*, vol. 112, p. 010404, Jan 2014.
- [142] T. Maier, H. Kadau, M. Schmitt, M. Wenzel, I. Ferrier-Barbut, T. Pfau, A. Frisch, S. Baier, K. Aikawa, L. Chomaz, M. J. Mark, F. Ferlaino, C. Makrides, E. Tiesinga, A. Petrov, and S. Kotochigova, “Emergence of chaotic scattering in ultracold er and dy,” *Phys. Rev. X*, vol. 5, p. 041029, Nov 2015.
- [143] M. Bartenstein, A. Altmeyer, S. Riedl, R. Geursen, S. Jochim, C. Chin, J. H. Denschlag, R. Grimm, A. Simoni, E. Tiesinga, C. J. Williams, and P. S. Julienne, “Precise determination of ${}^6\text{Li}$ cold collision parameters by radio-frequency spectroscopy on weakly bound molecules,” *Phys. Rev. Lett.*, vol. 94, p. 103201, Mar 2005.
- [144] J. Werner, A. Griesmaier, S. Hensler, J. Stuhler, T. Pfau, A. Simoni, and E. Tiesinga, “Observation of feshbach resonances in an ultracold gas of ${}^{52}\text{Cr}$,” *Phys. Rev. Lett.*, vol. 94, p. 183201, May 2005.
- [145] C. Ravensbergen, E. Soave, V. Corre, M. Kreyer, B. Huang, E. Kirilov, and R. Grimm, “Resonantly interacting fermi-fermi mixture of ${}^{161}\text{Dy}$ and ${}^{40}\text{K}$,” *Phys. Rev. Lett.*, vol. 124, p. 203402, May 2020.
- [146] F. Schäfer, N. Mizukami, and Y. Takahashi, “Feshbach resonances of large-mass-imbalance Er-Li mixtures,” *Phys. Rev. A*, vol. 105, p. 012816, Jan 2022.
- [147] C. Ticknor, C. A. Regal, D. S. Jin, and J. L. Bohn, “Multiplet structure of feshbach resonances in nonzero partial waves,” *Phys. Rev. A*, vol. 69, p. 042712, Apr 2004.
- [148] Y. Cui, C. Shen, M. Deng, S. Dong, C. Chen, R. Lü, B. Gao, M. K. Tey, and L. You, “Observation of broad d -wave feshbach resonances with a triplet structure,” *Phys. Rev. Lett.*, vol. 119, p. 203402, Nov 2017.
- [149] B. Zhu, S. Häfner, B. Tran, M. Gerken, J. Ulmanis, E. Tiemann, and M. Weidemüller, “Spin-rotation coupling in p-wave Feshbach resonances,” 2019.
- [150] L. Fouché, A. Boissé, G. Berthet, S. Lepoutre, A. Simoni, and T. Bourdel, “Quantitative analysis of losses close to a d -wave open-channel feshbach resonance in ${}^{39}\text{K}$,” *Phys. Rev. A*, vol. 99, p. 022701, Feb 2019.
- [151] K. M. Jones, P. D. Lett, E. Tiesinga, and P. S. Julienne, “Fitting line shapes in photoassociation spectroscopy of ultracold atoms: A useful approximation,” *Phys. Rev. A*, vol. 61, p. 012501, Dec 1999.
- [152] W. J. Childs, L. S. Goodman, and D. von Ehrenstein, “Magnetic hyperfine interaction of cr53,” *Physical Review*, 1963.

- [153] E. Arimondo, M. Inguscio, and P. Violino, “Experimental determinations of the hyperfine structure in the alkali atoms,” *Rev. Mod. Phys.*, vol. 49, pp. 31–75, Jan 1977.
- [154] G.-H. Jeung, D. Hagebaum-Reignier, and M. J. Jamieson, “Cold collisions of alkali-metal atoms and chromium atoms,” *Journal of Physics B: Atomic, Molecular and Optical Physics*, vol. 43, p. 235208, nov 2010.
- [155] See the Supplemental Material of our Ref. [139] (available at <http://link.aps.org/supplemental/10.1103/PhysRevLett.129.093402>), which includes additional references, for further details about theory model, extraction of resonance parameters, additional theory-experiment comparison, and prediction of scattering properties of other isotopic pairs.
- [156] C. Kohstall, M. Zaccanti, M. Jag, A. Trenkwalder, P. Massignan, G. M. Bruun, F. Schreck, and R. Grimm, “Metastability and coherence of repulsive polarons in a strongly interacting fermi mixture,” *Nature*, vol. 485, pp. 615–618, May 2012.
- [157] A. Viel and A. Simoni, “Feshbach resonances and weakly bound molecular states of boson-boson and boson-fermion pairs,” *Phys. Rev. A*, vol. 93, p. 042701, Apr 2016.
- [158] J. Li, J. Liu, L. Luo, and B. Gao, “Three-body recombination near a narrow feshbach resonance in ^6Li ,” *Phys. Rev. Lett.*, vol. 120, p. 193402, May 2018.
- [159] L. Vichi and S. Stringari, “Collective oscillations of an interacting trapped Fermi gas,” *Phys. Rev. A*, vol. 60, pp. 4734–4737, Dec 1999.
- [160] S. D. Gensemer and D. S. Jin, “Transition from collisionless to hydrodynamic behavior in an ultracold Fermi gas,” *Phys. Rev. Lett.*, vol. 87, p. 173201, Oct 2001.
- [161] G. Ferrari, M. Inguscio, W. Jastrzebski, G. Modugno, G. Roati, and A. Simoni, “Collisional properties of ultracold K-Rb mixtures,” *Phys. Rev. Lett.*, vol. 89, p. 053202, Jul 2002.
- [162] F. Ferlaino, R. J. Brecha, P. Hannaford, F. Riboli, G. Roati, G. Modugno, and M. Inguscio, “Dipolar oscillations in a quantum degenerate Fermi–Bose atomic mixture,” *Journal of Optics B: Quantum and Semiclassical Optics*, vol. 5, p. S3, apr 2003.
- [163] S. Zhang and T.-L. Ho, “Atom loss maximum in ultra-cold fermi gases,” *New Journal of Physics*, vol. 13, no. 5, p. 055003, 2011.
- [164] C. Regal. PhD thesis, University of Colorado, Boulder, 2006.
- [165] M. Greiner, C. A. Regal, and D. S. Jin, “Emergence of a molecular bose–einstein condensate from a fermi gas,” *Nature*, vol. 426, pp. 537–540, Dec 2003.
- [166] C. A. Regal, M. Greiner, and D. S. Jin, “Lifetime of molecule-atom mixtures near a feshbach resonance in ^{40}K ,” *Phys. Rev. Lett.*, vol. 92, p. 083201, Feb 2004.
- [167] W. Ketterle, D. S. Durfee, and D. M. Stamper-Kurn, “Making, probing and understanding bose-einstein condensates,” 1999.
- [168] W. Ketterle and M. W. Zwierlein, “Making, probing and understanding ultracold Fermi gases,” *Nuovo Cimento Rivista Serie*, vol. 31, pp. 247–422, May 2008.

- [169] K. Zaremba-Kopczy, M. Gronowski, A. Ciamei, M. Zaccanti, and M. Tomza, “Ab initio electronic structure of the LiCr molecule: prospects for the formation and precision measurements,” *Article in preparation*, 2025.
- [170] K. E. Strecker, G. B. Partridge, and R. G. Hulet, “Conversion of an atomic fermi gas to a long-lived molecular bose gas,” *Phys. Rev. Lett.*, vol. 91, p. 080406, Aug 2003.
- [171] C. A. Regal, C. Ticknor, J. L. Bohn, and D. S. Jin, “Creation of ultracold molecules from a Fermi gas of atoms,” *Nature*, vol. 424, pp. 47–50, July 2003.
- [172] E. Hodby, S. T. Thompson, C. A. Regal, M. Greiner, A. C. Wilson, D. S. Jin, E. A. Cornell, and C. E. Wieman, “Production efficiency of ultracold feshbach molecules in bosonic and fermionic systems,” *Phys. Rev. Lett.*, vol. 94, p. 120402, Mar 2005.
- [173] S. B. Papp and C. E. Wieman, “Observation of heteronuclear feshbach molecules from a $^{85}\text{Rb} - ^{87}\text{Rb}$ gas,” *Phys. Rev. Lett.*, vol. 97, p. 180404, Oct 2006.
- [174] A.-C. Voigt, M. Taglieber, L. Costa, T. Aoki, W. Wieser, T. W. Hänsch, and K. Dieckmann, “Ultracold heteronuclear fermi-fermi molecules,” *Phys. Rev. Lett.*, vol. 102, p. 020405, Jan 2009.
- [175] T. D. Cumby, R. A. Shewmon, M.-G. Hu, J. D. Perreault, and D. S. Jin, “Feshbach-molecule formation in a bose-fermi mixture,” *Phys. Rev. A*, vol. 87, p. 012703, Jan 2013.
- [176] T. Köhler, K. Góral, and P. S. Julienne, “Production of cold molecules via magnetically tunable feshbach resonances,” *Rev. Mod. Phys.*, vol. 78, pp. 1311–1361, Dec 2006.
- [177] T. Yamakoshi, S. Watanabe, C. Zhang, and C. H. Greene, “Stochastic and equilibrium pictures of the ultracold fano-feshbach-resonance molecular conversion rate,” *Phys. Rev. A*, vol. 87, p. 053604, May 2013.
- [178] P. Politzer and J. S. Murray, “The hellmann-feynman theorem: a perspective,” *Journal of Molecular Modeling*, vol. 24, p. 266, Aug 2018.
- [179] A. Yang, S. Botsi, S. Kumar, S. B. Pal, M. M. Lam, I. Čepaitė, A. Laugharn, and K. Dieckmann, “Singlet pathway to the ground state of ultracold polar molecules,” *Phys. Rev. Lett.*, vol. 124, p. 133203, Apr 2020.
- [180] S. T. Thompson, E. Hodby, and C. E. Wieman, “Ultracold molecule production via a resonant oscillating magnetic field,” *Phys. Rev. Lett.*, vol. 95, p. 190404, Nov 2005.
- [181] G. B. Partridge, K. E. Strecker, R. I. Kamar, M. W. Jack, and R. G. Hulet, “Molecular probe of pairing in the bec-bcs crossover,” *Phys. Rev. Lett.*, vol. 95, p. 020404, Jul 2005.
- [182] T. Mukaiyama, J. R. Abo-Shaeer, K. Xu, J. K. Chin, and W. Ketterle, “Dissociation and decay of ultracold sodium molecules,” *Phys. Rev. Lett.*, vol. 92, p. 180402, May 2004.
- [183] A. Z. Lam, N. Bigagli, C. Warner, W. Yuan, S. Zhang, E. Tiemann, I. Stevenson, and S. Will, “High phase-space density gas of nacs feshbach molecules,” *Phys. Rev. Research*, vol. 4, p. L022019, Apr 2022.

- [184] H. Ladjimi and M. Tomza, “Diatomic molecules of alkali-metal and alkaline-earth-metal atoms: interaction potentials, dipole moments, and polarizabilities,” *arXiv:2303.17527*, 2023.
- [185] T. S. Roussy, L. Caldwell, T. Wright, W. B. Cairncross, Y. Shagam, K. B. Ng, N. Schlossberger, S. Y. Park, A. Wang, J. Ye, and E. A. Cornell, “An improved bound on the electron’s electric dipole moment,” *Science*, vol. 381, p. 46, 2023.
- [186] S. S. Kondov, C.-H. Lee, K. H. Leung, C. Liedl, I. Majewska, R. Moszynski, and T. Zelevinsky, “Molecular lattice clock with long vibrational coherence,” *Nat. Phys.*, vol. 15, p. 1118, 2019.
- [187] K. H. Leung, B. Iritani, E. Tiberi, I. Majewska, M. Borkowski, R. Moszynski, and T. Zelevinsky, “Terahertz vibrational molecular clock with systematic uncertainty at the 10^{-14} level,” *Phys. Rev. X*, vol. 13, p. 011047, Mar 2023.
- [188] C. Cao, E. Elliott, J. Joseph, H. Wu, J. Petricka, T. Schäfer, and J. E. Thomas, “Universal quantum viscosity in a unitary fermi gas,” *Science*, vol. 331, no. 6013, pp. 58–61, 2011.
- [189] A. Sommer, M. Ku, and M. W. Zwierlein, “Spin transport in polaronic and superfluid fermi gases,” *New Journal of Physics*, vol. 13, no. 5, p. 055009, 2011.
- [190] A. Sommer, M. Ku, G. Roati, and M. W. Zwierlein, “Universal spin transport in a strongly interacting Fermi gas,” *Nature*, vol. 472, pp. 201–4, Apr. 2011.
- [191] G. M. Bruun, “Spin diffusion in fermi gases,” *New Journal of Physics*, vol. 13, p. 035005, mar 2011.
- [192] F. Reif, *Fundamentals of Statistical and Thermal Physics*. Fundamentals of Physics Series, McGraw-Hill, 1965.
- [193] G. E. Uhlenbeck and L. S. Ornstein, “On the theory of the brownian motion,” *Phys. Rev.*, vol. 36, pp. 823–841, Sep 1930.
- [194] R. Metzler and J. Klafter, “The random walk’s guide to anomalous diffusion: a fractional dynamics approach,” *Physics Reports*, vol. 339, no. 1, pp. 1–77, 2000.
- [195] A. Einstein, “Über die von der molekularkinetischen theorie der wärme geforderte bewegung von in ruhenden flüssigkeiten suspendierten teilchen,” *Annalen der Physik*, vol. 322, no. 8, pp. 549–560, 1905.
- [196] A. Einstein, “Zur theorie der brownschen bewegung,” *Annalen der Physik*, vol. 324, no. 2, pp. 371–381, 1906.
- [197] R. Huang, I. Chavez, K. M. Taute, B. Lukić, S. Jeney, M. G. Raizen, and E.-L. Florin, “Direct observation of the full transition from ballistic to diffusive brownian motion in a liquid,” *Nature Physics*, vol. 7, pp. 576–580, Jul 2011.
- [198] P. Langevin, “Sur la théorie du mouvement brownien. (French) [On the theory of Brownian motion],” *J-C-R-ACAD-SCI-PARIS*, vol. 146, pp. 530–533, 1908.
- [199] M. V. Smoluchowski, “Drei Vorträge über Diffusion, Brownsche Bewegung und Koagulation von Kolloidteilchen,” *Zeitschrift für Physik*, vol. 17, pp. 557–585, Jan. 1916.

- [200] Y. Chen, X. Wang, and W. Deng, “Subdiffusion in an external force field,” *Phys. Rev. E*, vol. 99, p. 042125, Apr 2019.
- [201] F. A. Oliveira, R. M. S. Ferreira, L. C. Lapas, and M. H. Vainstein, “Anomalous diffusion: A basic mechanism for the evolution of inhomogeneous systems,” *Frontiers in Physics*, vol. 7, 2019.
- [202] M. Abramowitz and I. Stegun, *Handbook of Mathematical Functions: With Formulas, Graphs, and Mathematical Tables*. Applied mathematics series, Dover Publications, 1965.
- [203] S. Finelli, “https://github.com/blochelectron/licr_pinballmachine.”
- [204] E. P. Wigner, “Lower limit for the energy derivative of the scattering phase shift,” *Phys. Rev.*, vol. 98, pp. 145–147, Apr 1955.
- [205] J. Taylor, *Scattering Theory: The Quantum Theory of Nonrelativistic Collisions*. Dover Books on Engineering, Dover Publications, 2012.
- [206] D. Blume, “Small mass- and trap-imbalanced two-component fermi systems,” *Phys. Rev. A*, vol. 78, p. 013613, Jul 2008.
- [207] F. Deuretzbacher, K. Plassmeier, D. Pfannkuche, F. Werner, C. Ospelkaus, S. Ospelkaus, K. Sengstock, and K. Bongs, “Heteronuclear molecules in an optical lattice: Theory and experiment,” *Phys. Rev. A*, vol. 77, p. 032726, Mar 2008.
- [208] M. Anderlini, D. Ciampini, D. Cossart, E. Courtade, M. Cristiani, C. Sias, O. Morsch, and E. Arimondo, “Model for collisions in ultracold-atom mixtures,” *Phys. Rev. A*, vol. 72, p. 033408, Sep 2005.
- [209] S. Barbosa, M. Kiefer-Emmanouilidis, F. Lang, J. Koch, and A. Widera, “Characterizing localization effects in an ultracold disordered fermi gas by diffusion analysis,” *Phys. Rev. Res.*, vol. 6, p. 033039, Jul 2024.
- [210] T. Schäfer, “Generalized theory of diffusion based on kinetic theory,” *Phys. Rev. A*, vol. 94, p. 043644, Oct 2016.
- [211] G. Roati, C. D’Errico, L. Fallani, M. Fattori, C. Fort, M. Zaccanti, G. Modugno, M. Modugno, and M. Inguscio, “Anderson localization of a non-interacting bose-einstein condensate,” *Nature*, vol. 453, pp. 895–898, Jun 2008.
- [212] B. Deissler, M. Zaccanti, G. Roati, C. D’Errico, M. Fattori, M. Modugno, G. Modugno, and M. Inguscio, “Delocalization of a disordered bosonic system by repulsive interactions,” *Nature Physics*, vol. 6, pp. 354–358, May 2010.
- [213] E. Lucioni, B. Deissler, L. Tanzi, G. Roati, M. Zaccanti, M. Modugno, M. Larcher, F. Dalfovo, M. Inguscio, and G. Modugno, “Observation of subdiffusion in a disordered interacting system,” *Phys. Rev. Lett.*, vol. 106, p. 230403, Jun 2011.
- [214] G. Semeghini, M. Landini, P. Castilho, S. Roy, G. Spagnolli, A. Trenkwalder, M. Fattori, M. Inguscio, and G. Modugno, “Measurement of the mobility edge for 3d anderson localization,” *Nature Physics*, vol. 11, pp. 554–559, Jul 2015.
- [215] S. E. Skipetrov and I. M. Sokolov, “Ioffe-regel criterion for anderson localization in the model of resonant point scatterers,” *Phys. Rev. B*, vol. 98, p. 064207, Aug 2018.

- [216] P. W. Anderson, “Absence of diffusion in certain random lattices,” *Phys. Rev.*, vol. 109, pp. 1492–1505, Mar 1958.
- [217] P. Massignan and Y. Castin, “Three-dimensional strong localization of matter waves by scattering from atoms in a lattice with a confinement-induced resonance,” *Phys. Rev. A*, vol. 74, p. 013616, Jul 2006.
- [218] A. Cosco, “Optimized production and probing of resonantly interacting lithium-chromium fermi mixtures,” 2023.
- [219] A. J. Matthies, J. M. Mortlock, L. A. McArd, A. P. Raghuram, A. D. Innes, P. D. Gregory, S. L. Bromley, and S. L. Cornish, “Long-distance optical-conveyor-belt transport of ultracold ^{133}Cs and ^{87}Rb atoms,” *Phys. Rev. A*, vol. 109, p. 023321, Feb 2024.
- [220] E. J. Heller, “Quantum proximity resonances,” *Phys. Rev. Lett.*, vol. 77, pp. 4122–4125, Nov 1996.
- [221] W. Childs, G. Goodman, and L. Goodman, “Electric-dipole moments in cai and caf by molecular-beam laser-rf double-resonance study of stark splittings,” *Journal of Molecular Spectroscopy*, vol. 115, no. 1, pp. 215–225, 1986.
- [222] L. Anderegg, S. Burchesky, Y. Bao, S. S. Yu, T. Karman, E. Chae, K.-K. Ni, W. Ketterle, and J. M. Doyle, “Observation of microwave shielding of ultracold molecules,” *Science*, vol. 373, no. 6556, pp. 779–782, 2021.
- [223] J.-R. Li, W. G. Tobias, K. Matsuda, C. Miller, G. Valtolina, L. De Marco, R. R. W. Wang, L. Lassablière, G. Quémener, J. L. Bohn, and J. Ye, “Tuning of dipolar interactions and evaporative cooling in a three-dimensional molecular quantum gas,” *Nature Physics*, vol. 17, pp. 1144–1148, Oct 2021.
- [224] B. Mukherjee, M. D. Frye, C. R. Le Sueur, M. R. Tarbutt, and J. M. Hutson, “Shielding collisions of ultracold CaF molecules with static electric fields,” *Phys. Rev. Res.*, vol. 5, p. 033097, Aug 2023.
- [225] X.-Y. Chen, A. Schindewolf, S. Eppelt, R. Bause, M. Duda, S. Biswas, T. Karman, T. Hilker, I. Bloch, and X.-Y. Luo, “Field-linked resonances of polar molecules,” *Nature*, vol. 614, pp. 59–63, Feb 2023.